THESE POUR OBTENIR LE GRADE DE DOCTEUR DE
L'ECOLE NATIONALE SUPERIEURE DE CHIMIE DE MONTPELLIER

En Chimie et Physico-Chimie des Matériaux

École doctorale Sciences Chimiques Balard (ED 459)

Unité de recherche Institut Européen des Membranes

Molecular doping of copper-based catalysts for the electrocatalytic conversion of CO_2 to multi-carbon products

Présentée par **Huali Wu**
Le 10 Novembre 2022

Sous la direction du **Pr. Pilippe MIELE**
et la co-direction du **Dr. Damien VOIRY**

Devant le jury composé de

Raffaella BUONSANTI, Professeur, Swiss Federal Institute of Technology Lausanne	Rapporteur
Cicero GIANCARLO, Associate Professeur, Politecnico di Torino	Rapporteur
Marc ROBERT, Professeur, Paris Cité University, CNRS	(President) Examinateur
Sara CAVALIERE, Professeur, Université de Montpellier	Examinateur
Philippe MIELE, Professeur, Université de Montpellier	Directeur
Damien VOIRY, Chargé de Recherche CNRS, Université de Montpellier	Co-directeur

Acknowledgements

First, I would like to thank my committee members, Professor Raffaella Buonsanti and Professor Cicero Giancarlo, for their valuable input on my work. In addition, thanks to Professor Marc Robert and Professor Sara Cavaliere for serving as the chairs of my oral defense committee. I appreciated all of your questions and different perspectives on my work based on your respective fields of expertise.

Then, I must give a big thanks to my principal adviser, Dr. Damien Voiry, for all his guidance, motivation, support and patience on my research work over the years. Damien is well known for the positivity and enthusiasm that he brings to research because these attributes are truly contagious. His encouragement and unending support have been invaluable for staying motivated in the face of failure that is inevitable during pursuing my PhD. By enabling me to engage with the broader CO_2-derived energy at IEM and ENSCM, I have developed a much better understanding of the diverse challenges and opportunities we face in transitioning to a more sustainable global energy economy. And, in doing so, I have been able to discover my passion for working to accelerate this transition in order to avoid the worst impacts of greenhouse gas. Last but not least, Damien has an incredible ability to connect and engage with basically anyone he speaks with. Not only does this make him a great communicator and mentor, but it has also opened up countless opportunities for collaborations, without which, it is an extreme understatement to say that my PhD would not have been the same. I cannot understate the pivotal role he has played in my personal and professional growth. I have learned so much from Damien during my time in his lab, and I really cannot thank him enough. Next, I need to give another big thanks to my second adviser Professor Philippe Miele, the leader of DM3 group in IEM, gave me suggestions and help on my research work during these years.

I also appreciate Dr. Luc Lajaunie, Dr. Eddy Petit, Dr. Valérie Flaud, Dr. Chrystelle Salameh and Dr. Nicolas Onofrio who had provided the big assistances for my samples' tests, data analysis and physical simulations over the years. I'm also grateful for Dr. Kun Qi, Dr. Ji Li, Dr. Lingqi Huang, Dr. Yang Zhang, and the PhD students Wensen Wang and Jiefeng Liu who helped me a lot in my research work and lives. We shared many happiness and sorrow together, especially since we haven't been back to China for at least three years because of the Covid. I've spent all the important Chinese holidays with all of you! I would also like to acknowledge Dr. Quentin Hanniet, Dr. Ghenwa Chawich, and the PhD students Joelle El Hayek, Hippolyte Dory and Bonito Aristide Karamoko who gave me a hand when I had some difficulties in French. They gave me many useful advices and helped me learn and realize a lot of French culture and cuisine. I would never forget them! Furthermore, I also want to thank the European Commission for funding my PhD, which is the European Research Council (ERC) under the European Union's Horizon 2020 research and innovation program (grant agreement no. 804320)

Last but certainly not least, I would like to thank my family for their unconditional love and support. I was the only child of my parents and it was very difficult for me to leave them and come to France to pursue my PhD. I thank my parents for their endless love, support and understanding. Finally, I want to thank my boyfriend Wei, who is always encouraging, caring and loving to me, even though I sometimes get angry with him when my experiments don't go well or papers are rejected. Thank you for always loving me and supporting me.

Résumé

L'augmentation rapide de la concentration de CO_2 due à la consommation de ressources fossiles constitue une grande menace pour l'environnement écologique de la planète et le développement durable de la société humaine. Pour réduire la concentration de CO_2 tout en assurant son recyclage, la réduction électrochimique est considérée comme une approche prometteuse et a attiré l'attention du monde entier au cours des dernières décennies. Le cuivre, qui est l'un des rares métaux de transition, peut catalyser l'électrolyse du CO_2 en produits multi-carbone tels que l'éthylène, l'éthanol, l'acétate, le propanol, qui ont des valeurs marchandes plus élevées et sont plus concentrés en énergie. Par conséquent, des efforts intenses ont été consacrés à l'amélioration de la sélectivité de la réaction vers la production de molécules C_{2+}, y compris l'alliage, le dopage de surface, la modification des ligands et l'ingénierie des interfaces.

Des recherches antérieures ont montré que les sites de cuivre partiellement oxydés ($Cu^{\delta+}$, $0<\delta<1$) à la surface des catalyseurs de cuivre peuvent faciliter la conversion du CO_2 en multicarbures en diminuant la barrière énergétique associée à la dimérisation du CO et à la formation de l'intermédiaire *OCCOH via un transfert de charge efficace entre les sites d'étape de surface et les intermédiaires réactionnels. Néanmoins, l'instabilité des espèces $Cu^{\delta+}$, en particulier aux potentiels cathodiques élevés pendant l'électrosynthèse de multicarbones, rend l'étude du rôle de $Cu^{\delta+}$ fastidieuse, et peut éventuellement se conduire à une perte rapide de la performance. C'est pourquoi le contrôle précis de l'état d'oxydation du Cu et de la présence d'espèces Cu^{+} à la surface des électrodes a récemment été au centre des préoccupations dans le domaine de la CO_2RR notamment *via* l'oxydation contrôlée, la polarisation pulsée ou fonctionnalisation.

Dans cette thèse, nous avons cherché à affiner le comportement des sites actifs à la surface des catalyseurs de cuivre *via* des stratégies d'ingénierie moléculaire. Nous avons tout d'abord modifié la surface du catalyseur bimétallique argent-cuivre avec des hétérocycles aromatiques tels que des dérivés de thiadiazole et de triazole afin d'améliorer la conversion du CO_2 en molécules d'hydrocarbures. Nous avons observé que la nature électrophile des groupes fonctionnels oriente la réaction vers la production d'espèces C_{2+} (éthanol et éthylène) et augmente la vitesse de réaction à la surface du catalyseur. En conséquence, nous avons obtenu une efficacité faradique (FE) élevée pour la formation de C_{2+} de ≈ 80 % et une efficacité énergétique en cellule complète de 20,3 % avec une densité de courant spécifique de 261,4 mA cm^{-2} pour le C_{2+} en utilisant des électrodes Ag-Cu fonctionnalisées. Nous anticipons que notre stratégie peut encore être étendue pour améliorer la sélectivité de la réaction vers la production de molécules multi-carbones spécifiques.

Par conséquent, sur la base de ces expériences de preuve de concept, nous avons ensuite exploré une bibliothèque de sels d'aryl diazonium avec différents degrés d'électrophilicité pour fonctionnaliser le catalyseur de cuivre. En combinant calculs de théorie fonctionnelle de la densité (DFT) avec les spectroscopies Raman et d'absorption des rayons X (XAS) en mode *operando*, nous avons mis en lumière le rôle de l'état d'oxydation de surface de $Cu^{\delta+}$ avec $0<\delta<1$ sur la sélectivité et le taux de formation de C_2H_4. En conséquence, nous avons obtenu une FE et une densité de courant spécifique pour le C_2H_4 aussi grandes que 83±2% et 212 mA cm^{-2} à partir d'une

électrode à base de cuivre partiellement oxydé: $Cu^{0.26+}$. Cela correspond à une efficacité énergétique de 26,9 % et à une consommation électrique (CE) de 61,4 kWh N^{-1} m^{-3}. En couplant avec une cellule membrane-électrode à base d'Ag pour générer du CO à partir de CO_2, nous avons obtenu un processus d'électrolyse en cascade avec une efficacité énergétique de ~40 % et un FE_{C2H4} de 86± 2 %, ce qui correspond à une CE record de seulement 25,6 kWh N^{-1} m^{-3}. Globalement, les résultats de cette thèse ouvrent la voie à des développements pratiques pour la réaction de conversion du CO_2 en C_2H_4 en utilisant l'ingénierie de la valence des sites Cu.

Abstract

The rapid increase of CO_2 concentration due to fossil energy consumption poses a great threat to the ecological environment of the planet and the sustainable development of human society. To reduce the concentration of CO_2 while achieving carbon recycling, the electrochemical reduction of CO_2 is considered a promising approach and has attracted worldwide attention in recent decades. So far, copper, which is one of the few transition metals, can effectively catalyze the electrolysis of CO_2 into multi-carbon products such as ethylene, ethanol, acetate, propanol, which have higher market values and are more energy concentrated. Therefore, intensive efforts have been devoted to improving the selectivity of the reaction towards the production of C_{2+} molecules, including alloying, surface doping, ligand modification and interface engineering.

It has been reported that partially oxidized copper ($Cu^{\delta+}$, $0<\delta<1$) sites on the surface of copper catalysts can facilitate the conversion of CO_2 to multi-carbons by decreasing the energy barrier associated with the CO dimerization and the formation of *OCCOH intermediate *via* efficient charge transfer between the surface step sites and the reaction intermediates. Nevertheless, the instability of $Cu^{\delta+}$ species, especially the high cathodic potentials during the electro-synthesis of multi-carbons, made the study of the role of $Cu^{\delta+}$ tedious, and it may eventually lead to a rapid loss of the performance. Therefore, the control of the oxidation state of Cu and the presence of Cu^{+} species on the surface of the electrodes has recently been a central focus in CO_2RR notably via controlled oxidation, pulse polarization, or molecular doping.

In this thesis, I sought to fine-tune the behavior of the active sites of copper-based catalysts surfaces through molecular engineering. I firstly modified the surface of the bimetallic silver-copper catalyst with aromatic heterocycles such as thiadiazole and triazole derivatives to increase the conversion of CO_2 into hydrocarbon molecules. We identified that the electron withdrawing nature of functional groups orients the reaction pathway towards the production of C_{2+} species (ethanol and ethylene) and enhances the reaction rate on the surface of the catalyst. As a result, we achieve a high Faradaic efficiency (FE) for the C_{2+} formation of ≈ 80% and full-cell energy efficiency of 20.3% with a specific current density of 261.4 mA cm^{-2} for C_{2+} using functionalized Ag-Cu electrodes. We anticipate that our strategy can further be extended to improve the selectivity of the reaction towards the production of specific multi-carbons molecules.

Therefore, based on this proof of concept experiments, we then explored a library of aryl diazonium salts with different electron-withdrawing ability to functionalize copper. By combining density functional theory (DFT) calculations with *operando* Raman and X-ray absorption spectroscopy (XAS), we identified the role of the surface oxidation state of $Cu^{\delta+}$ with $0<\delta<1$ on the selectivity and the formation rate of C_2H_4. As a result, we obtained a FE and a specific current density for C_2H_4 as large as 83±2% and 212 mA cm^{-2}, respectively on partially oxidized $Cu^{0.26+}$. This corresponds to an energy efficiency of 26.9% and an electrical power consumption (EPC) of 61.4 kWh $N^{-1}m^{-3}$. When coupled with an Ag-based membrane electrode assembly (MEA) cell to generate CO from CO_2 in a cascade flow process, an energy efficiency of ~40 % with a FE_{C2H4} of 86± 2% was achieved,

corresponding to a record low EPC of 25.6 kWh $N^{-1}m^{-3}$. Overall, this thesis provides a route towards practical developments for the CO_2-to-C_2H_4 conversion reaction using valence engineering of the Cu sites.

Publications

1. **H. Wu,** J. Li, Q. Kun, Y. Zhang, E. Petit, W. Wang, V. Flaud, N. Onofrio, B. Rebiere, L. Huang, C. Salameh, L. Lajaunie, P. Miele and D. Voiry, Improved electrochemical conversion of CO_2 to multicarbon products by using molecular doping. *Nature Communication* 12, 7210 (2021).
2. **H. Wu**, L. Huang, J. Timoshenko, K. Qi, W. Wang, J. Liu, Y. Zhang, S. Yang, E. Petit, V. Flaud, J. Li, C. Salameh, P. Miele, L. Lajaunie, B. R. Cuenya, D. Rao, D. Voiry, Selective and energy-efficient. electrosynthesis of ethylene via. valence engineering of the Cu sites. Submitted.
3. Y. Zhang, K. Qi, J. Li, B. A Karamoko, L. Lajaunie, F. Godiard, E. Oliviero, X. Cui, Y. Wang, Y. Zhang, **H. Wu**, W. Wang & D. Voiry, 2.6% cm^{-2} Single-Pass CO_2-to-CO Conversion Using Ni Single Atoms Supported on Ultra-Thin Carbon Nanosheets in a Flow Electrolyzer. *ACS Catalysis*, 2021, 11, 20, 12701–12711.
4. K. Qi, Y. Zhang, J. Li, C. Charmette, M. Ramonda, X. Cui, Y. Wang, Y. Zhang, **H. Wu**, W. Wang, X. Zhang & D. Voiry, Enhancing the CO_2-to-CO Conversion from 2D Silver Nanoprisms via Superstructure Assembly. *ACS Nano*, 2021, 15, 4.
5. J. Li, Y. Zhang, C. Liu, L. Zheng, E. Petit, K. Qi, Y. Zhang, **H. Wu,** W. Wang, A. Tiberj, X. Wang, M. Chhowalla, L. Lajaunie, R. Yu, and D. Voiry. 3.4% Solar-to-Ammonia Efficiency from Nitrate Using Fe Single Atomic Catalyst Supported on MoS_2 Nanosheets. *Advanced Functional Materials* 32.18 (2022): 2108316.

Table of Contents

Chapter 1. General introduction

1.1 Motivation for Electrochemical CO_2 reduction

Energy crisis and climate change on a global scale have made scientists increasingly enthusiastic about the research in the field of sustainable development[1]. Carbon dioxide (CO_2), made of carbon and oxygen elements, plays a critical role in the carbon cycle in earth's ecological system. The release of CO_2 by organisms and human industrial activities, and the fixation by green plants and ocean make the carbon cycle reaches a balance in nature[2]. However, the concentration of CO_2 in the atmosphere is continuously rising year by year, and global warming is increasing due to the rapid development of human industrialization in recent years. It is therefore very important and urgent to reduce the impact of greenhouse gases on the natural ecosystems. One of the most effective and economic methods to mitigate the side effects of CO_2 brought is to fix it and make it convert to the useful and sustainable fuels.

The current solutions to fix CO_2 can be classified into two main categories: (1) capture CO_2 and store it in the earth's crust, (2) chemically convert CO_2 molecules into carbon-based energy materials that can be reused[3-6]. Obviously, the latter is a faster and more sustainable solution, which may also be economically viable. Generally speaking, CO_2 can be converted by chemical methods such as photocatalytic or (electro-) catalytic reduction of CO_2[7-11]. However, in the process of carbon dioxide catalysis, a large amount of energy is consumed, and the low conversion rate of CO_2 cannot obtain obvious economic profits in the short term. Therefore, decreasing the energy consumed while improving the (1) catalytic efficiency and (2) selectivity and (3) conversion rate of CO_2 are critical to close carbon cycle at practical levels.

In recent years, the electrochemical conversion of CO_2 to carbon-based products has received much attention due to the many advantages of the electrocatalytic CO_2 reduction reaction (CO_2RR), such as mild reaction conditions normally operating at room temperature and atmospheric pressure, recyclable electrolytes, as well as reactions that are easily scalable to industrial-level development. (Fig.1)[12-16] Furthermore, electrocatalytic CO_2 reduction uses electric energy as driving force, which can be obtained from wind energy, solar energy and water energy that do not generate CO_2 again, thus lowering the carbon footprint.

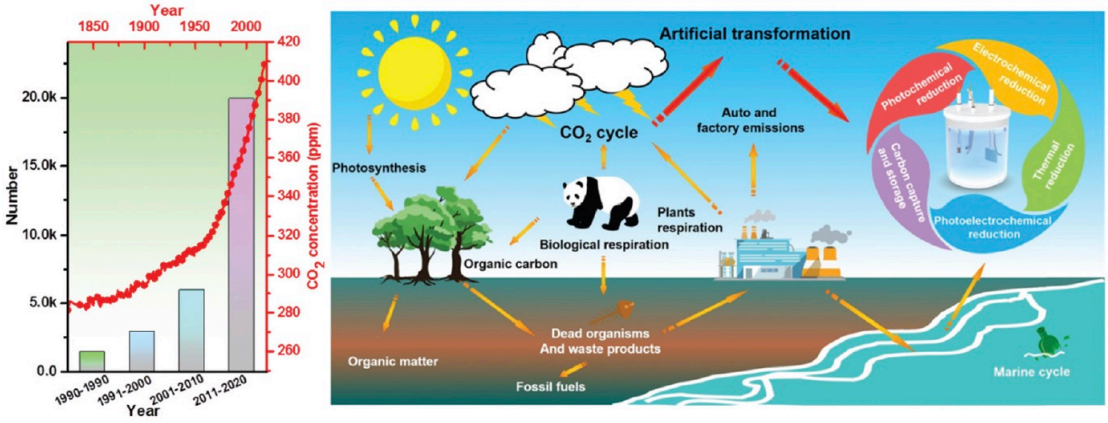

Fig.1 Surface average atmospheric CO_2 concentration (ppm) and statistics on the numbers of publications related to CO_2 reduction in the last few decades. (Data obtained from Web of Science, collected May 10, 2020) (left). Diagrammatic illustration of the carbon cycle (right)[13,14,16].

1.2 Electrochemical CO_2 reduction

1.2.1 Mechanisms for Electrochemical CO_2 reduction

The electrochemical reduction reaction of CO_2 is complex and involves multiple proton-coupled electrons transfer reactions depending on the products[7,17]. It mainly includes successive reaction steps as shown below: first, CO_2 is adsorbed on the surface of electrodes; second, electrons transfer and protons coupling with the dissociation of C=O bond and the formation of C-H and C-O bonds; third, the desorption of products from the electrocatalysts surface. Due to the linear chemical bonds, CO_2 is a rather chemically inert molecule and difficult to be activated. This explains why it is challenging to transform CO_2 into desirable products due to the high energy of 750 kJ/mol for the C=O bond. However, when carbon dioxide molecules adsorbed on the surface of the catalyst, its molecular configuration can be changed and the activation energy of its molecules can be reduced during electrocatalytic processes.

There are several configurations for the adsorbed CO_2 on catalysts (Fig. 2), which change depending on the applied potentials. The thermodynamic electrochemical half-reactions of CO_2 reduction and their associated standard electrode potentials are summarized and listed in Table 1. Although the thermodynamic potentials for different reactions are high, the experimental electrode potentials are usually much higher than theoretical values because of the relatively high overpotentials for activating CO_2 into $*CO_2^-$ intermediate.

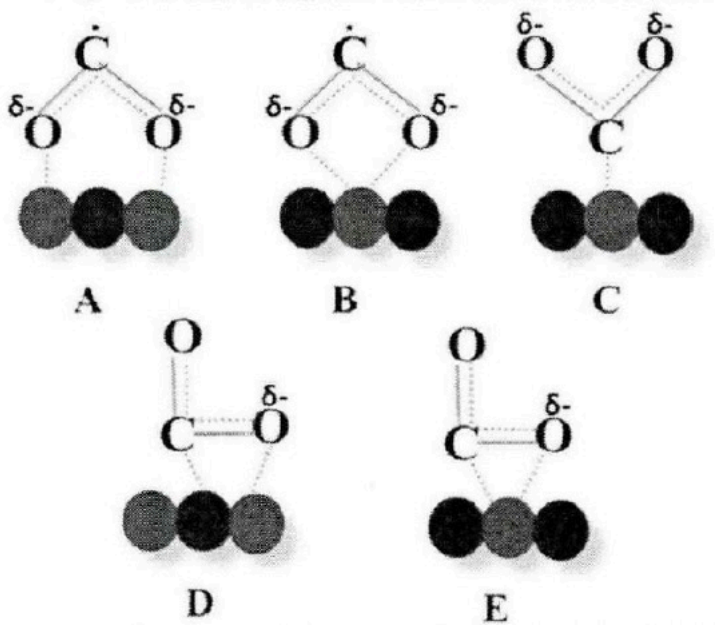

Fig 2. The different configurations of CO_2 adsorbed on catalysts.

Table1. Selected standard potentials of CO_2 in aqueous solutions (V *vs.* RHE) at 1atm and 25 ºC, calculated according to the standard Gibbs energies of reactants in reactions[7].

Thermodynamic reactions	Electrode potentials (V *vs.* RHE) under standard conditions
$CO_2 + e^- \rightarrow CO_2^-$	-1.9 V
$CO_2 + 2H^+ + 2e^- \rightarrow HCOOH(aq)$	-0.12 V
$CO_2 + 2H^+ + 2e^- \rightarrow CO(g)$	-0.1 V
$CO_2 + 6H^+ + 6e^- \rightarrow CH_3OH(aq)$	0.03 V
$CO_2 + 4H^+ + 4e^- \rightarrow C(s)$	0.21 V
$CO_2 + 8H^+ + 8e^- \rightarrow CH_4(g)$	0.17 V
$2CO_2 + 8H^+ + 8e^- \rightarrow CH_3COOH(aq)$	0.11 V
$2CO_2 + 10H^+ + 10e^- \rightarrow CH_3CHO(aq)$	0.06 V
$2CO_2 + 12H^+ + 12e^- \rightarrow C_2H_4(g)$	0.08 V
$2CO_2 + 12H^+ + 12e^- \rightarrow C_2H_5OH(aq)$	0.09 V
$2CO_2 + 14H^+ + 14e^- \rightarrow C_2H_6(g)$	0.14 V
$3CO_2 + 18H^+ + 18e^- \rightarrow C_3H_7OH(aq)$	0.1 V

The catalytic reactions follow different pathways and generate different products depending on the different catalysts. In general, CO_2 is usually reduced to formic acid on Pb, Hg, Ti, In, Sn, Cd and Bi, while it is converted to CO on Au, Ag, Zn, Pd and Ga[7]. Copper (Cu), as one of the few transition metals, can efficiently form multicarbon products such as ethylene, ethanol, acetate, propanol, which make it particular interesting to obtain higher market value chemicals from CO_2.

The origin of the different selectivity on these four groups of transition metals has been explained to be the result of their respective binding energy of the key CO_2RR and HER intermediates, including *H, *OCHO (bound to the surface through O), *COOH (bound to the surface through C), and *CO (* refers to the binding site). The unique ability of Cu to reduce CO_2 to multi-carbon products is attributed to the fact that it is the only metal that has a negative adsorption energy for *CO but a positive adsorption energy for *H, as illustrated in Fig. 3[18].

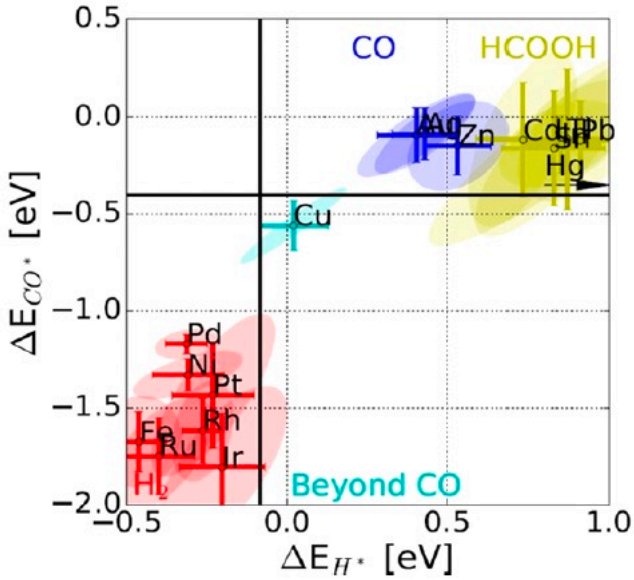

Fig 3. CO_2 reduction metal classification[18].

Since only copper has shown potentials for producing hydrocarbon products, such as ethanol, ethylene, n-propanol and so on, many researches have explored the possible reaction mechanisms. Fig. 4[12] shows the different pathways of multi-carbon products and the corresponding predicted activation energy of the intermediates. During the conversion of CO_2 to multi-carbon products, CO has been identified to be the most critical intermediate, which is involved in the formation of many hydrocarbons *via* C-C coupling reactions. We note that CO can eventually be protonated to form *CHO or *COH prior the C-C coupling step. For example, in the process of producing ethylene, there are two proposed pathways:

(1) $2\ ^*CO \rightarrow\ ^*COCO,\ \ ^*COCO + \ ^*H \rightarrow\ ^*COCOH$

(2) $\ ^*CO + \ ^*H \rightarrow\ ^*CHO\ ,\ \ ^*CHO + \ \ ^*CO \rightarrow\ ^*COCHO$

Ethylene would be produced by further deoxidation and hydrogenation of both $^*COCOH$ and $^*COCHO$ intermediates.

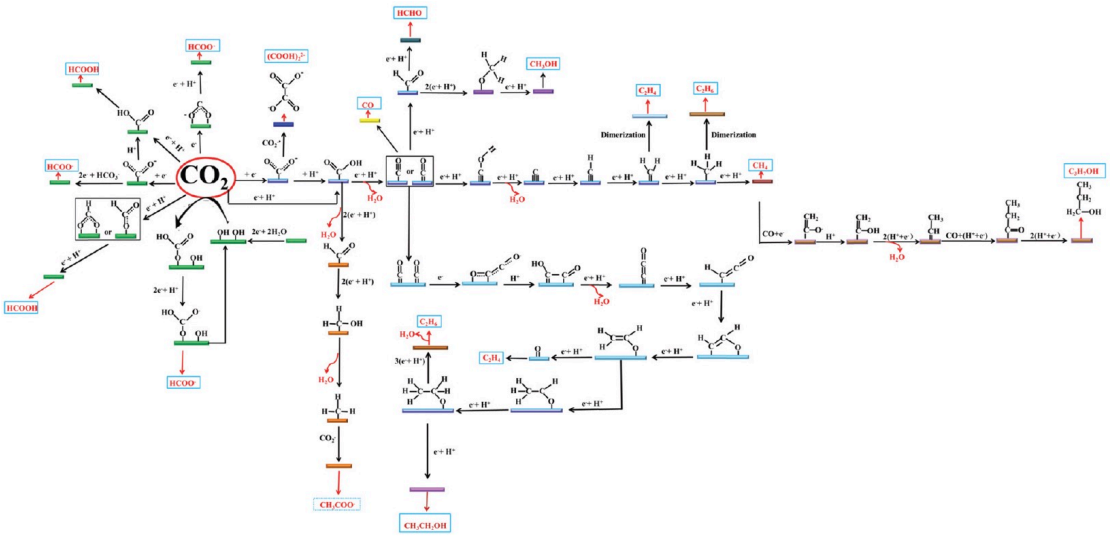

Fig. 4. The possible reaction roadmap of electrochemical CO_2 reduction reaction[12].

1.2.2 Evaluation indexes of Electrochemical CO_2 reduction

To evaluate and compare the performance of electrochemical CO_2 reduction, several indexes are usually considered and presented as follows:

(1) **Faradaic efficiency (FE, %)**, represents the percentage of electrons really involved in the formation of a target product in the total electrons consumed by the reaction, which reflects the selectivity of a product on a catalyst.

The Faradaic efficiency (FE) of each gas product was calculated as follows:

$$FE_{gas} = g_i \times v \times \frac{z_i}{RT} FP_0 \times \frac{1}{I_{total}} \times 100\% \qquad (1)$$

The Faradaic efficiency (FE) of each liquid product was calculated as follows:

$$FE_{liquid} = l_i \times \frac{z_i}{Q_{total}} F \times 100\% \qquad (2)$$

where g_i represents the volume fraction of gas product i; v represents the gas flow rate at the outlet in sccm; z_i represents the number of electrons required to produce one molecule of product i; I_{total} represents the total current; l_i represents the number of moles of liquid product i; and Q_{total} represents the charge passed while the liquid products are being collected. P_0 = 1.01 × 10 5 Pa, T = 273.15 K, F = 96,485 C mol^{-1} and R = 8.314 J mol^{-1}K^{-1}.

(2) **Current density (j, A cm^{-2})**, as the total current measured at a particular potential divided by the geometric area of the working electrode, is used to measure the reaction rate of the electrocatalytic reaction. It is of great significance to evaluate whether a catalyst or reaction system meets the requirements for large-scale production. The partial current density for a specific product represents the current density involved in the formation of a specific product and is also an important index for evaluating the catalyst performance. The specific current density can be used to extrapolate the Tafel slope and gained additional information about the reaction mechanism. The current density depends on the number of active sites on the catalyst, the mass transfer rate of the reaction system, and the impedance of the system (the rate of electrons transfers to the reactants on the electrode surface).

(3) **Overpotential (η),** is the additional driving force required to drive a reaction at a particular rate, and it can be calculated as follows,

$$\eta = E_{cat} - E^0 \qquad (3)$$

where E^0 represents the standard electrode potential of a specific product, and E_{cat} represents the potential applied to the working electrode. When evaluating the performance of the catalyst, the smaller the onset potential, the better the performance of the catalyst at a constant Faradaic efficiency. The overpotentials at both the anode and the cathode are important contributions to the cell voltage and strongly affect the energy efficiency (EE) of the conversion process, as shown below:

$$EE_i = \frac{(1.23 - E_i) \times FE_i}{(1.23 - E_{app})} \qquad (4)$$

Where E_i represents the thermodynamic potential (vs. RHE) for CO_2RR to species i; FE_i represents the Faradaic efficiency of species i; E_{app} refers to the applied potential (vs. RHE)

(4) Tafel slope, is obtained from the linear fit of the logarithm of overpotential and current density. It is also used to analyze electrochemical reaction mechanism and kinetics, and it can be calculated as follows,

$$\eta = a + b * log(j_{product}) \qquad (5)$$

Where b represents Tafel slope; a represents a constant which has some relationships with the interface structure between electrolyte and electrode; η is the overpotential; $j_{product}$ represents the specific current density for specific product. The rate determine step of CO_2RR can be deduced by calculating the Tafel slope.

(5) **Electrochemically active surface area (ECSA),** As the loading amount of catalyst on electrode and the specific surface area have big influences on the geometrical current density, the electrochemically active surface area (ECSA) is introduced to gauge the intrinsic activity of the catalyst. In electrochemical reactions, there are several methods to measure the ECSA, including the electrochemical double-layer capacitance (C_{dl}); underpotential deposition method (UPD) of hydrogen, copper or lead; hydrogen, oxygen or CO stripping and Redox peak calibration. Both electrochemical double-layer capacitance method (C_{dl}) and underpotential deposition method (UPD) are two common methods to examine the ECSA in CO_2RR.

(6) **Stability,** is an important parameter to evaluate the catalyst's practical performance. Generally, we can evaluate its stability by observing the change of the current with the increased time by cyclic voltammetry and galvanostatic or potentiostatic methods.

1.3 Current state of Electrochemical CO2 reduction reaction

Recently, more and more attention has been given to CO_2RR, as it offers several advantages such as controllable temperature and pressure, moderate reaction potentials, and the ability to scale up. In addition, CO_2RR is powered by electrical energy, which can be obtained from a renewable source such as wind, solar and hydro power, reducing the CO_2 footprint of the process. However, the biggest challenge for CO_2RR is the modest Faradaic efficiency and instability for specific products together with a low energy efficiency.

The electrocatalytic reduction of carbon dioxide has been studied for decades, and scientists are committed to develop and improve the activity of electrocatalysis to overcome various challenges in the electrocatalytic process. So far, catalysts with excellent electrocatalytic performance for the CO_2 reduction mainly include transition metals and their oxides, nitrides, sulfides, phosphating derivatives. Nanostructured metal catalysts usually show high specific surface area and abundant active sites on the specific facets, twin boundary or low coordination sites. Therefore, various nanostructured compounds based on metals and their alloys, sulfides, carbides have been synthesized with the controlled morphology, composition and exposed crystal planes, such as nanoparticles, nanosheets, nanorods, and so on. Ag, Au, Zn, Sn, Pb, Bi and Cu based nanomaterials have been widely investigated for the electrochemical CO_2 reduction. Taking Copper (Cu), as one of the few transition metals that

can efficiently produce valuable multi-carbon products, the selectivity toward one single product on Cu remains poor (below 50%) because of the inappropriate adsorption energy of intermediates.

According to the Sabatier principle, an ideal catalyst should bind with the intermediates appropriately, not too strongly, nor too weakly[19]. In general, the binding energy of chemical species on a catalyst highly depends on the structure and composition as well as the environment of the surface[20]. By tuning the binding energy of the intermediates, the surface's catalytic performance and the products can be consequently modified[21]. Ideal catalyst should optimize the binding energy of CO_2 and the multiple intermediates involved in the reaction. Therefore, intensive efforts are devoted to control the binding energies between catalysts and reaction intermediates by tailoring the Cu-based nanomaterials to improve CO_2RR selectivity and activity. This imposes the development of advanced physical and chemical strategies for tuning the electronic properties of Cu.

1.3.1 Controlling the size of catalyst

Nanostructured copper-based catalysts show excellent performance in CO_2 reduction. Engineering the size of the nanocrystals can effectively change the coordination number of the surface atoms and the adsorption behavior of active species, which are considered as an effective way to regulate catalytic selectivity[22]. In order to study the relationship between catalyst size and electrochemical performance, many researchers have synthesized a series of nanostructured copper-based catalysts, including copper single atom[23,24], nanoparticles[25-27], nanowires[27], nanosheets[28]. By embedding copper single atom into hollow carbon nanofibers, a Faradaic efficiency of 44% for methanol was achieved[23]. The authors attribute the remarkable performance to the synergistic effect between copper single atom and hollow carbon nanofibers[24]. The interaction between copper and hollow carbon nanofibers strengthens the adsorption energy of *CO intermediates, while the further protonation leads to the formation of *CHOH, a key reaction intermediate for methanol formation. It is generally believed that CO_2 electroreduction to multi-carbon products such as ethanol or ethylene may be catalyzed with significant yield only on metallic copper surfaces, implying large ensembles of copper atoms. Therefore, copper single atoms can only selectively catalyze CO, CH_4 and methanol. However, Fontecave et al[23] found that single copper atoms with a CuN_4 coordination environment in a nitrogen-doped conductive carbon matrix achieves aqueous CO_2 electroreduction to ethanol with a high Faradaic efficiency of 55 % under optimized conditions (electrolyte: 0.1 M $CsHCO_3$, potential: -1.2 V vs. RHE and gas-phase recycling set up), as well as CO electroreduction to C_2-products (ethanol and ethylene) with a Faradaic efficiency of 80 %. *Operando* X-ray adsorption (XAS) analysis shows that the copper single atom is converted into copper metal particles during the catalytic reaction, which can then return to the original single atom dispersion state when the voltage is stopped. Strasser group reported the effects of catalyst size on activity and selectivity of CO_2RR (Figs. 5-4a and b). They revealed that the smaller the catalysts' size, typically below 5 nm, the selectivity of H_2 and CO are increased, while the generation of multi-carbon products is inhibited. This is due to the strong adsorption capacity of *CO and *H at low coordination conditions that decreases the chance of *CO-*CO coupling. However, Alivisatos *et al* [29]. reported that a monodispersed Cu

nanoparticle with the size of 7 nm exhibited 76% CH_4 selectivity at -1.35 V. At the same time, the nanoparticles gradually merged to 25 nm during the reduction process. This however did not affect the Faradaic efficiency of CH_4 [29]. In contrast, the size of 20 nm Cu_2O cube nanocrystals will be gradually reduced into 2-4 nm while Faradaic efficiency of C_2H_4 was increased from 27% to 57.3% during the reduction process[30]. Cuenya group[31] found that the diffusion of CO_2 and the re-adsorption of intermediates influence the selectivity of final products. To do so, they studied the ratio of particle spacing to particle size IP/d based on experimental and first principal investigations (Figs. 5-4c, d and e).

1.3.2 Regulating the crystal facets of catalyst

Regulating nanocrystalline orientation is another effective way to regulate the specific product's selectivity. Studies have shown that different Cu crystal planes show different activity and selectivity during the CO_2RR process (Fig. 6), and the ratio of CH_4 and C_2H_4 is closely related to the orientation of Cu crystal facets[37,38]. The Cu (111) crystal facet is favorable for CH_4 formation, while the Cu (100) crystal facet contributes to C_2H_4 formation[32]. According to the crystal structure of copper, each copper atom on the surface of Cu (100) is surrounded by four nearest atoms with the distance of 2.57Å and four sub-neighboring atoms (3.64 Å), while the copper atom on the surface of Cu (111) is surrounded by six nearest atoms (2.57 Å). This means that Cu (100) surface has a lower coordination number than Cu (111) surface, which determines its selective adsorption intermediates and transition states[33]. Density Functional Theory (DFT) calculations have pointed out that *CHO intermediate is more easily adsorbed on Cu (100) crystal plane at lower overpotential so that the C-C coupling from two *CHO intermediates to produce C_2H_4 is more favorable than on Cu (111) surface[34]. This phenomenon was also observed by Hori et al. in his seminal experiments[35,36]. More recently, Sargent's group synthesized a 70% Cu (100) facet exposed catalyst with a Faradaic efficiency of 90% C_{2+} products by electrodepositing Cu under CO_2 assisted condition. This enhanced selectivity was attributed to the adsorption of specific intermediates on Cu (100) facet (Figs. 6a to 6d)[37]. Furthermore, the introduction of Step or Terrace defects on flat catalyst's surfaces would further affect the catalytic activity and reaction pathways. For example, Jaramillo et al[38] found that an improved selectivity toward oxygen-containing multi-carbon product can be achieved at low potential by introducing Cu (751) crystal facet through physical vapor deposition (PVD) epitaxy growth, Cu(S)-[n (110) x (100)] (n = 2 ~ 7). In this work, the authors proposed that at low potential, C-C coupling is a chemical reaction process, rather than an electrochemical process of proton coupled electron transfer. Compared with Cu (111) and (100), which have 6 and 4 adjacent copper atoms on the surface respectively, Cu (751) has only 2 nearest surface neighbors. Therefore, *CO is unlikely to be coupled with adjacent H*, which means it is difficult to achieve the hydrogenation of C-C, and therefore more oxygen-containing products will be produced (Figs. 6e and 6f) [38]. Alternatively, the control of the morphology can direct the reaction pathway. Porous three-dimensional copper dendrites also show good ethylene selectivity, while they do not have obvious crystal facets orientation. This

suggests that the surface roughness and the high-density defects are the most important factors for producing multi-carbon products[39,40].

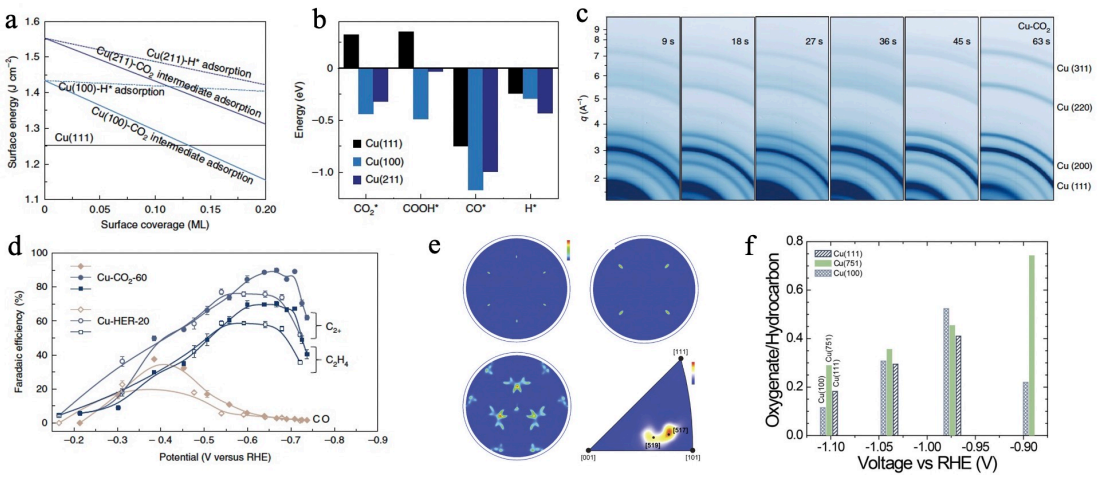

Fig 6. Crystal facets effects. a, Surface energy changes with the surface coverage of the CO_2RR (assuming the same coverages for all of the four intermediates) and HER intermediates. b, Adsorption energies of four intermediates on three facets of copper. c, two-dimensional GIWAXS patterns of the Cu-CO_2 catalysts with respect to the deposition time. d, a comparison of the Faradaic efficiencies of C_2H_4, C_{2+} and CO on Cu-CO_2-60 and Cu-HER-20 catalysts in 7 M KOH[37]. e, X-ray pole figures for Cu (200) on Ti/Al_2O_3(0001) (left top), Cu (200) on Si (100) (right top), Cu (111) on Si (111) (left bottom) and the Cu (751) on Si (111) (right bottom). f, Oxygenate/hydrocarbon ratio for>$2e^-$ reduction products as a function of potential for Cu (111), (751), and (100)[38].

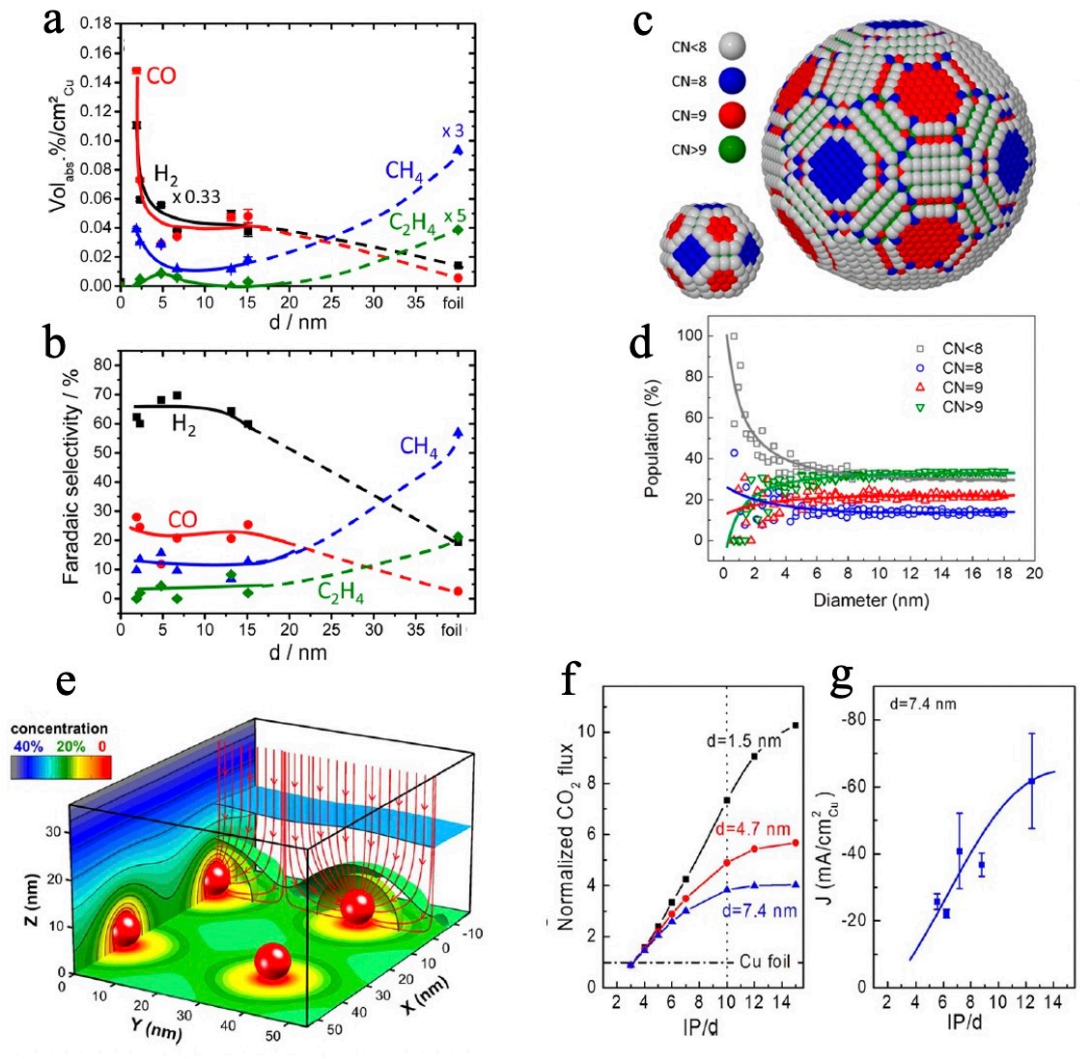

Fig 5. Nanoparticles size effect. (a) Particle size dependence of (a) the composition of gaseous reaction products (balance is CO_2) during catalytic CO_2 electroreduction over Cu NPs, (b) the Faradaic selectivity of reaction products during the CO_2 electroreduction on Cu NPs[25], (c) Ball models of spherical Cu NPs with 2.2 and 6.9 nm diameters. Surface atoms are color-coded according to their first neighbor coordination number (CN), CN < 8 (gray), CN = 8 (blue), CN = 9 (red), CN > 9 (green). (d) Population (relative ratio) of surface atoms with a specific CN as a function of particle diameter. (e) Simulation results of the CO_2 concentration distribution based on diffusion equations. The red arrows show the reactant flux toward the NPs. The color scale shows the concentration of CO_2 at a given distance from the NPs, as a percentage of its value in the bulk of the electrolyte. A diffusion layer thickness of 100 nm was assumed. (f) CO_2 flux obtained for NPs with different size and IP distances based on diffusion equations. The data are normalized by the corresponding flux obtained from a flat Cu foil. (g) Experimental current density obtained at −1.1 V (*vs* RHE) during the electrochemical reduction of CO_2 over 7.4 nm Cu NPs with distinct average IP spacing[31].

1.3.3 Interface effects

As both the electronic structure and the surface state of the heterogeneous catalyst would affect the adsorption free energy and the adsorption modes of CO_2 and the reaction intermediates, controlling the interfaces becomes important for the CO_2RR[41] The interface between two different components, including active/active and

active/inactive interfaces, promotes synergies between them. Metal oxides are usually unstable under CO_2RR, and the synergistic effect of the metal/metal oxide interface generated by partial reduction tends to produce highly active and high selective catalytic sites. The different valences of metal is also known to change the adsorption free energy of intermediates and promote water dissociation and C-C coupling Figs. 7a and 7b [42]. Furthermore, the metal/carbon-based material interface can make full use of the conductive skeleton and defects of graphene, nanotubes and nano-diamond and promote the formation and the stability of $CO_2^{\cdot-}$.

(1) The interface of metal/metal oxide

The metal/metal oxide interface form a highly active region and important connection points during the activation process of catalyst, which can improve the selectivity and the activity of the CO_2RR. Buonsariti et al[43]. synthesized a Cu/CeO_{2-x} heterodimer catalyst and demonstrated an excellent synergistic effect in CO_2RR. The Cu/CeO_{2-x} heterodimer showed good selectivity towards CO_2 reduction (over than 80% FE_{total}) with a FE for CH_4 as high as 54% at -1.2 V (*vs.* RHE) by using sol-gel method to combine two different sites (Cu and CeO_{2-x}) through the interface connection. DFT shows that the combination of oxygen vacancies site with intermediates binding to both Cu and Ce atoms at the same time was the lowest free energy pathway, which results in the breaking of the linear relationship between the *CHO and the *CO intermediates. The continuous formation of *CO at the interface and the high density of Cu sites effectively inhibits HER[43]. Sargent group reported a complementary approach in which they utilized hydroxide and oxide doping of a catalyst surface to tune the adsorbed hydrogen on Cu[44]. Density functional theory studies indicate that doping accelerates water dissociation and changes the hydrogen adsorption energy on Cu. The authors synthesized and investigated a series of metal-hydroxide-interface-doped-Cu catalysts, and found that the most efficient, Ce(OH)x-doped-Cu, exhibits an ethanol Faradaic efficiency of 43% and a partial current density of 128 mA cm^{-2}. Mechanistic studies, which combined investigation of hydrogen evolution performance with the results of *operando* Raman spectroscopy, showed that adsorbed hydrogen hydrogenates surface *HCCOH, a key intermediate whose fate determines branching to ethanol versus ethylene.

(2) The interface of metals/carbon-based materials

Compared with the noble catalysts, carbon-based materials have the advantages of low cost, high electrical activity, large specific surface area and good chemical stability, and can be used as the second component of the ideal catalytic interface. Nanodiamond (Nd) is one of the few catalysts that produce multi-carbon products in CO_2 reduction so far[45]. In addition, the N-doped nanodiamond (N-Nd) has a dominant N-sp3C component, which plays an important role in improving the electrocatalytic performance[46]. Cui et al. synthesized heterogeneous electrocatalysts by rational tuning of an assembly of nitrogen-doped nanodiamonds and copper nanoparticles[47]. High resolution transmission electron Microscopy (HRTEM) shows that a direct interface between N-Nd and Cu can be obtained in agreement with previous observations of the interface between Cu and N-doped carbon

nanomaterials. The catalyst exhibits a Faradaic efficiency of ~63% towards C_2 oxygenates at an applied potential of only -0.5 V vs. RHE. Moreover, this catalyst showed excellent stability for 120 h and only 19% activity decay. Density functional theory calculations show that CO binding is strengthened at the copper/nanodiamond interface. This suppresses the desorption of CO and promotes the formation of C_2 by lowering the barrier for the CO dimerization. Importantly, the inherent compositional tunability and electronic tunability of the catalyst assembly provide an unparalleled degree of control over the catalytic interface, and thus the energetics and kinetics of the reaction[47].

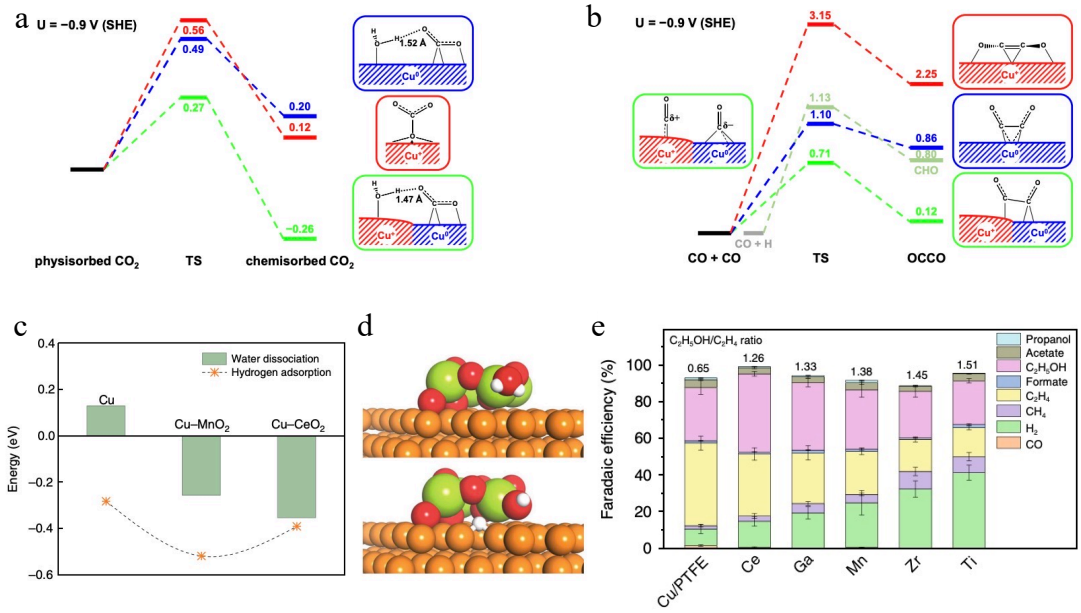

Fig 7. a, Interface effects. (a) Free energy profiles of CO dimerization in the metallic Cu matrix (blue), fully oxidized matrix (red), and Cu metal embedded in oxidized matrix (green) models and for CO hydrogenation to form surface CHO species. b, Free energy of water dissociation on different metal oxide-modified Cu surfaces[42]. c, Water activation on oxide/Cu interface. d, Surface configurations of CeO_2/Cu with and without adsorbed hydrogen. e, selectivity of various oxide/Cu interface electrode[44].

1.3.4 Alloying

Alloy nanoparticles can offer superior catalytic selectivity than single component nanoparticles in CO_2RR. To improve the selectivity and stability of copper catalyst, and decrease the overpotential for producing multi-carbon products, many researches focused on copper-based double metal catalysts[48]. The addition of a second metal to copper is considered to be an effective method for regulating the binding strength of the intermediates on catalytic surfaces, thereby modifying the selectivity and the reactivity [48]. A series of bimetallic catalysts, such as Cu-Au, Cu-Pd, Cu-In, Cu-Zn, Cu-Ni and Cu-Sn, have been shown to improve the surface activity of CO_2 reduction [49-53]. Studies on Cu-Ag alloy or Cu-modified Ag electrocatalysts show that Cu can improve the surface activity of CO_2 reduction to hydrocarbons. Especially, the adjustment of d-band structure and geometric effect of Cu-Au and Cu-Ag alloy catalysts allow the identification of several factors that affect the performance of the catalysts such as: surface adsorption energy of the bonded intermediates and the orientation of intermediates.

Alloying can be advantageously be used to tune the electronic structure of the catalyst surface through introducing another metallic element. According to the theoretical model of d-band, both the width of the d band center and the distance of the Fermi level would change the surface adsorption energy of the bonded intermediates (Fig. 8a). Alloying or bimetallic phase formation can induce surface recombination, change the binding energy of the target intermediate (and thus the reaction pathway), and improve reaction kinetics and selectivity. When a metal strongly bonds to C_{2+} intermediates (e.g., *CO, *COH, *COOH), the introduction of a second metal may weaken the metal-CO interaction while synergistically improve the production of multi-carbon products (Figs 8b and 8c). Indeed, *CO is an important intermediate in the formation of hydrocarbons and alcohols in CO_2RR, and the optimization of *CO binding energy by adjusting the composition of the alloy may contribute to the formation of C-C bond. Electrolyzing CO_2 to multi-carbon products such as ethylene, ethanol, acetate, propanol is thought to be more promising than C_1 products, since multi-carbon products possess higher market values and are more energy concentrated. Since CO, is the key intermediate to form C_{2+} products, a metal type with moderate CO adsorption energy is an important criterion when designing a CO_2RR active metal catalyst to promote the C-C coupling step. Au and Ag, for instance, have suitable CO binding energy. Conversely, copper (Cu) is one of the few transition metals to catalyze the electrolysis of CO_2 to multi-carbon products at acceptable current density. Alloying copper with other metals, which have the low CO adsorption energy is an effective method to tailor and obtain multi-carbon products. Sargent et al developed a bimetallic Ag/Cu catalyst that implements the proposed design toward an improved ethanol catalyst. It achieves a record Faradaic efficiency of 41% toward ethanol at 250 mA cm^{-2} and −0.67 V *vs* RHE, leading to a cathodic-side (half-cell) energy efficiency of 24.7%[59].

Alloying may also affect the way the reaction intermediates binds and interact collectively. Different binding modes of atoms (order, disorder and phase separation) show different selectivity for C_1 and C_{2+} products. The geometrically separated phases tend to selectively generate C_{2+} compounds. However, the catalytic performance determined by the geometric and structural effects or electronic effects usually depends on the different bimetallic systems. Many Cu-M bimetallic electrodes (where M refers to another metal) show high selectivity and high intrinsic activity in the production of CO. Experiments show that a variety of bimetals can convert CO_2 to CO with the FE_{CO} over than 80%. For example, Kenis[54] et al synthesized a range of bimetallic Cu–Pd catalysts with ordered, disordered, and phase-separated atomic arrangements (Cu_{at}:Pd_{at} = 1:1), as well as two additional disordered arrangements (Cu_3Pd and $CuPd_3$ with Cu_{at}:Pd_{at} = 3:1 and 1:3). When compared with the disordered and phase-separated CuPd catalysts, the ordered CuPd catalyst exhibits the highest selectivity for C_1 products (>80%) (Fig. 8d) Phase-separated CuPd and Cu_3Pd achieve higher selectivity (>60%) for C_{2+} products than $CuPd_3$ and ordered CuPd, which suggests that the probability of dimerization of C_1 intermediates is higher on surfaces with neighboring Cu atoms. Based on surface valence band spectra, geometric effects rather than electronic effects seem to be the key in determining the selectivity of bimetallic Cu–Pd catalysts. This observation implies that the selectivity towards two different products can be tuned by geometric arrangements (Figs. 9a-c).

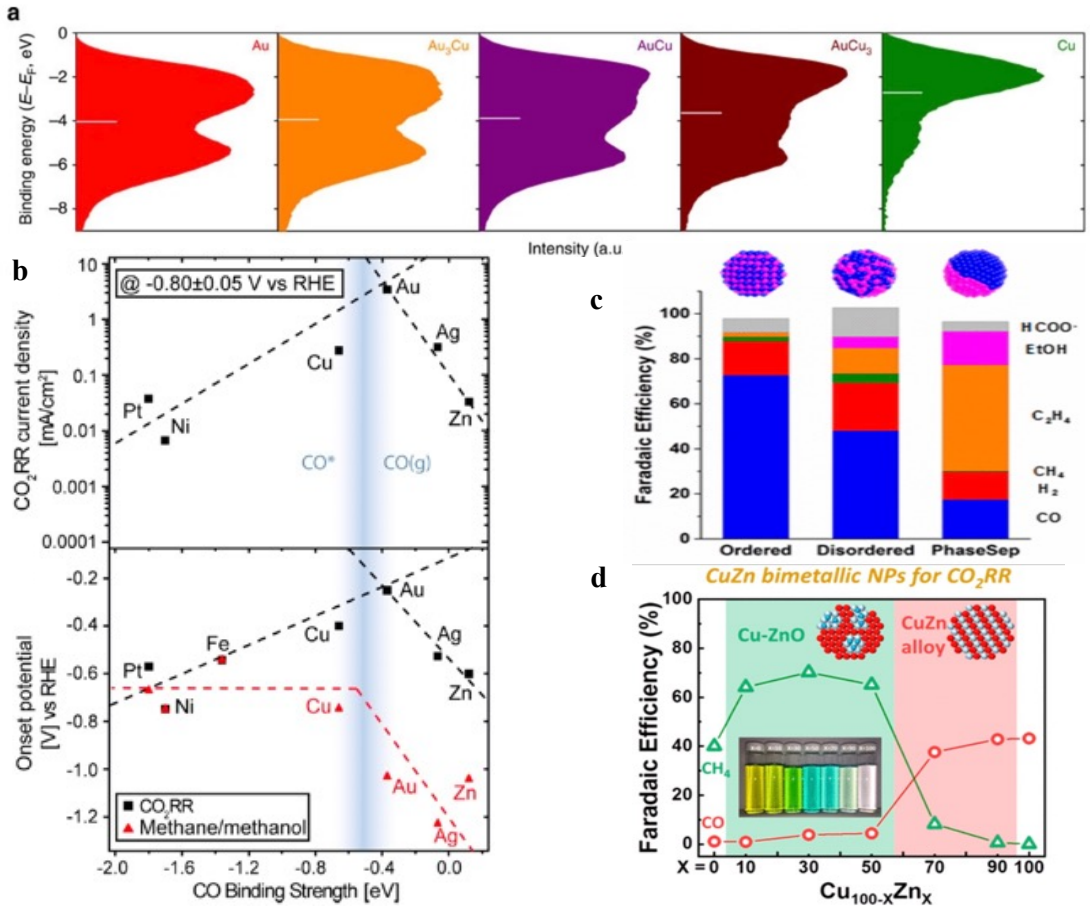

Fig 8. Alloying effect. (a) Surface valence band of Au-Cu bimetallic catalysts[56]. (b) Volcano plot of partial current density for CO_2RR and HER, CO_2RR, methane or methanol onset potentials vs. CO binding strength[57]. (d) CO_2RR selectivity for bimetallic CuZn catalysts[54]. (c) CO_2RR selectivity for bimetallic CuPd catalysts[58].

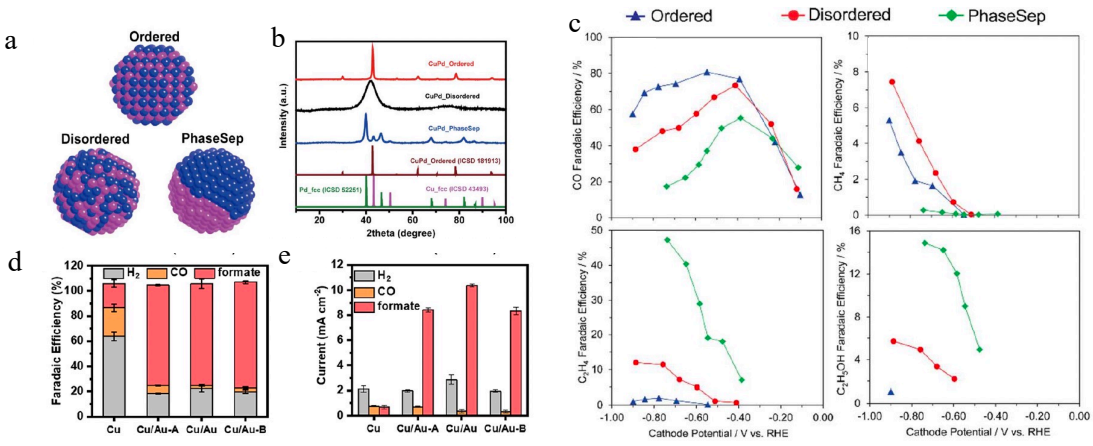

Fig 9. a, Schematic illustration of prepared CuPd nanoalloys with different structures. b, XRD patterns of prepared CuPd nanoalloys as well as previously reported Cu, Pd and CuPd alloys. c, Faradaic efficiencies for CO, CH_4, C_2H_4 and C_2H_5OH on bimetallic Cu-Pd catalysts with different mixing patterns: ordered, disordered, and phase-separated[58]. d, FE Distribution. e, partial current densities of products from CO_2 reduction catalyzed by Cu, Cu/Au, Cu/Au-A and Cu/Au−B at −0.6 V[55].

It is well known that strong interactions between two different types of metal nanoparticles can dramatically change their electrocatalytic properties. For instance, Au is well known to convert CO_2 to CO, but the selectivity for CO was decreased when combining Au with Cu nanoparticles together. Wang group[55] reported that the selectivity for formic acid is greatly enhanced when coupling Au with Cu, although Au by itself is neither high selective nor high active for electrochemical CO_2 reduction to formic acid. Cu/Au catalyst successfully produced formic acid at −0.4 V *vs* RHE in a near-neutral electrolyte and achieved a partial current density of 10.4 mA cm^{-2} with a Faradaic efficiency of 81% at −0.6 V. This was notably 15 times more active and 4 times more selective than the bare Cu catalyst derived in the same way (Figs. 9d and 9e). Electrochemical and spectroscopic investigations revealed that the interactions between the Cu and the Au catalyst lead to the disappearance of Au' characteristic electrocatalytic activity for reducing CO_2 to CO, while it contributes to oxidize CO and stabilize Cu^{1+} species on the Cu surface during CO_2RR. The high selectivity for formic acid production on Cu–Au bimetallic system opens up vast opportunities to improve the electrocatalytic reactivity using metal–metal interactions.

1.3.5 Tailoring the valence of catalyst

Numerous studies have shown that the valence of copper in copper oxides or copper-based catalyst plays a central role in the formation of multi-carbon products (Fig. 10)[60] Xie et al evaluated the role of two different catalytic sites by fabricating two kinds of four-atom-thick layers: pure cobalt metal, and co-existing domains of cobalt metal and cobalt oxide. They found that at lower overpotentials, the surface cobalt atoms of the atomically thin layers have higher intrinsic activity and selectivity towards formate production than surface cobalt atoms on bulk Co. Partial oxidation of the atomic layers further increases their intrinsic activity, allowing them to demonstrate stable current densities of about 10 mA cm^{-2} over 40 hours, with approximately 90% formate selectivity at an overpotential of only 0.24 V. These findings pointed to new opportunities for manipulating and improving the CO_2 electroreduction properties of metal systems, by controlling the structure down the atomic-scale and by the presence of metal[61]. Kanan group prepared Cu electrodes by annealing Cu foil in air and electrochemically reduced the resulting Cu_2O layers[62]. The CO_2RR activities of these electrodes exhibited a strong dependence on the initial thickness of the Cu_2O layer. Thin Cu_2O layers formed by annealing at 130 °C showed indistinguishable activities from those of polycrystalline Cu. In contrast, the electrode of Cu_2O layers formed at 500 °C exhibited the selectivity of 40% CO and 33% HCOOH[62]. Roldan group developed oxidized copper catalysts which displayed lower overpotentials and a record selectivity towards ethylene (60%) through facile and tunable oxygen plasma treatments[63]. Operando X-ray absorption spectroscopy and cross-sectional scanning transmission electron microscopy showed that copper oxides are surprisingly resistant to be reduced and Cu^+ species remain on the surface of copper electrode during the reaction. Their results demonstrated that the roughness of oxide-derived copper catalysts only plays a partial role in determining the catalytic performance, while the presence of Cu^+ is the key for lowering the onset potential and enhancing ethylene selectivity. To control the valence of copper,

Sargent group introduced boron atom into copper catalysts. Both C_2+ products selectivity and stability were found to be improved by tuning the valence of $Cu^{\delta+}$ ($0<\delta<1$) through controlling the loading amount of boron [64]. Simulations showed that the ability to tune the average oxidation state of copper enables control over the adsorption of CO and its subsequent dimerization allowing the formation of C_{2+} products. As a result, a Faradaic efficiency of 79 ± 2% for C_{2+} and a great stability of ~40 hours were achieved on boron-doped copper catalysts. These finding illustrate that the positive valence of copper can boost the conversion of CO_2 to carbon products and called for additional investigations[64].

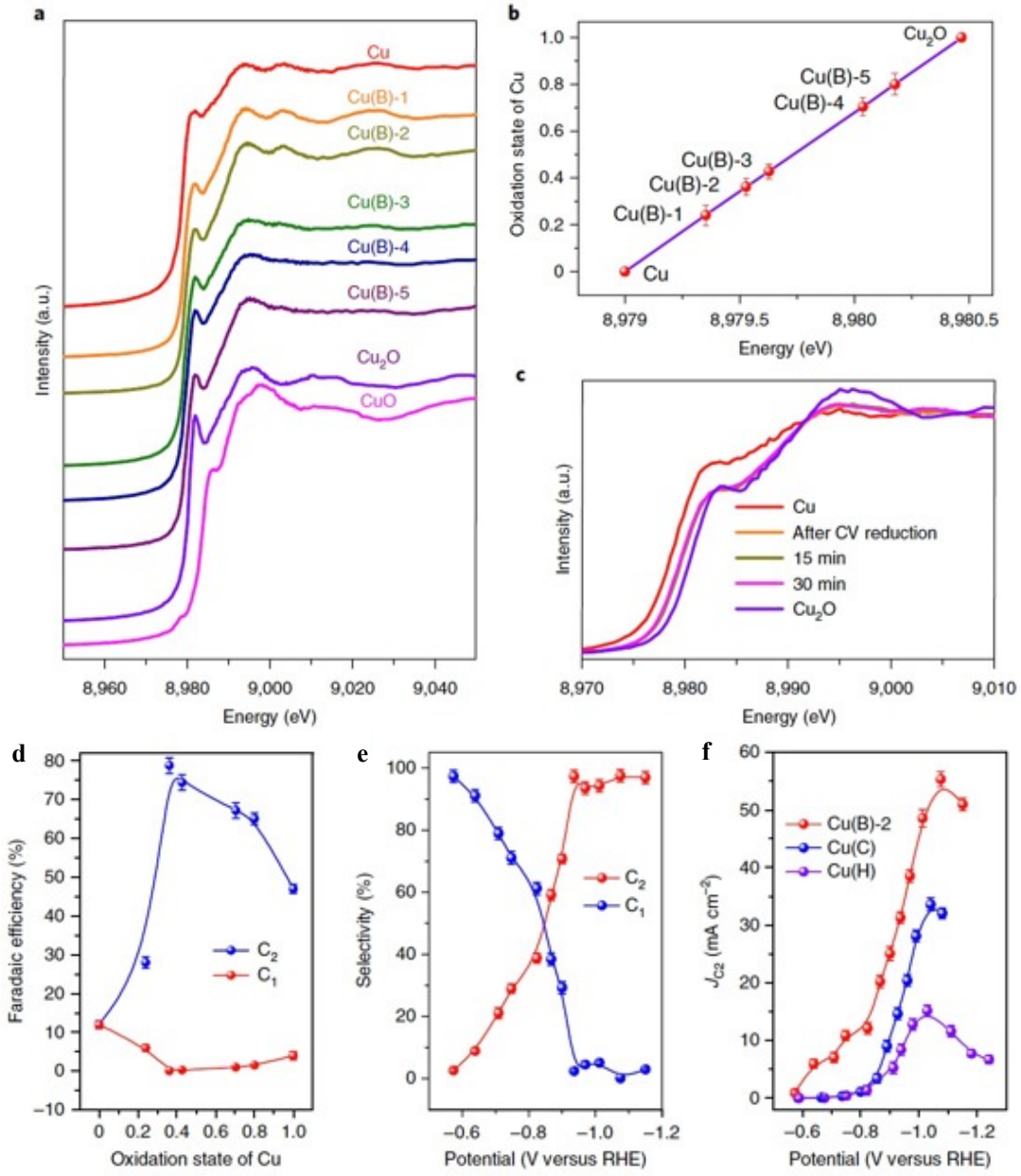

Fig 10. Oxide state effect. (a) Copper K-edge XANES spectra of Cu (B) after electrochemical reduction. (b) Schematic of the process to synthesis Cu(B). (c) CO_2RR performance on Cu(B)[64].

1.3.6 Spillover effects

CO is widely regarded as an indispensable and important reaction intermediate to generate multi-carbon products in CO_2RR. Regulating the coverage of *CO on the catalyst surface has been considered an effective strategy to obtain deeply reduced C_{2+} products. In other words, the introduction additional catalytic sites to specifically produce CO can be advantageously coupled to copper for the electrocatalysis CO to C_2 products in a two-step process (Fig. 11). For example, macrocyclic complexes and silver are regarded as good catalysts for the conversion of CO_2 to CO. Based on this, Jaramillo et al. deposited gold on the surface of polycrystalline copper by using plasma vapor deposition, which resulted in a high selectivity towards ethanol. The team believed that the high concentration of CO produced from CO_2 on the gold clusters contributes to favor the C-C coupling on the surface of copper[65].

Sargent et al proposed a cooperative catalyst strategy consisting of a molecule–metal catalyst interface in order to form a reaction-intermediate-rich local environment for the electrosynthesis of ethanol from CO_2 and H_2O. They implemented the strategy by functionalizing the copper surface with a family of porphyrin-based metallic complexes which are good at converting CO_2 to CO. Density functional theory (DFT) calculations show that increasing CO coverage on Cu surface can not only reduce the reaction energy of C–C coupling reaction, but also adjust the selectivity from ethylene to ethanol. This results in a CO_2-to-ethanol Faradaic efficiency of 41% and a partial current density of 124 mA cm^{-2} at -0.82 V *vs.* RHE.

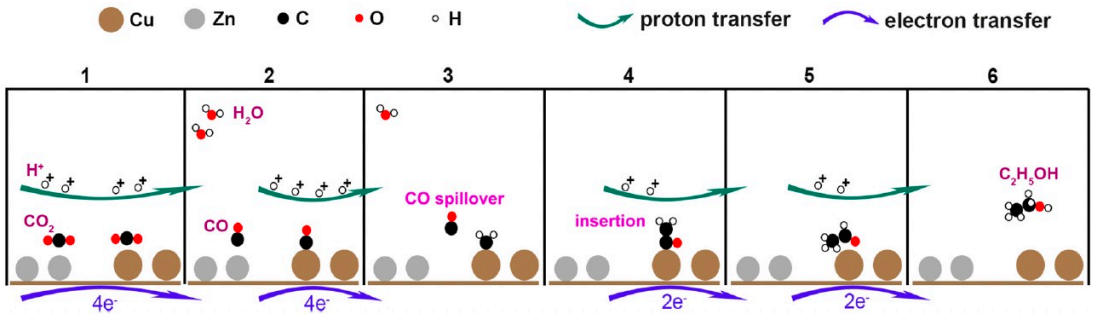

Fig 11. Proposed mechanism for the electroreduction of CO_2 to ethanol on Cu_xZn catalysts: stages 1→2, four protons and four electrons reduce two CO_2 molecules to CO on Cu and Zn, respectively; stages 2 → 3, four protons and four electrons reduce CO molecule to *CH_2 on Cu, while CO produced by Zn desorbs and migrates near the *CH_2; stages 3→4, CO inserts into the bond between Cu and *CH_2 to form *$COCH_2$; stages 4→5, two protons and two electrons reduce *$COCH_2$ to CH_3CHO (acetaldehyde); stages 5 → 6, two protons and two electrons reduce CH_3CHO to CH_3CH_2OH (ethanol). The protons transferred are presumably drawn from water molecules[66].

1.4 Dissertation Overview

1.4.1 The Research backgrounds

The development of electrocatalytic system that can selectivity convert CO_2 into valuable chemicals is considered as promising strategies to close the carbon cycle and mitigate the use of fossil fuels. This, however, will be only possible if this technology is technically and economically viable. Today, we witnessed a revival in the field of

electrochemistry, which has strongly benefited the CO_2RR. The main strategies can be classified into approaches: molecular catalysis and heterogenous catalysis.

Copper (Cu), as one of the few transition metals, can efficiently convert CO_2 to multi-carbon products such as ethylene, ethanol, acetate, propanol. Since multi-carbon products possess higher market values and are more energy concentrated, intensive efforts have been devoted to improve the reaction selectivity towards the production of C_2 and C_{2+} molecules. Examples of strategies for optimizing the Faradaic efficiency towards the production of C_{2+} species include alloying[59,67-69], surface doping[64,70], ligand modification[71,72], and interface engineering[43,73-75]. Designing Cu-based catalysts by adapting some of the concept of molecular catalysts in order to finely tailor the behavior of the active sites of metallic surfaces is currently regarded as the long-standing interest for the controlled design of novel electrocatalytic materials.

Alternatively, it has been reported that partially oxidized copper ($Cu^{\delta+}$, $0<\delta<1$) sites on the surface of copper catalysts can facilitate the conversion of CO_2 to multi-carbons by decreasing the energy barrier associated with the CO dimerization and the formation of *OCCOH intermediate via efficient charge transfer between the surface step sites and the intermediate[42,60,64,76,77]. Nevertheless, the instability of $Cu^{\delta+}$ species, especially the high cathodic potentials to electro-synthesize multi-carbons, made the study of the role of $Cu^{\delta+}$ tedious, and it may eventually lead to a rapid loss of the performance[78]. Therefore, the control of the oxidation state of Cu and the presence of Cu^{+} species on the surface of the electrodes has recently been a central focus in CO_2RR notably *via* controlled oxidation, pulse polarization, or molecular doping[60,79,80].

In this context, my PhD focuses on controlling the surface oxidation state of different Cu-based electrodes by developing molecular doping strategies. While several reports have shown that the CO_2RR properties are greatly influenced by the surface chemistry of the catalyst, the engineering of the valence state of Cu using molecular dopant has remained largely unexplored. This thesis manuscript will present the results I have obtained within the last three years. Specifically, I will outline how, by grafting an organic molecule onto the Cu surface, the catalytic properties of Cu can be tuned by removing electrons from the metal surface leading to the formation of $Cu^{\delta+}$ species ($0 < \delta < 1$).

1.4.2 The Research contents

My research has encompassed the following topics: (1) constructing different morphology Cu-based electrodes by adjusting the electrodeposition parameters to get the best pristine structure for CO_2RR; (2) evaluating the valence of Cu functionalized by different electron-withdrawing/donating molecular by X-ray absorption spectroscopy (XAS) and make clear about the relationship between valence and CO_2RR performance; (3) developing membrane-electrode-assembly (MEA) electrolyzers to examine the electrochemical performance of different Cu-based electrodes and achieve industrial grade current density; (4) identifying the role of the surface oxidation state of $Cu^{\delta+}$ ($0<\delta<1$) on the selectivity and the formation rate of multi-carbon products by combining density functional theory (DFT) calculations with *operando* Raman and X-ray absorption spectroscopy (XAS);

(5) achieving high energy efficiency (EE, %), high CO_2 single-pass conversion rate (SPC, %), and low electrical power consumption (EPC, %) based on $Cu^{\delta+}$ electrodes.

The manuscript is organized into four chapters. In the first chapter, the fundamentals of CO_2 electrochemical reduction reaction, the methods and parameters of performance evaluation; the current state of electrochemical CO_2 reduction reaction are introduced and discussed.

The second chapter summarizes the reported methods from literatures to suppress the main side reaction (hydrogen evolution reaction, HER) in CO_2 reduction reaction (CO_2RR) and N_2 reduction reaction (NRR).

The third chapter develops a bimetallic Ag-Cu catalyst functionalized by thiadiazole and triazole derivatives and found that the strong electron withdrawing groups based on aromatic heterocycles can effectively orient the pathway of the CO_2RR reactions towards the synthesis of C_{2+} molecules.

The last chapter is built on the results presented in the second chapter. A library of different electron-withdrawing aryl diazonium salts functionalized Cu catalysts are fabricated to elucidate the influence of Cu valence on the high selectivity of ethylene during the CO_2RR.

1.5 References

1 Lewis, N. S. & Nocera, D. G. Powering the planet: Chemical challenges in solar energy utilization. *Proceedings of the National Academy of Sciences* **103**, 15729-15735 (2006).

2 Olah, G. A., Goeppert, A. & Prakash, G. S. Chemical recycling of carbon dioxide to methanol and dimethyl ether: from greenhouse gas to renewable, environmentally carbon neutral fuels and synthetic hydrocarbons. *The Journal of organic chemistry* **74**, 487-498 (2009).

3 Schrag, D. P. Preparing to capture carbon. *science* **315**, 812-813 (2007).

4 Yuan, D. *et al.* Electrochemical activation of carbon dioxide for synthesis of dimethyl carbonate in an ionic liquid. *Electrochimica Acta* **54**, 2912-2915 (2009).

5 Whipple, D. T. & Kenis, P. J. Prospects of CO_2 utilization via direct heterogeneous electrochemical reduction. *The Journal of Physical Chemistry Letters* **1**, 3451-3458 (2010).

6 Agarwal, A. S., Zhai, Y., Hill, D. & Sridhar, N. The electrochemical reduction of carbon dioxide to formate/formic acid: engineering and economic feasibility. *ChemSusChem* **4**, 1301-1310 (2011).

7 Sakakura, T., Choi, J.-C. & Yasuda, H. Transformation of carbon dioxide. *Chemical reviews* **107**, 2365-2387 (2007).

8 Oloman, C. & Li, H. Electrochemical processing of carbon dioxide. *ChemSusChem: Chemistry & Sustainability Energy & Materials* **1**, 385-391 (2008).

9 Benson, E. E., Kubiak, C. P., Sathrum, A. J. & Smieja, J. M. Electrocatalytic and homogeneous approaches to conversion of CO_2 to liquid fuels. *Chemical Society Reviews* **38**, 89-99 (2009).

10 Lee, J., Kwon, Y., Machunda, R. L. & Lee, H. J. Electrocatalytic recycling of CO_2 and small organic molecules. *Chemistry–An Asian Journal* **4**, 1516-1523 (2009).

11 Windle, C. D. & Perutz, R. N. Advances in molecular photocatalytic and electrocatalytic CO_2 reduction. *Coordination Chemistry Reviews* **256**, 2562-2570 (2012).

12 Wang, G. *et al.* Electrocatalysis for CO_2 conversion: from fundamentals to value-added products. *Chemical Society Reviews* **50**, 4993-5061 (2021).

13 Sanz-Perez, E. S., Murdock, C. R., Didas, S. A. & Jones, C. W. Direct capture of CO_2 from ambient air. *Chemical reviews* **116**, 11840-11876 (2016).

14 Gao, P. *et al.* Direct conversion of CO_2 into liquid fuels with high selectivity over a bifunctional catalyst. *Nature chemistry* **9**, 1019-1024 (2017).

15 Aresta, M., Dibenedetto, A. & Angelini, A. Catalysis for the valorization of exhaust carbon: from CO_2 to chemicals, materials, and fuels. Technological use of CO_2. *Chemical reviews* **114**, 1709-1742 (2014).

16 Liang, J. *et al.* Recent progress and development in inorganic halide perovskite quantum dots for photoelectrochemical applications. *Small* **16**, 1903398 (2020).

17 Nitopi, S. *et al.* Progress and perspectives of electrochemical CO_2 reduction on copper in aqueous electrolyte. *Chemical reviews* **119**, 7610-7672 (2019).

18 Bagger, A., Ju, W., Varela, A. S., Strasser, P. & Rossmeisl, J. Electrochemical CO_2 reduction: a classification problem. *ChemPhysChem* **18**, 3266-3273 (2017).

19 Laursen, A. B. *et al.* Electrochemical hydrogen evolution: Sabatier's principle and the volcano plot. *Journal of Chemical Education* **89**, 1595-1599 (2012).

20 Tang, W. *et al.* The importance of surface morphology in controlling the selectivity of polycrystalline copper for CO_2 electroreduction. *Physical Chemistry Chemical Physics* **14**, 76-81 (2012).

21 Zhang, Y.-J., Sethuraman, V., Michalsky, R. & Peterson, A. A. Competition between CO_2 reduction and H_2 evolution on transition-metal electrocatalysts. *Acs Catalysis* **4**, 3742-3748 (2014).

22 Wang, Y., Han, P., Lv, X., Zhang, L. & Zheng, G. Defect and interface engineering for aqueous electrocatalytic CO_2 reduction. *Joule* **2**, 2551-2582 (2018).

23 Karapinar, D. *et al.* Electroreduction of CO_2 on single-site copper-nitrogen-doped carbon material: selective formation of ethanol and reversible restructuration of the metal sites. *Angewandte Chemie International Edition* **58**, 15098-15103 (2019).

24 Weng, Z. *et al.* Electrochemical CO_2 reduction to hydrocarbons on a heterogeneous molecular Cu catalyst in aqueous solution. *Journal of the American Chemical Society* **138**, 8076-8079 (2016).

25 Reske, R., Mistry, H., Behafarid, F., Roldan Cuenya, B. & Strasser, P. Particle size effects in the catalytic electroreduction of CO_2 on Cu nanoparticles. *Journal of the American Chemical Society* **136**, 6978-6986 (2014).

26 Duan, Y. X. *et al.* Amorphizing of Cu nanoparticles toward highly efficient and robust electrocatalyst for CO_2 reduction to liquid fuels with high faradaic efficiencies. *Advanced Materials* **30**, 1706194 (2018).

27 Ma, M., Djanashvili, K. & Smith, W. A. Controllable hydrocarbon formation from the electrochemical reduction of CO_2 over Cu nanowire arrays. *Angewandte chemie international edition* **55**, 6680-6684 (2016).

28 Zhao, Z. *et al.* Efficient and stable electroreduction of CO_2 to CH_4 on CuS nanosheet arrays. *Journal of Materials Chemistry A* **5**, 20239-20243 (2017).

29 Manthiram, K., Beberwyck, B. J. & Alivisatos, A. P. Enhanced electrochemical methanation of carbon dioxide with a dispersible nanoscale copper catalyst. *Journal of the American Chemical Society* **136**, 13319-13325 (2014).

30 Jung, H. *et al.* Electrochemical fragmentation of Cu_2O nanoparticles enhancing selective C–C coupling from CO_2 reduction reaction. *Journal of the American Chemical Society* **141**, 4624-4633 (2019).

31 Mistry, H. *et al.* Tuning catalytic selectivity at the mesoscale via interparticle interactions. *Acs catalysis* **6**, 1075-1080 (2016).

32 Schouten, K. J. P., Qin, Z., Pérez Gallent, E. & Koper, M. T. Two pathways for the formation of ethylene in CO reduction on single-crystal copper electrodes. *Journal of the American Chemical Society* **134**, 9864-9867 (2012).

33 Luo, W., Nie, X., Janik, M. J. & Asthagiri, A. Facet dependence of CO_2 reduction paths on Cu electrodes. *ACS Catalysis* **6**, 219-229 (2016).

34 Huang, Y., Handoko, A. D., Hirunsit, P. & Yeo, B. S. Electrochemical reduction of CO_2 using copper single-crystal surfaces: effects of CO* coverage on the selective formation of ethylene. *ACS catalysis* **7**, 1749-1756 (2017).

35 Hori, Y., Takahashi, I., Koga, O. & Hoshi, N. Selective formation of C_2 compounds from electrochemical reduction of CO_2 at a series of copper single crystal electrodes. *The Journal of Physical Chemistry B* **106**, 15-17 (2002).

36 Hori, Y., Takahashi, I., Koga, O. & Hoshi, N. Electrochemical reduction of carbon dioxide at various series of copper single crystal electrodes. *Journal of Molecular Catalysis A: Chemical* **199**, 39-47 (2003).

37 Wang, Y. *et al.* Catalyst synthesis under CO_2 electroreduction favours faceting and promotes renewable fuels electrosynthesis. *Nature Catalysis* **3**, 98-106 (2020).

38 Hahn, C. *et al.* Engineering Cu surfaces for the electrocatalytic conversion of CO_2: Controlling selectivity toward oxygenates and hydrocarbons. *Proceedings of the National Academy of Sciences* **114**, 5918-5923 (2017).

39 Reller, C. *et al.* Selective electroreduction of CO_2 toward ethylene on nano dendritic copper catalysts at high current density. *Advanced Energy Materials* **7**, 1602114 (2017).

40 Yang, K. D. *et al.* Morphology-directed selective production of ethylene or ethane from CO_2 on a Cu mesopore electrode. *Angewandte Chemie* **129**, 814-818 (2017).

41 Xie, C., Niu, Z., Kim, D., Li, M. & Yang, P. Surface and interface control in nanoparticle catalysis. *Chemical reviews* **120**, 1184-1249 (2019).

42 Xiao, H., Goddard, W. A., Cheng, T. & Liu, Y. Cu metal embedded in oxidized matrix catalyst to promote CO_2 activation and CO dimerization for electrochemical reduction of CO_2. *Proceedings of the National Academy of Sciences* **114**, 6685-6688 (2017).

43 Varandili, S. B. *et al.* Synthesis of Cu/CeO_{2-x} nanocrystalline heterodimers with interfacial active sites to promote CO_2 electroreduction. *Acs Catalysis* **9**, 5035-5046 (2019).

44 Luo, M. *et al.* Hydroxide promotes carbon dioxide electroreduction to ethanol on copper via tuning of adsorbed hydrogen. *Nature communications* **10**, 1-7 (2019).

45 Liu, Y. *et al.* Selective electrochemical reduction of carbon dioxide to ethanol on a boron-and nitrogen-Co-doped nanodiamond. *Angewandte Chemie* **129**, 15813-15817 (2017).

46 Liu, Y., Chen, S., Quan, X. & Yu, H. Efficient electrochemical reduction of carbon dioxide to acetate on nitrogen-doped nanodiamond. *Journal of the American Chemical Society* **137**, 11631-11636 (2015).

47 Wang, H. *et al.* Synergistic enhancement of electrocatalytic CO_2 reduction to C2 oxygenates at nitrogen-doped nanodiamonds/Cu interface. *Nature Nanotechnology* **15**, 131-137 (2020).

48 Zhu, W., Tackett, B. M., Chen, J. G. & Jiao, F. Bimetallic electrocatalysts for CO_2 reduction. *Electrocatalysis*, 105-125 (2020).

49 Watanabe, M., Shibata, M., Katoh, A., Sakata, T. & Azuma, M. Design of alloy electrocatalysts for CO2 reduction. *Journal of Electroanalytical Chemistry* **305**, 319-328 (1991).

50 Watanabe, M., Shibata, M., Katoh, A., Sakata, T. & Azuma, M. Design of alloy electrocatalysts for CO_2 reduction: improved energy efficiency, selectivity, and reaction rate for the CO_2 electroreduction on Cu alloy electrodes. *Journal of electroanalytical chemistry and interfacial electrochemistry* **305**, 319-328 (1991).

51 Lamaison, S. *et al.* Zn–Cu Alloy Nanofoams as Efficient Catalysts for the Reduction of CO_2 to Syngas Mixtures with a Potential-Independent H_2/CO Ratio. *ChemSusChem* **12**, 511-517 (2019).

52 Jedidi, A., Rasul, S., Masih, D., Cavallo, L. & Takanabe, K. Generation of Cu–In alloy surfaces from $CuInO_2$ as selective catalytic sites for CO_2 electroreduction. *Journal of Materials Chemistry A* **3**, 19085-19092 (2015).

53 Tan, D. *et al.* Cu x Ni y alloy nanoparticles embedded in a nitrogen–carbon network for efficient conversion of carbon dioxide. *Chemical science* **10**, 4491-4496 (2019).

54 Ma, S. *et al.* Electroreduction of carbon dioxide to hydrocarbons using bimetallic Cu–Pd catalysts with different mixing patterns. *Journal of the American Chemical Society* **139**, 47-50 (2017).

55 Tao, Z., Wu, Z., Yuan, X., Wu, Y. & Wang, H. Copper–gold interactions enhancing formate production from electrochemical CO_2 reduction. *ACS Catalysis* **9**, 10894-10898 (2019).

56 Kim, D., Resasco, J., Yu, Y., Asiri, A. M. & Yang, P. Synergistic geometric and electronic effects for electrochemical reduction of carbon dioxide using gold–copper bimetallic nanoparticles. *Nature communications* **5**, 1-8 (2014).

57 Kuhl, K. P. *et al.* Electrocatalytic conversion of carbon dioxide to methane and methanol on transition metal surfaces. *Journal of the American Chemical Society* **136**, 14107-14113 (2014).

58 Jeon, H. S. *et al.* Operando insight into the correlation between the structure and composition of CuZn nanoparticles and their selectivity for the electrochemical CO_2 reduction. *Journal of the American Chemical*

Society **141**, 19879-19887 (2019).

59 Li, Y. C. *et al.* Binding site diversity promotes CO_2 electroreduction to ethanol. *Journal of the American Chemical Society* **141**, 8584-8591 (2019).

60 Arán-Ais, R. M., Scholten, F., Kunze, S., Rizo, R. & Roldan Cuenya, B. The role of in situ generated morphological motifs and Cu (i) species in C_{2+} product selectivity during CO_2 pulsed electroreduction. *Nature Energy* **5**, 317-325 (2020).

61 Gao, S. *et al.* Partially oxidized atomic cobalt layers for carbon dioxide electroreduction to liquid fuel. *Nature* **529**, 68-71 (2016).

62 Li, C. W. & Kanan, M. W. CO_2 reduction at low overpotential on Cu electrodes resulting from the reduction of thick Cu_2O films. *Journal of the American Chemical Society* **134**, 7231-7234 (2012).

63 Mistry, H. *et al.* Highly selective plasma-activated copper catalysts for carbon dioxide reduction to ethylene. *Nature communications* **7**, 1-9 (2016).

64 Zhou, Y. *et al.* Dopant-induced electron localization drives CO_2 reduction to C_2 hydrocarbons. *Nature chemistry* **10**, 974-980 (2018).

65 Morales-Guio, C. G. *et al.* Improved CO_2 reduction activity towards C_{2+} alcohols on a tandem gold on copper electrocatalyst. *Nature Catalysis* **1**, 764-771 (2018).

66 Ren, D., Ang, B. S.-H. & Yeo, B. S. Tuning the selectivity of carbon dioxide electroreduction toward ethanol on oxide-derived Cu x Zn catalysts. *Acs Catalysis* **6**, 8239-8247 (2016).

67 Hoang, T. T. *et al.* Nanoporous copper–silver alloys by additive-controlled electrodeposition for the selective electroreduction of CO_2 to ethylene and ethanol. *Journal of the American Chemical Society* **140**, 5791-5797 (2018).

68 Lee, S., Park, G. & Lee, J. Importance of Ag–Cu biphasic boundaries for selective electrochemical reduction of CO_2 to ethanol. *Acs Catalysis* **7**, 8594-8604 (2017).

69 Chen, C. *et al.* Cu-Ag tandem catalysts for high-rate CO_2 electrolysis toward multicarbons. *Joule* **4**, 1688-1699 (2020).

70 Clark, E. L., Hahn, C., Jaramillo, T. F. & Bell, A. T. Electrochemical CO_2 reduction over compressively strained CuAg surface alloys with enhanced multi-carbon oxygenate selectivity. *Journal of the American Chemical Society* **139**, 15848-15857 (2017).

71 Buckley, A. K. *et al.* Electrocatalysis at organic–metal interfaces: identification of structure–reactivity relationships for CO_2 reduction at modified Cu surfaces. *Journal of the American Chemical Society* **141**, 7355-7364 (2019).

72 Han, Z., Kortlever, R., Chen, H.-Y., Peters, J. C. & Agapie, T. CO_2 reduction selective for C≥2 products on polycrystalline copper with N-substituted pyridinium additives. *ACS central science* **3**, 853-859 (2017).

73 Cui, W. G. & Hu, T. L. Incorporation of active metal species in crystalline porous materials for highly efficient synergetic catalysis. *Small* **17**, 2003971 (2021).

74 Bai, S. *et al.* Highly active and selective hydrogenation of CO_2 to ethanol by ordered Pd–Cu nanoparticles. *Journal of the American Chemical Society* **139**, 6827-6830 (2017).

75 Huang, J., Mensi, M., Oveisi, E., Mantella, V. & Buonsanti, R. Structural sensitivities in bimetallic catalysts for electrochemical CO_2 reduction revealed by Ag–Cu nanodimers. *Journal of the American Chemical Society* **141**, 2490-2499 (2019).

76 De Luna, P. *et al.* Catalyst electro-redeposition controls morphology and oxidation state for selective carbon dioxide reduction. *Nature Catalysis* **1**, 103-110 (2018).

77 Eilert, A., Roberts, F. S., Friebel, D. & Nilsson, A. Formation of copper catalysts for CO_2 reduction with high ethylene/methane product ratio investigated with in situ X-ray absorption spectroscopy. *The journal of physical chemistry letters* **7**, 1466-1470 (2016).

78 Lee, S., Kim, D. & Lee, J. Electrocatalytic production of C_3-C_4 compounds by conversion of CO_2 on a chloride-induced bi-phasic Cu_2O-Cu catalyst. *Angewandte Chemie* **127**, 14914-14918 (2015).

79 Dinh, C.-T. *et al.* CO_2 electroreduction to ethylene via hydroxide-mediated copper catalysis at an abrupt interface. *Science* **360**, 783-787 (2018).

80 Li, F. *et al.* Molecular tuning of CO_2-to-ethylene conversion. *Nature* **577**, 509-513 (2020).

Chapter 2. Electrocatalyst Microenvironment Engineering for Enhanced Product Selectivity in Carbon Dioxide and Nitrogen Reduction Reactions

2.1 Abstract

Carbon and nitrogen fixation strategies are regarded as alternative routes to produce valuable chemicals used as energy carriers and fertilizers that are traditionally obtained from nonsustainable and energy-intensive coal gasification (CO and CH_4) Fischer-Tropsch (C_2H_4) and Haber-Bosch (NH_3) processes. Recently, the electrocatalytic CO_2 reduction reaction (CO_2RR) and N_2 reduction reaction (NRR) have received tremendous attention with the merits of being energy-saving and environmentally friendly. To date, the development of the CO_2RR and NRR processes is primarily hindered by the competitive hydrogen evolution reaction (HER), however the corresponding strategies for inhibiting this undesired side reaction are still quite limited. Considering such complex reactions involving three gas-liquid-solid phases and successive proton-coupled electron transfers, it appears meaningful to review the current strategies for improving product selectivity in light of their respective reaction mechanisms, kinetics, and thermodynamics. Herein, based on the reaction pathways, we examine and discuss the recent progress in inhibiting the HER and optimizing the selectivity of the electrocatalytic CO_2RR and NRR by focusing on the following strategies: (a) limiting the proton/electron transfer kinetics; (b) shifting the chemical equilibrium, and (c) designing novel electrocatalysts and electrolytic systems. This review provides insights into the enhancement of the CO_2RR and NRR selectivity and efficiency by focusing on the activation of CO_2 and N_2 molecules on the catalyst surface, the regulation of the gas-liquid-solid three-phase interface and the development of novel electrolyzers.

2.2 Introduction

Excessive consumption of fossil fuels such as oil, coal, and natural gas has produced a record-breaking level of atmospheric carbon dioxide (CO_2), resulting in the adverse effect of climate change and the aggravation of the energy crisis (**Fig. 1a**).[1,2] Nitrogen (N_2) fixation *via* the conversion of atmospheric nitrogen to ammonia (NH_3) has been regarded as one of the most important challenges in the industry. Ammonia not only plays a key role in producing fertilizers to sustain the rising global population, but also serves as a green energy carrier and an alternative fuel, as demonstrated in **Fig. 1b**.[3-5] An appealing solution would consist of the fixation of CO_2 and N_2, which are highly abundant feedstocks, into valuable carbonaceous compounds such as carbon monoxide (CO), formic acid (HCOOH), methanol (CH_3OH), methane (CH_4), ethylene (C_2H_4), ethanol (CH_3CH_2OH), ammonia (NH_3) and urea (CH_4N_2O), powered by renewable sources.[6,7,8,9] In this context, the creation of large-scale electrolysis systems powered by solar, wind, wave, and hydro energy can relieve our dependence on the dwindling supplies of fossil fuels. However, owing to their intermittent nature, the fraction of energy generated from renewable sources is limited to only 30% unless practical strategies for large-scale energy storage become available.[10]

Among the various fixation strategies, electrocatalysis could be massively developed for the conversion and chemical storage of renewable energy in the form of fuels, as it can meet its promises in terms of cost efficiency and stability.[11] However, in aqueous electrolytes, the hydrogen evolution reaction (HER) occurs at potential ranges comparable to those associated with the CO_2RR and NRR. This, combined with a large number of available protons near the active sites makes the HER dominant, which results in an extremely low Faradaic efficiency and limits the product selectivity towards the desired hydrocarbons and ammonia.[12,13] To overcome the HER during both the CO_2RR and NRR, investigations have focused on designing novel catalytic materials with improved selectivity, and limiting the accessibility of electrons and/or protons during the successive electrochemical steps.[14] In addition, in the context of CO_2RR to multi-carbon products, increasing the availability of primary reduction products such as CO in the vicinity of the electrode surface is a key parameter to maximize selectivity towards multi-carbon products.

There exists an extensive amount of literature in both CO_2RR and NRR fields, including several recent reviews of specific subtopics.[15-18] Through a handful of selected examples we review the strategies for increasing selectivity towards value-added products in these emerging fields. The first part of the review provides an overview of the CO_2RR and NRR from a mechanistic and thermodynamic point of view. We then analysis the literature for optimizing catalyst selectivity by engineering the catalyst surface and the reaction interfaces. The third section of the review presents recent developments in electrolytes, notably ionic liquids and polymer-based electrolytes. This is followed by an overview of recent research on catalyst surface modification and three-phase interface engineering. In the last section, we expose the current challenge and future developments in the field.

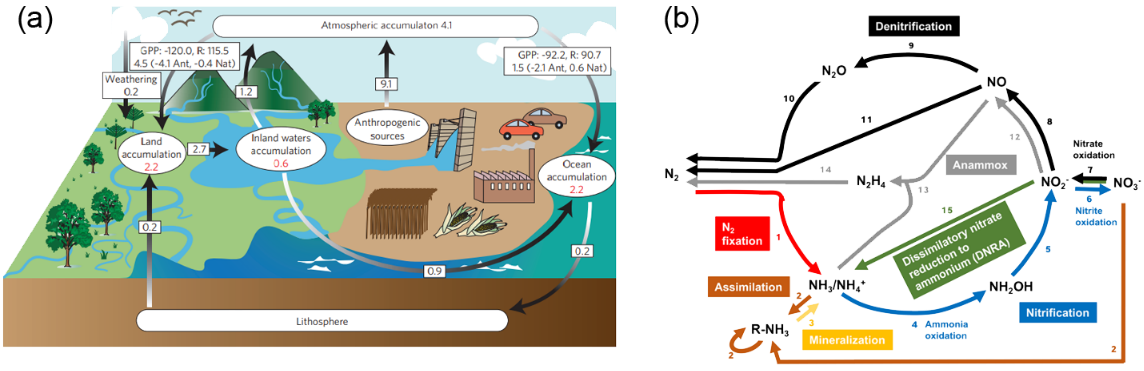

Fig 1. **(a)** Scheme of the carbon cycle. Reproduced from Ref.[2] with permission from Nature Publishing Group. **(b)** Cycle of biologically driven N-transformations that occur in natural and human-influenced terrestrial and marine environments. Reproduced from Ref.[5] with permission from the Royal Society of Chemistry.

2.3 Mechanistic and thermodynamic origin of multiple product generation in CO2RR and NRR

Both CO_2RR and NRR to value-added products involve multiple successive proton-coupled electron transfers (Table 1), which represent a significant kinetic challenge to be overcome to achieve high selectivity, in particular compared to the more kinetically facile two-electron hydrogen generation reaction.[19-21] This kinetic challenge is

in addition further complexified by the low availability of the reactants, as both CO_2 and N_2 have typically poor solubility in aqueous electrolytes.

Table 1. Selected standard potentials of CO_2 and N_2 in aqueous solutions (V *vs.* SHE) at 1.0 atm and 25 °C, calculated according to the standard Gibbs energies of the reactants in reactions. Reproduced from Ref.[22] with permission from American Chemical Society.

$$2H^+ + 2e^- \rightarrow H_2 \qquad (E^0 = 0\ V\ vs.SHE) \qquad (1)$$

$$N_2 + 8H^+ + 6e^- \rightarrow 2NH_4{}^+ \qquad (E^0 = 0.274\ V\ vs.SHE) \qquad (2)$$

$$CO_2 + 2H^+ + 2e^- \rightarrow CO + H_2O \qquad (E^0 = -0.106\ V\ vs.SHE) \qquad (3)$$

$$CO_2 + 2H^+ + 2e^- \rightarrow HCOOH \qquad (E^0 = -0.250\ V\ vs.SHE) \qquad (4)$$

$$2CO_2 + 12H^+ + 12e^- \rightarrow C_2H_4 + 4H_2O \qquad (E^0 = 0.064\ V\ vs.SHE) \qquad (5)$$

$$2CO_2 + 12H^+ + 12e^- \rightarrow C_2H_5OH + 3H_2O \qquad (E^0 = 0.084\ V\ vs.SHE) \qquad (6)$$

In addition, a thermodynamic challenge is associated to the CO_2RR, since proton reduction (HER) is more thermodynamically favourable than the reduction of CO_2 to most products (**Fig. 2a** and **Equations 3-6**).[22-24] Although less critical in the case of NRR, the standard electrochemical potential for the proton reduction reaction is yet close to that of the nitrogen reduction reaction (NRR) at 0.057 V *vs.* SHE (**Equation 2**). The intrinsic stronger binding of H atoms over N_2 on most metal surfaces, highlighted in **Fig. 2b**, further illustrates that challenge to increase NRR selectivity vs. HER.

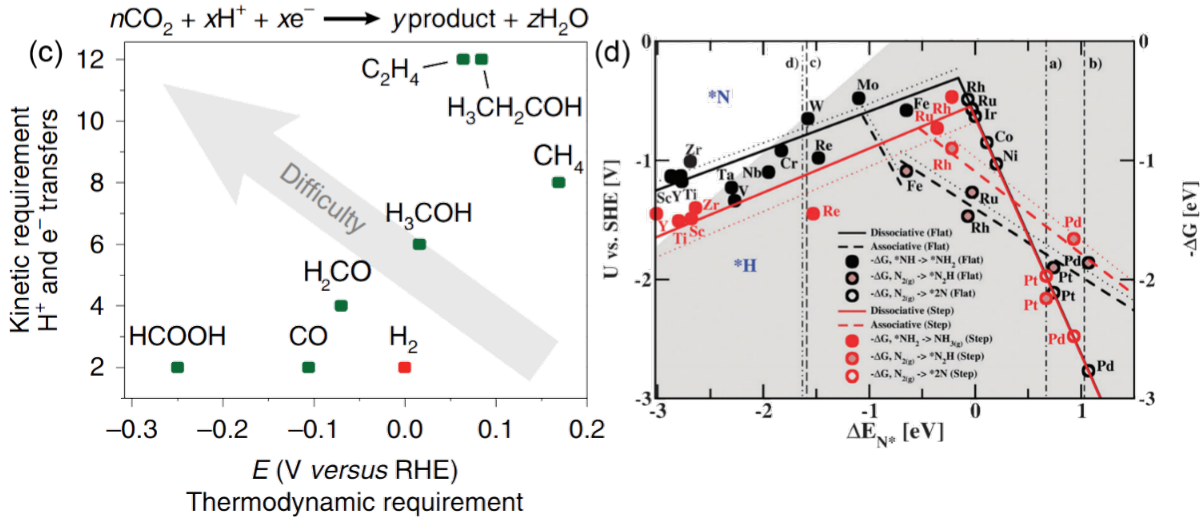

Fig 2. **(a)** Kinetic versus thermodynamic requirements of various CO_2 reduction reactions. The plotted values are based on the reaction equation given above the graph, made stoichiometric according to the product composition. Reproduced from Ref.[24] with permission from Nature Publishing Group. **(b)** Combined volcano diagrams (lines) for the flat (black) and stepped (red) transition metal surfaces for the reduction of nitrogen with a Heyrovsky-type reaction, without (solid lines) and with (dotted lines) H-bond effects. Reproduced from Ref.[25] with permission from the Royal Society of Chemistry.

This illustrate that three main challenges (thermodynamic, kinetic, or related to the mass-transport of the reactants) have to be overcome to reach high selectivity in CO_2RR and NRR. We will review in the next sections the three main axes currently explored toward that goal, being concentrated on catalyst design, electrolyte engineering and three-phase interface modulation.

2.4 Increasing selectivity via catalyst design

2.4.1 Catalyst nano-structuring for improved mass transport

Advancements in nanotechnology and characterization techniques have enabled a plethora of morphologies to be explored to improve catalytic activity and product selectivity. Porous materials have attracted particular attention due to their effect on the local chemical environment, including local pH and the mass transport of the reactant and intermediates.[38,39] The ability to increase effective active sites, both by maximizing surface area and facilitating the accessibility of such sites, makes porosity useful and interesting across a broad range of fields.[40] Such effects are especially crucial when considering the poor solubility of CO_2 and N_2 in aqueous electrolytes, which cause mass transport limitations and barriers to high activity and selectivity.

Hierarchical porous networks are found commonly in biological organisms as a strategy to mitigate mass transport limitations in the utilization of nutrients.[41] The three-dimensional networks were replicated in early work by Huan *et al.* who used gold nanodendrites for electrochemical sensing.[42] Their application in catalysis has recently appeared as an efficient strategy to increase current densities and catalyst selectivity in small molecule electroreduction and oxidation.

The dynamic hydrogen bubble templating (DHBT) method has been the most prominent technique to create such hierarchical porosity, which was recently comprehensively reviewed by the Bhargava group[43] and specifically for CO_2RR materials by the Broekmann group.[44] The process involves the electrodeposition of a metal from aqueous solutions of the respective cations, while co-generated hydrogen bubbles act as a dynamic template to create a metal foam. As the bubbles nucleate, grow and detach, a hierarchical pore structure forms with layers of pores of increasing diameter (**Fig. 3a**), including micropores in the submicron range and macropores 10-100 μm.[43] The DHBT technique is relatively simple, requiring aqueous solutions and no need for organic or inorganic templates (as in traditional metal foam synthesis),[45] high temperatures, high pressures or uncommon equipment. Nonetheless, additives such as citrate are common to influence crystal growth.[46-48] Bi- and multi-metallic catalysts are also possible by co-electrodeposition, galvanic replacement, stepwise electrodeposition or spontaneous decoration.[43] For example, many studies for CO_2RR have coupled copper with one other metal such as Ag, Sn, In or Zn. [49-53]

By fine-tuning parameters such as proton source and concentration, applied overpotential or current density, substrate material, and the metal source and concentration, the nanostructure can be carefully controlled and optimized. Broekmann and co-workers produced a dendritic Cu-based DHBT foam, and demonstrated a strong dependence of the C_2-product selectivity on the surface pore size diameter, with the optimal size being between

50 and 100 μm.[54] They identified the temporal trapping of gaseous intermediates inside these pores as the key to product selectivity. Intermediates such as CO and C_2H_4, which would otherwise be released into the bulk electrolyte, were entrapped in the pores of the foam catalyst, causing them to further react to form C_2H_6 (**Fig. 3b**). At -0.8 V vs RHE they achieved a 55 % faradaic efficiency for C_2 -products.

Such dendritic structures with large surface areas are common in this synthesis due to the deposition taking place at high current densities and therefore in the diffusion limited regime. Copper and oxide derived copper dendrites have had particular interest due to their apparent selectivity for multicarbon products.[55-58] Huan *et al*. produced a dendritic CuO material from DHBT that could be used both as a CO_2R and OER catalyst.[59,60] It consisted of a triple layer structure with a metallic Cu core covered by layers of Cu_2O and CuO (**Fig. 3c**). In electrocatalytic conditions, the CuO material is reduced to metallic Cu, generating nano-Kirkendall voids within the dendrite structures. These gas-accessible voids were proposed to enhance the confinement of secondary CO_2RR products, such as CO, resulting in FE_{C2+} over 50 %. By applying a continuous flow electrolyzer, they were able to reach a stable current of 25 mA/cm^2 with 2.95 V, equating to 21 % energy efficiency for hydrocarbon production. By coupling the cell to a photovoltaic cell, they achieved a 2.3 % solar-to-hydrocarbon efficiency.
DHBT foams for single-carbon products such as CO and formate have also been reported. A silver-foam with needle-shaped features in the mesopores was produced by using a citrate additive to control growth on the nanometer scale.[46] Between -0.3 to -1.2 V vs RHE 90% faradaic efficiency for CO was observed, however at higher over-potentials they produced C_2-products, with 51% CH_4 at -1.5V (**Fig. 3d**). This unusual activity for Ag was attributed to the catalyst morphology and nanostructure increasing *CO surface concentration and residence time. Recent work by Mayer and co-workers exemplifies the advantages of the simplicity of the DHBT method. In a one-step synthesis they used waste industrial Cu-Sn bronze as a material precursor to deposit a mesoporous $Cu_{10}Sn$ foam**.**[61] They achieved over 85 % faradaic efficiency for CO at -0.8 V vs RHE, over double that of the plain Cu-Sn bronze, with partial current densities three times higher. Du *et al.* prepared a nanoporous tin DHBT foam on a tin substrate and achieved a faradaic efficiency for formate of 90 % with current densities of 23 mA/cm^2.

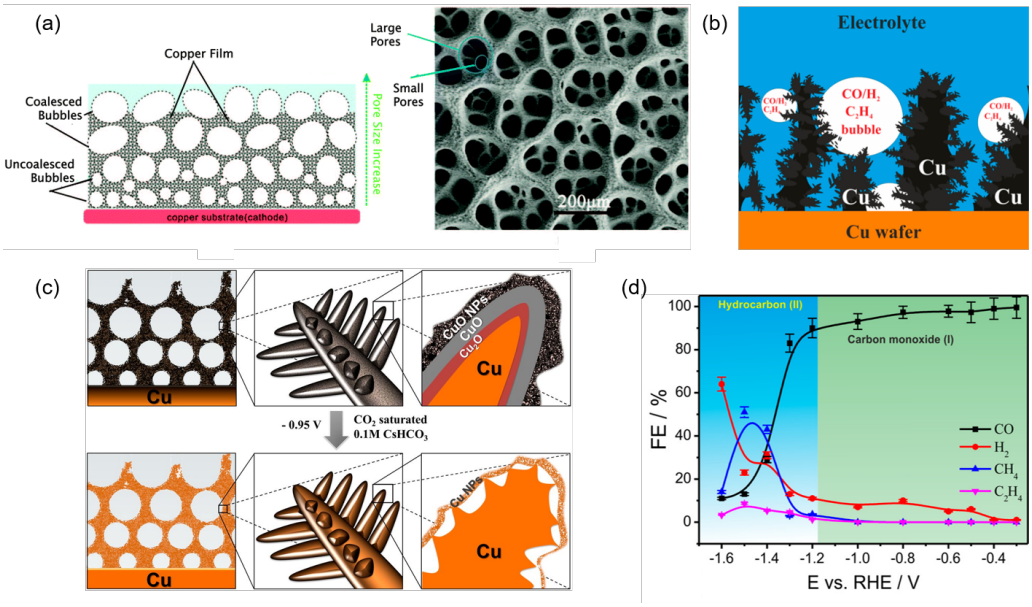

Fig 3. (a) Schematic illustration and SEM image of a copper DHBT foam, demonstrating the hierarchical pore structure. Reproduced from Ref.[43] and Ref.[56] with permission from the Royal Society of Chemistry and IOP Publishing. **(b)** Schematic illustration of gaseous CO_2R intermediates (CO and C_2H_4) and by-products (H_2) trapped within the porous Cu foam catalyst. Reproduced from Ref.[54] with permission from the American Chemical Society. **(c)** Schematic illustration of a dendritic CuO DHBT-foam before (top) and after (bottom) CO_2 electroreduction in 0.1 M $CsHCO_3$, showing the material reduction to metallic Cu and the formation of nano-Kirkendall voids. Reproduced from Ref.[60] with permission from the Proceedings of the National Academy of Sciences. **(d)** Potential dependent product distribution of the CO_2RR using a Ag-DHBT-foam catalyst by faradaic efficiency, showing the formation of hydrocarbons at potentials more negative than -1.2 V vs RHE. Reproduced from Ref.[46] with permission from the American Chemical Society.

Other morphology-based strategies have been utilized to modulate mass transport in CO_2 reduction, including the application of nanostructures such as nano-wires, sheets, needles, cones or tubes. Burdyny *et al.* explored the effect of nanomorphology of a silver catalyst on gas-evolution and subsequently bubble-induced mass transport.[62] By combing mathematical modelling and experimental observations using a dark field microscope, they compared bubble formation on nanoparticles, nanorods and nanoneedles, and found a mean bubble diameter of 97, 31 and 23 μm respectively. They illustrated that the generation of smaller bubbles improved long-range mass transport of CO_2, resulting in a small diffusion thickness and a 4-fold increase in limiting current density of CO production **(Fig. 4a)**. Surendranath and co-workers synthesised gold inverse opal thin films and found that changing the mesostructure by increasing porous film thickness could diminish HER 10-fold whilst maintaining activity for CO_2 to CO, enhancing the faradaic efficiency for CO from less than 5 % to over 80 %.[63] They attributed this to the formation of diffusional gradients. Studies into nanocavities and their performance and mechanism of action have emerged in recent years. Yang et al. utilised finite-element method simulations and experimental measurements on a multihollow cuprous oxide catalyst.[64] Analysis from X-ray absorption studies and operando Raman spectra indicated that the pore cavities confined *CO intermediates, which bound to Cu^+

sites and locally protected them against reduction during CO_2RR (**Fig. 4b**), as well as promoted C-C coupling. They achieved a C_{2+} product faradaic efficiency of 75 % and partial current density of 267 mA cm^{-2}.

As N_2 reduction is a comparatively new field with its own unique challenges, studies into morphological effects on catalytic activity and selectivity are less extensive. Although a range of nanostructures exist amongst the literature,[65] specific insight into the role morphology plays in catalysis is limited. Kumar *et al.* produced a multibranched PdCuIr catalyst with long-spined sea-urchin-like morphology.[66] The nanostructure had interconnected channels that could facilitate mass and charge transfer, yielding 13.43 µg h^{-1} $mg_{cat.}^{-1}$ NH_3 at a faradaic efficiency of 5.29 % (**Fig. 4d**). Another approach is to use porous frameworks as a support for catalysts. Wei et al. loaded ruthenium nanoparticles onto carbon nanotubes, which were also applied as the gas diffusion electrode.[67] Despite using a typical H-cell set-up, the GDE structure allowed N_2 gas to be flowed through the GDE and porous catalyst, instead of being solely solubilised in the electrolyte (**Fig. 4c**). They achieved a NH_3 yield rate of 2.1 nmol/cm^2s and faradaic efficiency of 13.5 %. Wang et al. deposited a porous Au film on a Ni foam.[68] They reported a NH_3 yield rate of 9.42 µg h^{-1} cm^{-2} and faradaic efficiency of 13.36 % at -0.2 V vs RHE, which they attributed partly to the interconnected porous structure.

A great range of nanostructures have been applied to the CO_2RR and NRR to regulate mass transport, and although strong correlations between structure and performance have been made, their mechanisms of action are often highly complex and difficult to define. Most theories focus on the mass transport of reactants and intermediates either through improved diffusion and convection or through their physical confinement in the catalyst pores. Considerable progress has been made by combining computational and experimental research, especially in the CO_2R field, however their application to new materials and fields such as N_2R could be improved.

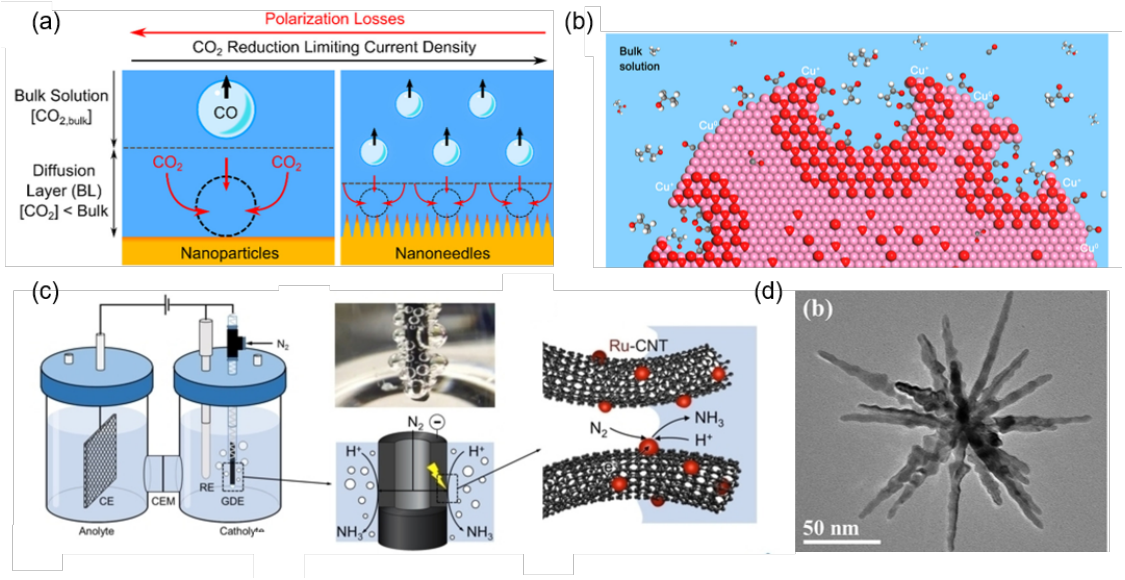

Fig 4. (a) Schematic showing the effect of catalyst nanostructure on bubble departure diameter and its impact on the diffusion boundary layer thickness and CO_2 mass transport. Reproduced from Ref[62] with permission from the American Chemical Society. **(b)** Schematic of a cuprous oxide catalyst with nanocavities that confine carbon intermediates such as

CO and C_2H_4. White: hydrogen; grey: carbon; red: oxygen; pink: copper. Reproduced from Ref.[64] with permission from the American Chemical Society. **(c)** Schematic illustration (left to right) and picture (middle-top) of the NRR in an H-cell with a microtubular Ru-CNT (carbon nanotube) gas diffusion electrode. Reproduced from Ref.[67] with permission from the European Chemical Societies Publishing. **(d)** TEM image of a PdCuIr catalyst with long-spined sea-urchin-like morphology. Reproduced from Ref.[66] with permission from the Royal Society of Chemistry.

2.4.2 Surface functionalization

Functionalizing the surface of the electrode or catalyst by organic or inorganic ligands has been frequently reported to adjust the interaction between adsorbed intermediates and catalysts, which not only inhibits the HER but also enhances the product selectivity. The concept of surface-bound ligands can be extended to covalently bonded molecules of the catalysts to tune the surface chemistry. In this section, we will review the different functionalization strategies that have been reported in CO_2RR and NRR (**Fig. 5a**).[69] To date, many organic additives, including amino acids, cysteamine, thiols, pyridinium, N-heterocyclic carbenes (NHCs), imidazolium salts, and inorganic anions, have been proposed to control the binding energy of CO_2RR reaction intermediates.[70,71] For instance, Kim *et al.* demonstrated a 94.2% FE for the production of CO from amine-capped Ag supported on carbon, thanks to the effective suppression of the HER and the intrinsic high selectivity towards the CO_2RR from Ag (**Fig. 5b**).[72] DFT calculations suggested that the amine-capped Ag nanoparticles stabilize the *COOH intermediate while destabilizing *H.[73] Conversely, thiol-capped Ag nanoparticles exhibited superior reaction rates towards both the HER and CO_2 reduction by indiscriminately increasing ΔG_{*H} and ΔG_{*COOH}.

As presented in **Fig. 5c**, Zhao *et al.* developed a simple modification strategy using amines to depress the hydrogen evolution reaction on ultrasmall Au NPs and promote CO_2-to-CO conversion.[74] The amine groups, as well as the molecular configuration, were found to play important roles in tuning the electrocatalytic activity of low-coordinated sites of the nanoparticles. The authors claimed that strong interactions between Au and the amine groups combined with the peculiar configuration are responsible for the improved CO_2RR performance. Remarkably, linear amines promoted the formation of CO, an effect which was enhanced by increasing the length of the alkyl chain, whereas the branched polyamine greatly depressed it. Wang *et al.* demonstrated 55% and 77% selectivities for ethylene and C_{2+} products, respectively, using a tricomponent copolymer to modify the surface of Cu electrodes.[75] Control experiments indicated that all three components of the copolymer are necessary for enhancing selectivity. The copolymer was obtained by ring-opening metathesis polymerization, thereby offering a new degree of freedom for tuning the selectivity. Xiao *et al.* successfully modified the d-band structure of a self-supporting nanoporous Mo_4P_3 catalyst by capping with a fluorosilane hydrophobic layer (**Fig. 5d**).[76] This approach weakens the ability to adsorb protons and simultaneously prevents water from approaching the active sites, thus further suppressing the HER. Hydrophobic Mo_4P_3 exhibits outstanding NRR performance, with an FE of as high as 10.1% and an NH_3 yield of 17.3 $\mu g\ h^{-1}\ cm^{-2}$. This strategy opens avenues for suppressing the HER and could be extended to other metal catalysts for the NRR and CO_2RR.

This field is rapidly growing, and we list below some important insights. Functionalizing metal electrodes with a reductive organic additive or an inorganic anion benefits hydrocarbon selectivity. The presence of selected organic films on the electrode promotes the reduction reactions at some potentials, while the inorganic anions are linked to increased adsorbed CO_{ads} coverage on the catalyst surface, thus stabilizing the intermediate.[77,78] The exact surface binding motifs of the ligands and precise mechanism for altered selectivity are still unclear. Understanding the precise nature of the interface remains a key challenge for attaining the desired catalytic properties.[79]

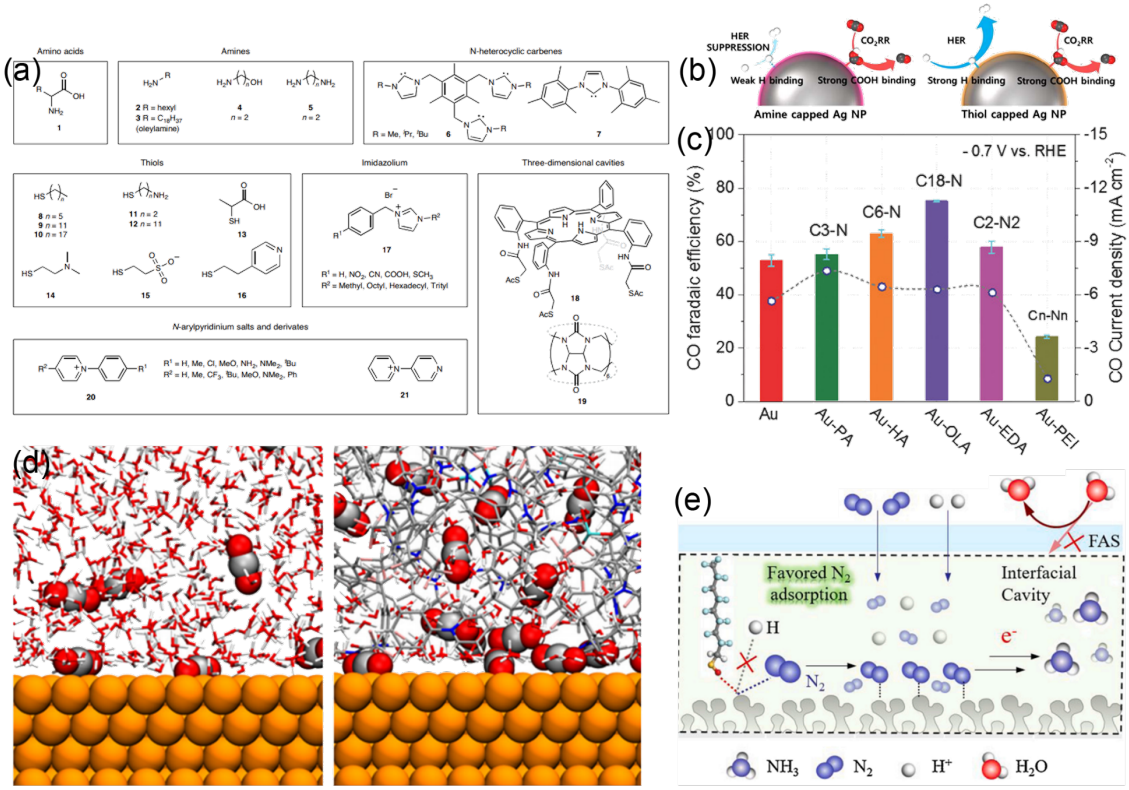

Fig 5. **(a)** Surface modifiers grouped into different classes used to modulate the local chemical environment around the catalytic site. (amino acids, amines, N-heterocyclic carbenes, thiols, imidazolium, three-dimensional cavities, N-arylpyridinium salts and derivatives). Reproduced from Ref.[69] with permission from Nature Publishing Group. **(b)** Schematic of the product selectivity, depending on the Ag NPs immobilized with an amine (or thiol)-containing anchoring agent. Reproduced from Ref.[72] with permission from the American Chemical Society. **(c)** FE_{CO} (column) and j_{CO} (circle) of gold catalysts with different surface amine modifications in CO_2-saturated 0.1 M $KHCO_3$ at -0.7 V *vs.* RHE. Reproduced from Ref.[74] with permission from Wiley. **(d)** Interface structure after 12 ns molecular dynamics simulations with a water/Cu interface and random copolymer with a water/Cu interface. Colour code: Cu, orange; C, grey; O, red; N, blue; F, pink; S, cyan; H, white. Reproduced from Ref.[75] with permission from the American Chemical Society. **(e)** Possible NRR mechanism at the surface of the hydrophobic catalyst. Reproduced from Ref.[76] with permission from Elsevier.

2.4.3 Crystal size and facet control

Tremendous advances have recently been made to engineer catalysts to lower the HER during the CO_2RR and NRR processes.[26] Compared with their bulk counterparts, nanostructured catalysts show original and often enhanced activity owing to their unique surface electronic and chemical properties. These properties can be finely adjusted to tune the activity and selectivity of electrocatalytic reactions. The surface of a nanomaterial catalyst typically consists of planar areas with single-crystalline orientations separated by steps and kink sites with lower coordination numbers. Complex atomic structures are therefore present at the interface between different grains in polycrystalline and/or nanostructured surfaces. Buonsanti *et al.* investigated the catalytic properties of exposed facets of Cu nanocatalysts at commercially relevant current densities (**Fig. 6a**).[27] The study revealed that facet-dependent selectivity could be retained in a gas-fed flow cell, showing greater HER suppression than a conventional H-cell. The (100) facets of Cu nanocubes have been identified to be selective for the evolution of C_2H_4, whereas the (111) facets of Cu octahedra are selective towards CH_4. Conversely, Cu spheres do not exhibit any specific product selectivity, suggesting that randomly mixed facets cannot depress the HER during the CO_2RR. Chorkendorff *et al.* systematically investigated the structure-selectivity relationship of Au single crystals for electrocatalytic CO_2 reduction (**Fig. 6b**).[28] Remarkably, they found that the kinetics for the formation of CO strongly depend on the surface structure. Under-coordinated sites, for instance, on the surface of Au(110) or at the step edges of Au(211), show at least 20-fold higher activity than more coordinated configurations – such as Au(100). By selectively poisoning under-coordinated sites with Pb, they identified the selectivity of these active sites towards the reduction of CO_2, effectively suppressing the HER.

Strasser *et al.* investigated the role of particle size in CO_2 electroreduction using size-controlled Cu nanoparticles (NPs).[29] A dramatic increase in the catalytic activity and selectivity of CO against H_2 was observed once the particle size was decreased, particularly for NPs smaller than 5 nm, as shown in **Fig. 6c**. Changes in the population of low-coordinated surface sites and their stronger chemisorption were linked to H_2 and CO selectivity. As shown in the inset of Figure 3c, a drastic increase in undercoordinated atoms is observed below a particle size of 2 nm with a coordination number lower than 8. These peculiar sites accelerate both hydrogen evolution and CO_2 reduction to CO *via* an increase in binding energy. However, the undercoordinated sites are unfavourable for the subsequent hydrogenation of CO, which lowers the hydrocarbon selectivity of the NPs. A plausible explanation for the observed trend is the reduced mobility of intermediate reaction species (CO and H) on the small NPs due to stronger bonding, which decreases the possibility of further recombination to form hydrocarbons. At intermediate particle sizes, the spherical particle model predicts low and constant populations of (100) and (111) facets, which is consistent with the reduced yet constant hydrocarbon selectivities observed for Cu NPs between 5 and 15 nm compared to Cu bulk surfaces. For these larger NPs, weaker binding of CO and H is expected, favouring hydrocarbon formation.

Another critical parameter for suppressing the HER with metal NP catalysts is the interparticle spacing. Mesoscale phenomena, such as interparticle reactant diffusion and re-adsorption of intermediates, can play an important role in the product selectivity for multistep reactions.[30,31] In this context, Mistry *et al.* showed that for

CO_2 electroreduction, decreasing the interparticle spacing for a constant nanoparticle size can suppress the HER, which further increases the selectivity for CH_4 and C_2H_4 owing to the increased possibility of the *CO intermediate re-adsorbing on a neighbouring particle and being further reduced (**Fig. 6d** and **6e**).[32] More importantly, this study uncovers general principles of tailoring NP activity and selectivity by carefully engineering the size and distance. These principles guide the rational design of mesoscopic catalyst architectures to enhance the production of the desired reaction products.[33]

Catalysts made of noble metals (Ru, Pt, Au, Rh and Pd) and transition metals (Fe, Mo and Co) have been extensively studied in the NRR process.[34] Rational design of electrocatalysts with specific active sites or facets has been successfully applied to limit the competitive HER while promoting NRR activity and selectivity.[35,36] For instance, Yang *et al.* reported an improved catalytic activity towards the NRR with an increased concentration of the (110) facet of molybdenum nanofilms.[37] Compared to commercial Mo foil, a one hundred-fold enhancement in catalytic activity was obtained at a low applied potential, with a maximum NH_3 formation rate of 3.09×10^{-11} mol s^{-1} cm^{-2} and an FE of 0.72% obtained in 10 mM H_2SO_4 electrolyte at -0.49 V *vs.* RHE and -0.29 V *vs.* RHE, respectively. The enhanced activity was attributed to both the surface morphology and the orientation of the exposed crystal facets. According to previous DFT studies, the adsorption energies of nitrogen and hydrogen on the Mo (110) facet are -1.1 eV and -0.7 eV, respectively, suggesting that the *N atoms would bind more strongly than *H atoms and would likely be reduced to NH_3 instead of H_2.[25]

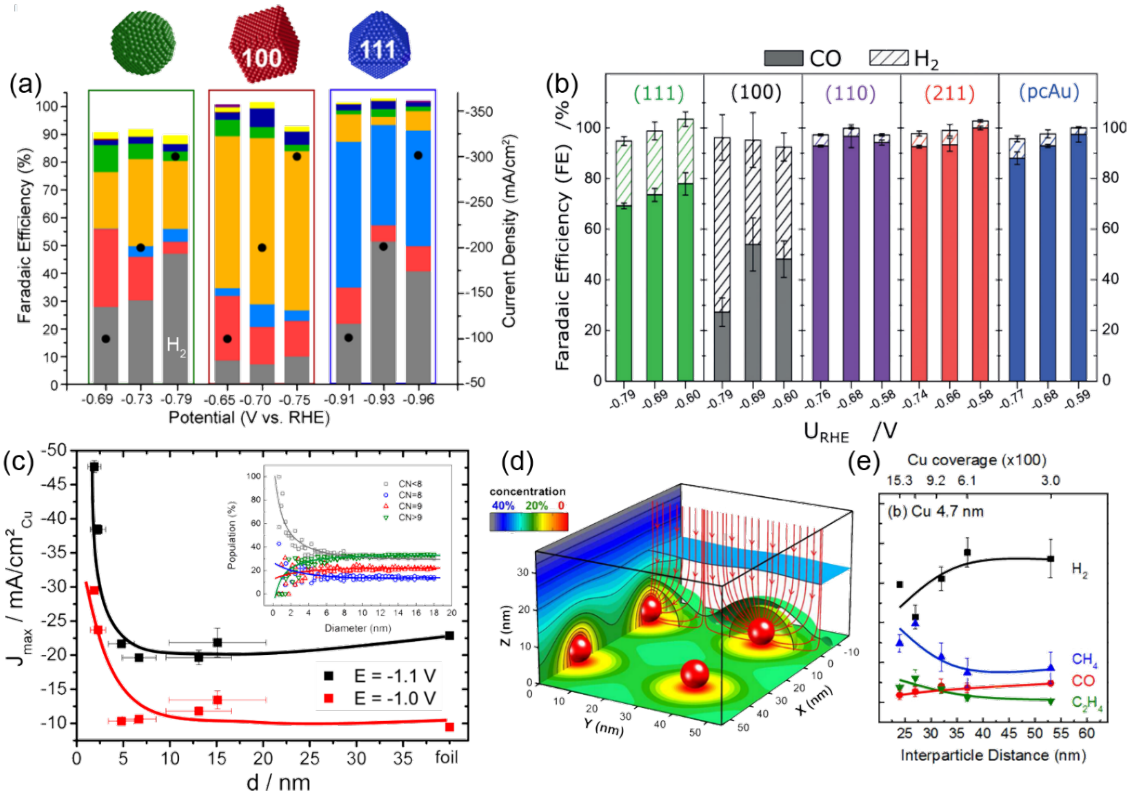

Fig 6. (a) Relation between the Faradaic efficiencies and potentials for different Cu morphologies (sphere, cube and octahedra). Reproduced from Ref.[27] with permission from the American Chemical Society. **(b)** Relation between the

Faradaic efficiencies and potentials with the exposure of different Au facets. Reproduced from Ref.[28] with permission from Wiley. **(c)** Particle size effect during catalytic CO_2 electroreduction. The Faradaic current densities at -1.1 and -1.0 V *vs.* RHE are plotted against the size of the Cu NP catalysts, and the inset shows the population (relative ratio) of surface atoms with a specific coordination number (CN) as a function of particle diameter. Reproduced from Ref.[29] with permission from the American Chemical Society. **(d)** Simulation results of the CO_2 concentration distribution based on diffusion equations. The red arrows show the reactant flux towards the NPs. The colour scale shows the concentration of CO_2 at a given distance from the NPs as a percentage of its value in the bulk of the electrolyte. A diffusion layer thickness of 100 nm was assumed. **(e)** Faradaic selectivity during the electroreduction of CO_2 at -1.1 V *vs.* RHE with a Cu interparticle distance of 4.7 nm. Reproduced from Ref.[32] with permission from the American Chemical Society.

2.4.4 Single site engineering

One of the main challenges of bulk metallic or metal-oxide/sulfide catalyst is the large distribution of accessible sites that may result to different favored reaction products and decreased selectivities. Presenting a much smaller distribution of active sites, single atom catalysts (SACs), represent an interesting strategy to increase the selectivity via a closer control of the active site. In the context of CO_2RR and NRR, SACs have been demonstrated as highly efficient to inhibit HER while promoting the targeted reactions.[80-83] Liu *et al.* established a general two-step approach to construct model SACs with precise structures (**Fig. 7a**).[84] This involves building well-defined molecular single-atom catalytic centres and linking them to a conductive carbon nanotube. The single-Ni-atom catalyst exhibited high CO_2RR activity, with a CO_2-to-CO faradaic efficiency of 99% and turnover frequency (TOF) of 100179 h^{-1} at a current density of 32.3 mA cm^{-2} and overpotential of 600 mV. Pan and coauthors reported the design of SACs with atomically dispersed Co sites anchored on polymer-derived hollow N-doped porous carbon spheres with a large surface area, abundant N coordination sites and high electrical conductivity.[85] As shown in **Fig. 7b**, the single-atom Co-N_5 site is also the dominant active center for CO_2 activation, and the rapid formation of *COOH is a key reaction intermediate compared with the coupling of protons followed by the fast desorption of CO.

SACs have also been applied to the NRR. Calculating free energies shows that all metal surfaces except for Pt (111) and Ir (111) exhibit positive relative energies on the top site for *H, which indicates that *H prefers bridge or hollow sites to top sites whereas *H is destabilized on the top site (**Fig. 7c**).[86] Thus, the suppressed proton adsorption originates from the availability of only the top adsorption sites on SACs, highlighting the fundamental role of the atomic ensemble effect in suppressing HER. Control of the conformation of the adsorbed molecules on single metal sites is an effective approach to purposefully improve the catalytic properties of SACs. Chen *et al.* performed DFT calculations to investigate the adsorption of N_2 on single metal sites.[87] In the case of a vertical end-on configuration followed by the formation of an oblique end-on *NNH molecule, the corresponding NRR process is energetically favourable (**Fig. 7d**). By targeting the two molecular configurations, single Ag sites with Ag-N_4 coordination were identified as the model catalyst for NRR. Experimentally, SACs composed of single Ag sites were prepared on N-doped carbon black (SA-Ag/NC) and demonstrated a high NH_3 yield rate (270.9 μg

h^{-1} mg_{cat}^{-1} or 69.4 mg $h^{-1}mgAg^{-1}$) and a desirable Faradaic efficiency (21.9%) in HCl aqueous solution under ambient conditions.

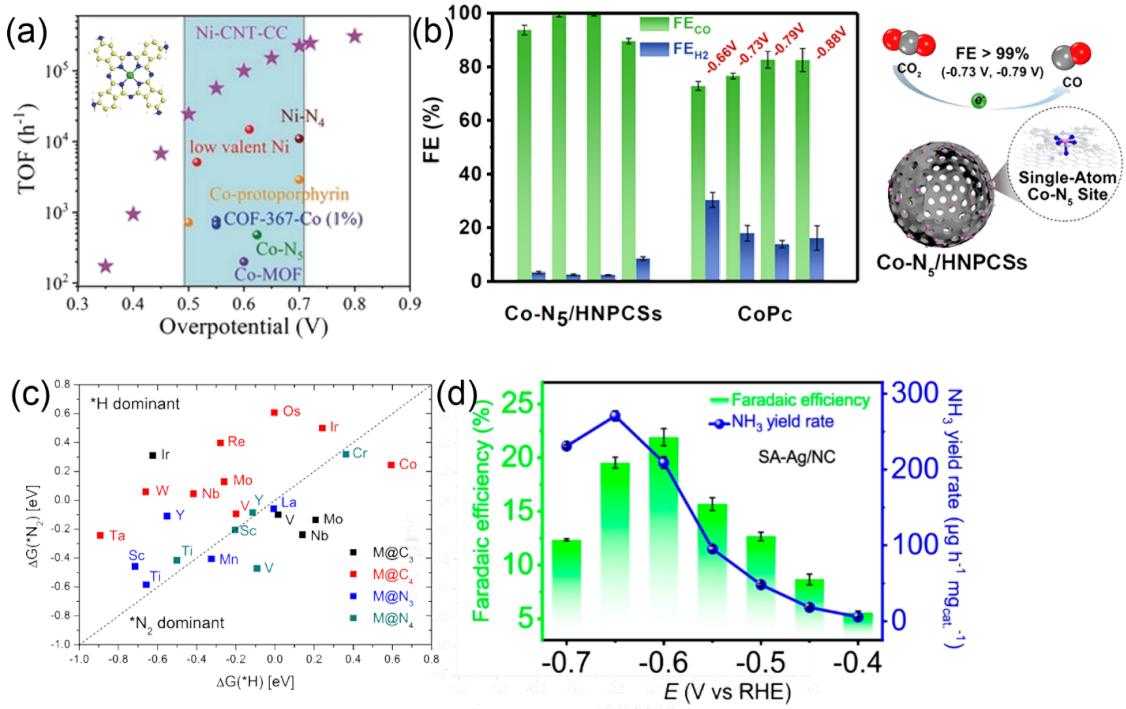

Fig 7. (a) TOF of Ni-CNT-CC compared with the TOFs of other state-of-the-art CO_2-to-CO reduction catalysts. Reproduced from Ref.[84] with permission from Wiley. **(b)** Comparison of the FE_{CO} and FE_{H2} of Co−N_5/HNPCSs and CoPc. Reproduced from Ref.[85] with permission from the American Chemical Society. **(c)** Calculated $\Delta G(^*H)$ and $\Delta G(^*N_2)$ on SACs that satisfy $\Delta GPDS \leq 1.0$ eV. The dashed line indicates $\Delta G(^*H) = \Delta G(^*N_2)$. SACs in the $\Delta G(^*H) > \Delta G(^*N_2)$ region ($^*N_2$ dominant region), under the dashed line, correspond to N_2 adsorption being more favourable than $^*H$ formation at 0 V *vs.* RHE. Reproduced from Ref.[86] with permission from the American Chemical Society. **(d)** Calculated FEs and yield rates of NH_3 over SA-Ag/NC. Reproduced from Ref.[87] with permission from the American Chemical Society.

2.5 The electrolyte: an active component to drive reactivity and enhance selectivity

2.5.1 Adjusting the local pH at the electrode/electrolyte interface

The pH value of the electrolyte greatly influences the equilibrium potential of the CO_2RR and NRR, as highlighted in the partial Pourbaix diagram for the CO_2RR and NRR provided in **Fig. 8a** and **Fig. 8b**.[88-90] [91]In addition to the thermodynamic cell potential, the cathodic and anodic overpotential is also heavily affected by pH, and highly alkaline media has often been applied to reduce cell voltage. A high local pH typically suppresses HER formation, thus favouring multicarbon products for the CO_2RR and ammonia selection for the NRR.[92,93] The groups of Sinton and Sargent have achieved remarkable results for the CO_2RR in highly alkaline media; using 7 M KOH (pH ≈ 15) they achieved a 1.3 A cm^{-2} partial current density for ethylene in a flow cell.[94] Engineering of the triple-phase interface was key to these results and will be discussed further in Section 5. Unfortunately for CO_2 electrolysis, the use of alkaline electrolyte is complicated by the fatal exergonic formation of carbonate,

which is detrimental to both energy and carbon efficiency.[95] Neutral bicarbonate electrolytes have been applied to reduce electrolyte consumption and to buffer the local pH, although at high currents CO_3^{2-} is still formed from CO_2 and electrogenerated OH^-. Several studies have explored the dependence of product distribution on local pH at the electrode/electrolyte interface, as well as the concentration and buffer capability of the electrolyte. In that line, a fine tuning of the product selectivity for CORR on Cu electrodes was achieved via the modulation of local pH upon variation of the electrolyte buffer capacity, CO_2 pressure, and current density.[96] Varela *et al.* proposed that electrolytes with a high buffer capacity could facilitate the transfer of coupled electrons/protons, thus being beneficial for the evolution of hydrogen.[97] In comparison, they found electrolytes with a low buffer capacity could suppress the formation of H_2 owing to the low concentration of protons near the electrode surface, favouring selectivity towards the formation of C_2H_4 (**Fig. 8c**). Conversely, applying a higher current density can also lead to a higher local pH. This is due to a high consumption rate of local protons compared to the rate of mass transport of protons from the bulk electrolyte. Huang *et al.* modelled an electrode surface and found that even in highly acidic electrolytes (pH 1), local neutrality and alkalinity could be created above 200 mA/cm^2.[98] They required at least 400 mA/cm^2 to produce multicarbon products. This improved carbon efficiency considerably, although energy efficiency remains problematic. Although a higher CO_2 pressure could result in a lower local pH at a constant electrolyte concentration, it favoured ethylene formation by increasing the local *CO concentration and the corresponding *CO surface coverage.[99] Recently, Chen *et al.* reported that adjusting the thickness of a highly porous Au film allows controlling the mass transfer resistance and increasing the local pH at the electrolyte/electrode interface of CO_2 reduction, which results in the promotion of the CO_2RR while inhibiting the HER.[100]

For the nitrogen reduction reaction, Xu *et al.* summarized the dependence of the formation of nitrogen-reduction intermediates on pH for aqueous media.[101] Due to the large overpotentials needed to activate N_2 and the low solubility of N_2 in aqueous electrolytes, when the applied overpotential is sufficient to trigger the electrochemical synthesis of NH_3, the reaction at the active sites quickly becomes controlled by the mass transport of N_2 molecules. Consequently, the presence of protons near the electrode surface leads to the uncontrolled production of hydrogen. As illustrated in **Fig. 8d**, Wang *et al.* gauged the NRR performance of commercial Pd/C in electrolytes with different pH values. Their observations revealed that the effective suppression of the HER activity in the neutral electrolyte was attributed to a higher barrier for mass and charge transfer.[102,103]

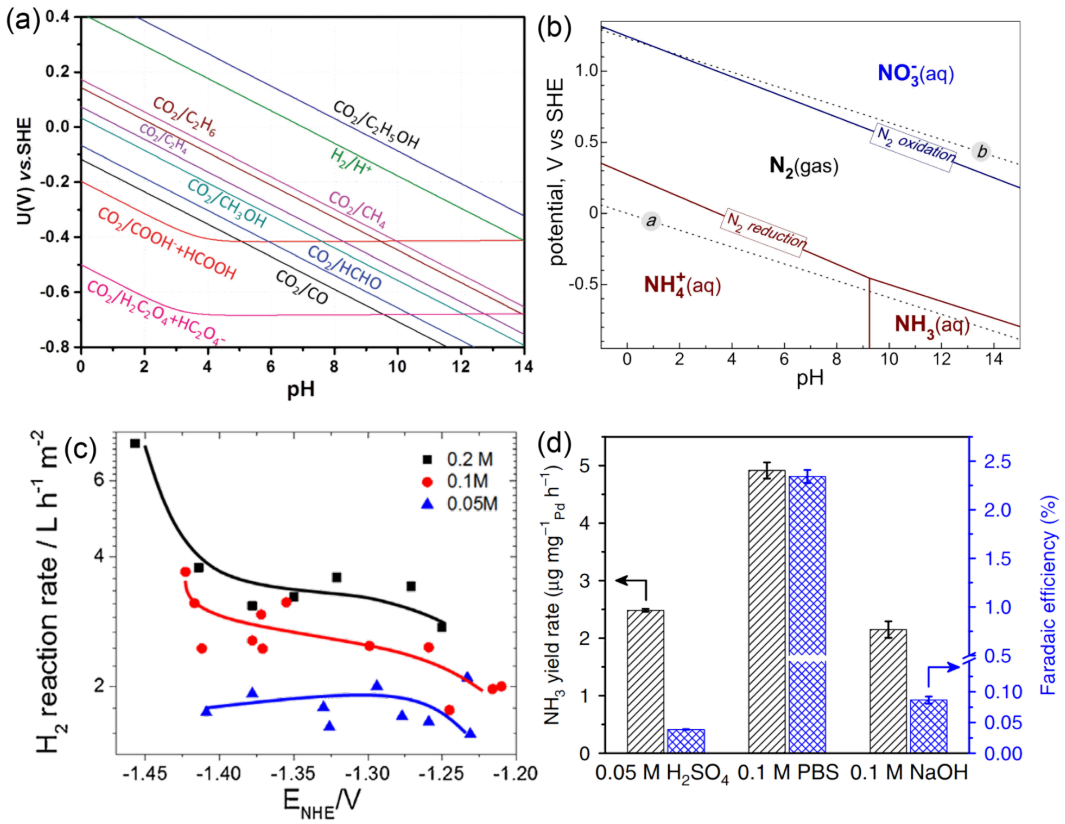

Fig 8. **(a)** Partial Pourbaix diagram for CO_2 reduction in aqueous solution that describes the relationship between the equilibrium potential of the associated reaction and pH, which is plotted based on thermodynamic data. Reproduced from Ref.[88] with permission from the Royal Society of Chemistry. **(b)** Partial Pourbaix diagram for the N_2-H_2O system. Solid lines correspond to N_2 reduction to NH_4^+ or NH_3 (red) and N_2 oxidation to NO_3^- (blue). Dotted lines *a* and *b* straddle the region of water reduction to H_2 and oxidation to O_2, respectively. Reproduced from Ref.[89] with permission from AAAS. **(c)** Formation rates of gas products as a function of applied electrode potentials in CO_2 saturated electrolytes with different buffer capacities. Reproduced from Ref.[97] with permission from Elsevier. (d) NH_3 yield rate and Faradaic efficiency of Pd/C processed in N_2-saturated electrolytes with different pH values. Reproduced from Ref.[102] with permission from AAAS.

2.5.2 Optimizing the components of the electrolyte: alkali metal cation effects

Bicarbonate or carbonate are the most investigated electrolyte salts employed for the CO_2RR as they provide a near-neutral pH but most importantly allow to maintain a stable and high dissolved CO_2 concentration upon operation.[104,105] Hence, while the anions are rarely varied in electrochemical studies, a wide range of studies have investigated the variation of the alkali cations. In CO_2RR, while the influence of alkali cations on product selectivity and catalyst efficiency are commonly accepted,[106] the origin of this effect is still largely debated in the literature. The influence of the used alkali metal cations on the CO_2RR activity and selectivity is generally attributed to the relatively high population of alkali cations in the outer Helmholtz plane (OHP). Early work from Monteiro *et al.* proposed that large cations are specifically adsorbed more easily on the catalyst surface because of the fewer coordinated water molecules.[107] Adsorbed cations can also elevate the potential at the OHP and decrease the local proton concentration, suppressing HER.[108] Alternatively, it was suggested that the cation size can significantly affect the rate of water hydrolysis by tuning the hydration energy.[109] For instance, the pKa value

of Li^+ was calculated to be three times higher than that of Cs^+. The hydrated Cs^+ acts as a buffer, maintaining a locally low pH near the electrode and increasing the local CO_2 concentration compared to Li^+ by 28 times (**Fig. 9a**). To gain more insight into the role of cations in electrocatalysis, Ringe *et al.* developed a combined ab initio/continuum model of cation and electric double layer field effects based on a continuum modified Poisson-Boltzmann approach (**Fig. 9b**).[110] By applying a single set of cation sizes derived from experimental data, the model showed quantitative agreement with the experiments for the catalyst system on both Ag and Cu. The model allows us to show that the surface charge density and the associated electric field are primarily altered by repulsive interactions amongst hydrated cations in the Helmholtz layer. The use of high-valent cations with a small hydration radius also increases the potential of zero charges or capacitance, which maximizes the surface charge density and the corresponding interfacial electric fields.[111] Bell's group provided insights regarding the beneficial effect of cations, particularly at relatively low overpotentials, for which the reaction rate does not perturb the local pH.[112] Notably, the hydrogen and CH_4 partial currents remained steady, while formate, C_2H_4, and C_2H_5OH formation rates increased when using large alkali cations. The cation size-independent production of H_2 and CH_4 was attributed to the zero dipole moment of $^*H$ and $^*CHO$, which are the corresponding reaction intermediates of the reactions (**Fig. 9c**).[113]

Alkali metal cations have also been used in recent work to promote the CO_2RR in strongly acidic medium. A key advantage to operating at a low pH is the improved carbon utilisation efficiency, which is limited in neutral and alkaline media due to the formation of carbonate. Sargent and co-workers utilised a cation-augmenting layer to sustain a high K^+ concentration at the copper catalyst surface.[98] They achieved 61 % faradaic efficiency for CO_2R products and 40 % for C_{2+} products at 1.2 A/cm^2, and by lowering the CO_2 flow they reached a single pass conversion efficiency of 77%. Gu et al. explored the effect of alkali cations on the CO_2RR in acid with tin oxide, gold and copper catalysts, achieving 90% faradaic efficiencies for formic acid and CO.[114] Using a simulation based on the Poisson-Nernst-Planck (PNP) model, they predicted that the origin of such striking effects was the modulation of electric fields, which inhibited the migration of hydrononium ions.

In the context of NRR, Hao *et al.* identified that the combination of bismuth and potassium cations contributes to the NRR process by simultaneously enhancing the selectivity and activity.[115] Potassium cations lower the free-energy change (ΔG) required by the potential-determining step (PDS) and regulate the proton diffusion process to make the reaction more selective for the reduction of nitrogen **(Fig. 9d**). As a result, the Bi-K^+ pair can promote the NRR to achieve a record-high Faradaic efficiency and ammonia yield at 66% and 200 mM NH_3 $g^{-1}h^{-1}$ in aqueous solutions and under ambient conditions.

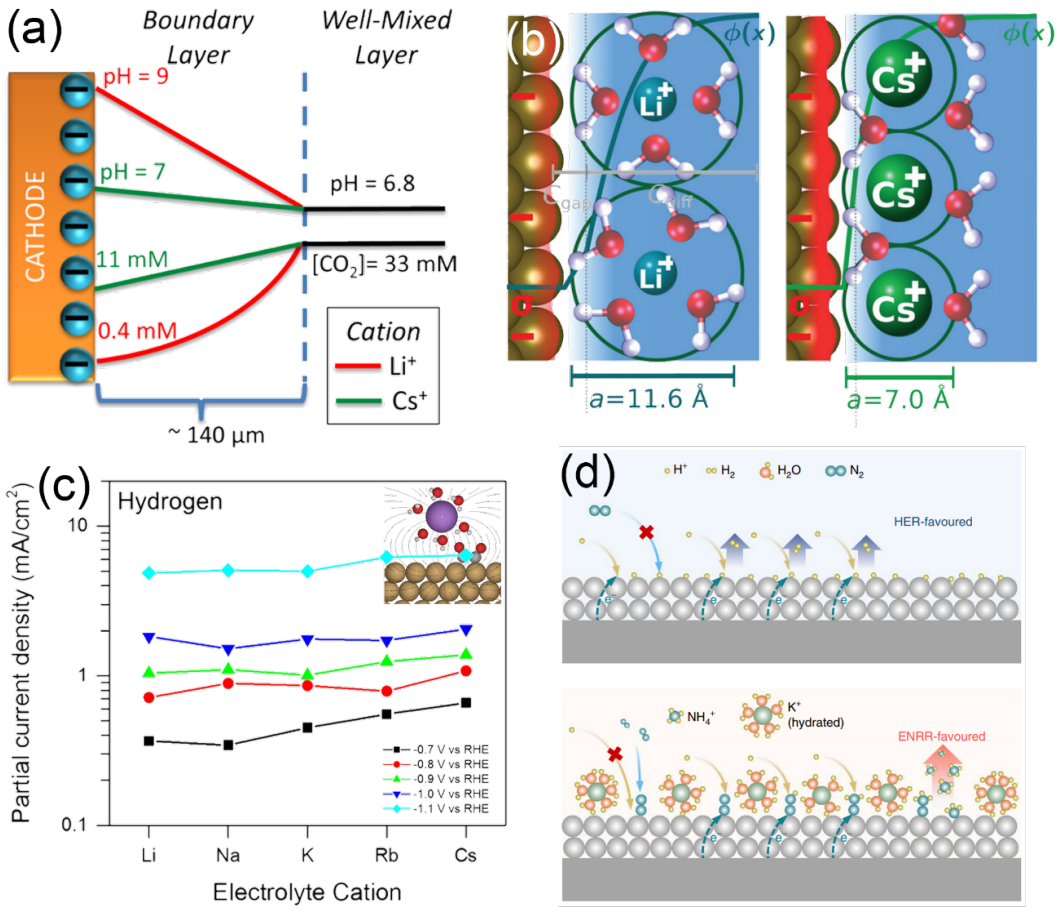

Fig 9. **(a)** Effect of cation hydrolysis on the electrochemical reduction of CO_2 over Ag. Distribution of pH and CO_2 concentration in the boundary layer. Hydrated Cs^+ buffers the cathode to maintain the pH close to 7 and to increase the CO_2 concentration. Reproduced from Ref.[109] with permission from the American Chemical Society. **(b)** Illustration of the origin of cation effects in field-driven electrocatalysis. Repulsive interactions between hydrated cations at the outer Helmholtz plane reduce the local concentration of cations, the surface charge density (depicted by the red-coloured region) and the electric double layer field. The diffuse layer that is explicitly modelled by the size-modified Poisson-Boltzmann (MPB) model is depicted, as well as the Helmholtz gap capacitance region and the interfacial ion diameter. Reproduced from Ref.[110] with permission from the Royal Society of Chemistry. **(c)** Average current densities obtained during bulk electrolysis as a function of metal cations at different potentials. Reproduced from Ref.[113] with permission from the American Chemical Society. **(d)** Without the presence of K^+ cations, protons can be readily transferred to the surface, and the HER will dominate. Once K^+ hinders proton transfer to the catalyst surfaces, nitrogen will be adsorbed preferentially, and the NRR is promoted. Reproduced from Ref.[115] with permission from Nature Publishing Group.

2.5.3 The search for novel electrolytes: ionic liquids and non-aqueous electrolytes

Ionic liquids (ILs), which are defined as salts that remain liquid below 100 °C, have been proven to be a promising new class of environmentally benign solvents.[116] By tuning the molecular structure and polarity of the IL, the CO_2 and N_2 absorption capacity and the ability to stabilize charged CO_2 and N_2 species can be tuned and optimized. ILs also possess several advantages, such as wide electrochemical windows, thermal and chemical stability, negligible volatility and electron transfer mediation for redox catalysis, which make them an interesting

alternative to promote the CO_2RR and NRR.[117] As they are nonaqueous by nature, ILs allow control of the aqueous content to an optimum level to provide protons for hydrocarbon formation while suppressing the HER.[118-122]

ILs have been extensively investigated for the CO_2RR because the cations of ILs can form a complex with CO_2 and accelerate its transportation. Rosen *et al.* reported the use of 1-ethyl-3-methylimidazolium tetrafluoroborate (EMIM-BF_4) as an IL electrolyte for the electrochemical conversion of CO_2 to CO on silver (**Fig. 10a**).[123] The IL system lowers the energy of the $^*CO_2$ intermediate via the formation of a complex intermediate, which lowers the energy associated with the initial step of the reduction reaction.[124] The formation of CO occured at very low onset overpotential, and the IL system demonstrated sustained production of CO for 7 hours with a FE_{CO} of more than 96%. ILs have also been applied with transition metal dichalcogenides, which are known to be more prone to promote the HER over other reduction reactions. Remarkably, Asadi *et al.* exfoliated WSe_2 nanoflakes to perform the electroreduction of CO_2 to CO using a 50 vol.% [Emim]BF_4/H_2O solution.[125] The current density, FE, and TOF in producing CO were all superior at lower overpotentials, suggesting a high selectivity for the CO_2RR (**Fig. 10b**). Copper selenide nanocatalysts have been identified to convert CO_2 to CH_3OH at low overpotentials in a [Bmim]PF_6/acetonitrile-H_2O mixed electrolyte.[126] In addition, in a [Bmim]BF_4-H_2O electrolyte, $MoTe_2$ could also be used as a catalyst for CO_2 reduction to CH_4 with a high FE of 83% at a relatively low overpotential.[127] Atifi *et al.* demonstrated that protic ionic liquids (PILs) derived from 1,8-diazabicyclo[5.4.0]undec-7-ene (DBU) effectively promote the electrochemical reduction of CO_2 to formate ($HCOO^-$) with high selectivity (**Fig. 10c**).[128] The use of PILs composed of the conjugate acid of DBU, $[DBU-H]^+$, efficiently catalysed the reduction of CO_2 to $HCOO^-$ ($FE_{HCOOH} \approx 80\%$) with significant suppression of CO and H_2 production ($FE_{CO} + FE_{H2} \approx 20\%$) in either acetonitrile or an acetonitrile/H_2O mixed electrolyte.

Ionic liquids and nonaqueous electrolytes with high N_2 solubility under ambient conditions can also increase the local concentration of N_2 near the catalyst surface by as much as 20 times compared to water on a volumetric basis.[129] MacFarlane and co-workers reported the use of ionic liquids with high N_2 solubility for the electroreduction of N_2 to ammonia at room temperature and atmospheric pressure.[130] As presented in **Fig. 10d**, FE_{NH_3} as high as 60% was achieved in [P6,6,6,14][eFAP]. Ortuño *et al.* used DFT calculations to explore the nature of N_2 adsorption on different ions, and found that a stronger interaction accompanied by charge-delocalization will result in stronger adsorption of N_2.[131] As shown in **Fig. 10e**, they found that on a Ru surface the presence of ILs reduces the relative electronic energy of the N_2RR intermediate N_2H^* more significantly than that of the HER intermediate, H_2^*, lowering the energy by 0.34 eV and 0.11 eV, respectively. Suryanto *et al.* identified the importance of the IL molar fraction (X_{IL}) on the physicochemical properties of the electrolyte mixture and the NRR performance.[132] An FE as high as 23.8 ± 0.8% with an NH_3 yield rate of $1.58 \pm 0.05 \times 10^{-11}$ mol s^{-1} cm^{-2} was achieved for $X_{IL} = 0.23$ at an optimal potential of -0.65 V *vs.* NHE (**Fig. 10f**). The significant drop in the NRR performance when further increasing X_{IL} highlights the role of 1H,1H,5H-octafluoropentyl 1,1,2,2-tetrafluoroethylene ether (FPEE) in facilitating the mass transport of N_2 in the electrolyte. The authors

also claimed that other factors correlating FE and X_{IL} could play a role, such as the presence of complex molecular interactions and the different diffusion behaviours of neutral N_2 molecules and polar H_2O within the mixed electrolyte system.[133]

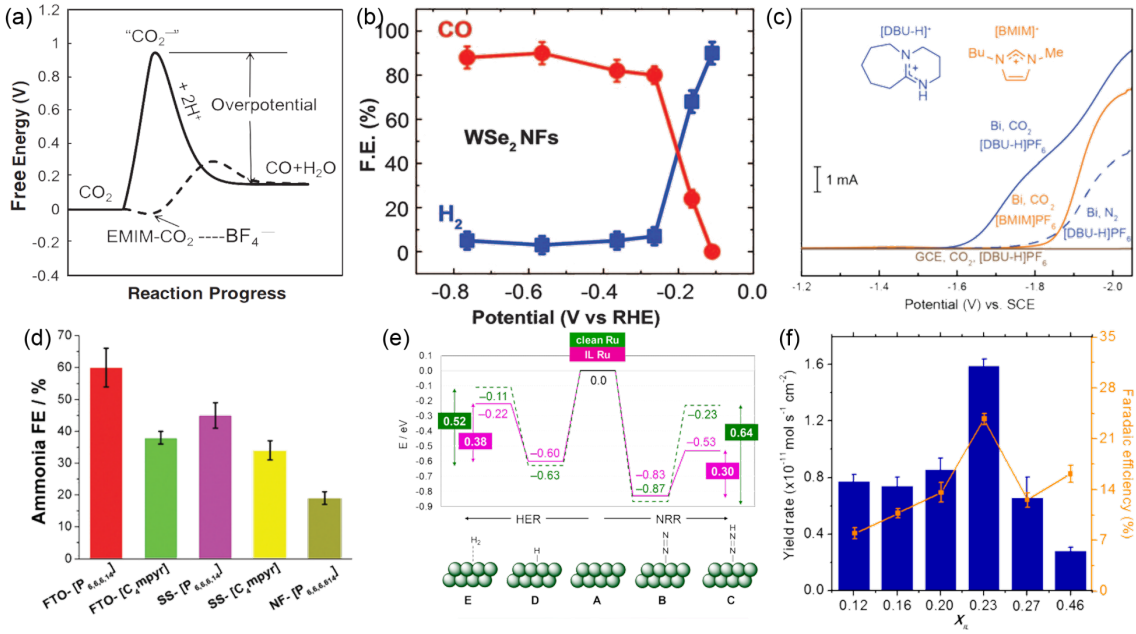

Fig 10. **(a)** Schematic of how the free energy of the system changes during the $CO_2 + 2H^+ + 2e^- \rightleftharpoons CO + H_2O$ reaction in water, acetonitrile (solid line) or EMIM-BF_4 (dashed line). Reproduced from Ref.[123] with permission from AAAS. **(b)** Overall FE_{CO} and FE_{H_2} at different applied potentials for WSe_2 NFs. The error bars represent the standard deviation of four measurements. Reproduced from Ref.[125] with permission from AAAS. **(c)** Linear sweep voltammograms were recorded for Bi-based and bare GCEs in MeCN containing 250 mM IL and 0.1 M $TBAPF_6$ under the saturation of Ar, N_2, or CO_2. Reproduced from Ref.[128] with permission from the American Chemical Society. **(d)** Faradaic efficiency for electroreduction of N_2-saturated ILs on various electrodes at a constant potential of 0.8 V *vs.* NHE. Reproduced from Ref.[130] with permission from the Royal Society of Chemistry. **(e)** Corresponding reaction energy profiles of such intermediates during the NRR (right) and HER (left) for clean (dashed green line) and IL-decorated (solid purple line) Ru surfaces. Reproduced from Ref.[131] with permission from the American Chemical Society. **(f)** Solvent-IL ratio (X_{IL}) dependence of the NH_3 yield and FE at -0.65 V *vs.* NHE. Reproduced from Ref.[132] with permission from the American Chemical Society.

2.5.4 Solid-state electrolyte designs

Conventional liquid electrolytes used in the CO_2RR and NRR, such as $KHCO_3$, Na_2SO_4, or KOH, mainly have three main purposes: *i*) to transport ions between the cathode and anode for efficient current flow, *ii*) to provide protons for successive PCET and *iii*) to solvate liquid products. The mixture of liquid products and ion impurities requires energy- and cost-intensive downstream separation steps to obtain pure products, which complicates the infrastructure for delocalized production.[134] To tackle this problem, the concept of solid-state electrolytes was proposed, inspired by progress in solid-state electrolytes for batteries.[135] A solid-state electrolyte is typically placed between ion-exchange membranes with close contact to efficiently transport the generated ions and minimize the ohmic loss of the device.[136] Remarkably, solid-state electrolytes have been proven to be very

successful for suppressing HER by limiting the flow of protons to the catalyst active sites during the electrochemical CO_2RR.[137,138] The Wang group have reported the continuous electrocatalyic conversion of CO_2 to pure liquid fuels using two electrode systems with solid electrolytes.[139,140] They applied a porous solid electrolyte (PSE) layer composed of styrenedivinylbenzene copolymer microspheres with sulfonic acid functional groups for proton conduction. Using a formic-acid-selective bismuth catalyst (FE_{HCOOH} ~97%), the electrochemically generated protons and formate anions could combine at the PSL to produce formic acid (**Fig. 11a**). By directly flowing a carrier gas instead of deionized water through the PSL, they were able to collect product vapours that could be condensed to form the pure product (almost 100 wt.% formic acid), alongside impressive current density and stability (**Fig. 11b**).

Diez-Ramírez *et al.* studied the electrochemical synthesis of ammonia promoted by potassium ions (K^+) on a Co_3Mo_3N-Ag electrocatalyst in a K-β''-Al_2O_3 solid electrolyte cell (**Fig. 11c**).[141] The catalyst exhibited volcano-type behaviour with applied voltage. At high overpotentials, more K^+ is pumped to the catalyst, and the rate of ammonia formation decreases due to the high surface concentration of potassium ions. The apparent poisoning effect was attributed to the blocking of active sites by K^+ and the formation of K-N-H poisoning compounds.Lan *et al.* employed an $H^+/Li^+/NH_4^+$ mixed conducting Nafion membrane as the electrolyte for the NRR.[142] The mixed conducting Nafion membrane increased the chemical compatibility of the acidic Nafion membrane with NH_3. Li^+ ions reduced NH_3 formation due to the blocking effect of Li^+ on the transferred protons, rendering a relatively lower current at a higher applied voltage. Sheets *et al.* proposed a novel polymer gel approach to convert N_2 to NH_3 at mild temperatures (30-60 °C) and pressures (20 psig).[143] As illustrated in **Fig. 11d**, the polymer gel electrolyte helped to control the rate of the HER by limiting water transport and boosting N_2 transport, thus improving the selectivity towards the NRR.

As an alternative to organic electrolytes, metal oxides have also been investigated as solid-state electrolytes for the NRR.[144] The working principle of solid oxide systems for the reduction of N_2 is that the anode and cathode are deposited on both sides of the metal oxides, which act as proton conductors, while H_2 is flowed over the anode for conversion into H^+. Protons are transported to the cathode, where the half-cell reaction between N_2 and H^+ takes place (**Fig. 11e**).[145] Skodra *et al.* used steam to supply protons to the cathode and $SrCe_{0.95}Yb_{0.05}O_3$ as the proton-conducting solid-state electrolyte, with Ru and Pd catalysts as the cathode and anode, respectively. Water vapour is first reduced to O_2 and H^+ by electrolysis, and protons are transported to the cathode through the proton conducting disk to react with N_2 and form NH_3. During the whole reaction process, only N_2 needed to be purified, and NH_3 was successfully formed in the temperature range of 450–700 °C.

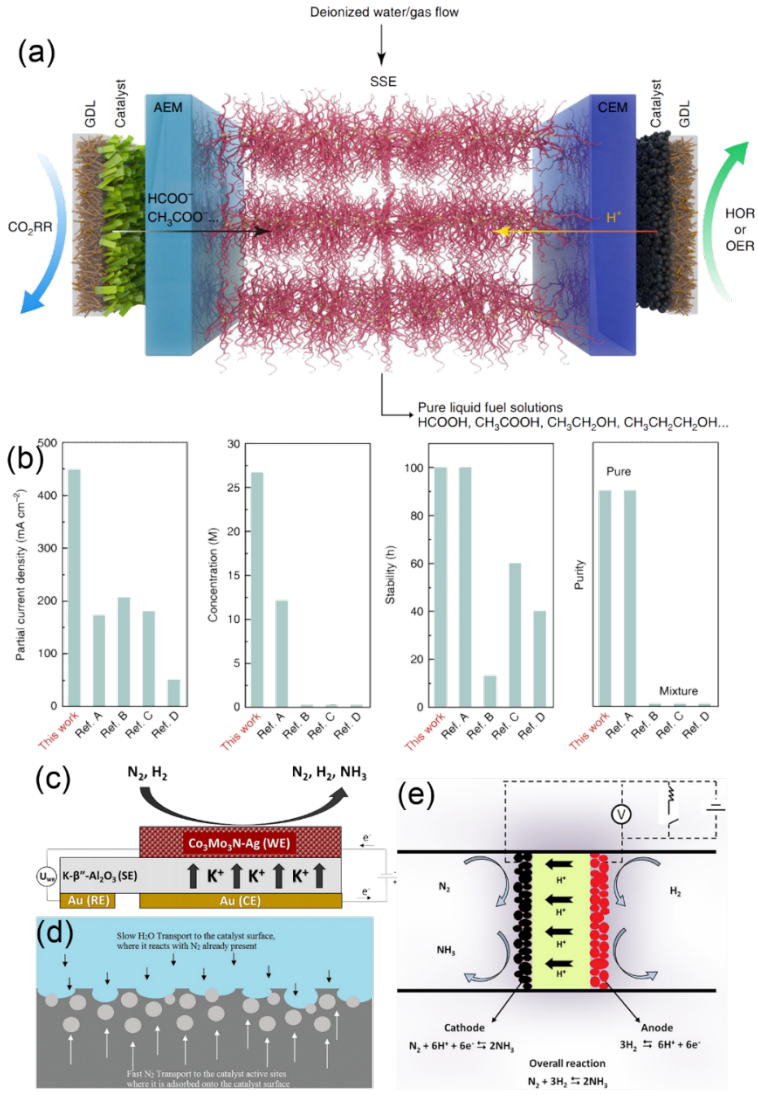

Fig 11. **(a)** Schematic illustration of the CO_2 reduction cell with a solid electrolyte. Reproduced from Ref.[139] with permission from Nature Publishing Group. **(b)** Electrochemical performance of our all-solid-state CO_2RR reactor compared with previous literature. Reproduced from Ref.[140] with permission from Nature Publishing Group. **(c)** Schematic diagram of the single-chamber K^+ conducting cell reactor used for the electrochemical promotion of ammonia synthesis. Reproduced from Ref.[141] with permission from the American Chemical Society. **(d)** Diagram of the transport of species at the cathode showing the benefit of limiting water transport *via* the polymer gel electrolyte. Reproduced from Ref.[143] with permission from the Royal Society of Chemistry. **(e)** Schematic of solid oxide cells for electrocatalytic N_2 reduction employing proton-conducting electrolytes. Reproduced from Ref.[145] with permission from Frontiers.

2.6 Three-phase interface engineering

The abundance of protons near the catalyst active sites makes the competing HER in aqueous electrolytes *via* direct water reduction dominant, resulting in low selectivity and activity of the CO_2RR and NRR.[146] A mitigation strategy resides in facilitating the accessibility of the catalyst to high concentrations of CO_2 or N_2 molecules. While protons (H^+) are readily available in aqueous solutions *via* water ionization, the supply of CO_2 and N_2 molecules to the catalyst surface is limited by their low concentration and slow diffusibility. In saturated aqueous

electrolytes, the solubility of CO_2 in H_2O is 3.3 $\times 10^{-2}$ mol L^{-1} at 298 K and 1 atm pressure, whereas the value for N_2 in H_2O remains as low as 6.8×10^{-4} mol L^{-1}.[147] For comparison, the concentration of protons in neutral electrolyte is typically 2.7-fold and 132-fold higher than the concentrations of CO_2 and N_2, respectively. Raciti et al. confirmed that the concentration of CO_2 molecules on the catalyst surface can even be completely depleted to zero under a strong reaction driving force.[148] Such a limitation constitutes a significant hurdle.

One approach to tackle this challenge consists of the realization of an efficient three-phase interface between gaseous CO_2, the liquid electrolyte and the solid catalyst. Under this condition, highly concentrated gas-phase CO_2 molecules can be delivered through a porous gas diffusion layer (GDL) to the catalyst surface directly. With higher CO_2 and lower H^+ surface concentrations, the HER can be significantly suppressed, and the CO_2RR performance can be improved. The properties of the GDL that supports the catalyst layer can affect CO_2 and water transport heavily, as recently reviewed by Berlinguette and co-workers.[149] Thinner GDE/catalyst layers shorten the CO_2 diffusion distance, raising the relative CO_2 concentration; however, excessively high concentrations can decrease multicarbon product formation by competing with intermediates such as CO for binding sites.[150] The wettability of the electrode can be modulated with pore size and hydrophobicity so that the pores do not become flooded with electrolyte, impeding CO_2 diffusion.[151]

Fine-tuning the local microenvironment near the catalyst surface has shown great enhancements in activity and product selectivity in the CO_2RR. Wakerley *et al.* demonstrated a bioinspired strategy with a hydrophobic coating of long-chain alkanethiols on dendritic Cu, which leads to a drastic increase in CO_2 reduction selectivity (**Fig. 12a**).[24] A "plastron effect" was proposed based on the hydrophobicity of animal fur or skin. As a gaseous layer forms at the surface of the electrode, it increases the local CO_2 concentration and enables high selectivity for C_2 products on Cu. This study led to the identification of the role of hydrophobicity and the formation of gaseous voids as effective levers to orient the reaction pathway towards the formation of multicarbon products, opening directions for future electrode designs. More recently, Xing *et al.* showed that a hydrophobic microenvironment can significantly enhance CO_2 electrolysis by facilitating reactant diffusion (**Fig. 12b**).[152] Using commercial copper nanoparticles dispersed with hydrophobic polytetrafluoroethylene (PTFE) nanoparticles, they reported improved activity and Faradaic efficiency for CO_2 reduction with a partial current density >250 mA cm^{-2} and a single-pass conversion of 14% at moderate potentials. Importantly, this performance was approximately twice as large as that of regular electrodes without added PTFE. Similar findings were also observed from a Bi-based catalyst modified with PTFE nanoparticles in the catalyst layer to demonstrate a partial current density of 677 mA cm^{-2} for formate and 35% single-pass CO_2 conversion at -0.7 V *vs.* RHE (**Fig. 12c**). Pham et al. compared various ionomeric binders on a Cu catalyst, and achieved a 77 % faradaic efficiency and 600 mA cm^{-2} partial current density for C_{2+} products at -0.76 V vs RHE using a fluorinated ethylene propylene (FEP) binder.[153] They attributed these results to the hydrophobic properties of FEP. The Sinton and Sargent groups have also done notable work on modulating the three-phase interface in continuous flow and membrane electrode assembly (MEA) electrolyzers, enabling high current densities (e.g. > 1 A cm^{-2}) to be achieved.[94,138] For example, they

presented a catalyst:ionomer bulk heterojunction (CIBH) architecture, which had both hydrophilic and hydrophobic functionalities. By having different domains that favoured gas and ion transport routes, they were able to decouple gas, ion and electron transport, extending the reaction interface from the submicrometer to the several micrometer range.[51] These examples illustrate that moderate hydrophobicity of the catalyst layer can establish a microenvironment with a balance between gaseous CO_2 and liquid electrolytes inside the catalyst layer. Such microenvironments – equivalent to microreactors – reduce the thickness of the diffusion layer, accelerate CO_2 mass transport and link highly active reaction zones at the interfaces between the three phases involved in the reaction.[154] The triple-phase interface can also be tuned by applying ionomers to control pH and CO_2/H_2O concentrations. Bell and co-workers postulated that anion-exchange ionomers (e.g. sustanion) increase CO_2 solubility, cation-exchange ionomers (e.g. nafion) increase local pH by trapping OH^- ions, and both types increase water concentration.[155] By optimizing a bilayer ionomer coating and coupling to pulsed electrolysis, they achieved 90 % faradaic efficiency for C_{2+} products and just 4 % for H_2.

When applying large potentials at the electrodes, the kinetically facile HER becomes preferable to the reduction of N_2 due to the relatively low energy barrier associated with the reaction. It was suggested that the HER should always dominate at normal proton concentrations near the metal electrode surface. However, when few protons or electrons are provided, the NRR may preferentially occur, as recently observed experimentally. Designing a triple-phase interface for NRR can increase the local N_2 concentration and improve $*N_2$ adsorption, whilst limiting the availability of protons by reducing contact with the electrolyte.[156,157] Using this strategy, Zhang *et al.* realized triple-phase electrolysis *via in situ* fabrication of Au nanoparticles located on hydrophobic carbon fiber paper (Au/CFP) (**Fig. 12d**).[158] The hydrophobic carbon fibres facilitated the formation of three-phase contact points (TPCPs) for N_2, the liquid electrolyte and the Au NPs. Chen *et al.* improved the three-phase reactions by using hydrophobic layers on both sides of the catalyst and reported an improved ammonia formation rate of 1.06×10^{-11} mol $cm^{-2}s^{-1}$ using a 30% Fe_2O_3-CNT electrocatalyst (**Fig. 12e**).[159] The ammonia formation rate and NH_3 Faradaic selectivity were improved by 158% and 571%, respectively, compared to the traditional configuration based on the two-phase interface. According to the authors, excessive suppression of the HER is not, however, beneficial to NRR activity, although it can lead to higher Faradic efficiency (**Fig. 12f**). A sharp decrease in the local concentration of protons does not benefit the NRR process, as protons are necessary for the successive PCET steps associated with the formation of ammonia. These investigations point out that although the release of hydrogen is a competitive reaction, protons are paradoxically essential to increase the ammonia yield.[160]

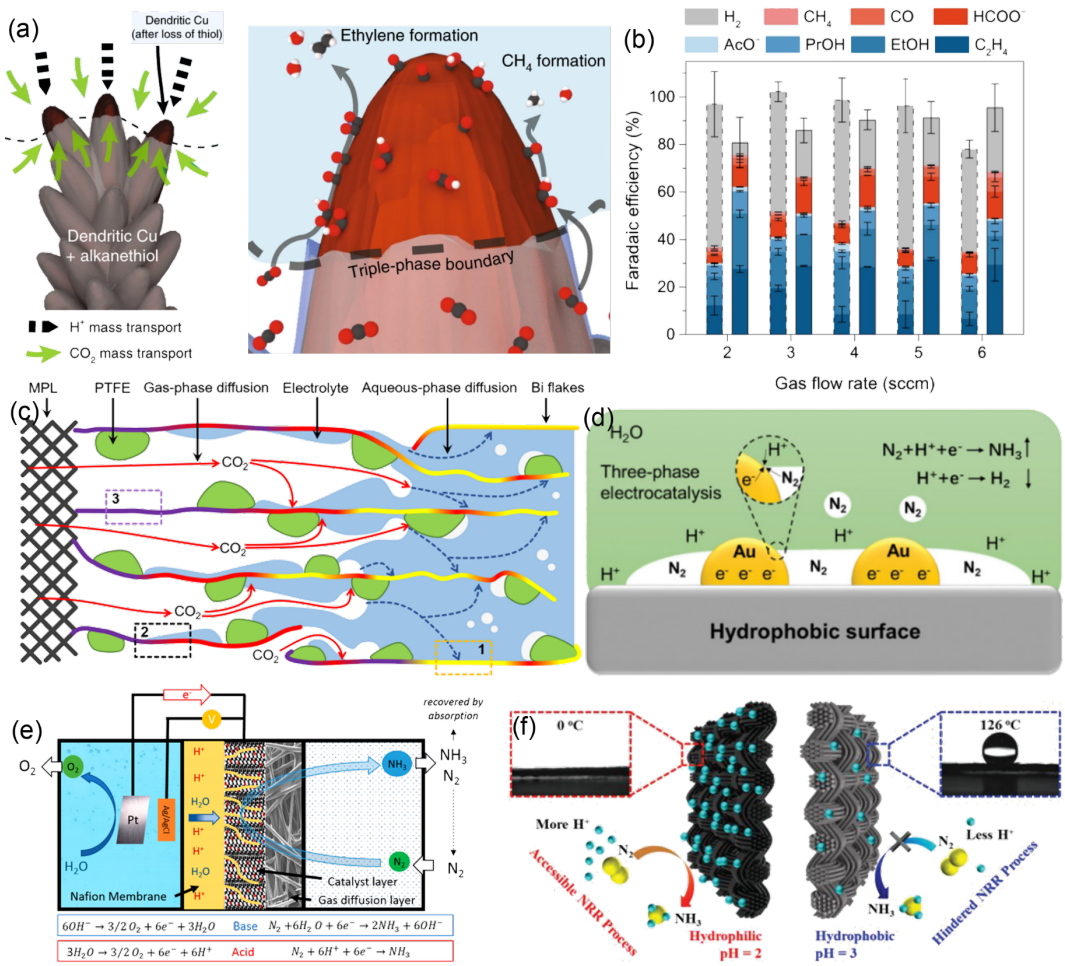

Fig 12. **(a)** Operation of the hydrophobic dendrite, illustrating the enhanced CO_2 mass transport from the triple-phase boundary between the electrolyte, the electrode and gaseous CO_2 and the resultant formation of key products on the surface. Reproduced from Ref.[24] with permission from Nature Publishing Group. **(b)** Faradaic efficiencies for the CO_2RR on the two electrodes (dash: AvCarb MGL370 + Cu/C; solid: AvCarb GDS2230 + Cu/C) at -1.0 V *vs.* RHE with various CO_2 flow rates. Reproduced from Ref.[152] with permission from Nature Publishing Group. **(c)** Schematic illustration of CO_2 mass transport inside the catalyst layer with added PTFE, including gas-phase diffusion (solid red arrows) and aqueous-phase diffusion (dashed blue arrows). The dashed rectangles indicate catalyst areas that are only exposed to the electrolyte, exposed to both electrolyte and gaseous CO_2, and only exposed to gaseous CO_2. Reproduced from Ref.[161] with permission from the American Chemical Society. **(d)** Schematic illumination of three-phase contact for N_2 (gas), the electrolyte (liquid), and the catalyst (solid) at the hydrophobic interface. Reproduced from Ref.[158] with permission from Wiley. **(e)** Schematic view of the three-phase reactor for electrochemical ammonia synthesis. Reproduced from Ref.[159] with permission from the American Chemical Society. **(f)** NRR catalytic mechanism of Mo_2C/C under proton-suppressed and proton-enriched conditions. Reproduced from Ref.[160] with permission from Wiley.

2.7 Conclusions and Perspectives

The industrial development of the CO_2RR and NRR is currently plagued by low Faradaic and energy efficiencies. The successive PCET steps associated with the corresponding reaction intermediates increase the complexity and complicate the search for an ideal catalyst. The simplicity of the HER mechanism and the abundant presence of

protons in traditional electrolytes make the production of hydrogen a competitive and parasitic reaction that consumes a significant amount of electrons to the detriment of the fixation of CO_2 and N_2. A central approach to alleviating this bottleneck is to minimize the side reaction of hydrogen evolution. Two main strategies have shown promise but still require further investigation; they involve *a)* favouring the thermodynamics of the desired reaction and *b)* adjusting kinetics that favour the desired pathways to the detriment of the HER.

Controlling the reaction thermodynamics.

Improved comprehension of the reaction mechanism has recently enabled fast progress in the design of materials and the corresponding active sites with improved selectivity. This approach has also been used to reduce the energy barrier of the targeted reaction to a lower value compared to that of the HER. For instance, theoretical studies have suggested that step sites may very well dominate CO_2RR and NRR activity, although experimental validation of this remains a challenge. However, the catalyst surface has been shown to reconstruct under reaction conditions. This calls for precise *in situ* observations of the formation of undercoordinated defects or step sites during the reaction to understand the mechanism for HER inhibition during the reaction under dynamic conditions. The development of operando characterization techniques to probe the active sites together with improved numerical predictions – in particular under realistic environmental conditions – will allow further improvements in the selectivity of the catalyst. The fields will also benefit from the development of isotopic experiments using ^{13}C, ^{15}N and ^{2}H. In particular, the use of D^+ could advantageously be used to determine the role of protons during electrochemical processes.

Controlling the reaction kinetics.

Based on the mechanism of the CO_2RR and NRR, limiting the accessibility of protons from the electrolyte and electrons over the surface of the catalyst has been found to effectively inhibit the kinetically preferred HER, eventually leading to enhanced CO_2RR and NRR selectivity. Surprisingly, excessively restricting the accessibility of protons and electrons may hinder the whole conversion efficiency of the CO_2RR and NRR to some degree. The balance between selectivity and conversion efficiency therefore necessitates further clarification in future studies. This will be achieved by controlling the local pH at the catalyst surface by tuning the surface chemistry and triple phase interface, modulating the nanostructure, or *via* the use of nonaqueous electrolytes.

Future challenges and opportunities.

From the viewpoint of the catalyst and the reaction products, cathodic degradation and the inactivation of reaction sites are responsible for the rapid loss in activity. As reactions proceed, undesirable intermediates or poisonous byproducts preferably deposit on the catalyst surface and affect the catalysis process. This phenomenon may decrease the effective area of the electrocatalyst, accelerate cathodic degradation and orient the reaction towards the formation of hydrogen. The demonstration of catalysts with ultralong stability of > 5000 hours remains a milestone to validate the industrial potential of the CO_2RR and NRR. Combining experiments and theoretical research holds potential for guiding the design of both catalysts and electrolyzers for CO_2RR and NRR. From

this perspective, machine learning will help rapid screening of catalysts with high selectivity based on massive data in the silico database by focusing on near-optimal bond energy with adsorbates, such as *CO and *N_2H.

Overall, this review has presented and discussed the most important developments for suppressing the HER and improving product selectivity during the fixation of CO_2 and N_2. Future developments in the field will emphasize combining efforts to enhance catalyst selectivity while controlling the mass transport of reactants and protons. From this perspective, rapid progress in the design of electrolyzers using new solid electrolytes and in the control of interfaces at the active sites should make it possible to achieve industry-relevant performances, as recently reported in several contributions.[140,162]

2.8 References

1 Li, X. *et al.* Exclusive Ni-N_4 sites realize near-unity CO selectivity for electrochemical CO_2 reduction. *J. Am. Chem. Soc.* **139**, 14889-14892 (2017).

2 Battin, T. J. *et al.* The boundless carbon cycle. *Nat. Geosci.* **2**, 598-600 (2009).

3 Wan, Y., Xu, J. & Lv, R. Heterogeneous electrocatalysts design for nitrogen reduction reaction under ambient conditions. *Mater. Today* **27**, 69-90 (2019).

4 Foster, S. L. *et al.* Catalysts for nitrogen reduction to ammonia. *Nat. Catal.* **1**, 490-500 (2018).

5 Zhang, X., Ward, B. B. & Sigman, D. M. Global nitrogen cycle: critical enzymes, organisms, and processes for nitrogen budgets and dynamics. *Chem. Rev.* **120**, 5308-5351 (2020).

6 Aresta, M., Dibenedetto, A. & Angelini, A. Catalysis for the valorization of exhaust carbon: from CO_2 to chemicals, materials, and fuels. Technological use of CO_2. *Chem. Rev.* **114**, 1709-1742 (2014).

7 Guo, X. *et al.* Tackling the activity and selectivity challenges of electrocatalysts toward the nitrogen reduction reaction via atomically dispersed biatom catalysts. *J. Am. Chem. Soc.* **142**, 5709-5721 (2020).

8 Seh, Z. W. *et al.* Combining theory and experiment in electrocatalysis: Insights into materials design. *Science* **355** (2017).

9 Liu, K. H. *et al.* Advanced catalysts for sustainable hydrogen generation and storage via hydrogen evolution and carbon dioxide/nitrogen reduction reactions. *Prog. Mater. Sci.* **92**, 64-111 (2018).

10 Yang, W., Dastafkan, K., Jia, C. & Zhao, C. Design of electrocatalysts and electrochemical cells for carbon dioxide reduction reactions. *Adv. Mater. Technol.* **3**, 1700377 (2018).

11 Tackett, B. M., Sheng, W. & Chen, J. G. Opportunities and challenges in utilizing metal-modified transition metal carbides as low-cost electrocatalysts. *Joule* **1**, 253-263 (2017).

12 Du, Y. *et al.* Regulating surface state of WO_3 nanosheets by gamma irradiation for suppressing hydrogen evolution reaction in electrochemical N_2 fixation. *Nano Research*, 1-7 (2020).

13 Zhang, S., Fan, Q., Xia, R. & Meyer, T. J. CO_2 reduction: From homogeneous to heterogeneous electrocatalysis. *Acc. Chem. Res.* **53**, 255-264 (2020).

14 Guo, W., Zhang, K., Liang, Z., Zou, R. & Xu, Q. Electrochemical nitrogen fixation and utilization: theories,

advanced catalyst materials and system design. *Chem. Soc. Rev.* **48**, 5658-5716 (2019).

15 Ren, Y. *et al.* Strategies to suppress hydrogen evolution for highly selective electrocatalytic nitrogen reduction: challenges and perspectives. *Energy & Environmental Science* **14**, 1176-1193, doi:10.1039/D0EE03596C (2021).

16 Deng, B., Huang, M., Zhao, X., Mou, S. & Dong, F. Interfacial Electrolyte Effects on Electrocatalytic CO2 Reduction. *ACS Catalysis* **12**, 331-362, doi:10.1021/acscatal.1c03501 (2022).

17 Ozden, A. *et al.* Carbon-efficient carbon dioxide electrolysers. *Nature Sustainability*, doi:10.1038/s41893-022-00879-8 (2022).

18 Wen, G. *et al.* Engineering Electrochemical Surface for Efficient Carbon Dioxide Upgrade. *Advanced Energy Materials* **12**, 2103289, doi:https://doi.org/10.1002/aenm.202103289 (2022).

19 Deng, J., Iñiguez, J. A. & Liu, C. Electrocatalytic nitrogen reduction at low temperature. *Joule* **2**, 846-856 (2018).

20 Chen, K. *et al.* Water-dispersible $CsPbBr_3$ perovskite nanocrystals with ultra-stability and its application in electrochemical CO_2 reduction. *Nano-Micro Lett.* **13**, 1-13 (2021).

21 Qi, K. *et al.* Enhancing the CO_2-to-CO conversion from 2D silver nanoprisms *via* superstructure assembly. *ACS Nano* **15**, 7682-7693 (2021).

22 Qiao, J., Liu, Y., Hong, F. & Zhang, J. A review of catalysts for the electroreduction of carbon dioxide to produce low-carbon fuels. *Chem. Soc. Rev.* **43**, 631-675 (2014).

23 Schneider, J., Jia, H., Muckerman, J. T. & Fujita, E. Thermodynamics and kinetics of CO_2, CO, and H^+ binding to the metal centre of CO_2 reduction catalysts. *Chem. Soc. Rev.* **41**, 2036-2051 (2012).

24 Wakerley, D. *et al.* Bio-inspired hydrophobicity promotes CO_2 reduction on a Cu surface. *Nat. Mater.* **18**, 1222-1227 (2019).

25 Skulason, E. *et al.* A theoretical evaluation of possible transition metal electro-catalysts for N_2 reduction. *Phys. Chem. Chem. Phys.* **14**, 1235-1245 (2012).

26 Wang, Y. *et al.* Advanced electrocatalysts with single-metal-atom active sites. *Chem. Rev.* **120**, 12217-12314 (2020).

27 De Gregorio, G. L. *et al.* Facet-dependent selectivity of Cu catalysts in electrochemical CO_2 reduction at commercially viable current densities. *ACS Catal.* **10**, 4854-4862 (2020).

28 Mezzavilla, S., Horch, S., Stephens, I. E., Seger, B. & Chorkendorff, I. Structure sensitivity in the electrocatalytic reduction of CO_2 with Gold catalysts. *Angew. Chem. Int. Ed.* **58**, 3774-3778 (2019).

29 Reske, R., Mistry, H., Behafarid, F., Roldan Cuenya, B. & Strasser, P. Particle size effects in the catalytic electroreduction of CO_2 on Cu nanoparticles. *J. Am. Chem. Soc.* **136**, 6978-6986 (2014).

30 Seidel, Y. *et al.* Mesoscopic mass transport effects in electrocatalytic processes. *Faraday Discuss.* **140**, 167-184 (2009).

31 Ono, L. K. & Roldan-Cuenya, B. Effect of interparticle interaction on the low temperature oxidation of

CO over size-selected Au nanocatalysts supported on ultrathin TiC films. *Catal. Letters* **113**, 86-94 (2007).

32 Mistry, H. *et al.* Tuning catalytic selectivity at the mesoscale via interparticle interactions. *ACS Catal.* **6**, 1075-1080 (2016).

33 Mistry, H., Varela, A. S., Kühl, S., Strasser, P. & Cuenya, B. R. Nanostructured electrocatalysts with tunable activity and selectivity. *Nat. Rev. Mater.* **1**, 1-14 (2016).

34 Cui, X., Tang, C. & Zhang, Q. A review of electrocatalytic reduction of dinitrogen to ammonia under ambient conditions. *Adv. Energy Mater.* **8**, 1800369 (2018).

35 Bao, D. *et al.* Electrochemical reduction of N_2 under ambient conditions for artificial N_2 fixation and renewable energy storage using N_2/NH_3 cycle. *Adv. Mater.* **29**, 1604799 (2017).

36 Shi, M. *et al.* Au sub-nanoclusters on TiO_2 toward highly efficient and selective electrocatalyst for N_2 conversion to NH_3 at ambient conditions. *Adv. Mater.* **29**, 1606550 (2017).

37 Yang, D., Chen, T. & Wang, Z. Electrochemical reduction of aqueous nitrogen (N_2) at a low overpotential on (110)-oriented Mo nanofilm. *J. Mater. Chem. A* **5**, 18967-18971 (2017).

38 Pan, F. & Yang, Y. Designing CO2 reduction electrode materials by morphology and interface engineering. *Energy & Environmental Science* **13**, 2275-2309, doi:10.1039/D0EE00900H (2020).

39 Wagner, A., Sahm, C. D. & Reisner, E. Towards molecular understanding of local chemical environment effects in electro- and photocatalytic CO2 reduction. *Nature Catalysis* **3**, 775-786, doi:10.1038/s41929-020-00512-x (2020).

40 Li, F., MacFarlane, D. R. & Zhang, J. Recent advances in the nanoengineering of electrocatalysts for CO2 reduction. *Nanoscale* **10**, 6235-6260, doi:10.1039/C7NR09620H (2018).

41 Trogadas, P. & Coppens, M. O. Nature-inspired electrocatalysts and devices for energy conversion. *Chem Soc Rev* **49**, 3107-3141, doi:10.1039/c8cs00797g (2020).

42 Huan, T. N. *et al.* A three-dimensional gold nanodendrite network porous structure and its application for an electrochemical sensing. *Biosensors and Bioelectronics* **27**, 183-186, doi:https://doi.org/10.1016/j.bios.2011.06.011 (2011).

43 Plowman, B. J., Jones, L. A. & Bhargava, S. K. Building with bubbles: the formation of high surface area honeycomb-like films via hydrogen bubble templated electrodeposition. *Chemical Communications* **51**, 4331-4346, doi:10.1039/c4cc06638c (2015).

44 Vesztergom, S. *et al.* Hydrogen Bubble Templated Metal Foams as Efficient Catalysts of CO_2 Electroreduction. *ChemCatChem* **13**, 1039-1058, doi:10.1002/cctc.202001145 (2020).

45 Du, R. *et al.* Engineering Self-Supported Noble Metal Foams Toward Electrocatalysis and Beyond. *Advanced Energy Materials* **10**, 1901945, doi:https://doi.org/10.1002/aenm.201901945 (2020).

46 Dutta, A., Morstein, C. E., Rahaman, M., Cedeño López, A. & Broekmann, P. Beyond Copper in CO2 Electrolysis: Effective Hydrocarbon Production on Silver-Nanofoam Catalysts. *ACS Catalysis* **8**, 8357-8368, doi:10.1021/acscatal.8b01738 (2018).

47 Wang, J., Wang, H., Han, Z. & Han, J. Electrodeposited porous Pb electrode with improved electrocatalytic performance for the electroreduction of CO2 to formic acid. *Frontiers of Chemical Science and Engineering* **9**, 57-63, doi:10.1007/s11705-014-1444-8 (2015).

48 Qin, B., Wang, H., Peng, F., Yu, H. & Cao, Y. Effect of the surface roughness of copper substrate on three-dimensional tin electrode for electrochemical reduction of CO2 into HCOOH. *Journal of CO2 Utilization* **21**, 219-223, doi:https://doi.org/10.1016/j.jcou.2017.07.012 (2017).

49 Dutta, A. *et al.* Activation of bimetallic AgCu foam electrocatalysts for ethanol formation from CO2 by selective Cu oxidation/reduction. *Nano Energy* **68**, 104331, doi:https://doi.org/10.1016/j.nanoen.2019.104331 (2020).

50 Lee, H., Kim, J., Choi, I. & Ahn, S. H. Nanostructured Ag/In/Cu foam catalyst for electrochemical reduction of CO2 to CO. *Electrochimica Acta* **323**, 133102, doi:https://doi.org/10.1016/j.electacta.2018.11.101 (2019).

51 Zeng, J. *et al.* Advanced Cu-Sn foam for selectively converting CO2 to CO in aqueous solution. *Applied Catalysis B: Environmental* **236**, 475-482, doi:https://doi.org/10.1016/j.apcatb.2018.05.056 (2018).

52 Rahaman, M., Kiran, K., Zelocualtecatl Montiel, I., Dutta, A. & Broekmann, P. Suppression of the Hydrogen Evolution Reaction Is the Key: Selective Electrosynthesis of Formate from CO2 over Porous In55Cu45 Catalysts. *ACS Applied Materials & Interfaces* **13**, 35677-35688, doi:10.1021/acsami.1c07829 (2021).

53 Lamaison, S. *et al.* High-Current-Density CO2-to-CO Electroreduction on Ag-Alloyed Zn Dendrites at Elevated Pressure. *Joule* **4**, 395-406, doi:10.1016/j.joule.2019.11.014 (2020).

54 Dutta, A., Rahaman, M., Luedi, N. C., Mohos, M. & Broekmann, P. Morphology Matters: Tuning the Product Distribution of CO2 Electroreduction on Oxide-Derived Cu Foam Catalysts. *ACS Catalysis* **6**, 3804-3814, doi:10.1021/acscatal.6b00770 (2016).

55 Shin, H.-C. & Liu, M. Copper Foam Structures with Highly Porous Nanostructured Walls. *Chemistry of Materials* **16**, 5460-5464, doi:10.1021/cm048887b (2004).

56 Zhang, H., Ye, Y., Shen, R., Ru, C. & Hu, Y. Effect of Bubble Behavior on the Morphology of Foamed Porous Copper Prepared via Electrodeposition. *Journal of The Electrochemical Society* **160**, D441-D445, doi:10.1149/2.019310jes (2013).

57 Rashid, N., Bhat, M. A. & Ingole, P. P. Dendritic copper microstructured electrodeposits for efficient and selective electrochemical reduction of carbon dioxide into C1 and C2 hydrocarbons. *Journal of CO2 Utilization* **38**, 385-397, doi:https://doi.org/10.1016/j.jcou.2020.02.017 (2020).

58 Malik, K., Bajaj, N. K. & Verma, A. Effect of catalyst layer on electrochemical reduction of carbon dioxide using different morphologies of copper. *Journal of CO2 Utilization* **27**, 355-365, doi:https://doi.org/10.1016/j.jcou.2018.07.020 (2018).

59 Huan, T. N. *et al.* A Dendritic Nanostructured Copper Oxide Electrocatalyst for the Oxygen Evolution Reaction. *Angew Chem Int Ed Engl* **56**, 4792-4796, doi:10.1002/anie.201700388 (2017).

60 Huan, T. N. *et al.* Low-cost high-efficiency system for solar-driven conversion of CO2 to hydrocarbons. *Proc Natl Acad Sci U S A* **116**, 9735-9740, doi:10.1073/pnas.1815412116 (2019).

61 Stojkovikj, S. *et al.* Electrocatalyst Derived from Waste Cu–Sn Bronze for CO2 Conversion into CO. *ACS Applied Materials & Interfaces* **13**, 38161-38169, doi:10.1021/acsami.1c05015 (2021).

62 Burdyny, T. *et al.* Nanomorphology-Enhanced Gas-Evolution Intensifies CO2 Reduction Electrochemistry. *ACS Sustainable Chemistry & Engineering* **5**, 4031-4040, doi:10.1021/acssuschemeng.7b00023 (2017).

63 Yoon, Y., Hall, A. S. & Surendranath, Y. Tuning of Silver Catalyst Mesostructure Promotes Selective Carbon Dioxide Conversion into Fuels. *Angewandte Chemie International Edition* **55**, 15282-15286, doi:https://doi.org/10.1002/anie.201607942 (2016).

64 Yang, P.-P. *et al.* Protecting Copper Oxidation State via Intermediate Confinement for Selective CO2 Electroreduction to C2+ Fuels. *Journal of the American Chemical Society* **142**, 6400-6408, doi:10.1021/jacs.0c01699 (2020).

65 Yang, B., Ding, W., Zhang, H. & Zhang, S. Recent progress in electrochemical synthesis of ammonia from nitrogen: strategies to improve the catalytic activity and selectivity. *Energy & Environmental Science* **14**, 672-687, doi:10.1039/D0EE02263B (2021).

66 Kumar, R. D. *et al.* Trimetallic PdCuIr with long-spined sea-urchin-like morphology for ambient electroreduction of nitrogen to ammonia. *Journal of Materials Chemistry A* **7**, 3190-3196, doi:10.1039/C8TA10562F (2019).

67 Wei, X., Vogel, D., Keller, L., Kriescher, S. & Wessling, M. Microtubular Gas Diffusion Electrode Based on Ruthenium-Carbon Nanotubes for Ambient Electrochemical Nitrogen Reduction to Ammonia. *ChemElectroChem* **7**, 4679-4684, doi:10.1002/celc.202001370 (2020).

68 Wang, H. *et al.* Electrochemical Fabrication of Porous Au Film on Ni Foam for Nitrogen Reduction to Ammonia. *Small* **15**, 1804769, doi:https://doi.org/10.1002/smll.201804769 (2019).

69 Wagner, A., Sahm, C. D. & Reisner, E. Towards molecular understanding of local chemical environment effects in electro-and photocatalytic CO_2 reduction. *Nat. Catal.* **3**, 775-786 (2020).

70 Magnussen, O. M. Ordered anion adlayers on metal electrode surfaces. *Chem. Rev.* **102**, 679-726 (2002).

71 Li, F. *et al.* Molecular tuning of CO_2-to-ethylene conversion. *Nature* **577**, 509-513 (2020).

72 Kim, C. *et al.* Insight into electrochemical CO_2 reduction on surface-molecule-mediated Ag nanoparticles. *ACS Catal.* **7**, 779-785 (2017).

73 Lim, H. *et al.* Embedding covalency into metal catalysts for efficient electrochemical conversion of CO_2. *J. Am. Chem. Soc.* **136**, 11355-11361 (2014).

74 Zhao, Y., Wang, C., Liu, Y., MacFarlane, D. R. & Wallace, G. G. Engineering surface amine modifiers of ultrasmall gold nanoparticles supported on reduced graphene oxide for improved electrochemical CO_2 reduction. *Adv. Energy Mater.* **8**, 1801400 (2018).

75 Wang, J. *et al.* Selective CO_2 electrochemical reduction enabled by a tricomponent copolymer modifier on a copper surface. *J. Am. Chem. Soc.* **143**, 2857-2865 (2021).

76 Xiao, L. *et al.* Effects of hydrophobic layer on selective electrochemical nitrogen fixation of self-supporting nanoporous Mo_4P_3 catalyst under ambient conditions. *Appl. Catal. B: Environ.* **286**, 119895 (2021).

77 Huang, Y., Ong, C. W. & Yeo, B. S. Effects of electrolyte anions on the reduction of carbon dioxide to ethylene and ethanol on copper (100) and (111) surfaces. *ChemSusChem* **11**, 3299-3306 (2018).

78 Varela, A. S., Ju, W., Reier, T. & Strasser, P. Tuning the catalytic activity and selectivity of Cu for CO_2 electroreduction in the presence of halides. *ACS Catal.* **6**, 2136-2144 (2016).

79 Nam, D. H. *et al.* Molecular enhancement of heterogeneous CO_2 reduction. *Nat. Mater.* **19**, 266-276 (2020).

80 Wang, Z., Yu, Z. & Zhao, J. Computational screening of a single transition metal atom supported on the C_2N monolayer for electrochemical ammonia synthesis. *Phys. Chem. Chem. Phys.* **20**, 12835-12844 (2018).

81 Qi, K., Chhowalla, M. & Voiry, D. Single atom is not alone: Metal-support interactions in single-atom catalysis. *Mater. Today* **40**, 173-192 (2020).

82 Wang, Y. *et al.* Revealing the intrinsic peroxidase-like catalytic mechanism of heterogeneous single-atom Co–MoS 2. *Nano-Micro Letters* **11**, 1-13 (2019).

83 Qi, K. *et al.* Single-atom cobalt array bound to distorted 1T MoS_2 with ensemble effect for hydrogen evolution catalysis. *Nat. Commun.* **10**, 1-9 (2019).

84 Liu, S. *et al.* Elucidating the electrocatalytic CO_2 reduction reaction over a model single-atom nickel catalyst. *Angew. Chem. Int. Ed.* **59**, 798-803 (2020).

85 Pan, Y. *et al.* Design of single-atom Co-N_5 catalytic site: a robust electrocatalyst for CO_2 reduction with nearly 100% CO selectivity and remarkable stability. *J. Am. Chem. Soc.* **140**, 4218-4221 (2018).

86 Choi, C. *et al.* Suppression of hydrogen evolution reaction in electrochemical N_2 reduction using single-atom catalysts: A computational guideline. *ACS Catal.* **8**, 7517-7525 (2018).

87 Chen, Y. *et al.* Highly productive electrosynthesis of ammonia by admolecule-targeting single Ag sites. *ACS Nano* **14**, 6938-6946 (2020).

88 Wang, G. *et al.* Electrocatalysis for CO_2 conversion: from fundamentals to value-added products. *Chem. Soc. Rev.* (2021).

89 Chen, J. G. *et al.* Beyond fossil fuel-driven nitrogen transformations. *Science* **360** (2018).

90 Hori, Y. in *Modern aspects of electrochemistry* 89-189 (Springer, 2008).

91 Varela, A. S. *et al.* pH effects on the selectivity of the electrocatalytic CO_2 reduction on graphene-embedded Fe-N-C motifs: Bridging concepts between molecular homogeneous and solid-state heterogeneous catalysis. *ACS Energy Lett.* **3**, 812-817 (2018).

92 Billy, J. T. & Co, A. C. Experimental parameters influencing hydrocarbon selectivity during the electrochemical conversion of CO_2. *ACS Catal.* **7**, 8467-8479 (2017).

93 Rosca, V., Duca, M., de Groot, M. T. & Koper, M. T. Nitrogen cycle electrocatalysis. *Chem. Rev.* **109**, 2209-2244 (2009).

94 De Arquer, F. P. G. *et al.* CO_2 electrolysis to multicarbon products at activities greater than 1 A cm^{-2}. *Science* **367**, 661-666 (2020).

95 Rabinowitz, J. A. & Kanan, M. W. The future of low-temperature carbon dioxide electrolysis depends on solving one basic problem. *Nature Communications* **11**, 5231, doi:10.1038/s41467-020-19135-8 (2020).

96 Zhang, F. & Co, A. C. Direct evidence of local pH change and the role of alkali cation during CO_2 electroreduction in aqueous media. *Angew. Chem. Int. Ed.* **59**, 1674-1681 (2020).

97 Varela, A. S., Kroschel, M., Reier, T. & Strasser, P. Controlling the selectivity of CO_2 electroreduction on copper: The effect of the electrolyte concentration and the importance of the local pH. *Catal. Today* **260**, 8-13 (2016).

98 Huang, J. E. *et al.* CO₂ electrolysis to multicarbon products in strong acid. *Science* **372**, 1074-1078, doi:doi:10.1126/science.abg6582 (2021).

99 Kas, R., Kortlever, R., Yılmaz, H., Koper, M. T. & Mul, G. Manipulating the hydrocarbon selectivity of copper nanoparticles in CO_2 electroreduction by process conditions. *ChemElectroChem* **2**, 354-358 (2015).

100 Chen, C., Zhang, B., Zhong, J. & Cheng, Z. Selective electrochemical CO_2 reduction over highly porous gold films. *J. Mater. Chem. A* **5**, 21955-21964 (2017).

101 Xu, H. *et al.* Electrochemical ammonia synthesis through N_2 and H_2O under ambient conditions: Theory, practices, and challenges for catalysts and electrolytes. *Nano Energy* **69**, 104469 (2020).

102 Wang, J. *et al.* Ambient ammonia synthesis via palladium-catalyzed electrohydrogenation of dinitrogen at low overpotential. *Nat. Commun.* **9**, 1-7 (2018).

103 Strmcnik, D., Lopes, P. P., Genorio, B., Stamenkovic, V. R. & Markovic, N. M. Design principles for hydrogen evolution reaction catalyst materials. *Nano Energy* **29**, 29-36 (2016).

104 Wuttig, A., Yoon, Y., Ryu, J. & Surendranath, Y. Bicarbonate is not a general acid in Au-catalyzed CO_2 electroreduction. *J. Am. Chem. Soc.* **139**, 17109-17113 (2017).

105 Gao, D., Arán Ais, R. M., Jeon, H. S. & Cuenya, B. R. Rational catalyst and electrolyte design for CO_2 electroreduction towards multicarbon products. *Nat. Catal.* **2**, 198-210 (2019).

106 Gao, D. *et al.* Activity and selectivity control in CO_2 electroreduction to multicarbon products over CuO_x catalysts via electrolyte design. *ACS Catal.* **8**, 10012-10020 (2018).

107 Monteiro, M. C. *et al.* Absence of CO_2 electroreduction on copper, gold and silver electrodes without metal cations in solution. *Nat. Catal.*, 1-9 (2021).

108 Sa, Y. J. *et al.* Catalyst-electrolyte interface chemistry for electrochemical CO_2 reduction. *Chem. Soc. Rev.* **49**, 6632-6665 (2020).

109 Singh, M. R., Kwon, Y., Lum, Y., Ager III, J. W. & Bell, A. T. Hydrolysis of electrolyte cations enhances the electrochemical reduction of CO_2 over Ag and Cu. *J. Am. Chem. Soc.* **138**, 13006-13012 (2016).

110 Ringe, S. *et al.* Understanding cation effects in electrochemical CO_2 reduction. *Energy Environ. Sci.* **12**, 3001-3014 (2019).

111 Ringe, S. *et al.* Double layer charging driven carbon dioxide adsorption limits the rate of electrochemical carbon dioxide reduction on Gold. *Nat. Commun.* **11**, 1-11 (2020).

112 Schizodimou, A. & Kyriacou, G. Acceleration of the reduction of carbon dioxide in the presence of multivalent cations. *Electrochim. Acta* **78**, 171-176 (2012).

113 Resasco, J. *et al.* Promoter effects of alkali metal cations on the electrochemical reduction of carbon dioxide. *J. Am. Chem. Soc.* **139**, 11277-11287 (2017).

114 Gu, J. *et al.* Modulating electric field distribution by alkali cations for CO2 electroreduction in strongly acidic medium. *Nature Catalysis* **5**, 268-276, doi:10.1038/s41929-022-00761-y (2022).

115 Hao, Y. C. *et al.* Promoting nitrogen electroreduction to ammonia with bismuth nanocrystals and potassium cations in water. *Nat. Catal.* **2**, 448-456 (2019).

116 Wang, B., Qin, L., Mu, T., Xue, Z. & Gao, G. Are ionic liquids chemically stable? *Chem. Rev.* **117**, 7113-7131 (2017).

117 Shkrob, I. A. & Wishart, J. F. Charge trapping in imidazolium ionic liquids. *J. Phys. Chem. B* **113**, 5582-5592 (2009).

118 Feaster, J. T. *et al.* Understanding the influence of [EMIM]Cl on the suppression of the hydrogen evolution reaction on transition metal electrodes. *Langmuir* **33**, 9464-9471 (2017).

119 Johnson, K. E. What's an ionic liquid? *Interface-Electrochemical Society* **16**, 38-41 (2007).

120 Alvarez Guerra, M., Albo, J., Alvarez Guerra, E. & Irabien, A. Ionic liquids in the electrochemical valorisation of CO_2. *Energy Environ. Sci.* **8**, 2574-2599 (2015).

121 Zhang, S. *et al.* Ionic liquid-based green processes for energy production. *Chem. Soc. Rev.* **43**, 7838-7869 (2014).

122 Klähn, M. & Seduraman, A. What determines CO_2 solubility in iIonic liquids? A molecular simulation study. *J. Phys. Chem. B* **119**, 10066-10078 (2015).

123 Rosen, B. A. *et al.* Ionic liquid-mediated selective conversion of CO_2 to CO at low overpotentials. *Science* **334**, 643-644 (2011).

124 Rey, N. G. & Dlott, D. D. Effects of water on low-overpotential CO_2 reduction in ionic liquid studied by sum-frequency generation spectroscopy. *Phys. Chem. Chem. Phys.* **19**, 10491-10501 (2017).

125 Asadi, M. *et al.* Nanostructured transition metal dichalcogenide electrocatalysts for CO_2 reduction in ionic liquid. *Science* **353**, 467-470 (2016).

126 Yano, H., Tanaka, T., Nakayama, M. & Ogura, K. Selective electrochemical reduction of CO_2 to ethylene at a three-phase interface on copper (I) halide-confined Cu-mesh electrodes in acidic solutions of potassium halides. *J. Electroanal. Chem.* **565**, 287-293 (2004).

127 Liu, X. *et al.* Highly active, durable ultrathin $MoTe_2$ layers for the electroreduction of CO_2 to CH_4. *Small*

14, 1704049 (2018).

128 Atifi, A., Boyce, D. W., DiMeglio, J. L. & Rosenthal, J. Directing the outcome of CO_2 reduction at bismuth cathodes using varied ionic liquid promoters. *ACS Catal.* **8**, 2857-2863 (2018).

129 Stevanovic, S. & Gomes, M. C. Solubility of carbon dioxide, nitrous oxide, ethane, and nitrogen in 1-butyl-1-methylpyrrolidinium and trihexyl (tetradecyl) phosphonium tris (pentafluoroethyl) trifluorophosphate (eFAP) ionic liquids. *J. Chem. Thermodyn.* **59**, 65-71 (2013).

130 Zhou, F. *et al.* Electro-synthesis of ammonia from nitrogen at ambient temperature and pressure in ionic liquids. *Energy Environ. Sci.* **10**, 2516-2520 (2017).

131 Ortuño, M. A., Hollóczki, O., Kirchner, B. & López, N. r. Selective electrochemical nitrogen reduction driven by hydrogen bond interactions at metal-ionic liquid interfaces. *J. Phys. Chem. Lett.* **10**, 513-517 (2019).

132 Suryanto, B. H. *et al.* Rational electrode-electrolyte design for efficient ammonia electrosynthesis under ambient conditions. *ACS Energy Lett.* **3**, 1219-1224 (2018).

133 Araque, J. C., Yadav, S. K., Shadeck, M., Maroncelli, M. & Margulis, C. J. How is diffusion of neutral and charged tracers related to the structure and dynamics of a room-temperature ionic liquid? Large deviations from stokes–Einstein behavior explained. *J. Phys. Chem. B* **119**, 7015-7029 (2015).

134 Mellmann, D., Sponholz, P., Junge, H. & Beller, M. Formic acid as a hydrogen storage material-development of homogeneous catalysts for selective hydrogen release. *Chem. Soc. Rev.* **45**, 3954-3988 (2016).

135 Manthiram, A., Yu, X. & Wang, S. Lithium battery chemistries enabled by solid-state electrolytes. *Nat. Rev. Mater.* **2**, 1-16 (2017).

136 Han, N., Ding, P., He, L., Li, Y. & Li, Y. Promises of main group metal-based nanostructured materials for electrochemical CO_2 reduction to formate. *Adv. Energy Mater.* **10**, 1902338 (2020).

137 Gabardo, C. M. *et al.* Combined high alkalinity and pressurization enable efficient CO_2 electroreduction to CO. *Energy Environ. Sci.* **11**, 2531-2539 (2018).

138 Gabardo, C. M. *et al.* Continuous carbon dioxide electroreduction to concentrated multi-carbon products using a membrane electrode assembly. *Joule* **3**, 2777-2791 (2019).

139 Xia, C. *et al.* Continuous production of pure liquid fuel solutions via electrocatalytic CO_2 reduction using solid-electrolyte devices. *Nat. Energy* **4**, 776-785 (2019).

140 Fan, L., Xia, C., Zhu, P., Lu, Y. & Wang, H. Electrochemical CO_2 reduction to high-concentration pure formic acid solutions in an all-solid-state reactor. *Nat. Commun.* **11**, 1-9 (2020).

141 Díez-Ramírez, J. *et al.* Enhancement of ammonia synthesis on a Co_3Mo_3N-Ag electrocatalyst in a K-βAl_2O_3 solid electrolyte cell. *ACS Sustain. Chem. Eng.* **5**, 8844-8851 (2017).

142 Lan, R. & Tao, S. Electrochemical synthesis of ammonia directly from air and water using a $Li^+/H^+/NH_4^+$ mixed conducting electrolyte. *RSC Adv.* **3**, 18016-18021 (2013).

143 Sheets, B. L. & Botte, G. G. Electrochemical nitrogen reduction to ammonia under mild conditions enabled by a polymer gel electrolyte. *Chem. Comm.* **54**, 4250-4253 (2018).

144 Guo, X., Du, H., Qu, F. & Li, J. Recent progress in electrocatalytic nitrogen reduction. *J. Mater. Chem. A* **7**, 3531-3543 (2019).

145 Garagounis, I., Kyriakou, V., Skodra, A., Vasileiou, E. & Stoukides, M. Electrochemical synthesis of ammonia in solid electrolyte cells. *Front. Energy Res.* **2**, 1 (2014).

146 Chang, X., Wang, T. & Gong, J. CO_2 photo-reduction: insights into CO_2 activation and reaction on surfaces of photocatalysts. *Energy Environ. Sci.* **9**, 2177-2196 (2016).

147 Weiss, R. F. in *Deep Sea Research and Oceanographic Abstracts.* 721-735 (Elsevier).

148 Raciti, D., Mao, M., Park, J. H. & Wang, C. Mass transfer effects in CO_2 reduction on Cu nanowire electrocatalysts. *Catal. Sci. Technol.* **8**, 2364-2369 (2018).

149 Lees, E. W., Mowbray, B. A. W., Parlane, F. G. L. & Berlinguette, C. P. Gas diffusion electrodes and membranes for CO2 reduction electrolysers. *Nature Reviews Materials* **7**, 55-64, doi:10.1038/s41578-021-00356-2 (2022).

150 Tan, Y. C., Lee, K. B., Song, H. & Oh, J. Modulating Local CO2 Concentration as a General Strategy for Enhancing C−C Coupling in CO2 Electroreduction. *Joule* **4**, 1104-1120, doi:https://doi.org/10.1016/j.joule.2020.03.013 (2020).

151 Weng, L.-C., Bell, A. T. & Weber, A. Z. Modeling gas-diffusion electrodes for CO2 reduction. *Physical Chemistry Chemical Physics* **20**, 16973-16984, doi:10.1039/C8CP01319E (2018).

152 Xing, Z., Hu, L., Ripatti, D. S., Hu, X. & Feng, X. Enhancing carbon dioxide gas-diffusion electrolysis by creating a hydrophobic catalyst microenvironment. *Nat. Commun.* **12**, 1-11 (2021).

153 Pham, T. H. M. *et al.* Enhanced Electrocatalytic CO2 Reduction to C2+ Products by Adjusting the Local Reaction Environment with Polymer Binders. *Advanced Energy Materials* **12**, 2103663, doi:https://doi.org/10.1002/aenm.202103663 (2022).

154 Li, J. *et al.* Efficient electrocatalytic CO_2 reduction on a three-phase interface. *Nat. Catal.* **1**, 592-600 (2018).

155 Kim, C. *et al.* Tailored catalyst microenvironments for CO2 electroreduction to multicarbon products on copper using bilayer ionomer coatings. *Nature Energy* **6**, 1026-1034, doi:10.1038/s41560-021-00920-8 (2021).

156 Kordali, V., Kyriacou, G. & Lambrou, C. Electrochemical synthesis of ammonia at atmospheric pressure and low temperature in a solid polymer electrolyte cell. *Chem. Comm.*, 1673-1674 (2000).

157 Yang, X. *et al.* Mechanistic insights into electrochemical nitrogen reduction reaction on vanadium nitride nanoparticles. *J. Am. Chem. Soc.* **140**, 13387-13391 (2018).

158 Zhang, J. *et al.* Three-phase electrolysis by gold nanoparticle on hydrophobic interface for enhanced electrochemical nitrogen reduction reaction. *Adv. Sci.* **7**, 2002630 (2020).

159 Chen, S. *et al.* Room-temperature electrocatalytic synthesis of NH_3 from H_2O and N_2 in a gas-liquid-solid three-phase reactor. *ACS Sustain. Chem. Eng.* **5**, 7393-7400 (2017).

160 Cheng, H. *et al.* Molybdenum carbide nanodots enable efficient electrocatalytic nitrogen fixation under

ambient conditions. *Adv. Mater.* **30**, 1803694 (2018).

161 Xing, Z., Hu, X. & Feng, X. Tuning the microenvironment in gas-diffusion electrodes enables high-rate CO_2 electrolysis to formate. *ACS Energy Lett.* **6**, 1694-1702 (2021).

162 Lee, S., Kim, M., Lee, K. T., Irvine, J. T. & Shin, T. H. Enhancing electrochemical CO_2 reduction using Ce (Mn, Fe) O_2 with La (Sr) Cr (Mn) O_3 cathode for high-temperature solid oxide electrolysis cells. *Adv. Energy Mater.*, 2100339 (2021).

Chapter 3. Improved electrochemical conversion of CO_2 to multi-carbon products by using molecular doping

3.1 Abstract

The conversion of CO_2 into desirable multicarbon products *via* the carbon dioxide reduction reaction (CO_2RR) hold promise to achieve a circular carbon economy. In this chapter, I report a strategy in which we modify the surface of bimetallic silver-copper catalyst with aromatic heterocycles such as thiadiazole and triazole derivatives to increase the conversion of CO_2 into hydrocarbon molecules. We identified that the electron withdrawing nature of functional groups orients the reaction pathway towards the production of C_{2+} species (ethanol and ethylene) and enhances the reaction rate on the surface of the catalyst. As a result, we achieve a high Faradaic efficiency for the C_{2+} formation of ≈ 80% and full-cell energy efficiency of 20.3% with a specific current density of 261.4 mA cm^{-2} for C_{2+} using functionalized Ag-Cu electrodes.

3.2 Introduction

This chapter is dedicated to use the electron withdrawing nature of functional groups to modify the catalyst surface to orient the reaction pathway towards the production of C_{2+} species. As introduced in chapter 1, the electrochemical reduction of CO_2 to hydrocarbons using renewable energy is regarded as an effective way to close the carbon cycle *via* the conversion of CO_2 into chemical precursors or fuels[1,2]. The electrochemical CO_2 reduction reaction (CO_2RR) toward single carbon products has achieved tremendous progress[3], especially for the production of C_1 molecules such as carbon monoxide (CO) or methane (CH_4)[4-7]. Copper (Cu), as one of the few transition metals, can efficiently catalyze the electrolysis of CO_2 to multi-carbon products such as ethylene, ethanol, acetate, propanol[8], which possess higher market values and are more energy concentrated. Therefore, intensive efforts have been devoted to improve the reaction selectivity towards the production of C_2 and C_{2+} molecules, including alloying[9-12], surface doping1[3,14], ligand modification[15,16], and interface engineering[17-20]. Among these strategies, designing Cu-based catalysts by adapting some of the concept of molecular catalysts in order to finely tailor the behavior of the active sites of metallic surfaces is currently regarded as the long-standing interest for the controlled design of novel electrocatalytic materials. Increasing the oxidation state of copper has been suggested to improve the CO_2RR performance and notably the formation of C_{2+} species[14,21,22]. Various strategies are being explored to prepare $Cu^{\delta+}$ by using controlled oxidation *via* plasma treatments or doping with boron and halides[14, 23-25]. Alternatively, molecular engineering of either the electrolyte or the catalyst surface has recently been proposed for orienting the selectivity of the reaction by stabilizing intermediates, inhibiting proton diffusion, or acting as redox mediators during the electrochemical CO_2 reduction reaction (CO_2RR)[26-30]. Organic species such as N-aryl pyridinium salts[31,32], imidazole[33-35], thiol[36-37] and cysteamine[38] have been reported as effective lever to tune the reaction selectivity toward the formation of specific products by stabilizing key reaction intermediates. Functionalization of alkyl chains can also lead to better CO_2RR performance by suppressing the

competitive hydrogen evolution reaction (HER) *via* the creation of hydrophobic regions on the surface of the catalyst[37, 39, 40].

In Chapter 3, I will present an effective strategy to control the surface oxidation state of bimetallic Ag-Cu electrodes by using functionalization for tuning the oxidation state of $Cu^{\delta+}$. By combining Auger and X-ray absorption spectroscopies (XAS), we identified that the grafting of aromatic heterocyclic functional groups can efficiently dope the surface of Cu by withdrawing electrons from the metal surface leading to the formation of $Cu^{\delta+}$ species. Compared to pristine non-functionalized and alkyl-functionalized electrodes, the modified electrodes display a clear improvement of the reaction rates and Faradaic efficiency towards the production of C_{2+} products. *Operando* Raman and X-ray absorption spectroscopy (XAS) suggest that the presence of $Cu^{\delta+}$ with $0 < \delta < 1$ favors the formation of adsorbed CO with the atop conformation which is a known key intermediate specie involved in the C-C coupling step associated with the formation of multi-carbon products. When assembled in a membrane electrode assembly (MEA) electrolyzer, the catalyst delivers a Faradaic efficiency (FE) for C_{2+} products of 80 ± 1 % and a total C_{2+} energy efficiency (EE) of 20.3% for the full cell.

3.3 Experimental methods

3.3.1 Materials

Chemicals

Copper sulfates ($CuSO_4$, 99%), silver nitrate ($AgNO_3$, 99%), ammonium sulfate(99%, ethylenediamine($NH_2CH_2CH_2NH_2$, 99.5%), potassium hydroxide (KOH, 90%) potassium bicarbonate($KHCO_3$, 99.7%), sulfuric acid(H_2SO_4, 99.99%), Iridium (III) chloride hydrate ($IrCl_3 \cdot xH_2O$, 99.9%), 5-Amino-1,3,4-thiadiazole-2-thiol($C_2H_3N_3S_2$,95%), 3-amino-1,2,4-triazole-5-thiol($C_2H_4N_4S$,99%), cysteamine(C_2H_7NS,99%) and 1-Propanethiol (C_3H_8S, 99%) were purchased from Sigma-Aldrich. Nafion 117 and anion exchange membrane (Fumapem FAA-3-50), gas diffusion layer (Freudenberg, H23C6), and titanium mesh were obtained from Fuel Cell Store. All chemicals were used as received. All aqueous solutions were prepared using deionized water with a resistivity of 18.2 MΩ cm^{-1}.

Electrodes preparation

Before depositing catalysts, gas diffusion electrode (GDE) was treated with sulfuric acid by sonicating 20 minutes. After acid treatment, the remaining acid was rinsed with deionized water for 5 min three times, and gas diffusion layer was dried at room temperature. To obtain the working electrodes, 15 $\%_{at.}$ Ag-Cu catalysts were prepared through a pulse electrodeposition approach under CO_2 bubbling condition. Firstly, electrochemical deposition of the Ag catalyst was performed using a potentiostat (VSP potentiostat from Bio-Logic Science Instruments). The electrolyte used was composed of 0.01 M $AgNO_3$, 0.6 M $(NH_4)_2SO_4$, and 0.04 M ethylenediamine. Ag catalyst was electrodeposited on GDE at a current density of 15 mA cm^{-2} with on- and off-time pulsing parameters of 0.25 and 3 s, respectively. Then, the Cu was electrodeposited on Ag at a constant current density of -400 mA cm^{-}

^{2} for 45 s to obtain the 15 $\%_{at.}$ Ag-Cu electrode. The solution consisted of 0.2 M $CuSO_4$ and 1M H_2SO_4 with continuously CO_2 bubbling.

Functionalization of the Ag-Cu electrodes

The different functional groups (organic chemicals(5-Amino-1,3,4-thiadiazole-2-thiol(N_2SN), 1,3,4-thiadiazole-2,5-dithiol (N_2SS), 3-amino-1,2,4-triazole-5-thiol(N_3N), cysteamine(C_2N) and 1-Propanethiol (C_3)) were dissolved in ethanol to a fixed concentration of 5 mM. The Ag-Cu electrodes were treated by the different functional solutions *via* drop-casting 20 µL of the solution containing the different thiol reagents on the GDE. After 5 min, the electrode was washed with ethanol and dried under argon flow.

Physical characterizations

A field emission scanning electron microscope (TESCAN Mira3) was employed to observe the morphology of samples. Aberration-corrected high-resolution (scanning) TEM imaging (HR-(S)TEM), energy-dispersive X-ray spectroscopy (EDS) and spatially-resolved electron energy-loss spectroscopy (SR-EELS) were performed using a FEI Titan Cubed Themis microscope which was operated at 80 kV. The Themis is equipped with a double Cs aberration corrector, a monochromator, an X-FEG gun, a super EDS detector, and an Ultra High Resolution Energy Filter (Gatan Quantum ERS) which allows for working in Dual-EELS mode. HR-STEM imaging was performed by using high-angle annular dark-field (HAADF) and annular dark-field (ADF) detectors. SR-EELS spectra were acquired with the monochromator excited allowing an energy resolution of 1.1 eV with an energy dispersion of 0.4 eV/pixel. Liquid products were quantified by 1H NMR spectroscopy (600 MHz Avance III Bukrer with a cryorobe Prodigy TCI) using deionized water with 0.1 % (w/w) of DSS (Sodium trimethylsilyl propane sulfonate) like internal standard for the quantification of the ethanol and formate. An 1D sequence water suppression with excitation sculpting with gradients(zgesgp)was used for the acquisition (Number of scan = 32, Delay D1=30 s). X-ray photoelectron spectroscopy (XPS) measurements were carried out on Thermo Electron ESCALAB 250 System using Al Kα X-ray radiation (1486.6 eV) for excitation. Raman measurements were conducted using a Renishaw in Via Raman microscope and an ×50 objective (Leica) equipped with a 633 nm laser. *Operando* Raman measurements were carried out using a modified liquid-electrolyte flow cell using a 20 s integration time and averaging 10 scans per region. The spectra were recorded and processed using the Renishaw WiRE software (version 4.4). An Ag/AgCl electrode and a Pt plate were used as the reference and counter electrodes respectively. *Ex situ* X-ray absorption spectra at the copper K-edges and *Operando* X-ray absorption spectroscopy (XAS) measurements at the copper K-edges were collected at Beijing Synchrotron Radiation Facility (BSRF) on beamline 1W1B and the SOLEIL synchrotron SAMBA beamline, respectively.

***Operando* X-ray absorption spectroscopy (XAS)**

Ex-situ and *operando* XAS measurements at the copper K-edges were collected at Beijing Synchrotron Radiation Facility (BSRF) on beamline 1W1B and the SOLEIL synchrotron SAMBA beamline, respectively. *Operando* Cu K-edge XAS measurements of functionalized Ag-Cu were obtained by using a Si(111) monochromator at the Cu K-edge for energy selection. The beam size was 1 × 0.5 mm. The signals were collected in fluorescence mode using a 13-channel Ge detector. The intensity of the incident radiation was measured with an ionization chamber (I_0) filled with an N_2 (500 mbar)/He (500 mbar) mixture. Two additional ionization chambers filled with 1700 mbar N_2 (in I_1 chamber) and an Ar (150 mbar)/N_2(850 mbar) mixture (in I_1 chamber) were used for measurements in transmission mode in the case of the reference samples. A custom-built electrochemical cell was used for operando XAS measurements. The applied potential was controlled by a VSP potentiostat (Bio-Logic Science Instruments). A platinum wire and Ag/AgCl electrode (3M KCl) were used as counter and reference electrodes, respectively. For the XAS studies, 15%at. Ag-Cu was firstly electrodeposited on gas diffusion layer (GDL, Sigracet 22 BB, Fuel Cell Store) used as gas diffusion electrode (GDE) and then functional solutions were drop-coated on the catalyst side, while the other side of the GDL was covered with polyamide tape. The GDL was then tape on a graphite foil and subsequently, the electrode was mounted in the *operando* cell with the graphite foil acting as a working electrode and window. A 0.5 M solution of $KHCO_3$ was used as electrolyte for the CO_2RR and the cell was continuously purged with CO_2 during the measurements. All measurements were performed at constant potentials of -1.2 V, -1.1 V, -1.0 V and -0.9 V *vs.* RHE. Time-resolved spectra under CO_2RR conditions were acquired every 30 min until no further changes were observed.

Data alignment and normalization of the X-ray absorption near edge structure (XANES) spectra were carried out using the Athena software. Fitting of the Cu K-edge extended X-ray absorption fine structure (EXAFS) spectra $\chi(k)k^2$ of the as-prepared catalysts was carried out in R-space in the range from R_{min} = 1 Å up to R_{max} = 2.1 Å, while for the catalysts in the reduced state, R_{min} = 1.0 Å to R_{max} = 3.0 Å were used. The Fourier transforms were carried out in the k-range from 3.0 $Å^{-1}$ to 10.0 $Å^{-1}$ with a k-weighting of 1, 2 and 3. Fitting parameters were the coordination numbers N, interatomic distances R, disorder factors σ^2 for Cu-O and Cu-Cu paths, as well as the corrections to the photoelectron reference energies ΔE_0. The S_0^2 factors was set to 0.831.

Computational details

All density functional theory (DFT) calculations were carried out in the Vienna Ab-initio Simulation Package (VASP) code with the projector augmented-wave (PAW) method. The exchange–correlation energy was treated using a general gradient approximation (GGA) with the Perdew–Burke–Ernzerhof (PBE) formalism. A plane-wave basis with a kinetic energy cutoff of 500 eV was chosen to expand the electronic wave functions. To investigate the possible binding modes between functional molecular and catalysts, a 5 layers of Cu (111) slab (7.7386 Å×7.7386 Å), in which the two bottom layers were kept fixed during relaxation, was built with a vacuum space of about 20 Å. For the geometrical optimizations, all atoms were fully relaxed to the ground state with the convergence of energy and forces setting to 1.0×10^{-5} eV and 0.01 eV $Å^{-1}$, where a 3×3×1 Γ-centered Monkhorst-

Pack schemed *k*-mesh was used to sample the first Brillouin zone. To compare the bond strength between each group of functional molecular and Cu (111), the adsorption energy (E_{ads}) is calculated by using the following formula:

$$E_{ads} = E_{Cu/FM} - E_{Cu} - E_{FM} \quad (1)$$

where $E_{Cu/FM}$, E_{Cu} and E_{FM} denote the total electronic energies of an adsorbed system, a clean Cu (111) surface, and the free functional molecular, respectively. The DFT calculated were performed in collaboration with Ji Li from the University of Shaanxi University of Science & Technology.

3.3.2 Electrochemical measurements

All electrochemical measurements were carried out at ambient temperature and pressure using a VSP electrochemical station from Bio-Logic Science Instruments equipped with a 5 A booster and FRA32 module. The cell voltages reported in all figures were recorded without iR correction. All the potentials in the H-cell were converted to values with reference to the RHE using:

$$E_{RHE} = E_{Ag/AgCl} + 0.197\ V + 0.0591 * pH \quad (2)$$

In the H-cell configuration, Ag/AgCl reference electrode (3 M KCl) and Pt plate were used as reference and counter electrodes respectively. The electrolyte consisted in a 0.5 M $KHCO_3$ solution (99.9%, Sigma Aldrich), which was saturated with alternatively CO2 (≥99.998, Linde) or Ar (5.0, Linde). Prior any experiment, the electrolyte solutions were saturated by bubbling CO_2 or Ar for at least 20 min.

The electrochemically active surface area (ECSA) of the different catalysts was determined using Pb underpotential deposition in H-cell. An Ar-saturated solution of 100 mM $HClO_4$ + 1 mM $Pb(ClO_4)_2$ was used as electrolyte. The working electrode was held at −0.7 V vs. Ag/AgCl for 10 min and then cyclic voltammetry was recorded between −0.7 and 0.7 V vs. Ag/AgCl at 10 mV s^{-1}. Pt foil was used as the counter electrode, while Ar (Linde, 99.998 %) was continuously supplied to the electrolyte. The ECSA values for Cu and Ag were calculated assuming the deposition of a monolayer of Pb atoms over Cu and Ag surface with a conversion factor of 310 μC cm^{-2} and 260 mC cm^{-2}, respectively.

The MEA electrolyzer (Dioxide Materials) was comprised of the Ag-Cu cathode, a Ti-IrO_x mesh anode and an anion exchange membrane (AEM, Fumasep FAA-3-50, Fuel cell store). The anode and cathode flow fields are made of titanium and stainless steel with geometric active areas of 4 cm^2 respectively. The anode was prepared by depositing IrO_x on a titanium support (0.002'' thickness, Fuel Cell Store) by a dip coating followed by thermal annealing. Briefly, the titanium mesh was firstly degreased with acetone and DI water, then etched in a 6 M HCl (Reagent Grade, Bioshop) solution heated to 80 °C to 90 °C for 45 min before dip coating. The solution used for dip coating consisted of 30 mg of $IrCl_3.xH_2O$ (Alfa Aesar) dissolved in 10 mL of an iso-propanol solution with 10% concentrated HCl. The etched titanium mesh was dipped into the $IrCl_3$ solution, dried in an oven at 100 °C for 10 min before calcination in air at 500 °C for 10 min. The dipping and calcination process was repeated until a suitable loading was achieved (2 mg cm^{-2}).

The AEM was firstly placed between the anode and cathode flow fields and then assembled together (Supplementary Figures 24 and 25). The flow fields were mainly responsible for the effective supply in aqueous anolyte solution and humidified CO_2 over the respective surfaces of anode and cathode electrodes. The anode and cathode gaskets were placed between the flow fields and the respective electrodes to ensure proper sealing. An anion exchange membrane (Fumapem FAA-3-50) (Dioxide Materials) was activated in 0.5 M aqueous KOH solution for at least 24 hours, washed with deionized water and used as the anion-exchange membrane (AEM). A 0.1 M $KHCO_3$ anolyte solution was circulated through the anode side of the electrolyzer with the constant flow rate of 30 ml/min *via* a peristaltic pump, while the fully humidified CO_2 was supplied to the cathode side with the constant flow rate of 10 standard cubic centimeters per minute (sccm). After three-minutes of initial operation, a full-cell potential of -2.8 V was applied to the electrolyzer and the potential then was gradually increased from -2.8 V with the increments of -0.10 V or -0.05 V. The voltage increments were made upon complete stabilization of the corresponding current, typically 15-20 min.

3.3.3 Quantification of the CO2RR products

The electrochemical data were recorded while simultaneously collecting the CO_2RR gas products by using an automatic sampler connected to the cathode outlet. A cold trap was used a collect the liquid products before the sampler. For each applied potential, the gas products were collected at least 3 times with proper time intervals. The gas alliquots were then injected into an online gas chromatograph (Agilent, Micro GC-490) equipped with a TCD detector and Molsieve 5A column continuously. Hydrogen and argon (99.9999%) were used as the carrier gases. Liquid products were quantified by 1H NMR spectroscopy (600 Mhz Avance III Bukrer with a cryorobe Prodigy TCI) using deionized water with 0.1 % (w/w) of DSS (Sodium trimethylsilylpropanesulfonate) like internal standard for the quantification of the ethanol and formate. An 1D sequence water suppression with excitation sculpting with gradients(zgesgp) was used for the acquisition (Number of scan = 32, Delay D1=30 s). Owing to the liquid product crossover, the FE values of the liquid products were calculated based on the total amount of the products collected on the anode and cathode sides during the same period.

Stability measurements in the MEA configuration

For the stability test, the MEA electrolyzer was operated at a constant voltage of -4.55 V with a continuous feeding in CO_2. The gas products were collected at frequent time intervals. The FE values were calculated from the average value obtained from three successive injections. As for the liquid products, the total liquid products were collected at the end of the experiments.

Faradaic Efficiency and Energy Efficiency Calculations

The Faradaic efficiency (FE) of each gas product was calculated as follows:

$$FE_{gas} = g_i \times v \times \frac{z_i}{RT} P_0 \times \frac{1}{I_{total}} \times 100\% \quad (3)$$

The Faradaic efficiency (FE) of each liquid product was calculated as follows:

$$FE_{liquid} = l_i \times \frac{z_i}{Q_{total}} F \times 100\% \quad (4)$$

The formation rate (R) for each species(i) was calculated as follows:

$$R_i = \frac{Q_{total} \times FE_i}{96485 \times z_i \times t \times S} \quad (5)$$

The full-cell energy efficiencies (EE) was calculated as follows:

$$EE = \frac{(1.23 - E_i) \times FE_i}{E_{cell}} \quad (6)$$

where g_i represents the volume fraction of gas product i; v represents the gas flow rate at the outlet in sccm; z_i represents the number of electrons required to produce one molecule of product i; I_{total} represents the total current; l_i represents the number of moles of liquid product i; and Q_{total} represents the charge passed while the liquid products are being collected. P_0 = 1.01 × 10 5 Pa, T = 273.15 K, F = 96,485 C mol^{-1} and R = 8.314 Jmol^{-1}K^{-1}; t represents the electrolysis time (h); S represents the geometric area of the electrode (cm^2); E_i represents the thermodynamic potential (versus RHE) for CO_2RR to species i and E_{cell} represents the cell voltage in two-electrode setup.

3.4 Results and discussion

3.4.1 Catalyst design and characterization

We fabricated the functionalized bimetallic catalyst by using a two-step strategy based on the controlled electrodeposition of Ag and Cu followed by the modification of the catalyst surface *via* functionalization (Fig. 1a). The Ag-Cu electrodes were prepared by firstly depositing Ag on gas diffusion electrodes (GDE) using pulsed electrodeposition. The silver structure grows in the form of a dendritic fish-bone structure with sharp Ag nanoneedles (Fig. 2). The Ag layer was then used as a scaffold for the deposition of copper. The final structure of the catalyst on the GDE electrodes was found to be porous where Cu is preferentially deposited on Ag (Figs. 1b and c, Fig. 3). The catalytic performance of pure Cu and Ag-Cu electrodes were systematically investigated (Figs. 3 and 4), and our results indicated appropriate loading of Ag contributes to the enhancement of the formation of CO, which may further facilitate C_{2+} production on copper. We determined the optimum composition to be 15 %at. Ag in Ag-Cu (labeled as 15 %$_{at.}$ Ag-Cu).

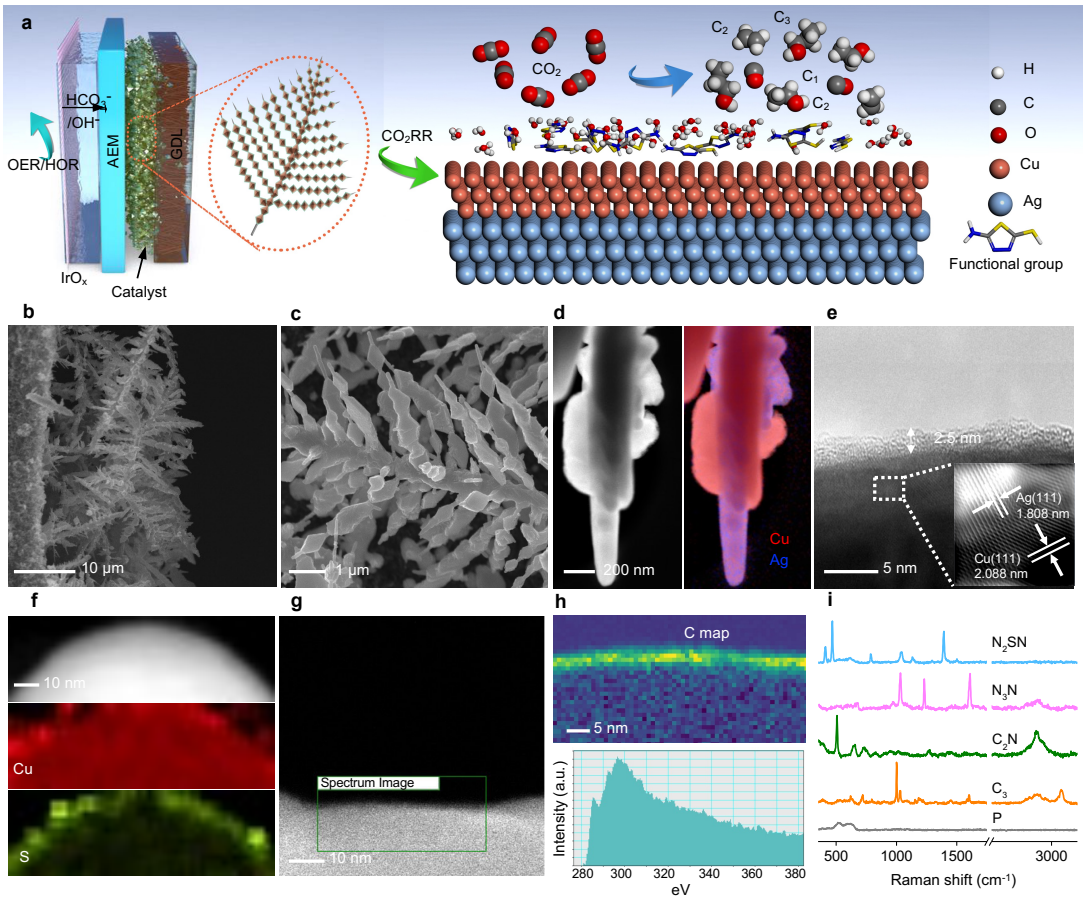

Fig. 1. Structural and elemental composition of the functionalized Ag-Cu catalysts. (a), Schematic representation of the functionalized Ag-Cu electrodes in a membrane electrode-assembly. (b), (c), Cross-section (c) and top-view (c) scanning electron microscope (SEM) images of the functionalized hierarchical Ag-Cu catalyst on a gas diffusion electrode (GDE). (d), High-angle annular dark-field scanning transmission electron microscopy (HAADF-STEM) image (left) and corresponding Cu and Ag EDS elemental maps of N_2SN-functionalized Ag-Cu (right). (e), High-resolution transmission electron microscope (HR-TEM) micrograph of the N_2SN-functionalized electrode (e). (f), HAADF-STEM image and the corresponding Cu and S EDS elemental maps taken from a section of Cu surface on the N_2SN-functionalized Ag-Cu electrode. (g), HAADF-STEM image of the Cu surface of N_2SN-functionalized Ag-Cu. (h) (top), Electron energy loss spectroscopy (EELS) elemental mapping of C taken from the area marked by the box in (g). (h) (bottom), EELS spectrum of the C-K edge with fine structures characteristics of carbon linked to heteroatoms from N_2SN layer on the Cu surface. (i), Raman spectra of pristine (non-functionalized) Ag-Cu (gray), C_3-functionalized Ag-Cu (orange), C_2N-functionalized Ag-Cu (green), N_3N-functionalized Ag-Cu (purple) and N_2SN-functionalized Ag-Cu (blue).

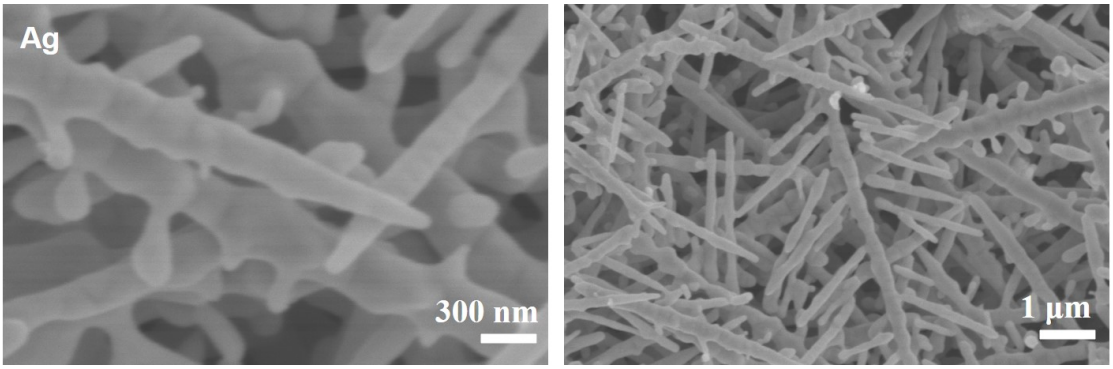

Fig. 2 SEM images of pure Ag.

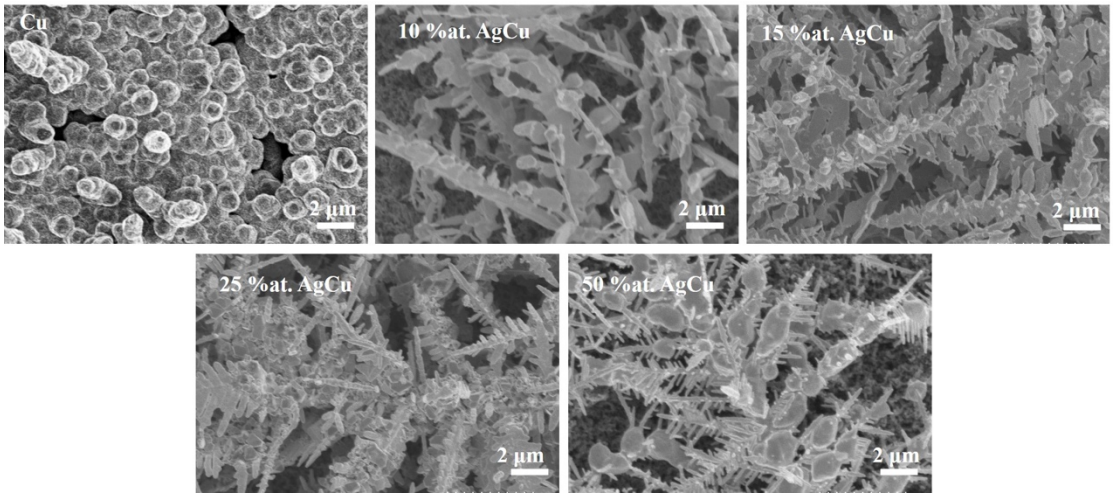

Fig. 3 SEM images of the Ag-Cu electrodes with different Ag atomic ratios. SEM images of different atomic ratios of Ag in Ag-Cu electrodes (0%at., 10 %at., 15 %at., 25 %at. and 50 %at.).

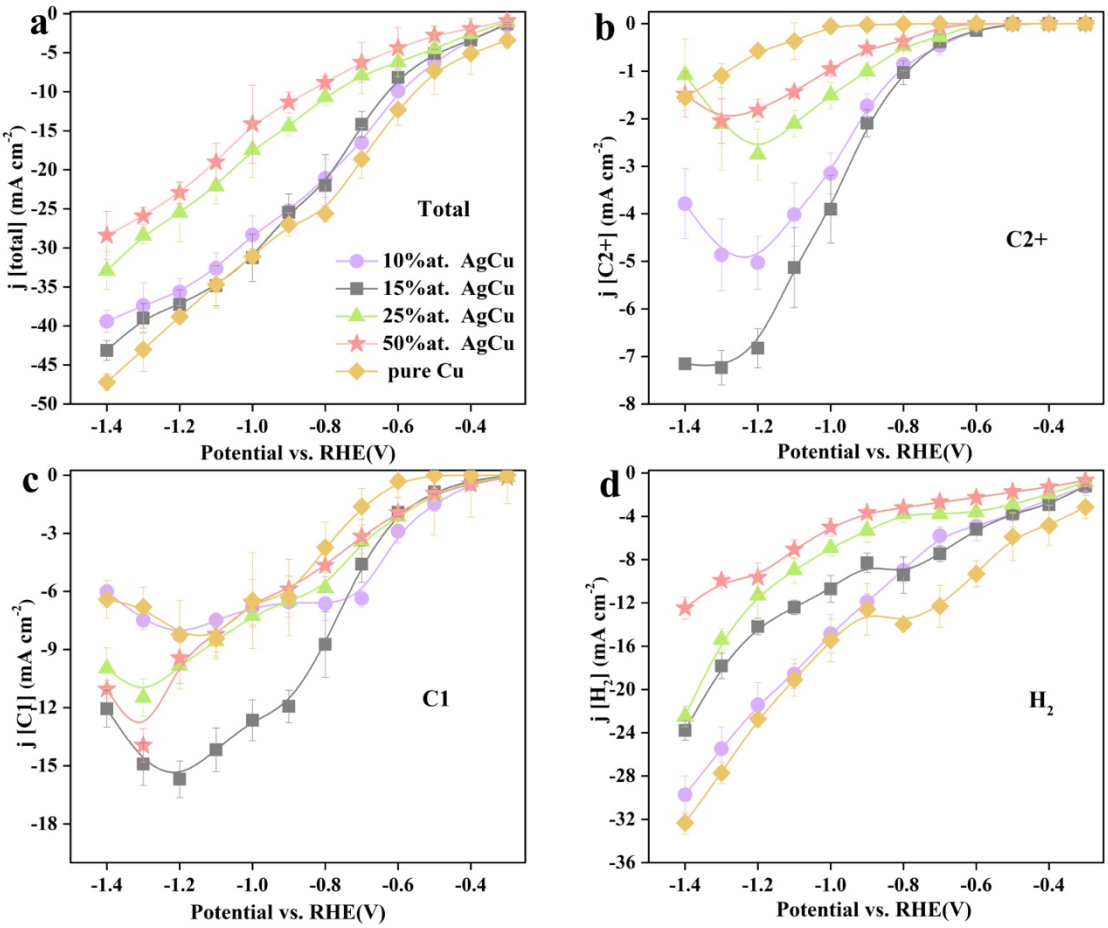

Fig. 4 Comparisons of the current density on the different catalysts measured in the H-cell reactors. The current density for the different Ag atomic ratios in Ag-Cu catalysts (0%at. AgCu, 10%at. AgCu, 15%at. AgCu, 25%at. AgCu, and 50%at. AgCu).

To control the oxidation state of Cu, we sought to functionalize the catalyst with thiol molecules *via* dip coating. We selected thiadiazole (N_2SN) and triazole (N_3N) derivatives as electron deficient functional molecules to react with the surface of the catalyst[41-44](Fig. 5). For comparison, the bimetallic electrodes were also modified with 1-propanethiol (C_3) and cysteamine (C_2N) as model short alkyl and alkyl amine functional groups (Figs. 5 and 6).

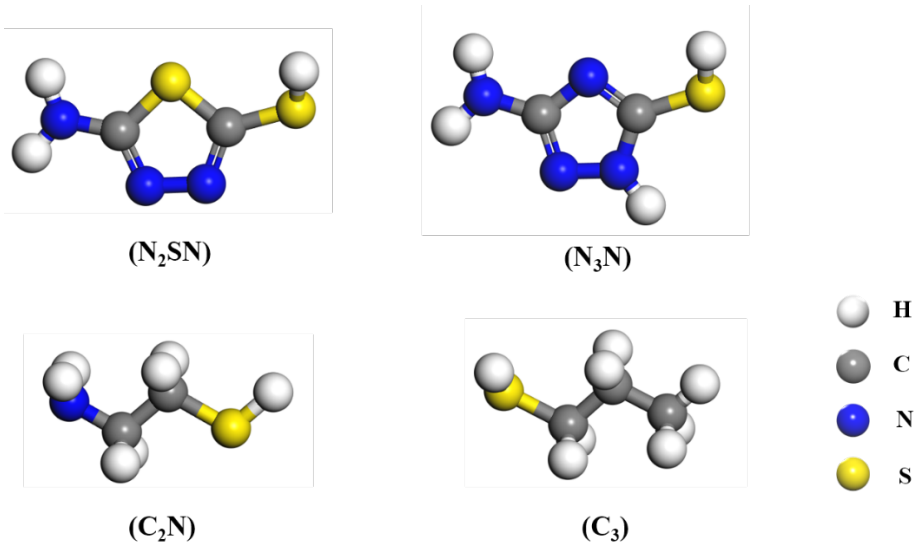

Fig. 5 Molecular structures of the different molecules used for the functionalization of Ag-Cu.

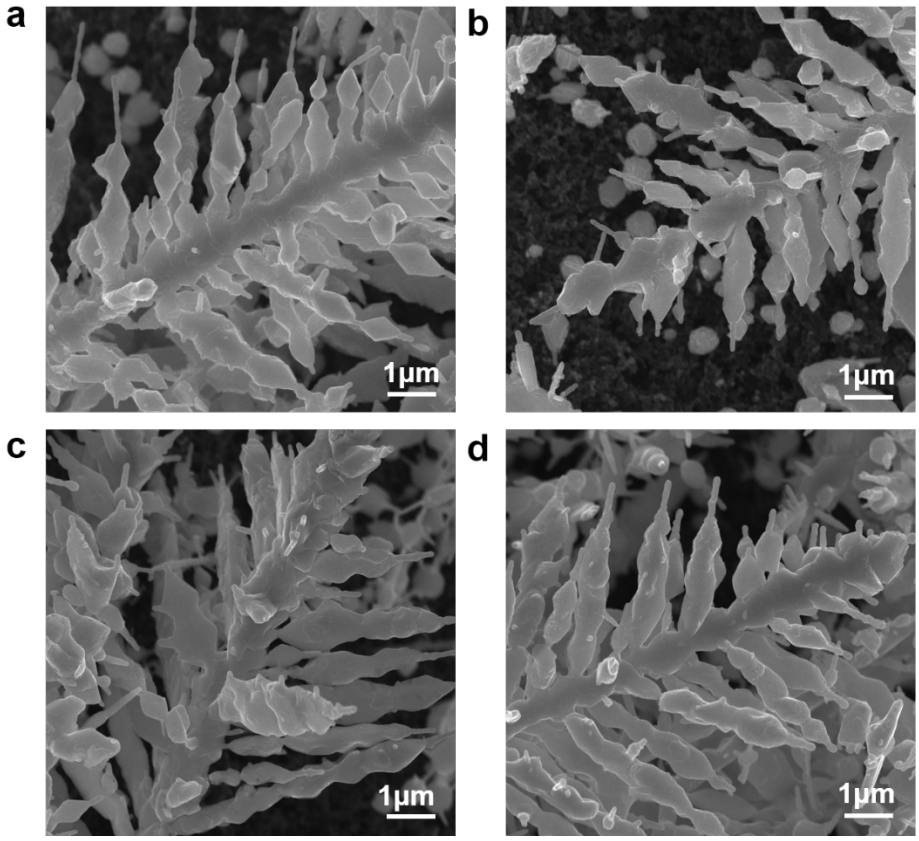

Fig. 6 SEM figures for the pristine and functionalized Ag-Cu. SEM figures of different functional groups modified 15 %at. Ag-Cu electrodes: P (a), (b) N_3N, (c) C_2N and (d) C_3.

The modification of the electrode is clearly visible from the change of the water contact angle that varies between 86° and 129° depending on the nature of the functional groups compared to 84° for the pristine catalyst (Fig. 7). To verify the presence of the functional groups, we performed energy-dispersive X-ray spectroscopy (EDS). The corresponding elemental map shows the uniform distribution of S, N and C on Ag-Cu electrode whereas a thin amorphous layer is observed under high resolution TEM on the surface of the catalyst with a thickness of ≈ 2.5 nm (Figs. 1d, e, f and Fig. 8). The existence of an organic layer on the Ag-Cu electrodes is further confirmed by the high-angle annular dark-field scanning transmission electron microscopy (HAADF-STEM) and the electron energy loss spectroscopy (EELS) mapping of the carbon and sulfur elements. Remarkably, the EELS spectrum of the C-K edge displays fine structures characteristics of carbon linked to heteroatoms at ≈ 292 eV (Figs. 1 g and h, Fig. 9). Raman and Fourier transformed infrared (FTIR) spectroscopies were also used to further confirm the successful attachment of the functional groups on the surface of the catalyst (Fig. 1i and Fig. 10). The Raman signatures of the different grated molecules were detected on the surface of the Ag-Cu electrodes, while strong FTIR bands at 1303 cm^{-1}, 1584 cm^{-1} and 1622 cm^{-1} are only presented on N_2SN-, N_3N- and C_2N-functionalized Ag-Cu electrodes and attributed to the C-C or C-N stretching, the NH_2 scissor and

the C-N stretching modes respectively[45-47] (Fig. 10). The successful functionalization with thiadiazole and triazole is further confirmed from the deconvolution of the X-ray photoelectron spectra from the S2p and N1s regions respectively (Figs. 11b and c). The peak of S2p was deconvoluted into three doublets at 162.75, 164.23 and 168.31eV for the $S2p_{3/2}$, corresponding to S-H and S-C bonds on both thiadiazole and triazole, respectively[48] Analogously, the N1s spectrum (Fig. 11c) can be divided into three components at 398.24, 399.63 and 400.70 eV, which reflects the existence of N-N, C-N, and N-H bonds on the surface of functionalized electrodes. The presence of crystalline Ag and Cu on the gas diffusion electrode was further observed from the X-ray diffraction patterns, whereas the presence of distinct peaks from the Ag and Cu facets agrees with the absence of alloy structure of the bimetallic catalyst. (Fig. 12). To clarify the orientation of the aromatic heterocycles on the catalyst surface, we carried out density functional theory (DFT) calculations to estimate the total energy and the binding energy of thiadiazole on Cu using a model with 5 Cu (111) slabs (Figs. 13 and 14). Among the different configurations tested, the adsorption of thiadiazole is more stable when the N_2-N_3 nitrogen atoms of the diazole sit on Cu (111) and the binding energy is estimated to -1.08 eV – at least 0.37 eV lower than for the other configurations (Table 1).

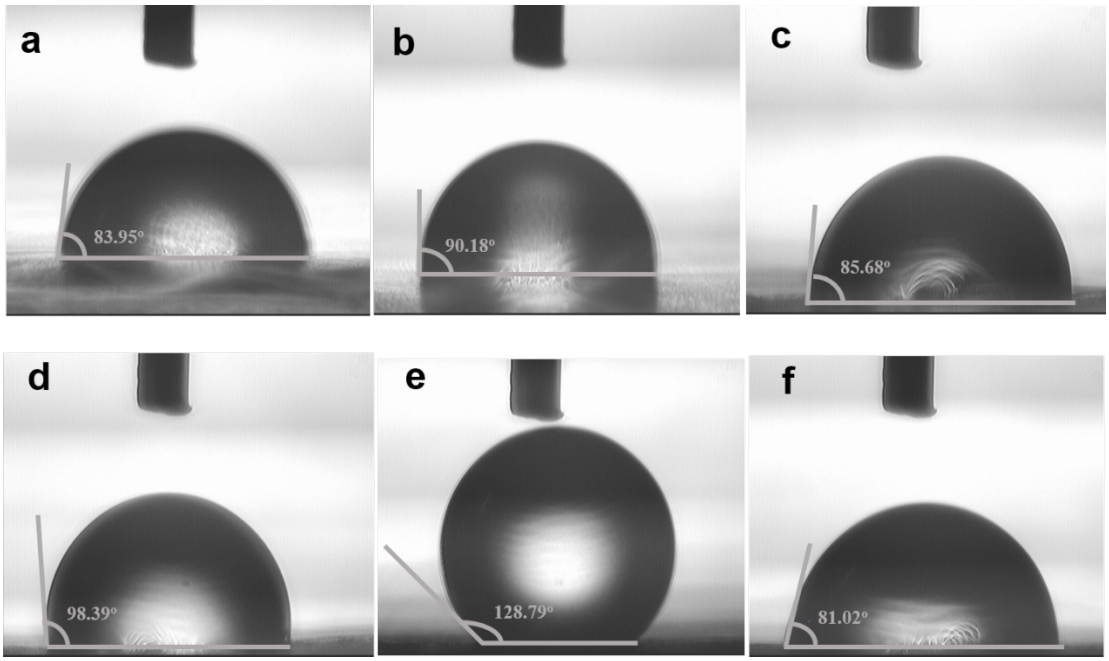

Fig. 7 Wettability of the pristine and functionalized Ag-Cu electrodes. The water contact angles measured for 15 %at. Ag-Cu: P (a), N_2SN (b), N_3N (c), C_2N (d), C_3 (e) and N_2SS (f) before CO_2RR.

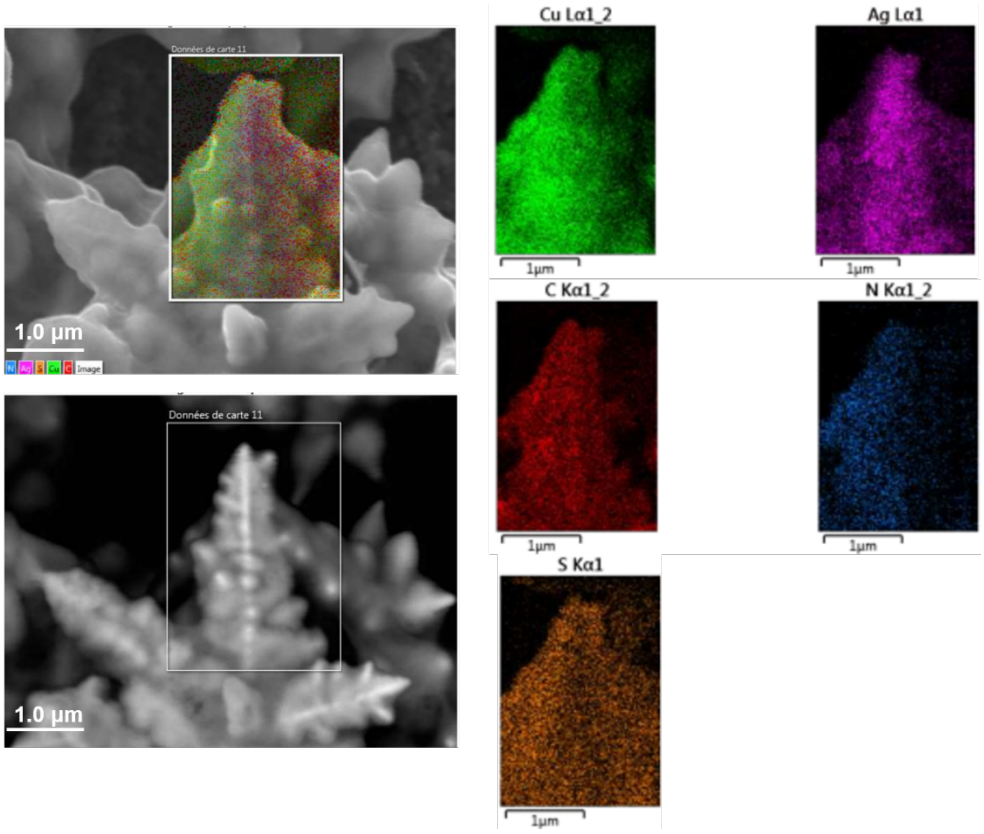

Fig. 8 Structural and compositional analyses of the 15 %at. Ag-Cu-N_2SN catalyst. Low magnification SEM images (top left panel) and the related EDX elemental mapping of Cu, Ag, C, N, and S (right panels).

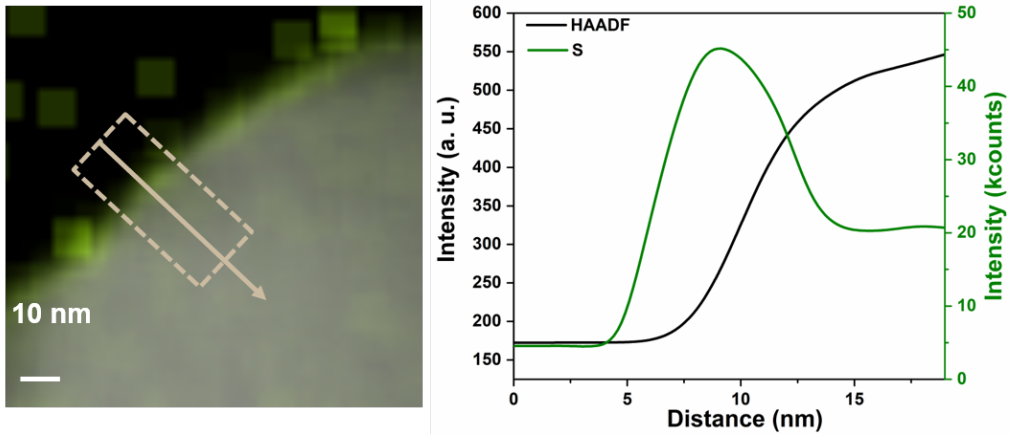

Fig. 9 HAADF-STEM data of N_2SN-functionalized Ag-Cu catalyst. Right panel: The superposition of the HAADF-STEM image of the N_2SN functionalized Ag-Cu ultrathin section with the sulfur (S) EDS elemental map. The arrow highlights the area used to extract the intensity profiles. Left panel: The corresponding intensity profiles of the HAADF-STEM images and S elemental map.

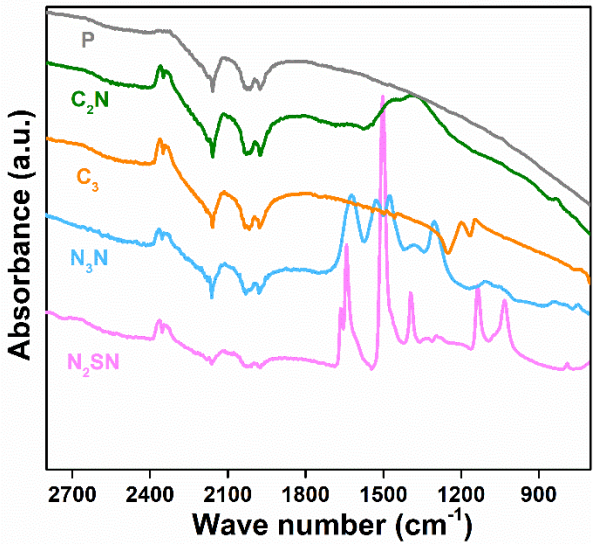

Fig. 10 Fourier transformed infrared (FTIR) spectra of the pristine functional groups. The ATR-FTIR spectra of pristine (non-functionalized) 15 %at. Ag-Cu (gray), 15 %at. Ag-Cu-N_2SN (purple), 15 %at. Ag-Cu-N_3N (blue), 15 % at. Ag-Cu-C_2N (green) and 15 %at. Ag-Cu-C_3 (orange) before CO_2RR.

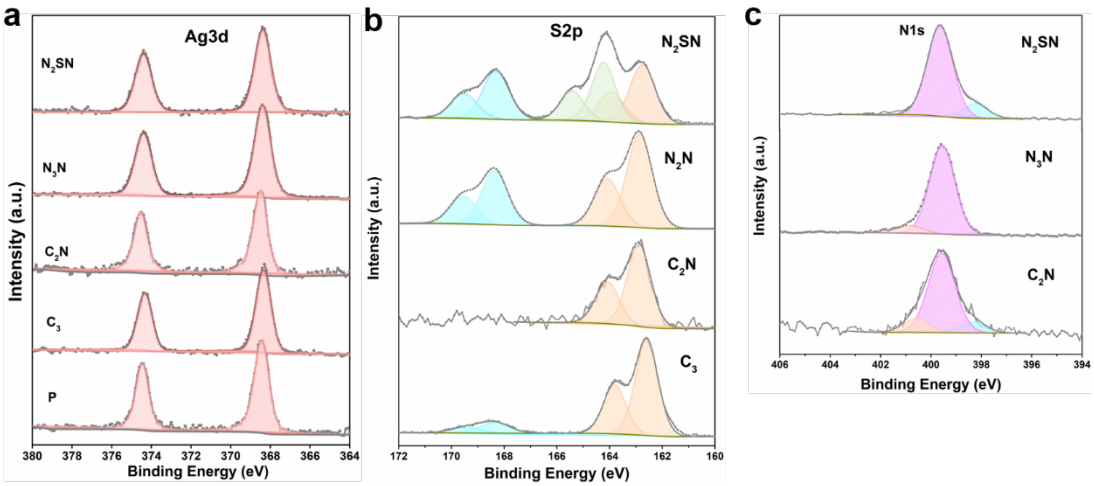

Fig. 11 X-ray photoelectron spectra (XPS) spectra of the different Ag-Cu catalysts. The high-resolution XPS spectra of the Ag3d (a), S2p (b) and N1s (c) regions of the different functionalized 15 %at. Ag-Cu catalysts before reaction.

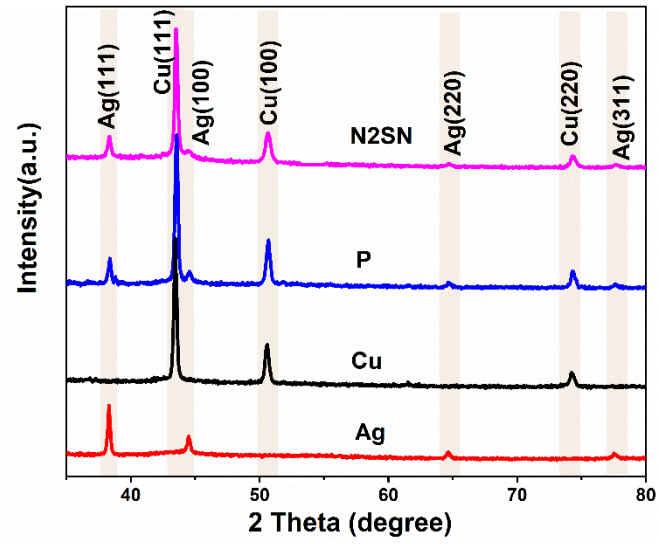

Fig. 12 X-ray diffraction (XRD) data of the different Ag-Cu catalysts. Powder XRD spectra of 15 %at. Ag-Cu and 15 %at. Ag-Cu-N_2SN compared with Cu, Ag metals used as references.

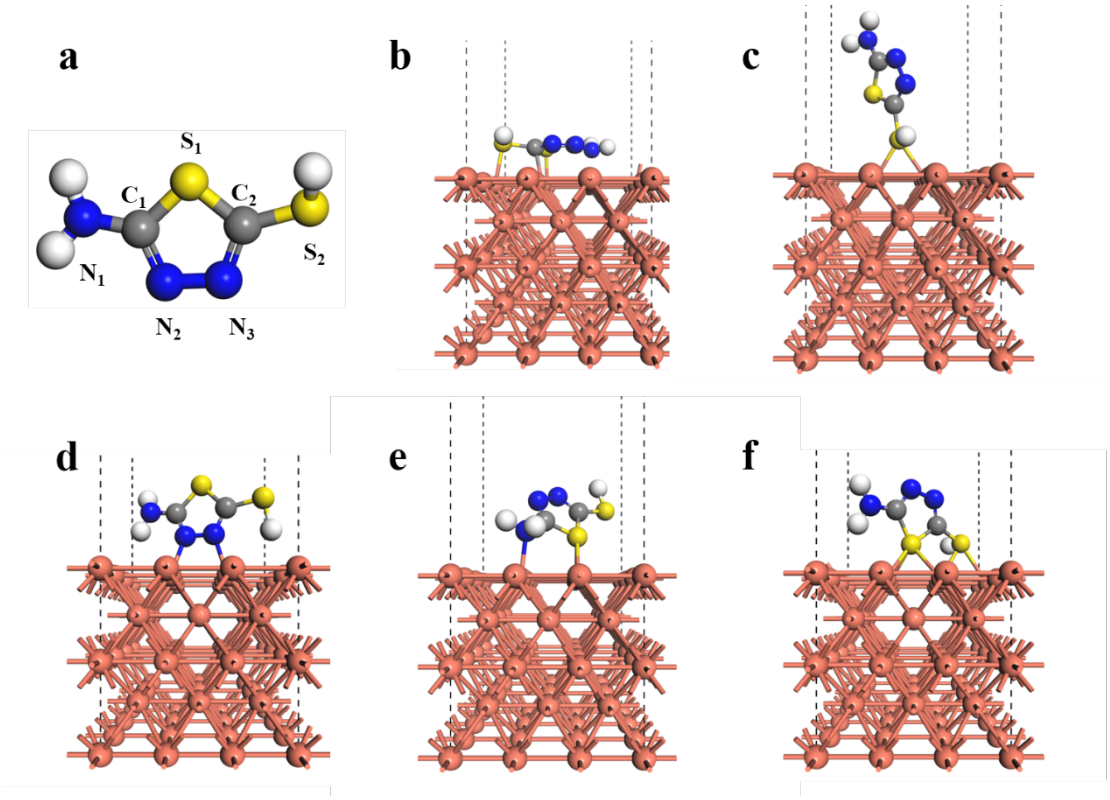

Fig. 13 Schematic representations of the different configurations of N_2SN on Cu (side view). Molecular structure of N2SN (a), S1-C2-S2 flat model (b), S1 model (c), N2-N3 model (d), N1-S1 model (e) and S1-S2 model (f).

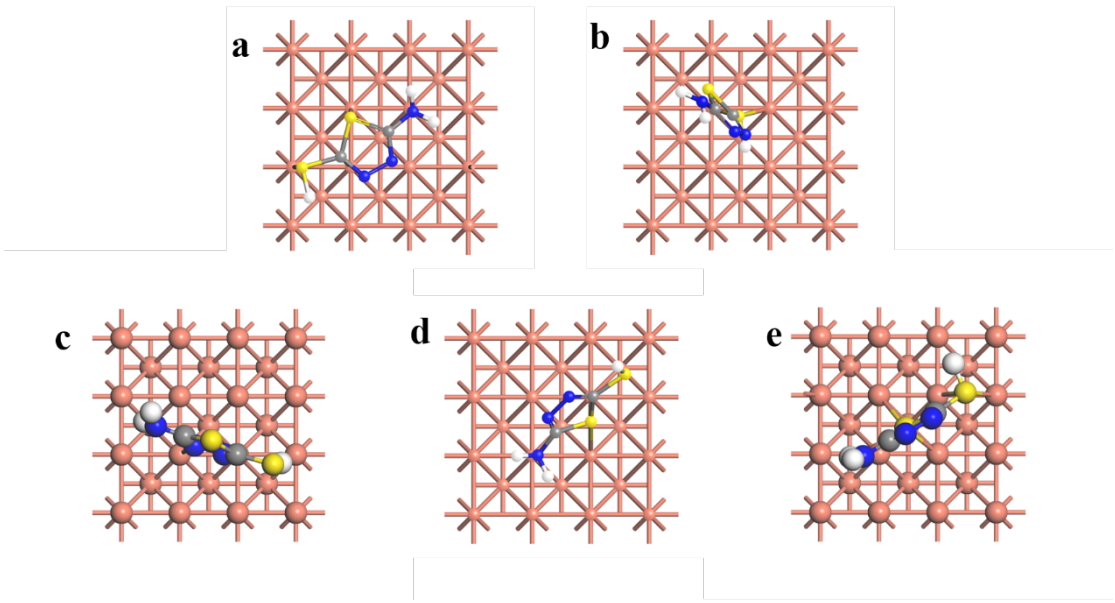

Fig. 14 The different configurations of N_2SN on Cu (top view) used for the calculation results summarized in Supplementary Table 1. S1-C2-S2 flat model (a), S1 model (b), N2-N3 model (c), N1-S1 model (d) and S1-S2 model (e).

Table 1 Summary of the total energy and adsorption energy of the different configurations of the thiadiazole-functionalized Cu catalyst. The different configurations are presented in Fig 13.

Configuration	Energy (eV)	Slab (eV)	Functional molecular (eV)	Adsorption energy (eV)
S_1-C_2-S_2	-222.80	-161.30	-60.79	-0.71
S_1	-222.40	-161.30	-60.79	-0.30
N_2-N_3	-223.58	-161.30	-60.79	-1.08
N_1-S_1	-222.53	-161.30	-60.79	-0.44
S_1-S_2	-222.63	-161.30	-60.79	-0.53

3.4.2 Investigation of the CO2 electro-reduction

The functionalized electrodes were electrochemically tested in a H-cell reactor using Argon and CO_2-saturated 0.5 M $KHCO_3$ electrolyte solutions. Fig. 15a shows that thiadiazole (N_2SN) and triazole (N_3N) functionalized electrodes exhibit the highest current density and lowest onset potential in CO_2-saturated solution. We then evaluated the Faradaic efficiency (FE) by using nuclear magnetic resonance (NMR) and gas chromatography (GC) (See details in the Methods section). H_2, CO, formate, CH_4 and C_{2+} products were formed on the bimetallic electrode (Fig. 16). Remarkably, the Faradaic efficiency for C_1 and H_2 – obtained *via* the CO_2RR and HER – decreased after functionalization with thiazole and thiadiazole, while the FE for C_{2+} products sharply increases (Fig. 15b). Ethylene and ethanol are the major C_{2+} products detected, together with trace amount of acetate and n-propanol (Fig. 16). The FE for C_{2+} on N_2SN- and N_3N-functionalized electrodes are estimated to 57.3 % and 51.0% at -1.2 V versus the reversible hydrogen electrode (*vs.* RHE) compared to only 18% for the pristine catalyst

corresponding to enhancements of 3.1 and 2.8 folds respectively (Fig. 15b). The selectivity towards the formation of C_{2+} products for both thiazole and thiadiazole functional groups increases continuously with increasing voltage from -0.3 to -1.2 V *vs.* RHE and starts decreasing after -1.3 V, whereas the values of FE for C_1 products and H_2 exhibit a volcano-shaped dependence with the applied potentials (Figs. 17a and b). This leads to an obvious enhancement of the specific current density for C_{2+} products ($j_{C_{2+}}$) up to 5 folds at -1.2 V *vs.* RHE (Fig. 15c). Conversely, the functionalization of the Ag-Cu electrodes with short alkyl or amino alkyl chains does not suppress the HER pathway nor improve the CO2RR activity (Fig. 15d). C_2N- and C_3- modified catalysts clearly display lower activities towards the CO2RR, notably with a minimal production of C_{2+} species and a relatively large FE for the evolution of H_2. Our results therefore highlight the importance of the nature of the functional groups on the CO_2RR performance. To better evaluate the selectivity of C_{2+} products on thiadiazole- and triazole-functionalized Ag-Cu electrodes, we calculated the ratio in FE for C_{2+} products and hydrogen ($FE_{C_{2+}}/FE_{H_2}$) (Fig. 15e). Compared with pristine and alkyl functionalized electrodes, both N_2SN and N_3N functional groups present the largest $FE_{C_{2+}}/FE_{H_2}$ ratios – illustrating that the functionalization with aromatic heterocycles efficiently directs the reaction pathway towards the formation of C_{2+} products while suppressing the HER. To get a more accurate estimation of the intrinsic CO2RR performance of the functionalized Ag-Cu electrodes, we estimated the electrochemically active surface area of Cu (Cu ECSA) and Ag (Ag ECSA) in 15at.% Ag-Cu and N_2SN-15at.% Ag-Cu catalysts using Pb underpotential deposition (Pb UPD) (Figs. 18 and 19, and Table 2). The partial current densities for C_{2+} products measured in H-cell were normalized by the ECSA values for Cu. Remarkably, we found that the ECSA-normalized partial current density on N_2SN functionalized Ag-Cu is 5.3 mA cm^{-2}, which is around 5 times larger than that for pristine 15at.% Ag-Cu (Fig. 19). Electrochemical impedance spectroscopy (EIS) measurements were performed to explore the charge transfer processes on the surface of the different electrodes during the electrolysis of CO_2. The charge transfer resistance of the N_2SN- and N_3N- functionalized electrodes is not substantially perturbed compared to that of the pristine bimetallic catalyst (Fig. 20). On the contrary, the resistance is significantly larger in the case of electrodes functionalized with 1-propanthiol and cysteamine indicating that the charge transfer is strongly affected; likely due to the strong hydrophobicity of the surface of the alkyl-functionalized catalyst.

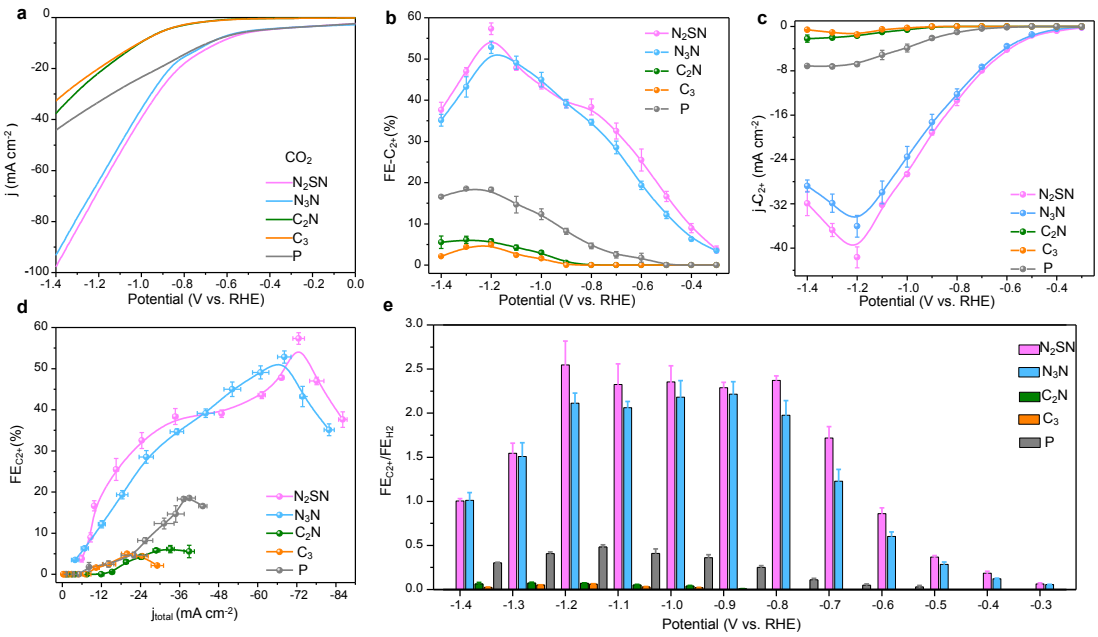

Fig. 15 CO_2RR performance of the functionalized Ag-Cu electrodes in a H-cell. (a), Linear scan voltammetry (LSV) curves measured for different samples: N_2SN, N_3N, C_2N, C_3 functionalized Ag-Cu compared to pristine (P) Ag-Cu in CO_2-saturated 0.5 M $KHCO_3$ at electrochemical potential (V) from 0 to -1.4 V *vs.* RHE. Scan rate, 20 mV s^{-1}. **(b),** Faradaic efficiency (FE) values for C_{2+} products on different samples at various potentials ranging from -0.3 to −1.4 V *vs.* RHE and measured in 0.5 M $KHCO_3$. **(c),** *j*–V plots of the partial current densities for the C_{2+} products (ethylene and ethanol). **(d),** Relationships between the FE for C_{2+} and the total current density for all the catalysts **(e),** Selectivity for C_{2+} products over hydrogen based on the ratio in FEs of C_{2+} and hydrogen. The error bars in **b–e** correspond to the standard deviation of three independent measurements.

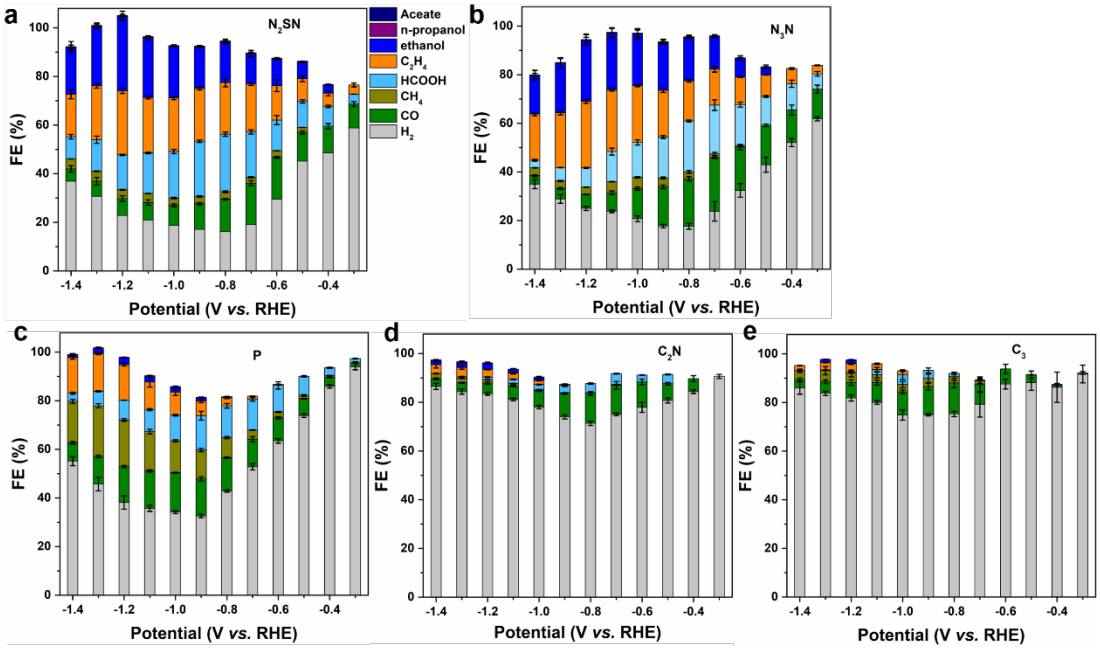

Fig. 16 Comparisons of the Faradaic efficiencies on the different catalysts measured in the H-cell reactors. The Faradaic efficiency for the different products on N_2SN-(a), N_3N-(b), C_2N-(d) and C_3-(e) Ag-Cu electrodes, as well as pristine sample (c).

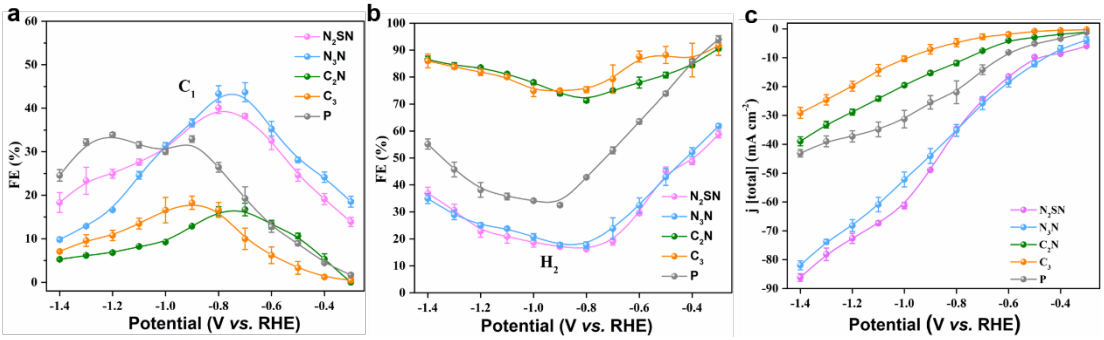

Fig. 17 CO_2RR performance in the H-cell reactors. a, b FE values for C_1 products (a) and H_2 (b) on the different catalysts at various potentials ranging from -0.3 to −1.4 V vs. RHE in 0.5 M $KHCO_3$. c, j–V plots of the total current densities versus the RHE on different samples in 0.5 M $KHCO_3$.

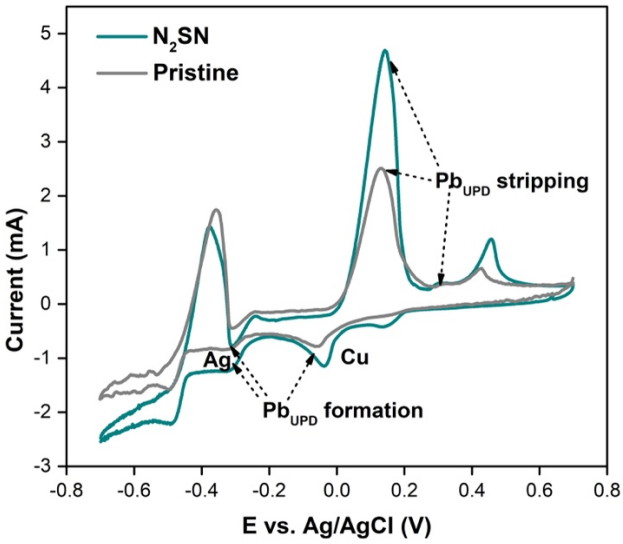

Fig. 18 CVs for different samples measured in 100 mM $HClO_4$ + 1 mM $Pb(ClO_4)_2$.

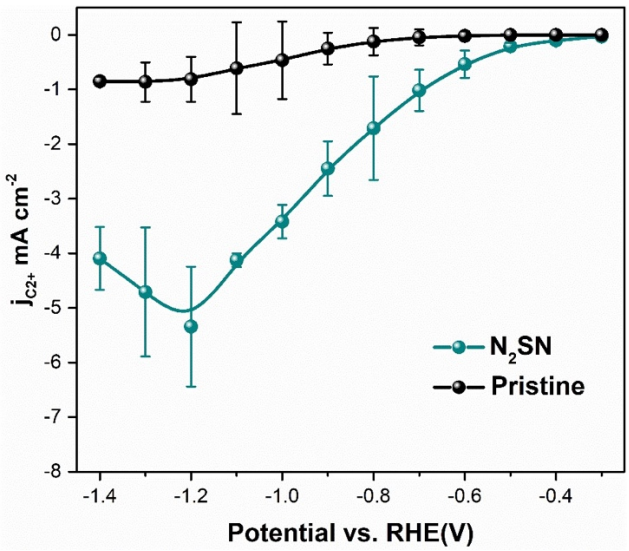

Fig. 19 Partial C_{2+} products current density normalized to Cu ECSA for 15at.% Ag-Cu and N2SN-15at.% Ag-Cu catalysts versus potential for CO_2RR in H-cell.

Table 2. Summary of the XPS data for N_2SN-functionalized Ag-Cu at different reaction times. The atomic ratio N/Cu refers to the functionalization degree per Cu atom.

	Cu (at.%)	N (at.%)	Ratios of N/Cu
Before	9.98	6.28	0.63
0.5 h	12.97	8.43	0.65
1 h	9.89	6.03	0.61
24 h	18.53	10.56	0.57
100 h	15.10	8.91	0.59

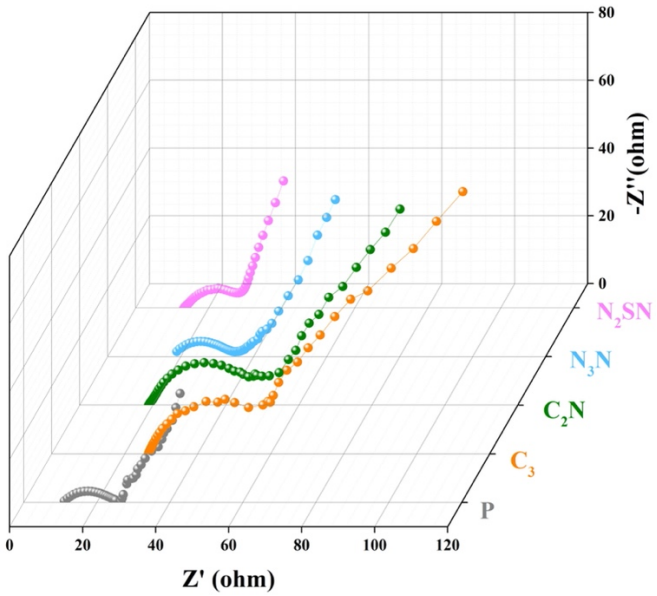

Fig. 20 Electrochemical impedance spectroscopy (EIS) measured for the different Ag-Cu catalysts. The EIS spectra measured in the H-cell configuration for pristine (non-functionalized) 15 %at. Ag-Cu (gray), 15 %at. Ag-Cu-N_2SN (purple), 15 %at. Ag-Cu-N_3N (blue), 15 % at. Ag-Cu-C_2N (green) and 15 % at. Ag-Cu-C_3 (orange). The EIS data were recorded in CO_2-saturated 0.5 M $KHCO_3$ solution.

To gauge the stability of the functionalization, we operated the electrodes at a potential of -1.2 V *vs.* RHE for more than 20 hours in the H-cell reactor, while recording the current density and continuously analyzing the products of the reaction (Fig. 21). The N_2SN- and N_3N-functionalized electrodes demonstrated stable performance with a retention of the current density of 94% and 91% respectively – sharply improved compared to that of pristine Ag-Cu at 78%. The FE for C_{2+} of N_2SN and N_3N functionalized Ag-Cu electrodes remains as high as 54% and 46.5% after 20 hours, which demonstrate that the selectivity for the reaction pathway on the

surface of the electrode is not modified during electrolysis. To further confirm the apparent stability of the functionalized electrode, we performed XPS spectroscopy to evaluate the N:Cu ratio after 30 min, 1 hour, 24 hours and 100 hours. The ratio is found to be virtually constant suggesting a robust grafting of the functional groups on the catalyst surface (Figs. 22 and 23, Table 3).

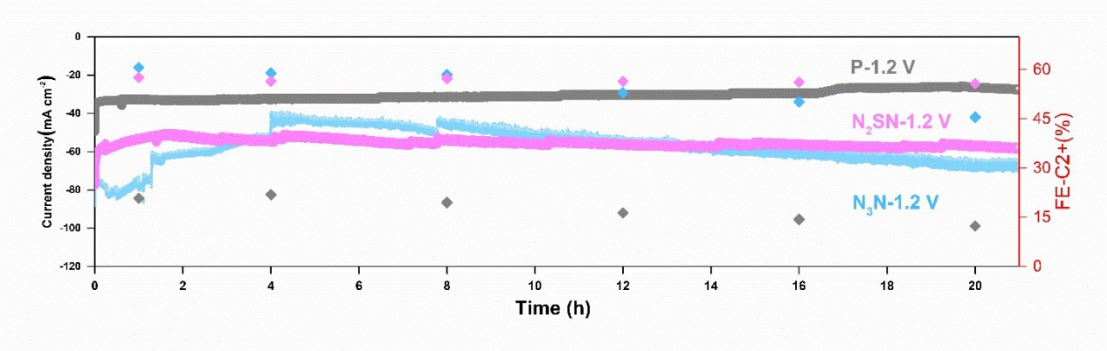

Fig. 21 Stability measurements of N_2SN-, N_3N- functionalized Ag-Cu compared with pristine Ag-Cu measured in the H-cell reactors. The stability of Ag-Cu-N_2SN, Ag-Cu-N_3N and Ag-Cu were obtained at -1.2 V vs. RHE without iR correction.

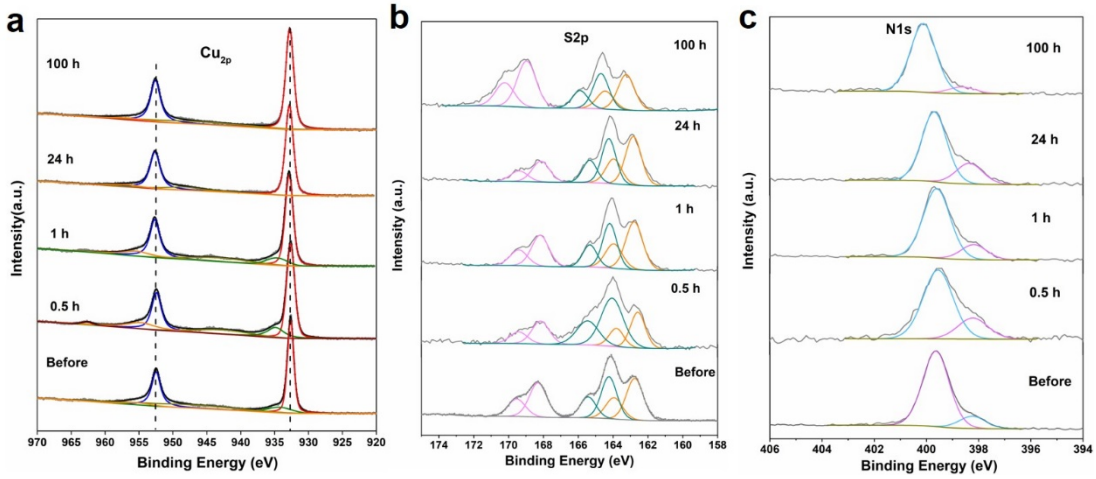

Fig. 22 X-ray photoelectron spectra of N_2SN before and after CO_2RR. The XPS data from the Cu2p (a), S2p (b) and N1s (c) regions were measured before and after operation up to 100 h at -1.2 V vs. RHE.

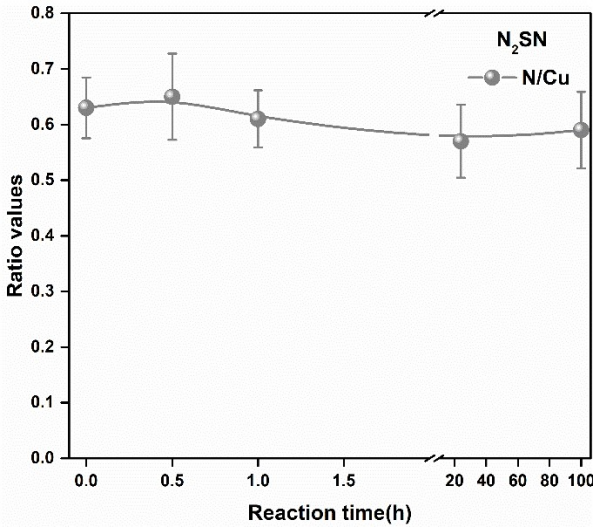

Fig. 23 Estimated atomic N/Cu ratio of the N_2SN-Ag-Cu electrodes along the CO_2RR operating time. The atomic N/Cu ratio of Ag-Cu-N_2SN were estimated from the deconvoluted XPS spectra shown in Fig. 19.

Table 3. Summary of the Cu binding energy from the Auger $L_3M_{45}M_{45}$ transition modes for pristine, N_2SN-, N_3N-, C_2N-, C_3-functionalized Ag-Cu samples and H_2O_2-oxidized Ag-Cu.

Samples	^1G (eV)	^3F (eV)
Ag-Cu(P)	918.3	921.0
N_2SN	915.8	918.4
N_3N	916.0	918.7
C2N	915.9	918.2
C_3	915.9	918.2
H_2O_2-Ag-Cu	917.5	——

3.4.3 XAS and in-situ Raman analysis

Next, we sought to explain the fundamental mechanism responsible for the improved CO_2RR properties using *ex-situ* X-ray photoelectron spectroscopy (XPS) and *operando* XAS. XPS was firstly used to characterize the surface composition and determine the oxidation state of Cu. From the Cu2p region, no significant change of the oxidation state of Cu can be detected from the functionalized catalysts (Fig. 24a left). For comparison, after exposure to H_2O_2, the electrodes are clearly oxidized as confirmed by the apparition of $Cu2p_{3/2}$ signals at binding energy at 934.6 eV and the satellite peak at 942.6 eV, which is attributed to the formation of Cu^{2+} [48]. Our XPS results confirm that functionalization does not lead to a dramatic modification of the oxidation state of the surface of the Cu since there were no evident oxidation peaks in Cu2p. It is well-known that the small change of binding energy between Cu^{1+} and Cu^0 makes the precise identification of Cu^{1+} impossible from the Cu2p regions[10]. To overcome this limitation, we therefore used the Cu Auger $L_3M_{45}M_{45}$ transition to qualitatively discuss the presence of Cu^{1+} in functionalized Ag-Cu as this mode is known to be more sensitive to the modification of the

electron density on the d-band of the metals[49, 50]. The Cu Auger $L_3M_{45}M_{45}$ transition arises from a single L_3 (2p3/2) core-hole decay *via* the Auger process involving two M_{45} (3d) electrons for the formation of a final $3d^8$ configuration[51-54]. The right panel of Fig. 24a presents the two final-state terms splitting from L–S coupling ^1G and ^3F, whose peak energy positions provide information on the valence configuration of Cu[22,51]. According to the previous investigations, the peak energy positions of ^1G for the different oxidation states copper are detected at 917.1, 915.8, and 918.0 eV for CuO, Cu_2O, and Cu, respectively[51–53]. Such differences are mainly due to the modification of the 3d and O_{2p} electron configurations[54]. Compared with Cu0, the ^1G peak in copper oxide is downshifted in energy and presents a broader shape, while the ^3F peak is solely visible in the case of Cu^0 [22,55]. For pristine and C_3- and C_2N- functionalized Ag-Cu, we observed that the energy positions of the ^1G peak are located at 918.3 eV(pristine), 915.9 eV (C_3 and C_2N), respectively, while the distinct ^3F peak is detected at 918.2 eV for both C_3- and C_2N-Ag-Cu, in agreement with the existence of Cu^0 (Table 4). Conversely, in the case of the N_2SN- and N_3N samples, the ^1G peak is identified at 915.8 and 916.0 eV, respectively, which is lower than that for Cu^0 and Cu^{2+} and close to that of Cu^{1+} (915.8 eV). We also note that the ^3F peak is also visible for both samples pointing out the presence of Cu^0. These results indicate that the valence state of the N_2SN and N_3N samples may be $Cu^{\delta+}$ with $0 < \delta < 1$.

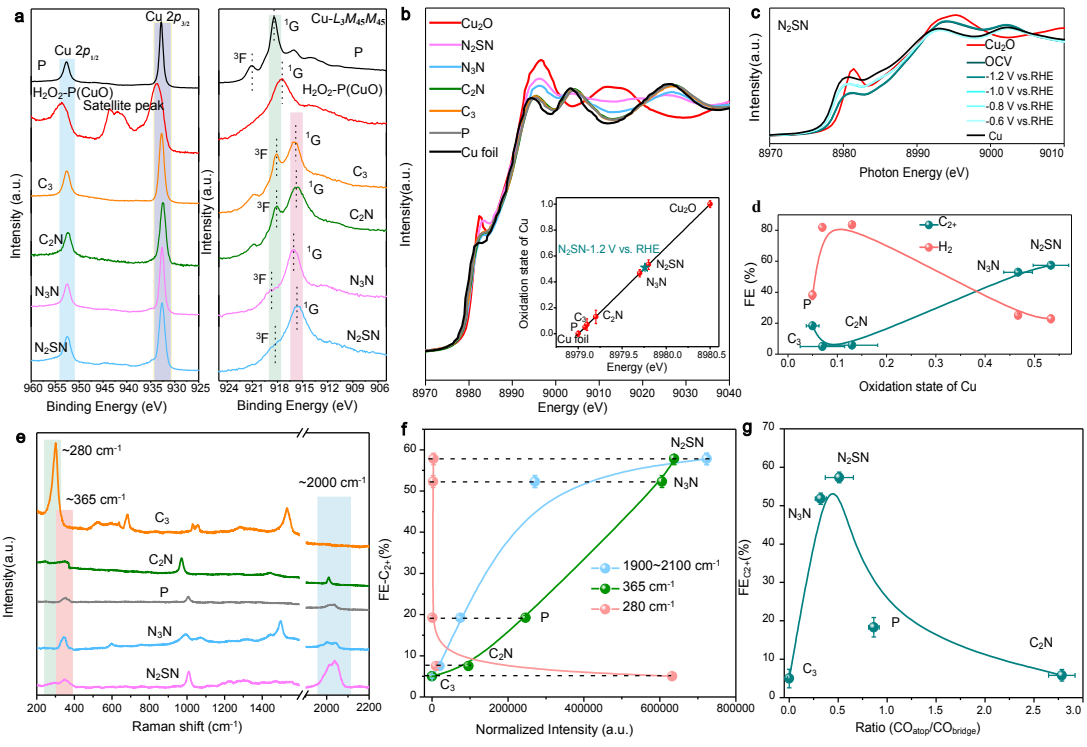

Fig. 24 Physical characterizations of the functionalized electrodes using XPS and *operando* Raman and XAS spectroscopy. (a), High-resolution spectra of the Cu2p regions and Cu $L_3M_{45}M_{45}$ Auger transition modes measured by *ex-situ* X-ray photoelectron spectroscopy (XPS) of pristine Ag-Cu sample (P), H_2O_2-treated Ag-Cu (H_2O_2-P), C_3-, C_2N-, N_3N- and N_2SN-functionalized Ag-Cu electrodes. (b), *Ex-situ* and *operando* Copper K-edge X-ray absorption near edge structure (XANES) spectra of pristine and functionalized Ag-Cu electrodes. Inset: Average oxidation state of copper for the corresponding electrodes. (c), *Operando* Cu K-edge XANES spectra of N_2SN- functionalized Ag-Cu electrode during CO2RR. The

measurements were performed after holding the applied potential for 30 minutes. (d), Evolution of the Faradaic efficiency for C_{2+} and H_2 measured at -1.2 V *vs.* RHE with the oxidation state of Cu. (e), *Operando* Raman spectra for pristine, C_3-, C_2N-, N_3N- and N_2SN-, functionalized Ag-Cu during CO2RR at a fixed potential of -1.2 V *vs.* RHE. The spectra for all the other potentials are presented in Supplementary Fig. 15. (f), Relationship between the FE for C_{2+} products and the Raman peak areas of the frustrated rotational mode of CO at 280 cm^{-1}, the Cu–CO stretch at 365 cm^{-1} and the C≡O stretch at 1900–2120 cm^{-1}, respectively. (g), Relationship between the FE for C_{2+} molecules and the ratio of CO_{atop} and CO_{bridge} on different Ag-Cu electrodes. The ratio was obtained from the integrated areas of the deconvoluted peaks of the Raman spectra (Fig. 29).

Table 4. Summary of the XANES data. E_0 and corresponding oxidation states (δ) of Cu.

Samples	**Cu foil**	**P**	**C_3**	**C_2N**	**N_3N**	**N_2SN**	**Cu_2O**
E_0	8979	8979.08	8979.1	8979.2	8979.7	8979.8	8980.5
δ	0	+0.05	+0.07	+0.13	+0.47	+0.53	+1

To precisely evaluate the electronic states of copper on functionalized Ag-Cu electrodes and eliminate the air effect on the electrode, we then performed *in-situ* X-ray absorption near-edge spectroscopy (XANES). The absorption edges of functionalized catalysts reside between those of copper metal (Cu^0) and Cu_2O (Cu^{1+}) used as references (Fig. 24b). To better compare the influence of the different functional groups, we estimated the copper oxidation state as a function of copper K-edge energy shift (Fig. 24b). The oxidation state of copper in the N_2SN- and N_3N- functionalized Ag-Cu was found to be +0.53 and +0.47 respectively – pointing out the withdrawing properties of the selected heterocycles (Table 5). Remarkably, C_3- and C_2N- functionalized samples displayed a minimal shift by comparing with pristine Ag-Cu electrode and the Cu reference, suggesting the alkyl groups are not prone to modulate the oxidation state nor the coordination environment of Cu. To explore the stability of electron-withdrawing ability of the grafted heterocycles, we measured the oxidation state of Cu *post* CO2RR using *in-situ* XANES. After 30 min of operation at -1.2 V *vs.* RHE in the testing cell, the oxidation state of copper was estimated be + 0.51 (Inset Figs. 24b and c). This value is similar to that obtained from the freshly prepared samples: +0.53, which demonstrates the stability of the oxidation state of the functionalized Ag-Cu electrodes. Similarly, no obvious shift of the Cu K-edge was observed from the *in-situ* XANES measurements at increasing applied potential up to -1.2 V vs. RHE and the spectra virtually overlap. This confirms the robustness of the oxidation state of the Cu thanks to the stable attachment of the functional groups (Fig. 24c, and Fig. 25). To better understand the role of $Cu^{\delta+}$ on the CO2RR properties, we investigated the influence of the copper oxidation state on the FE for C_{2+} and H_2 (Fig. 24d). Remarkably, we identified a strong correlation between the oxidation state and the FE for C_{2+}, which points out that the larger oxidation state of Cu benefits the CO_2RR properties and the formation of C_{2+} products in line with recent findings from the literature[51, 56]. To finally exclude any hydrophobicity effect on the enhanced selectivity for formation of C_{2+} products, we sought to prepare

functionalized electrodes with similar water contact angles as for pristine Cu counterpart. We identified 1,3,4-thiadiazole-2,5-dithiol, N_2SS that shares the same thiadiazole structure, exhibits a water contact angle of 81° compared to 83.9° for pristine non-functionalized Cu. In H-cell configuration, the Faradaic efficiency for the formation of C_{2+} molecules on N_2SS-Ag-Cu reaches 43.7% at -1.2 V vs. RHE compared to only 18.3% for Ag-Cu (Fig. 26). To further demonstrate that the water contact angle has limited influence on the improved C_{2+} selectivity, we plotted the Faradaic efficiency as function of the water contact angle. No relationship is clearly observed, emphasizing that the origin of the improved selectivity for C_{2+} is not primarily due to the surface properties of the Cu electrodes but rather the electron withdrawing nature of the aromatic heterocycles as evidenced by our operando X-ray absorption spectroscopy measurements (Figs 7, 26 and 27).

Table 5 Estimated ratios (in peak area) between the atop CO and the bridge CO obtained from the deconvoluted spectra. The data represents the average values obtained from two independent sets of samples.

Electrode	Ratio (atop/bridge)
N_2SN	0.51
N_3N	0.32
C_2N	2.78
C_3	0

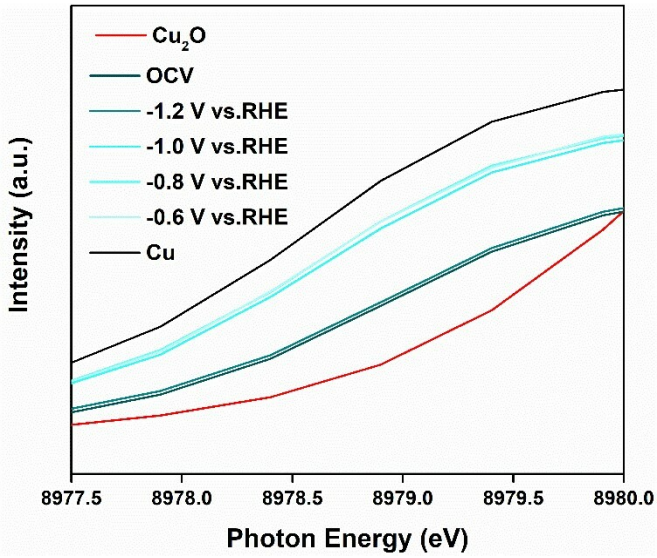

Fig. 25 Cu K-edge X-ray absorption near edge structure (XANES) spectra of the different Ag-Cu catalysts. Magnification of the operando Cu K-edge XANES spectra of N_2SN-functionalized Ag-Cu electrode during CO_2RR. The operando XANES measurements were performed after applying a fixed potential vs. RHE for 30 minutes.

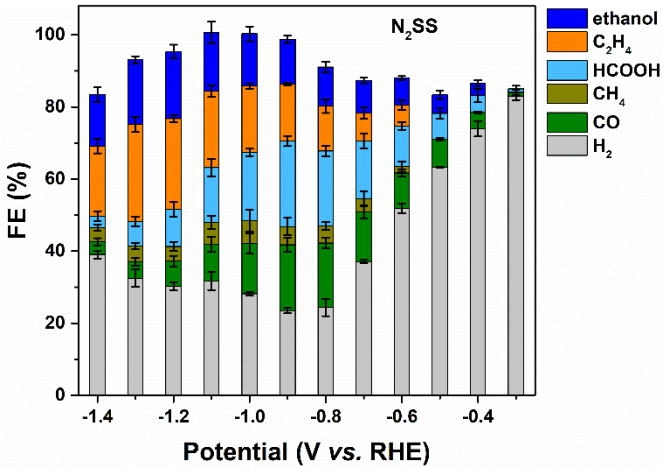

Fig. 26 The Faradaic efficiency for the different products on N2SS functionalized 15at.% Ag-Cu catalyst.

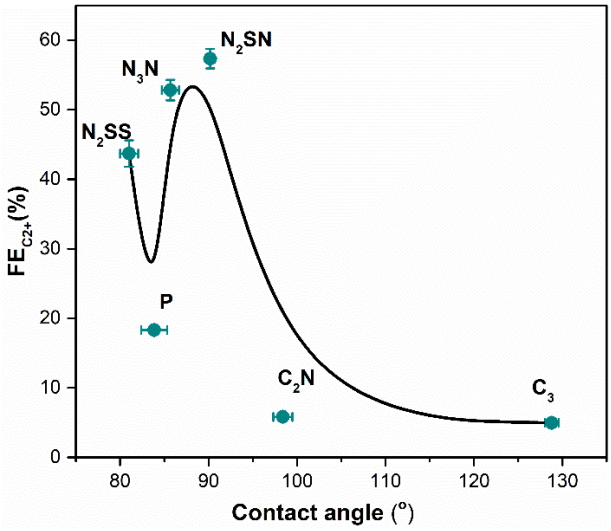

Fig. 27 The relationship between water contact angle and Faradaic efficiency of C_{2+} products in H-cell for 15at.% Ag-Cu(P), N_2SN, N_3N, C_2N, C_3 and N_2SS.

It is well known that the formation of multi-carbon products in CO_2RR proceeds *via* the formation of the *CO intermediate, and its subsequent dimerization in CO=CO or *CO-COH intermediates[57-59]. To gain insight into the C–C coupling mechanism on functionalized and pristine Ag-Cu during CO_2RR, the surface of the catalysts was probed using *operando* Raman spectroscopy in order to ellucidate the interactions between the catalyst surface and the adsorbed *CO intermediate (Fig. 24e and Fig. 28, and Table 7). The presence of the surface-absorbed *CO was identified from the vibration modes at ≈ 280 cm^{-1} and ≈ 365 cm^{-1} that originate from the Cu–CO frustrated rotation and Cu–CO stretch, respectively[60, 61]. The broad band in the range of 1900–2120 cm^{-1} was assigned to the C≡O stretch. To confirm that the detected signals are solely due to the CO_2RR, the Raman spectra were also recorded using Ar-saturated K_2SO_4 as a controlled experiment and no peaks were detected at these frequencies (Fig. 28f). The Raman vibration modes around 1900–2120 cm^{-1} have recently been the focus of several studies and there is currently a general agreement that the high frequency region (>2000 cm^{-1}) and the low frequency region (1900–2000 cm^{-1}) originates to atop-bound CO and bridge-bound CO. Atop (CO_{top}) and

bridge (CO_{bridge}) configurations correspond to a CO bound on top of one Cu atom and between two Cu atoms respectively[50, 62, 63]. Compared to pristine as well as 1-propanthiol- and cysteamine-functionalized electrodes, N_2SN- and N_3N-functionalized Ag-Cu exhibit the relatively intense signals at 365 cm^{-1} and 1900–2000 cm^{-1}. Our systematic investigations revealed that the intensities of both regions are also found to increase with the overpotentials[32] (Figs. 28a and b). Importantly, we observed that there is an obvious relationship between the peaks at 365 cm^{-1} and 1900-2100 cm^{-1} and the Faradaic efficiency towards the formation of C_{2+} products (Fig. 24f) by following literatures to fit these peaks area[32, 50.] These results therefore point out the strong correlation between the density of adsorbed *CO on the catalyst surface and the formation of C-C bonds in agreement with the *CO being the key intermediate involved in the dimerization reaction and the formation of C_{2+} products. We note that 1-propanethiol functionalized Ag-Cu electrodes display the most intense peak at 280 cm^{-1} whereas no peak are detected at 1900–2120 cm^{-1}. This indicates the adsorbed *CO is not present in the form of CO_{atop} nor CO_{bridge} configurations. We speculate that the hydrophobic surface of the 1-propanethiol functionalized Ag-Cu induces the existence of a high energy barrier for the protons to reach the surface of the catalyst that prevents the stabilization of the *CO in these bound configurations as previously proposed for other transition metals[50]. Interestingly, we observed a volcano-shaped relationship between the Faradaic efficiency for C_{2+} products and the ratio of atop-bound CO to bridge-bound CO on the surface of Ag-Cu (Figs. 24g and 29). The Faradaic efficiency reaches a maximum for a ratio of CO_{atop} to CO_{bridge} of 0.4-0.5 corresponding to thiadiazole and triazole functionalized catalysts, while the ratio decreases for 1-propanethiol and increases for pristine and cysteamine respectively. We hypothesized that the density of CO_{atop} and CO_{bridge} on the surface of the catalysts is influenced by the electron withdrawing ability of the heterocycles as suggested by the volcano shaped relationship between the oxydiation state of Cu and the ratio of CO_{atop} to CO_{bridge} (Fig. 30). Overall our *ex-situ* and *operando* characterizations of the modified bimetallic catalyst establish an obvious correlation between the electron withdrawing ability of the functional groups and the oxidation state of Cu, which translate into a larger concentration of adsorbed *CO on the electrode surface and ultimately a higher probability for *CO to dimerize.

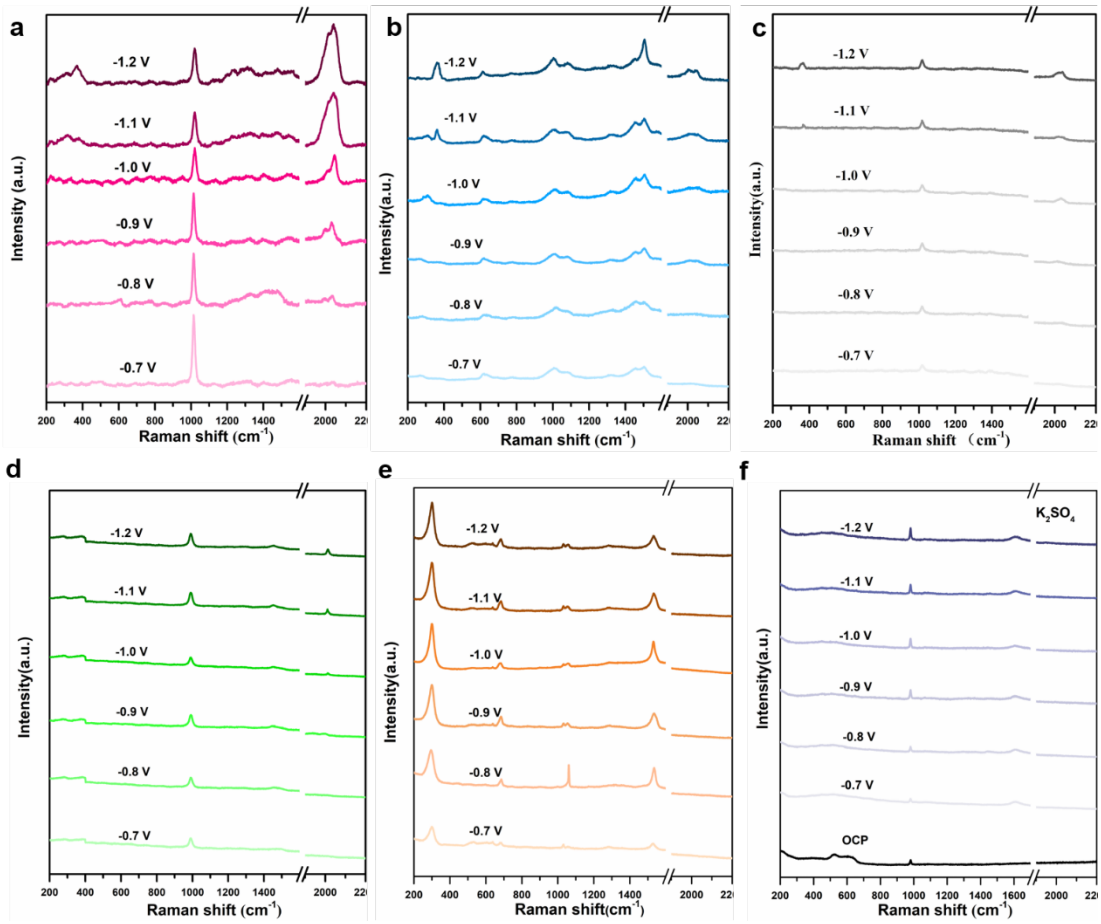

Fig. 28 Operando Raman spectra of (a) N_2SN-, (b) N_3N-, (c) C_2N-, and (d) C_3-functionalized Ag-Cu electrodes compared with (e) pristine Ag-Cu. ae, The operando Raman measurements were carried out between -0.7 V and -1.2 V vs. RHE in a CO_2-saturated $KHCO_3$ solution. To confirm that the signals are solely coming from the CO_2RR, the N_2SN-functionalized Ag-Cu catalyst was also tested in an Ar saturated K_2SO_4 electrolyte solution (f).

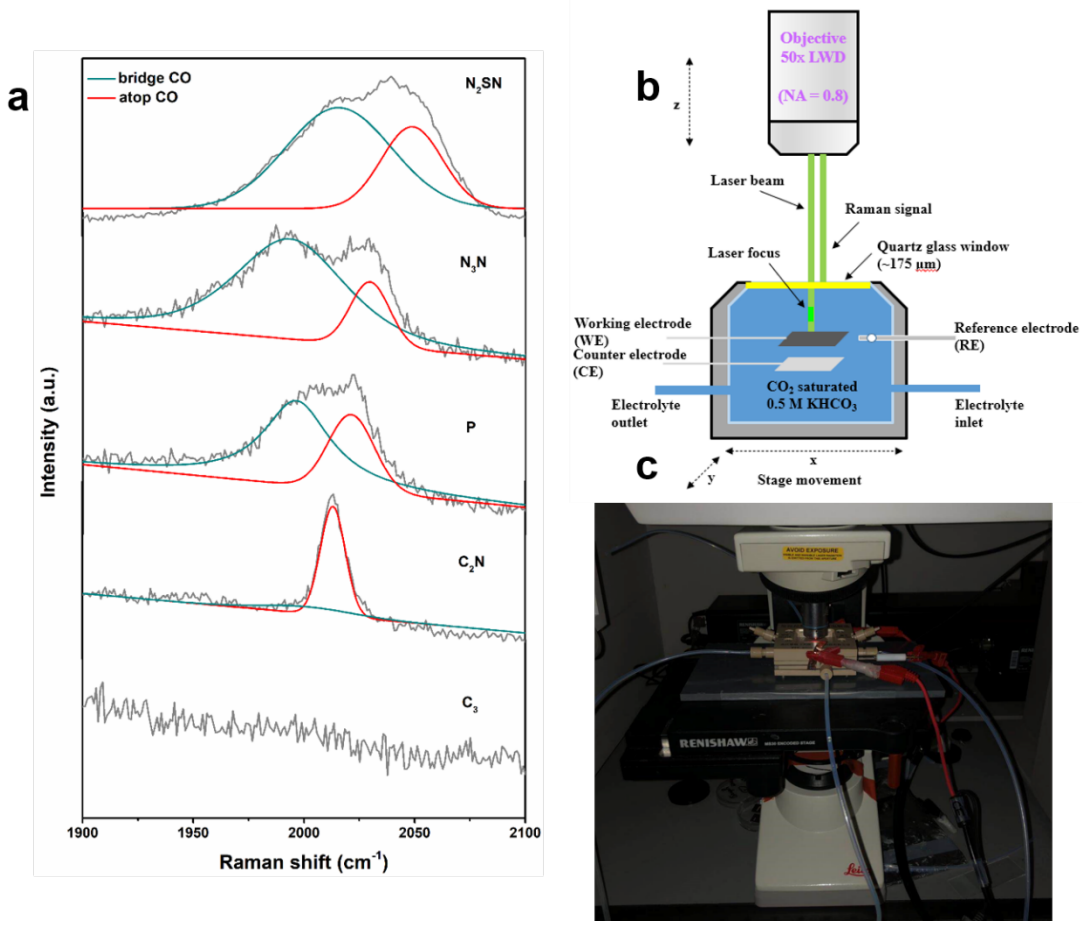

Fig. 29 Deconvolution of the Raman signals around 2000 cm^{-1}. Right panel: Operando Raman spectra centered around 2000 cm^{-1} representing the C≡O stretch region on pristine and functionalized Ag-Cu electrodes. The asymmetric signals were deconvoluted into two components for the atop and the bridge CO using Lorentzian curves. The ratio of the intensities (in area) of the two bands is summarized in Supplementary Table 6. Left panel: Schematic representation and photograph of the operando setup.

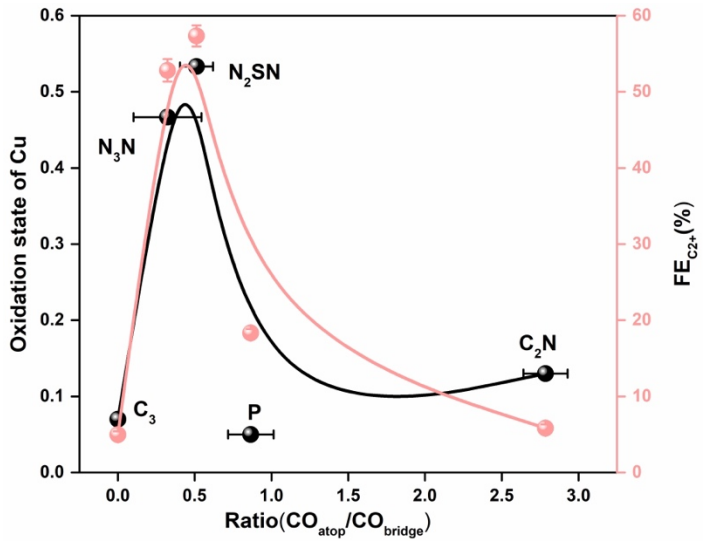

Fig. 30 Relationship between the ratio of CO_{atop} and CO_{bridge} with the oxidation degree of Cu obtained from our XANES measurements.

3.4.4 CO2RR using a membrane–electrode-assembly (MEA)

To evaluate the potential of our approach for practical applications towards the electrosynthesis of C_{2+} products, we integrated the different functionalized bimetallic electrodes into 4 cm^2 membrane–electrode-assembly (MEA) flow electrolyzers (Figs. 31 and 32). The synthesized liquid products at the cathode were collected by using a cold trap connected to the cathode gas outlet. We also analyzed the liquid products in the anolyte to detect liquid products that may have crossed over the membrane electrolyte. We firstly scrutinized the activity of N_2SN-functionalized Ag-Cu in a MEA electrolyzer by flowing Ar (used as blank experiment) and CO_2 in the cathode compartment (Supplementary Fig. 29) and found that the catalyst can convert CO_2 when operating in a catholyte-free MEA system. We then characterized the current-voltage response of all the functionalized catalysts between -2.8 V and -4.8 V and a constant flow of CO_2 of 10 standard cubic centimeters per minute (sccm) (Fig. 33a). The total current for the different Ag-Cu electrodes increased from 4×10^{-2} A up to over 1.6 A. The N_2SN-functionalized electrodes displayed the largest specific current density for C_{2+} at 261 mA cm^{-2} together with the maximum FE for C_{2+} products and the lowest FE for H_2 at ~80% and 14%, respectively (Figs. 33b, 34a and 35a). Remarkably the selectivity for the C_{2+} products increase together with the electrolysis response when increasing the operating potential of the full cell. The catalytic activity towards the competitive HER concurrently decreases up to -4.55 V (Figs. 33b and 35c). Compared to pristine Ag-Cu, the FE for C_{2+} products from N_2SN- and N_3N-functionalized electrodes demonstrated an average enhancement for C_{2+} of 3.1 and 2.6 folds respectively over the extended range of full-cell potentials (Figs. 33c and 36). To further assess the performance of the functionalized Ag-Cu electrodes in the MEA devices, we calculated the ratio of $j_{C_{2+}}$ to j_{C_1} for the different potential. We found that Ag-Cu functionalized with thiadiazole displays the largest values and the ratio reaches at a maximum value of ≈ 10 at a current density of 261.4 mA cm^{-2} (Fig. 37). These results demonstrate that the controlled orientation of the reaction pathways towards the synthesis of ethanol and ethylene observed in the H-cell reactors can be transposed to the MEA devices (Fig. 31). We also found that the total FE for gaseous products gradually decreased with the increase of the full-cell voltage indicating a shift toward the formation of liquid products at high operating potential. The Faradaic efficiency for ethanol and n-propanol reached 16.5% and 6.1% at a voltage of -4.4 V (Fig. 34a)

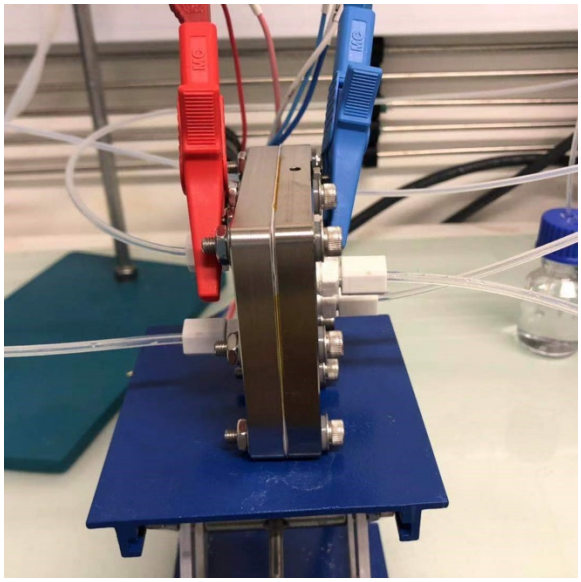

Fig. 31 Photograph of a 4-cm^{-2} membrane–electrode-assembly (MEA) cell.

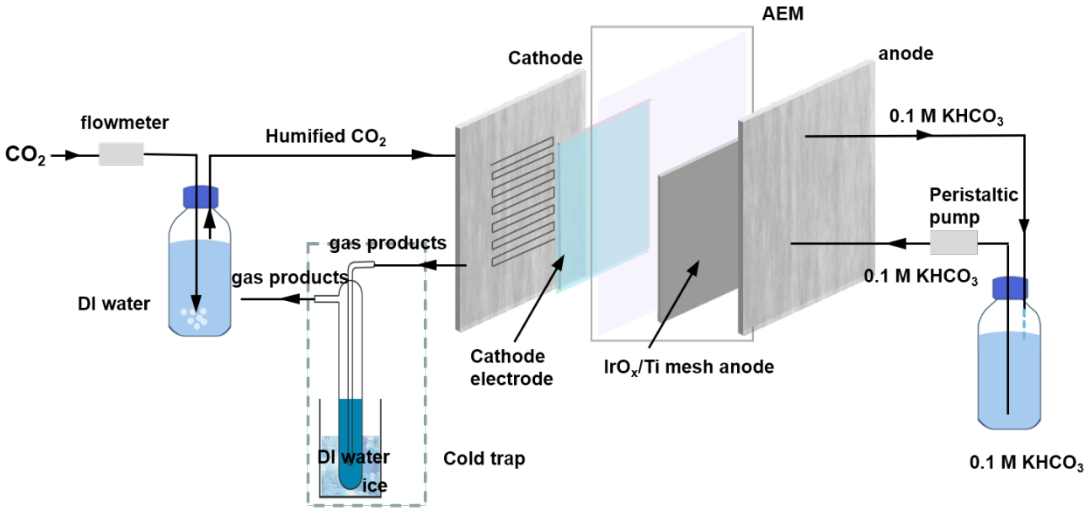

Fig. 32 Schematic representation of the experimental setup for the CO_2 electrolysis in a MEA electrolyzer. The geometric area of the cathode is 4 cm^2, of which 45% is the gas channel while the rest 55% is the land area.

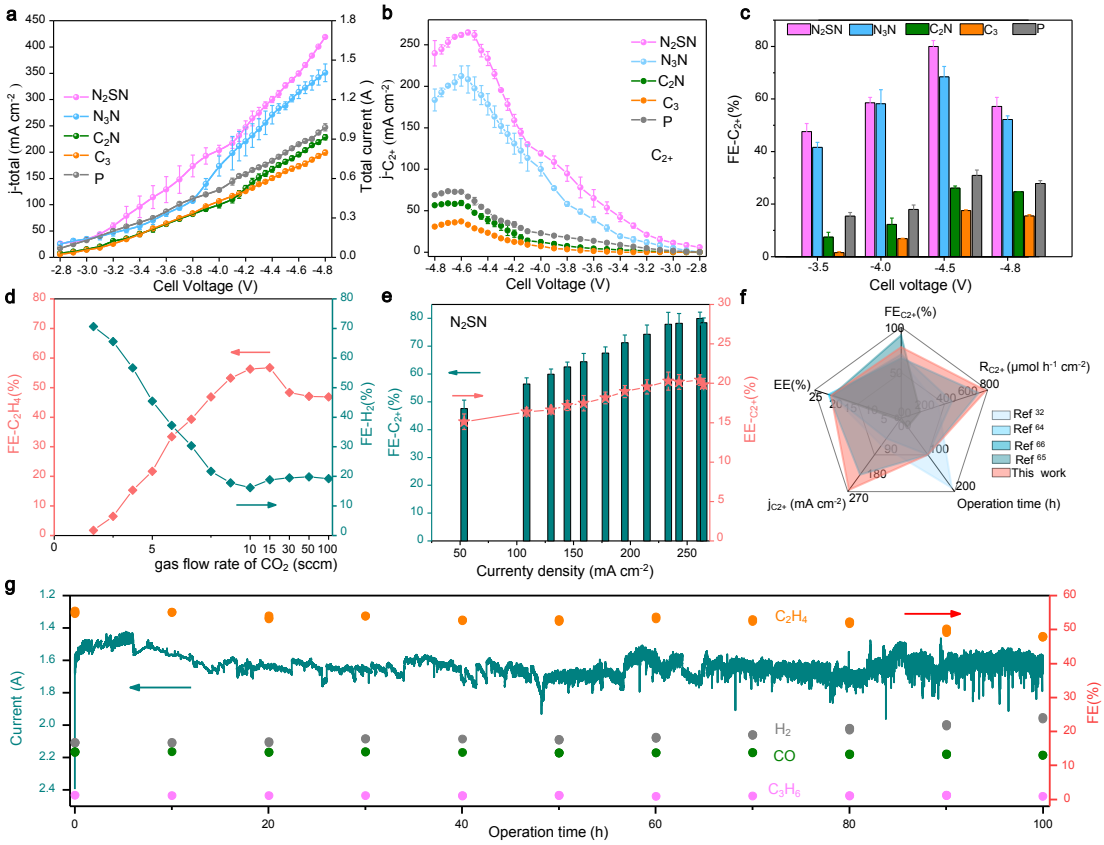

Fig. 33 CO_2RR performance of the functionalized Ag-Cu electrodes measured in MEA electrolyzers. (a), Relationship between the current and cell voltage relationship of pristine, C_3-, C_2N-, N_3N- and N_2SN- functionalized electrodes. The error bars represent the standard deviation of the current density of three independent samples during the entire operation and for each cell voltage. The CO_2RR electrolysis was operated using CO_2 with a flow rate of 10 sccm, 0.1M $KHCO_3$ anolyte with a flow rate of 30 mL min−1. (b), Corresponding partial current density for the C_{2+} products. (c), Comparison of FEs for C_{2+} on the different Ag-Cu electrodes measured at full-cell potentials ranging between -3.5 and -4.8 V. (d), Evolution of the Faradaic efficiency for C_{2+} and H_2 with the CO_2 flow rate. (e), Evolution of the FEs and full-cell energy efficiency (EE) for C_{2+} as a function of specific current densities for C_{2+} on the N_2SN- functionalized Ag-Cu electrode. The error bars represent the standard deviation of three independent samples measured under different current densities. (f), Comparison of the performance metrics of the MEA electrolyzers based on N_2SN-functionalized Ag-Cu cathodes with literature benchmark. For each report, the plotted values are those corresponding to the longest duration test[32, 65-67]. (g), CO_2RR performance of N_2SN-Ag-Cu catalyst at a full-cell potential of -4.55 V and with a 10 sccm feed in CO_2 over 100 hours. The anolyte consisted in a 0.1 M $KHCO_3$ solution with a flow rate of 30 ml min^{-1}. The blue line represents the current density recorded during the extended CO_2RR experiment (primary y axis). Each orange, gray, green and purple spheres represent the FEs for C_2H_4, H_2, CO and C_2H_6 averaged from three independent measurements (secondary y axis).

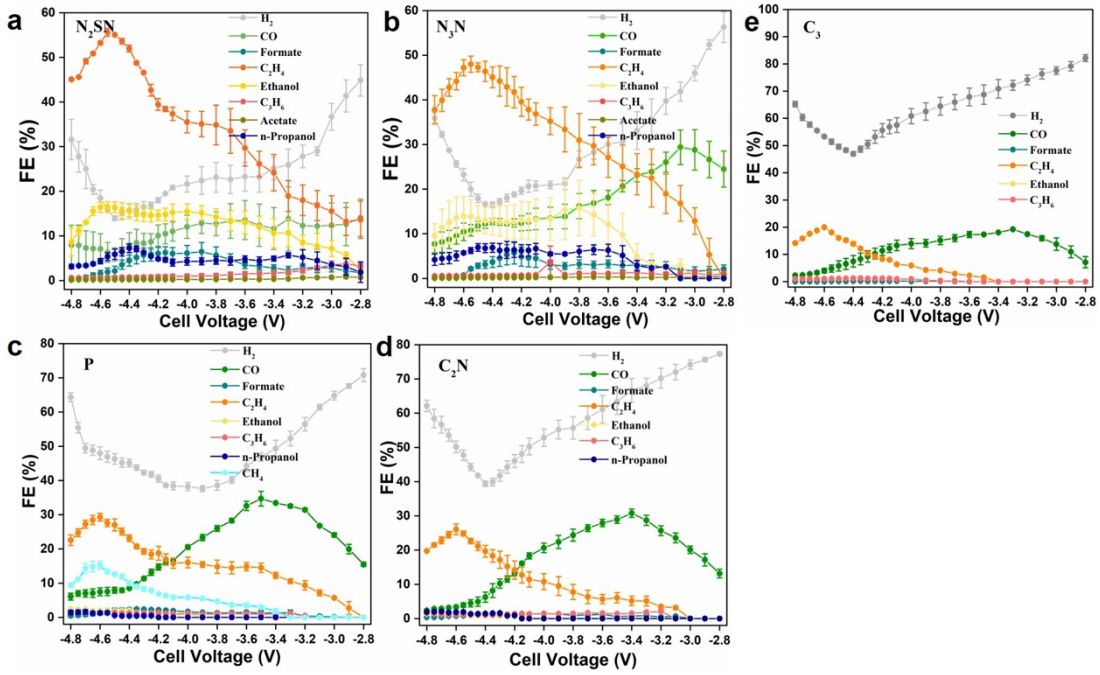

Fig. 34 Electrocatalytic CO_2RR properties of the MEA electrolyzers using the different Ag-Cu catalysts. The corresponding Faradaic efficiency for the gas and liquid products on N_2SN-Ag-Cu (a), N_3N-Ag-Cu (b), C_2NAg- Cu (d), C_3-Ag-Cu (e) compared to pristine (c) catalysts at increasing cell voltages. The error bars represent the standard deviation of the measurements based on three independent samples.

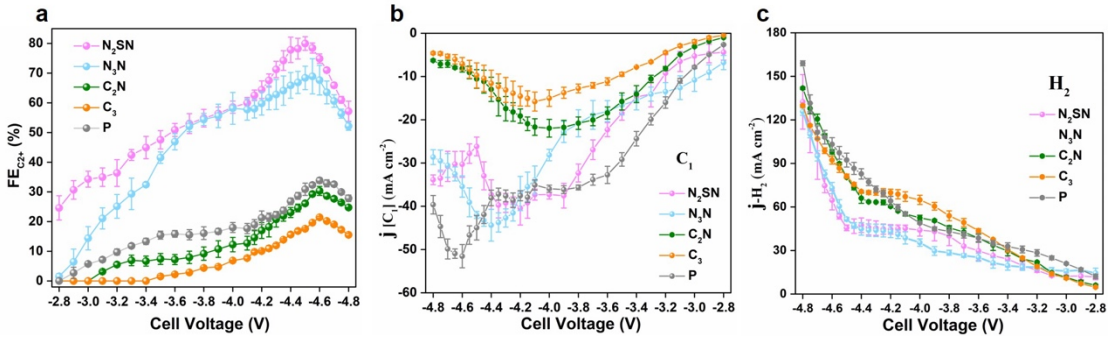

Fig. 35 CO_2 electroreduction performance in the MEA electrolyzers. Faradaic efficiency for the C_{2+} (C_2H_4, C_2H_5OH, n-propanol and acetate) (a), j–V plots of the partial current densities for the C1 (CO, CH_4 and HCOOH) (b) and H_2 products (c) on N_2SN-Ag-Cu, N_3N-Ag-Cu, C_2N-Ag-Cu, C_3-Ag-Cu compared to pristine measured with a 0.1 M $KHCO_3$ anolyte solution.

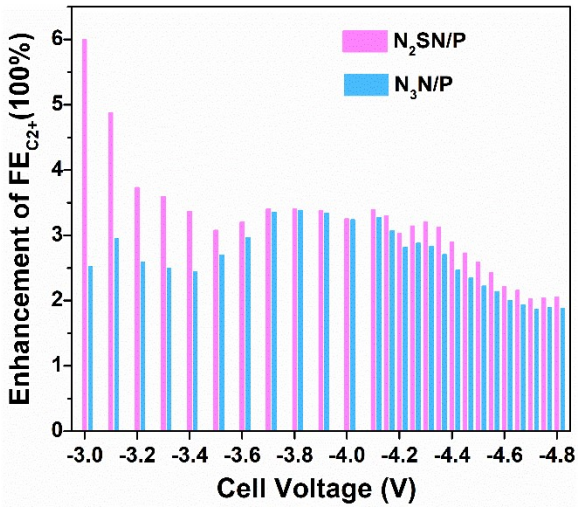

Fig. 36 Enhancement factor of FEC_{2+} for N_2SN-Ag-Cu and N3NAg-Cu compared to pristine.

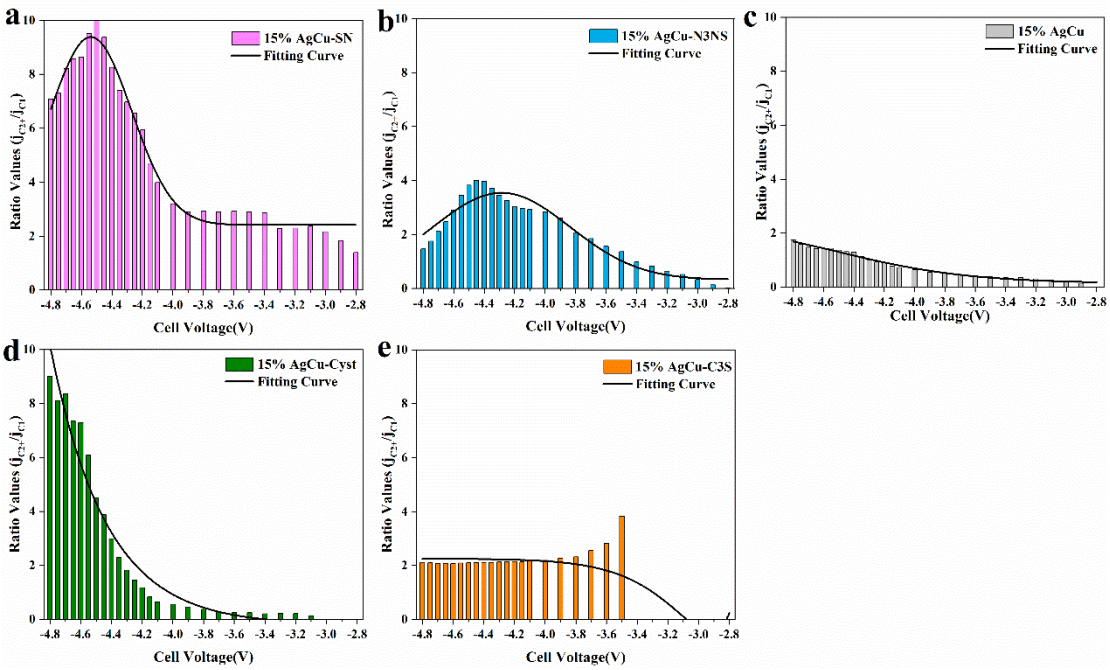

Fig. 37 Selectivity for $C_{1\text{-}2+}$ hydrocarbons on the different electrodes in the MEA electrolyzers. The estimated ratio for jc_2 and jc_1 on the different Ag-Cu electrodes measured with a 0.1 M $KHCO_3$ anolyte solution.

To better understand the influence of operating conditions on the CO_2RR performance of the MEA device, we varied the CO_2 flow rate from 3 to 100 sccm at a constant full-cell potential of -4.55 V. When using N_2SN-functionalized Ag-Cu electrodes, the FE for ethylene reached a peak at 56% at ~10 sccm (Fig. 33d) together with a sharply reduced FE for H_2 at only 15.2%. The selectivity for ethylene rapidly drops down to only ~5% for a CO_2 flow rate of 3 sccm, suggesting that the feed in CO_2 is not sufficient to produce enough *CO to dimerize on the surface of the catalyst. The relationships between CO_2 flow rates, cell voltages; Faradaic efficiencies for the main gas products (H_2, CO and C_2H_4) were explored and we found that the FE_{C2H4} decreases when increasing the CO_2 flow rate and the optimal flow rate is 10 sccm even when operating under high voltage and high current

density (Fig. 38). Conversely, the Faradaic efficiency for H_2 increases when increasing the CO_2 flow rate, which further demonstrates that the decrease in the C_{2+} performance is not caused by the insufficient feed in CO_2. We also estimated the full-cell energy efficiency ($EE_{full\text{-}cell}$) for N_2SN-functionalized Ag-Cu for the different operating potential. Both the FE and $EE_{full\text{-}cell}$ values for C_{2+} products increased with the increase of the current density and achieved a maximum FE_{C2+} of ≈ 80 ± 1% and an $EE_{full\text{-}cell}$ of 20.3% at a specific current density larger than 260 mA cm^{-2} for the production of C_{2+} (Fig. 33e). By comparing the performance metrics of N_2SN-functionalized Ag-Cu with previous literature benchmarks based on MEA devices, we observed that thiadiazole -functionalized Ag-Cu allows achieving outstanding performance notably thanks to a high CO_2-to-C_{2+} conversion rate of 785 µmol h^{-1} cm^{-2} (Fig. 33f).

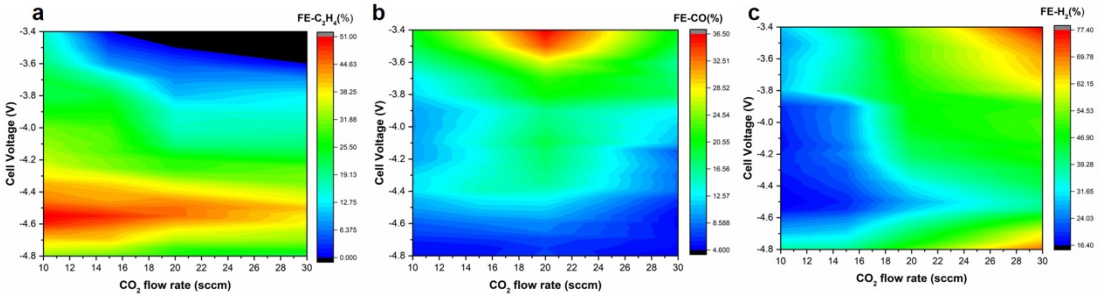

Fig. 38 The influence of CO_2 gas flow rate on different products selectivity at different voltages. (a) C_2H_4, (b) CO and (c) H_2.

We finaly examined the stability of the N_2SN-functionzlized Ag-Cu electrodes in a full-cell MEA electrolyzer under continuous operation at a CO_2 flow rate of 10 sccm and a cell voltage of -4.55V. The performance of the cell was found to be stable over 100 hours with an average FE of 51% for ethylene and an average current of around 1.6 A (Fig. 33g). After 100 hours, the retention of the FE for ethylene and the current were estimated to be 48% and 1.58A corresponding to retentions of 94% and 99% respectively. The stability of the CO_2RR properties is further accompanied by a high stability of the catalyst morphology and microstructure (Fig. 39).

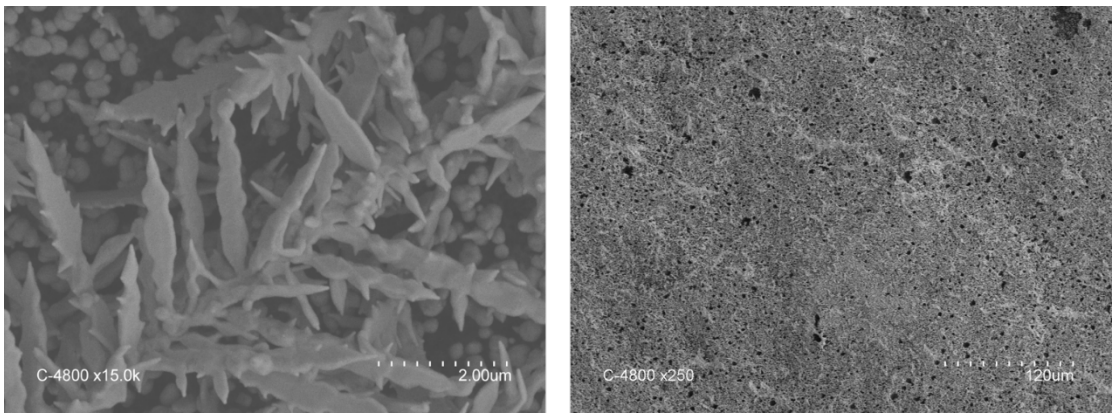

Fig. 39 SEM pictures of the N_2SN-Ag-Cu catalyst after electrolysis in MEA.

3.5 conclusions

Our study describes an original and robust molecular engineering strategy to tune the oxidation state of Cu electrodes *via* functionalization. We identified that strong electron withdrawing groups based on aromatic heterocycles can effectively orient the pathway of the CO_2RR reactions towards the synthesis of C_{2+} molecules. Functionalization of the surface of a bimetallic Ag-Cu catalyst with thiadiazole and triazole derivatives led to an enhancement of the $FE_{C_{2+}}$ up to ≈ 80 ± 1%, corresponding to ratios of $FE_{C_{2+}}$ to FE_{C_1} and $FE_{C_{2+}}$ to FE_{H_2} of 10 and 5.3 respectively. By combining Auger and XANES spectroscopy we identified that the superior performance towards the CO_2-to-C_{2+} conversion originates from the controlled oxidation state of $Cu^{\delta+}$ atoms with $0 < \delta < 1$. The functionalized Ag-Cu electrodes were found stable, which translates into a prolonged production of C_{2+} products for >100h.

3.6 References

1. Bushuyev, O. S.. *et al.* What should we make with CO_2 and how can we make it? *Joule* **2**, 825-832 (2018).
2. Whipple, D. T.&Kenis, P. J. Prospects of CO_2 utilization via direct heterogeneous electrochemical reduction. *J Phys Chem Lett* **1**, 3451-3458 (2010).
3. Ross, M. B.. *et al.* Designing materials for electrochemical carbon dioxide recycling. *Nat Catal* **2**, 648-658 (2019).
4. Ross, M. B.. *et al.* Electrocatalytic rate alignment enhances syngas generation. *Joule* **3**, 257-264 (2019).
5. Ren, S.. *et al.* Molecular electrocatalysts can mediate fast, selective CO_2 reduction in a flow cell. *Science* **365**, 367-369 (2019).
6. Gu, J.. *et al.* Atomically dispersed Fe^{3+} sites catalyze efficient CO_2 electroreduction to CO. *Science* **364**, 1091-1094 (2019).
7. Liu, M.. *et al.* Enhanced electrocatalytic CO_2 reduction via field-induced reagent concentration. *Nature* **537**, 382-386 (2016).
8. Hori, Y., Murata, A.&Takahashi, R. Formation of hydrocarbons in the electrochemical reduction of carbon dioxide at a copper electrode in aqueous solution. *J Chem Soc, Faraday Trans1* **85**, 2309-2326 (1989).
9. Hoang, T. T.. *et al.* Nanoporous copper–silver alloys by additive-controlled electrodeposition for the selective electroreduction of CO_2 to ethylene and ethanol. *J Am Chem Soc* **140**, 5791-5797 (2018).
10. Li, Y. C.. *et al.* Binding site diversity promotes CO_2 electroreduction to ethanol. *J Am Chem Soc* **141**, 8584-8591 (2019).
11. Lee, S., Park, G.&Lee, J. Importance of Ag–Cu biphasic boundaries for selective electrochemical reduction of CO2 to ethanol. *ACS Catal* **7**, 8594-8604 (2017).
12. Chen, C.. *et al.* Cu-Ag Tandem Catalysts for High-Rate CO_2 Electrolysis toward Multicarbons. *Joule* **4**, 1688-1699 (2020).
13. Clark, E. L., Hahn, C., Jaramillo, T. F.&Bell, A. T. Electrochemical CO_2 reduction over compressively strained CuAg surface alloys with enhanced multi-carbon oxygenate selectivity. *J Am Chem Soc* **139**, 15848-

15857 (2017).

14. Zhou, Y.. *et al.* Dopant-induced electron localization drives CO_2 reduction to C_2 hydrocarbons. *Nat Chem* **10**, 974-980 (2018).

15. Buckley, A. K.. *et al.* Electrocatalysis at Organic–Metal Interfaces: Identification of Structure–Reactivity Relationships for CO_2 Reduction at Modified Cu Surfaces. *J Am Chem Soc* **141**, 7355-7364 (2019).

16. Han, Z.. *et al.* CO_2 reduction selective for C≥ 2 products on polycrystalline copper with N-substituted pyridinium additives. *ACS Cent Sci* **3**, 853-859 (2017).

17. Cui, W. G.&Hu, T. L. Incorporation of Active Metal Species in Crystalline Porous Materials for Highly Efficient Synergetic Catalysis. *Small*, 2003971 (2020).

18. Bai, S.. *et al.* Highly active and selective hydrogenation of CO_2 to ethanol by ordered Pd–Cu nanoparticles. *J Am Chem Soc* **139**, 6827-6830 (2017).

19. Huang, J.. *et al.* Structural sensitivities in bimetallic catalysts for electrochemical CO_2 reduction revealed by Ag–Cu nanodimers. *J Am Chem Soc* **141**, 2490-2499 (2019).

20. Varandili, S. B.. *et al.* Synthesis of Cu/CeO_{2-x} Nanocrystalline Heterodimers with Interfacial Active Sites To Promote CO_2 Electroreduction. *ACS Catal* **9**, 5035-5046 (2019).

21. Chou, T.-C.. *et al.* Controlling the oxidation state of the Cu electrode and reaction intermediates for electrochemical CO_2 reduction to ethylene. *J Am Chem Soc* **142**, 2857-2867 (2020).

22. Zhang, W.. *et al.* Atypical oxygen-bearing copper boosts ethylene selectivity toward electrocatalytic CO_2 reduction. *J Am Chem Soc* **142**, 11417-11427 (2020).

23. Yang, P.-P.. *et al.* Protecting copper oxidation state via intermediate confinement for selective CO_2 electroreduction to C_{2+} fuels. *J Am Chem Soc* **142**, 6400-6408 (2020).

24. Gao, D.. *et al.* Selective CO2 Electroreduction to Ethylene and Multicarbon Alcohols via Electrolyte-Driven Nanostructuring. *Angew Chem Int Ed* **58**, 17047-17053 (2019).

25. Wang, H.. *et al.* Rapid and scalable synthesis of cuprous halide-derived copper nano-architectures for selective electrochemical reduction of carbon dioxide. *Nano Lett* **19**, 3925-3932 (2019).

26. Cui, X.. *et al.* Bridging homogeneous and heterogeneous catalysis by heterogeneous single-metal-site catalysts. *Nat Catal* **1**, 385-397 (2018).

27. Copéret, C.. *et al.* Eine Brücke zwischen industriellen und wohldefinierten Trägerkatalysatoren. *Angew Chem Int Ed* **130**, 6506-6551 (2018).

28. Copéret, C., Chabanas, M., Petroff Saint-Arroman, R.&Basset, J. M. Homogeneous and heterogeneous catalysis: bridging the gap through surface organometallic chemistry. *Angew Chem Int Ed* **42**, 156-181 (2003).

29. Pelletier, J. r. m. D.&Basset, J.-M. Catalysis by design: Well-defined single-site heterogeneous catalysts. *Acc Chem Res* **49**, 664-677 (2016).

30. Copéret, C.. *et al.* Bridging the Gap between Industrial and Well-Defined Supported Catalysts. *Angew Chem Int Ed* **57**, 6398-6440 (2018).

31. Thevenon, A., Rosas-Hernández, A., Peters, J. C.&Agapie, T. In-Situ Nanostructuring and Stabilization of Polycrystalline Copper by an Organic Salt Additive Promotes Electrocatalytic CO_2 Reduction to Ethylene. *Angew Chem Int Ed* **58**, 16952-16958 (2019).

32. Li, F.. *et al.* Molecular tuning of CO2-to-ethylene conversion. *Nature* **577**, 509-513 (2020).

33. Rosen, B. A.. *et al.* Ionic liquid–mediated selective conversion of CO_2 to CO at low overpotentials. *Science* **334**, 643-644 (2011).

34. Cao, Z.. *et al.* Chelating N-heterocyclic carbene ligands enable tuning of electrocatalytic CO_2 reduction to formate and carbon monoxide: surface organometallic chemistry. *Angew Chem Int Ed* **130**, 5075-5079 (2018).

35. Lau, G. P.. *et al.* New insights into the role of imidazolium-based promoters for the electroreduction of CO2 on a silver electrode. *J Am Chem Soc* **138**, 7820-7823 (2016).

36. Kim, C.. *et al.* Achieving selective and efficient electrocatalytic activity for CO_2 reduction using immobilized silver nanoparticles. *J Am Chem Soc* **137**, 13844-13850 (2015).

37. Wakerley, D.. *et al.* Bio-inspired hydrophobicity promotes CO_2 reduction on a Cu surface. *Nature Mater* **18**, 1222-1227 (2019).

38. Kim, C.. *et al.* Insight into electrochemical CO2 reduction on surface-molecule-mediated Ag nanoparticles. *ACS Catal* **7**, 779-785 (2017).

39. Fang, Y.&Flake, J. C. Electrochemical reduction of CO2 at functionalized Au electrodes. *J Am Chem Soc* **139**, 3399-3405 (2017).

40. Zhong, Y.. *et al.* An Artificial Electrode/Electrolyte Interface for CO2 Electroreduction by Cation Surfactant Self-Assembly. *Angew Chem Int Ed* **132**, 19257-19263 (2020).

41. Dena, A. S. A., Muhammad, Z. A.&Hassan, W. M. Spectroscopic, DFT studies and electronic properties of novel functionalized bis-1, 3, 4-thiadiazoles. *Chem Zvesti* **73**, 2803-2812 (2019).

42. Sherif, E.-S. M., Erasmus, R.&Comins, J. Corrosion of copper in aerated acidic pickling solutions and its inhibition by 3-amino-1, 2, 4-triazole-5-thiol. *J Colloid Interface Sci* **306**, 96-104 (2007).

43. Pan, Y.-C.. *et al.* 2-Amino-5-(4-pyridinyl)-1, 3, 4-thiadiazole monolayers on copper surface: Observation of the relationship between its corrosion inhibition and adsorption structure. *Corros Sci* **73**, 274-280 (2013).

44. Sherif, E.&Park, S.-M. Effects of 2-amino-5-ethylthio-1, 3, 4-thiadiazole on copper corrosion as a corrosion inhibitor in aerated acidic pickling solutions. *Electrochim Acta* **51**, 6556-6562 (2006).

45. Ren, D.. *et al.* Selective electrochemical reduction of carbon dioxide to ethylene and ethanol on copper (I) oxide catalysts. *ACS Catal* **5**, 2814-2821 (2015).

46. Deng, Y.&Yeo, B. S. Characterization of electrocatalytic water splitting and CO2 reduction reactions using in situ/operando Raman spectroscopy. *ACS Catal* **7**, 7873-7889 (2017).

47. Mallouk, T.. *et al.* 2-aminobenzenethiol functionalized Ag-decorated nanoporous Si photoelectrodes for selective CO2 reduction. *Angew Chem Int Ed*, (2020).

48. Dilimon, V., Denayer, J., Delhalle, J.&Mekhalif, Z. Electrochemical and spectroscopic study of the self-

assembling mechanism of normal and chelating alkanethiols on copper. *Langmuir* **28**, 6857-6865 (2012).

49. Biesinger, M. C. Advanced analysis of copper X-ray photoelectron spectra. *Surf Interface Anal* **49**, 1325-1334 (2017).

50. Fielicke, A., Gruene, P., Meijer, G.&Rayner, D. M. The adsorption of CO on transition metal clusters: A case study of cluster surface chemistry. *Surf Sci* **603**, 1427-1433 (2009).

51. Arán-Ais, R. M.. *et al.* The role of in situ generated morphological motifs and Cu (i) species in C_{2+} product selectivity during CO2 pulsed electroreduction. *Nat Energy* **5**, 317-325 (2020).

52. Favaro, M.. *et al.* Subsurface oxide plays a critical role in CO2 activation by Cu (111) surfaces to form chemisorbed CO2, the first step in reduction of CO2. *Proc Nat Acad Sci,* **114**, 6706-6711 (2017).

53. Pauly, N., Tougaard, S.&Yubero, F. LMM Auger primary excitation spectra of copper. *Surf Sci* **630**, 294-299 (2014).

54. Tahir, D.&Tougaard, S. Electronic and optical properties of Cu, CuO and Cu_2O studied by electron spectroscopy. *J Phys Condens Matter* **24**, 175002 (2012).

55. Barman, S.&Sarma, D. Investigation of the L_3-$M_{45}M_{45}$ Auger spectra of Cu, Cu_2O and CuO. *J Phys Condens Matter* **4**, 7607 (1992).

56. Raciti, D.&Wang, C. Recent advances in CO2 reduction electrocatalysis on copper. *ACS Energy Lett* **3**, 1545-1556 (2018).

57. Cheng, T., Xiao, H.&Goddard, W. A. Full atomistic reaction mechanism with kinetics for CO reduction on Cu (100) from ab initio molecular dynamics free-energy calculations at 298 K. *Proc Nat Acad Sci,* **114**, 1795-1800 (2017).

58. Kortlever, R.. *et al.* Catalysts and reaction pathways for the electrochemical reduction of carbon dioxide. *J Phys Chem Lett* **6**, 4073-4082 (2015).

59. Montoya, J. H., Shi, C., Chan, K.&Nørskov, J. K. Theoretical insights into a CO dimerization mechanism. in CO2 electroreduction. *J Phys Chem Lett* **6**, 2032-2037 (2015).

60. Chernyshova, I. V., Somasundaran, P.&Ponnurangam, S. On the origin of the elusive first intermediate of. CO2 electroreduction. *Proc Nat Acad Sci,* **115**, E9261-E9270 (2018).

61. Akemann, W.&Otto, A. Vibrational modes of CO adsorbed on disordered copper films. *J Raman Spectrosc* **22**, 797-803 (1991).

62. Gunathunge, C. M.. *et al.* Spectroscopic observation of reversible surface reconstruction of copper electrodes under CO2 reduction. *J Phys Chem C* **121**, 12337-12344 (2017).

63. Clark, R. J. H.&Hester, R. E. *Spectroscopy for surface science*. John Wiley & Sons (1998).

64. Gabardo, C. M.. *et al.* Continuous carbon dioxide electroreduction to concentrated multi-carbon products using a membrane electrode assembly. *Joule* **3**, 2777-2791 (2019).

65. Merino-Garcia, I.. *et al.* Cu oxide/ZnO-based surfaces for a selective ethylene production from gas-phase CO2 electroconversion. *J CO2 Util* **31**, 135-142 (2019).

66. Ozden, A.. *et al.* High-Rate and Efficient Ethylene Electrosynthesis Using a Catalyst/Promoter/Transport Layer. *ACS Energy Lett* **5**, 2811-2818 (2020).

67. Wang, X., *et al.* Efficient electrically powered CO2-to-ethanol via suppression of deoxygenation. *Nature Energy*, *5*(6), 478-486 (2020).

Chapter 4. Selective and energy-efficient electrosynthesis of ethylene via valence engineering of the Cu sites

4.1 Abstract

The electrosynthesis of ethylene (C_2H_4) in Membrane-electrode-assembly (MEA) cells with high selectivity and large current density is a promising flow process strategy for the conversion of CO_2 or CO into valuable products. Although considerable progress has been made in meeting industrial requirements in terms of Faradaic efficiency (FE) and formation rate, selectivity towards the formation of a single type of multi-carbon (C_{2+}) product has not been demonstrated to date. Here, we evaluated a library of aryl diazonium salts to functionalize Cu catalysts in order to elucidate the influence of Cu valence on the formation of multicarbon products during the CO_2RR. By combining density functional theory (DFT) calculations with *operando* Raman and X-ray absorption spectroscopy (XAS), we identified the role of the surface oxidation state of $Cu^{\delta+}$ with $0<\delta<1$ on the selectivity and the formation rate of C_2H_4. As a result, we report a FE and a specific current density for C_2H_4 as large as 83±2% and 212 mA cm^{-2}, respectively on partially oxidized $Cu^{0.26+}$. This corresponds to an energy efficiency of 26.9% and an electrical power consumption (EPC) of 61.4 kWh $N^{-1}m^{-3}$. The conversion performance was further improved by using a perfluorinated sulfonic acid (PFSA) ionomer to reach a record-high FE for C_2H_4 of 89±3% at a specific current density of 536 mA cm^{-2}. When coupled with an Ag-based MEA cell to generate CO from CO_2 in a cascade flow process, an energy efficiency of ~40 % with a FE_{C2H4} of 86± 2% was achieved, corresponding to a record low EPC of 25.6 kWh $N^{-1}m^{-3}$.

4.2 Introduction

The global consumption of fossil fuels induces profound environmental repercussions and is responsible for colossal emission of > 35 Gt of CO_2 every year. The pledge of net zero emission by 2050 requires the development of economically viable technologies to reuse the emitted CO_2 and close the carbon cycle. The electrochemical CO_2 reduction reaction (CO_2RR) provides a promising and sustainable route to convert CO_2 into valuable chemicals and fuels when powered by renewable electricity[1,2]. Ethylene has been identified as a desirable multicarbon product of the CO_2RR owing to its high commercial value and large market size with an annual global production of 140 million metric tons and a market value of 182 billion USD[3]. Techno-economic analyses (TEA) emphasized the necessity to operate CO_2RR at specific current densities larger than 200 mA cm^{-2} while minimizing the power input (or cell voltage)[4]. Although the best reported performance of CO_2-to-ethylene electrocatalysis: >80% Faradaic efficiency at 400 mA cm^{-2} in flow cell, has shorten the distance toward to industry development, the limited stability is still insufficient to compete with traditional ethylene production from fossil sources as well as bio-based ethylene[3,5-8].

Zero-gap membrane electrode assembly (MEA) cells, comprising a cathode, membrane, and anode, offer the potential to achieve industry-relevant current densities with high selectivity and formation rates, while the continuous flow process provides a large mass transfer boundary layer with high local CO_2 concentration near

the planar electrodes[9-11]. The absence of catholyte makes MEA cells more stable than traditional flow cells by mitigating the electrode flooding and the precipitation of salts, resulting in greater operating stability and reduced operational expenses (OPEX)[11,12]. The exploitation of MEA cells with high selectivity and high current density for the ethylene production as well as prolonged stability, is thus expected to lowers the threshold of economic viability to replace fossil sources for ethylene production. To date, the selectivity and the specific current density for ethylene in MEA systems are however limited to <80% and < 200 mA cm^{-2} (Refs.[6,13]).

It has been reported that partially oxidized copper sites: $Cu^{\delta+}$, $0<\delta<1$ facilitate the conversion of CO_2 to C_{2+} products by decreasing the energy barrier associated with the CO dimerization and the formation of *OCCOH intermediate[14-18]. Investigations of the role of $Cu^{\delta+}$ proved to be tedious, while the intrinsic instability of $Cu^{\delta+}$ species, especially at high cathodic potentials, leads to a rapid loss of performance[19]. The control of the valence of the Cu sites and the presence of Cu^{+} species on the surface of the electrodes has recently been a central focus in CO_2RR notably via controlled oxidation, pulse polarization, or molecular doping[6,11,16.]

Aryl diazonium salts, as one of the classic electrophile reagents, the reduction of diazonium salts has been frequently employed for the covalent modification of surfaces since the first demonstration in 1992[20-24]. The strong interfacial bonding of aryl groups on metal surface makes it much stable and widely applied in various fields, including corrosion protection[24-26], biosensors' development[27-29], antibacterial activity[27,30] and drug delivery[27,31,32]. Compared with other electrophile reagents (thiols, carbene, and halogen molecules [33-38]) which usually makes copper fully oxidized, the electrophile ability of aryl diazonium salts can be tailored by easily substituting the hydrogen atoms on the aryl with different electro-withdrawing groups. When grafting different diazonium salts on copper, the oxidation degree of copper becomes controlled and keeps stable due to the strong interfacial bonding of aryl groups on metal surface [24,27,31] Therefore, tailoring the oxidation state of copper by functionalizing different aryl diazonium salts becomes feasible and effective.

Herein, we report a functionalization strategy based on aryl diazonium salts used as electrophile reagents with a strong affinity for electron-rich copper metal. We identified that the nature of different substituted aryl groups can precisely tailor the oxidation state of surface Cu sites as confirmed by our density functional theory (DFT) calculations. We predict that controlled doping of Cu can facilitate C-O bond breaking followed by C-H hydrogenation of the $*CH_2CHOH$ intermediate, which favors the selective formation of ethylene (C_2H_4) over ethanol (C_2H_5OH) during the CO_2RR. We corroborated the DFT results by integrating the aryl functionalized catalysts into an MEA flow cell. By tailoring the valence of the Cu sites, we achieved a FE_{C2H4} of 83% at a current density of 212 mA cm^{-2} for the electrosynthesis of ethylene from CO2 with an optimal oxidation state for Cu of +0.26. This corresponds to a ~200% increase of the ethylene formation rate compared to the pristine Cu and a C_2H_4 vs. C_{2+} selectivity greater than 97% and a sustained stability for 120 hours. When fed with CO, the MEA cell demonstrated a FE for C_2H_4 of ~86% with a full cell energy efficiency of ~40 %, setting a new benchmark for the formation of ethylene from CO.

4.3 Experimental methods

4.3.1 Materials

Catalyst preparation. The catalysts were electrodeposited at a constant current of -15 mA cm^{-2} for 300 s on an acid-treated gas diffusion layer (Sigracet 22BB, for characterizations) with CO_2 gas flow (60 sccm). The solution consisted of 0.1 M copper bromide (98%, Sigma-Aldrich), 0.2 M sodium tartrate dibasic dihydrate (purum pro analysis ≥ 98.0% non-aqueous titration (NT), Sigma-Aldrich), and 1 M KOH. Nafion 117 and anion exchange membrane (Sustainion® X37-50), gas diffusion layer, and titanium mesh were obtained from the Fuel Cell Store. All chemicals were used as received. All aqueous solutions were prepared using deionized water with a resistivity of 18.2 MΩ cm^{-1}.

Functionalized Electrodes preparation. The Cu electrodes were functionalized using a aqueous solution of aryl diazonium salts consisting of 2-Methyl-4-(2-methylphenylazo)benzenediazonium salt (NN), 4-Amino-4′-methoxydiphenylamine-diazonium chloride (N), 2,5-Dimethoxy-4-([4-nitrophenyl]azo)benzenediazonium chloride hemi(zinc chloride) salt (NNN), 4-Methoxybenzenediazonium tetrafluoroborate (OCH_3), 4-Bromobenzenediazonium tetrafluoroborate (Br), 4-Nitrobenzenediazonium tetrafluoroborate (NO_2) and 4-Diazo-*N*,*N*-diethylaniline fluoroborate($N(C_2H_5)_2$). The solutions were prepared with a fixed concentration of 3 mM concentration. The aryl diazonium salts were electrodeposited onto the Cu-GDL electrode using a three-electrode setup with Cu-GDL electrode, Ag/AgCl (3.5 M KCl) and a Pt plate as working, reference and counter electrodes, respectively. A constant current of 0.70 mA cm^{-2} was applied for 100 s on the Cu-GDL electrode (~2.0 × 2.0 cm^2 for MEA) by using a potentiostat (VSP potentiostat from Bio-Logic Science Instruments). After electrodeposition, the electrode was rinsed with DI water, dried under Ar, and stored in glovebox for further use.

Ionomer deposition. Cu-NN electrodes were modified by spray-coating a PFSA solution. The PFSA solution were prepared by using 700 mg of ionomer (Nafion perfluorinated resin solution, product #527084-25 ml purchased from Sigma Aldrich)) and 25 ml methanol (99.8%, anhydrous, Sigma Aldrich). The optimal loading with ionomer was achieved by tuning the spray-coating conditions in order to reach a desired loading of 1.75 mg cm^{-2}. Samples were dried for at least 24 h at room temperature in a vacuum chamber before operation.

Materials characterization. A field emission scanning electron microscope (TESCAN Mira3) was employed to observe the morphology of samples. Aberration-corrected high-resolution (scanning) TEM imaging (HR-(S)TEM), energy-dispersive X-ray spectroscopy (EDS) and spatially-resolved electron energy-loss spectroscopy (SR-EELS) were performed using a FEI Titan Cubed Themis microscope which was operated at 80 kV. The Themis is equipped with a double Cs aberration corrector, a monochromator, an X-FEG gun, a super EDS detector, and an Ultra High Resolution Energy Filter (Gatan Quantum ERS) which allows for working in Dual-EELS mode. HR-STEM imaging was performed by using high-angle annular dark-field (HAADF) and annular dark-field

(ADF) detectors. SR-EELS spectra were acquired with the monochromator excited allowing an energy resolution of 1.1 eV with an energy dispersion of 0.4 eV/pixel. X-ray photoelectron spectroscopy (XPS) measurements were carried out on Thermo Electron ESCALAB 250 System using Al Kα X-ray radiation (1486.6 eV) for excitation. Raman measurements were conducted using a Renishaw in Via Raman microscope and an ×50 objective (Leica) equipped with a 633 nm laser. *Operando* Raman measurements were carried out using a modified liquid-electrolyte flow cell using a 20 s integration time and averaging 10 scans per region. The spectra were recorded and processed using the Renishaw WiRE software (version 4.4). Ag/AgCl (3.5 M KCl) and a Pt plate were used as the reference and counter electrodes, respectively.

X-ray absorption spectroscopy (XAS). *Ex situ* X-ray absorption spectra at the copper K-edges and Operando X-ray absorption spectroscopy (XAS) measurements at the copper K-edges were collected at ALBA Synchrotron Radiation Facility (Barcelona) on beamline CLAESS and SOLEIL Synchrotron Radiation Facility (Saclay) on beamline SAMBA, respectively. Measurements were performed mainly in fluorescence mode, but transmission XAS data were also collected for comparison.

In SOLEIL Synchrotron Radiation Facility (Saclay), the beamline is equipped with a sagittally Si (111) monochromator at the Cu K-edge for energy selection. The beam size was 1 × 0.5 mm. The signals were collected in fluorescence mode using a 13-channel Ge detector. The intensity of the incident radiation was measured with an ionization chamber (I_0) filled with an N_2 (500 mbar)/He (500 mbar) mixture. Two additional ionization chambers filled with 1700 mbar N_2 (in I_1 chamber) and an Ar (150 mbar)/N_2(850 mbar) mixture (in I_1 chamber) were used for measurements in transmission mode in the case of the reference samples.

The X-ray absorption spectroscopy (XAS) measurements were performed in ALBA Synchrotron Radiation Facility (Barcelona). The intensities of the incident radiation and transmitted radiation were measured with ionization chamber detectors I_0 and I_1 filled with pure N_2 (I_0 chamber) or 70:30 N_2 and Kr mixture (I_1 chamber). Fluorescence data were collected using energy selective 6-channel Si drift detector. Si (111) monochromator was used for energy selection. XAS data for Cu foil, Cu_2O, and CuO reference samples were also collected for comparison and data alignment.

For the XAS studies, Cu was firstly electrodeposited on gas diffusion layer (GDL, Sigracet 22 BB, Fuel Cell Store) used as gas diffusion electrode (GDE) and then functional solutions were drop-coated on the catalyst side, while the other side of the GDL was covered with polyamide tape. The GDL was then taped on a graphite foil and subsequently, the electrode was mounted in our home-built single compartment cell, where the samples on graphite foil acted as a working electrode. Pt mesh and Ag/AgCl were used as counter and reference electrodes, respectively. The applied potential was controlled with BioLogic potentiostat. As for the electrolyte, we used an aqueous solution of CO_2-saturated 0.5M $KHCO_3$ that was continuously circulated through the cell using a peristaltic pump. The electrolyte was continuously purged with CO_2 with a flow rate of 20 ml/min. All

measurements were performed at constant potentials of -0.98 V, -0.93 V, -0.88 V and -0.83 V vs. RHE. Time-resolved spectra under CO_2RR conditions were acquired every 12-15 min until no further changes were observed.

Data alignment and normalization of the X-ray absorption near edge structure (XANES) spectra were carried out using the Athena software. Fitting of the Cu K-edge extended X-ray absorption fine structure (EXAFS) spectra $\chi(k)k^2$ of the catalysts was carried out in R-space in the range from R_{min} = 1.0 Å up to R_{max} = 2.7 Å. The Fourier transforms were carried out in the k-range from 3.0 $Å^{-1}$ to 10.0 $Å^{-1}$ with a k-weighting of 1, 2 and 3. Fitting parameters were the coordination numbers N, interatomic distances R, disorder factors σ^2 for Cu-O and Cu-Cu paths, as well as the corrections to the photoelectron reference energies ΔE_0. Amplitude reduction factor S_0^2 = 0.94 was determined from the fitting of EXAFS spectra for Cu foil.

Computational details.

Based on density functional theory, all calculations in this paper are performed by Vienna Ab-initio simulation software package (VASP)[71] using the projected- augmented-wave (PAW) method[72] and the Perdew-Burke-Ernzerhof (PBE) exchange correlation functional[42]. The energy cutoff was set to 400 eV and the Brillouin zone was sampled by a Gamma 1×1×1 K-point grid for structural optimization, while the 3×3×1 K-point grid was used for electronic state analysis. During structure optimization, the position of all the atoms except the bottom layer were relaxed and convergence criterion for the maximum force and energy on each atom was set to -0.05 eV/A˚ and 10^{-4} eV, respectively. In order to accurately describe the weak interactions, the dispersion-corrected DFT-D3 method[42] was employed to consider the van der Waals (vdW) interaction. To simulate the catalyst model in theory calculations, we designed a (2x2) super cell Cu (111), including 4 metal atoms in x direction, 4 metal atoms in y direction and 3 layers in z direction. Periodic boundary conditions were used in all directions and 20 Å of vacuum layer was used in the z direction to separate the slabs. The configuration and the surface coverage of functional groups was set to be 20 % in the model of modified Cu catalysts according to the characterization results from reaction mechanism and experiments. The two uppermost slab layers and the adsorbates are allowed to relax.

Theoretically valence analysis the theoretically valence of copper was calculated using the Bader Charge Analysis script written by Henkelman and co-workers[73]. The valence state of surface Cu atoms were evaluated according to the number of electrons obtained by the grafted aryl diazonium salts. We calculate the electronic charge (NCharge) of aryl diazonium salt bonded Cu atom by using the formal Bader charge from the outermost valence electron number (NValence) of Cu atom (1 for Cu) to subtract the calculated Bader charge of Cu (NBader), as follows[6,14,18]:

$$NCharge = NValence - NBader \quad (1)$$

After functionalizing with different aryl diazonium salts, the valences of bonded Cu atoms are characterized by positive charges with the values of +0.149 e, +0.206 e, +0.219 e, +0.260 e, +0.497 e, +0.630 e and +0.787 e for $N(C_2H_5)_2$, OCH_3, N, NN, NNN, Br and NO_2 functional groups, respectively.

The CO/CO_2 adsorption energy over functionalized Cu The adsorption energy of a CO/CO_2 molecule over a Cu surface in the presence and absence of functional groups was calculated by Equation:

$$Ead=E_{(CO,slab)} - E_{(slab)} - E_{(CO,gas)} \quad (2)$$

where *E(co, slab)* represents the total energy for a CO molecule over the Cu slab; Eslab is the total energy of the bare slab and E(co, gas) is the carbon monoxide gas phase energy. Here, the more negative value of the adsorption energy represents a stronger binding strength of the CO molecule. The same condition on CO_2 adsorption energy calculations.

The reaction energy of 2CO* dimerization over functionalized Cu To theoretically investigate the OC-CO coupling energy barriers on different Cu surface, a climbing image nudged elastic band (CI-NEB) method[74] was used to explore the transition state, followed by the dimer method to converge the saddle point within 0.05 eV/Å. Four windows are inserted between the initial state (IS) and the final state (FS) to find the transition state (TS) when calculating the CO-CO coupling process on both pure Cu and Cu-NN. At all intermediate and transition states, we applied a solvated surface with one layer of water molecules via the Neugebauer and Scheffler method to take the effect of solvation into account: five water molecules are added near the surface[6,14,18,74,75] Since Goodpaster, Norskov, Goddard, Neurock, and others have widely explored and simulated electric fields and charging effects by different methods[76-79]. In this work, we applied the Neugebauer and Scheffler method to include an applied electric field (-0.8 to 0.8 V/Å) [79]which was parallel to the vacuum layer to examine how an applied electric field may influence the selectivity of ethylene and ethanol in the presence of aryl diazonium salt (NN). According to the standard hydrogen electrode, the Gibbs free energy can be calculated as,

$$\Delta G=\Delta E\_DFT+\Delta E\_ZPE-T\Delta S \quad (3)$$

where T = 298.15 K, ΔE, ΔEZPE and ΔS are the total electron energy difference, zero-point energy difference and entropy change, respectively. This formula was proposed by Nørskov et al., since the entropy change is small, its effect can be ignored.

The relationship between Cu valence and CO_2 adsorption energy To understand how the NN-bonded Cu atom affects the valence of neighboring Cu atoms and the related CO_2 adsorption energy on differently neighboring Cu atoms, we took aryl diazonium salt (NN) functionalized Cu catalyst as an example to evaluate their relationships by a larger surface structure model. A (3x3) super cell Cu (111), including 6 metal atoms in x direction, 6 metal atoms in y direction and 3 layers in z direction was adopted as a computational model. A total of 10 kinds of CO_2 adsorption models with different distances (C-Cu, the C here refers to C in the CO_2 molecular) were constructed, and the distance between NN-bonded Cu atom and C atom of CO_2 molecule is 2.597 ~ 9.556 Å.

Electrochemical in H-Cell and MEA configuration. All electrochemical measurements were carried out at ambient temperature and pressure using a VSP electrochemical station from Bio-Logic Science Instruments equipped with a 5 A booster and FRA32 module. The cell voltages reported in all figures were recorded without iR correction. All the potentials in the H-cell were converted to values with respect to the RHE potential using:

$$E_{RHE}=E_{Ag/AgCl}+0.197\ V+0.0591*pH \qquad (4)$$

In the H-cell configuration, Ag/AgCl (3.5 M KCl) and a Pt plate were used as reference and counter electrodes respectively. The electrolyte consisted in a 0.5 M KOH solution (99.9%, Sigma Aldrich), which was saturated with alternatively CO_2 (≥99.998, Linde) or Ar (5.0, Linde). Prior to any experiment, the anolyte and catholyte solutions were saturated by bubbling CO_2 or Ar for at least 20 min.

The MEA electrolyzer (Dioxide Materials) was composed of the Cu cathode, a Ti-IrO_x mesh anode and an anion exchange membrane (AEM, Sustainion® X37-50, Fuel cell store). The anode and cathode flow fields are made of titanium and stainless steel with geometric active areas of 4 cm^2 respectively. The anode was prepared by depositing IrO_x on a titanium support (0.002'' thickness, Fuel Cell Store) by a dip coating followed by thermal annealing. Briefly, the titanium mesh was firstly degreased with acetone and DI water, then etched in a 6 M HCl (Reagent Grade, Bioshop) solution heated to 80 °C to 90 °C for 45 min before dip coating. The solution used for dip coating consisted of 30 mg of $IrCl_3.xH_2O$ (Alfa Aesar) dissolved in 10 mL of an iso-propanol solution with 10% concentrated HCl. The etched titanium mesh was dipped into the $IrCl_3$ solution, dried in an oven at 100 °C for 10 min before calcination in air at 500 °C for 10 min. The dipping and calcination process was repeated until a suitable loading was achieved (2 mg cm^{-2})[119].

The AEM was firstly placed between the anode and cathode flow fields and then assembled together. The flow fields were mainly responsible for the effective supply in aqueous anolyte solution and humidified CO_2 over the respective surfaces of anode and cathode electrodes. The anode and cathode gaskets were placed between the flow fields and the respective electrodes to ensure proper sealing. An anion exchange membrane (Sustainion® X37-50) (Dioxide Materials) was activated in 1 M aqueous KOH solution for at least 24 hours, washed with deionized water and used as the anion-exchange membrane (AEM). A 0.5 M $KHCO_3$ anolyte solution was circulated through the anode compartment of the electrolyzer with the constant flow rate of 30 ml/min *via* a peristaltic pump, while CO_2 was supplied to the cathode side with a constant flow rate of 10 standard cubic centimeters per minute (sccm). After three-minutes of initial operation, a full-cell potential of -3.0 V was applied to the electrolyzer and the potential then was gradually increased with increments of -0.10 V or -0.05 V. The current was stabilized for 15-20 min between two voltage increments.

CO_2-to-C_2H_4 measurements in the cascade MEA system

An Ag electrode was used to convert CO_2 into CO in 0.1M $KHCO_3$ solution. The MEA cell possessed the same geometric active area of 4 cm^2. The first MEA setup was operated at -3.8 V with a CO_2 inlet flow rate of 10 sccm. The outlet of the first MEA setup was connected to a CO_2 capture solution using a 30 wt % ethanolamine aqueous solution. Purified CO was then supplied to the second MEA cell for conversion of CO to C_2H_4. 1 M KOH was used as the anolyte, and the CO-to-ethylene conversion was evaluated at different potentials from -2.0 to -3.0 V.

Quantification of the CO_2RR products. The electrochemical data were recorded while simultaneously collecting the CO_2RR gas products by using an automatic sampler connected to the cathode outlet. A cold trap was used a collect the liquid products before the sampler. For each applied potential, the gas products were collected at least 3 times with proper time intervals. The gas alliquots were then injected into an online gas chromatograph (Agilent, Micro GC-490) equipped with a TCD detector and Molsieve 5A column continuously. Hydrogen and argon (99.9999%) were used as the carrier gases. Liquid products were quantified by 1H NMR spectroscopy (600 Mhz Avance III Bukrer with a cryorobe Prodigy TCI) using deionized water with 0.1 % (w/w) of DSS (Sodium trimethylsilylpropanesulfonate) like internal standard for the quantification of the ethanol and formate. An 1D sequence water suppression with excitation sculpting with gradients(zgesgp) was used for the acquisition (Number of scan = 32, Delay D1=30 s). Owing to the liquid product crossover, the FE values of the liquid products were calculated based on the total amount of the products collected on the anode and cathode sides during the same period.

Stability measurements in the MEA configuration. For the stability tests, the MEA electrolyzer was operated at a constant voltage of -3.55 V with a continuous feed in CO_2. The gas products were collected at frequent time intervals and FE values were calculated from the average value obtained from three successive injections. As for the liquid products, the total liquid products were collected at the end of the experiments.

Faradaic Efficiency, Selectivity, Energy Efficiency and Energy power consumption Calculations. The Faradaic efficiency (FE, %) of each gas product was calculated as follows:

$$FE_{gas} = g_i \times v \times \frac{z_i}{RT} FP_0 \times \frac{1}{I_{total}} \times 100\% \qquad (5)$$

The Faradaic efficiency (FE, %) of each liquid product was calculated as follows:

$$FE_{liquid} = l_i \times \frac{z_i}{Q_{total}} F \times 100\% \qquad (6)$$

The formation rate (R) for each species(i) was calculated as follows:

$$R_i = \frac{Q_{total} \times FE_i}{96485 \times z_i \times t \times S} \qquad (7)$$

The single-pass conversion rate (SPC, %) of CO_2 to C_2H_4 was calculated as follows:

$$SPC = \frac{C_{C2H4} \times flow\ rate_{outlet}}{C_{CO2} \times flow\ rate_{inlet}} \times 100 \qquad (8)$$

The full-cell energy efficiencies (EE, %) was calculated as follows:

$$EE = \frac{(1.23 - E_i) \times FE_i}{E_{cell}} \qquad (9)$$

The selectivity (%) of ethylene was calculated as follows:

$$Selectivity_{C2H4} = \frac{2R_{C2H4}}{R_{CO} + R_{HCOOH} + 2R_{C2H4} + 2R_{C2H5OH}} \qquad (10)$$

The electrical power consumption (EPC, kWh) characterizes the amount of electric energy (typically expressed in kWh) that is required for producing 1 Nm^3 of product gas, and it was calculated as follows:

$$EPC = \frac{E_{cell} \times n \times F}{FE \times V_m} \qquad (11)$$

where g_i represents the volume fraction of gas product i; v represents the gas flow rate at the outlet in sccm; z_i represents the number of electrons required to produce one molecule of product i; I_{total} represents the total current; l_i represents the number of moles of liquid product i; Q_{total} represents the charge passed while the liquid products are being collected; C_{C2H4} and C_{CO2} represents the concentrations of C_2H_4 and CO_2 measured by online GC. P_0 = 1.01 × 10 5 Pa, T = 273.15 K, F = 96,485 C mol^{-1} and R = 8.314 $Jmol^{-1}K^{-1}$; t represents the electrolysis time (h); S represents the geometric area of the electrode (cm^2); E_i represents the thermodynamic potential (versus RHE) for CO_2RR to species i and E_{cell} represents the cell voltage in two-electrode setup (-1.15 V for CO_2-to-C_2H_4, and -1.06 V for CO-to-C_2H_4); V_m is the molar volume of ideal gas under normal conditions.

4.4 Results and discussion

4.4.1 Density functional theory calculations

We first carried out Bader charge analysis to investigate the impact of the electron-withdrawing ability of the substituted aryl groups on the valence of Cu based on the functionalization mechanisms (Fig.1a, and Supplementary Figs.1 and 2). Our calculations indicate that the nature of different substituents on the phenyl group can finely tailor the theoretical valence of diazotized Cu atoms[39,40] (Fig. 1b, Supplementary Figs.3 to 5 and Table 1). Our findings suggest that the nature of the substituents on the phenyl ring is to modulate the local electron density on copper and thereby precisely tune the oxidation state of both functional groups bonded Cu atoms and the neighboring Cu atoms (Fig. 1c). Consequently, new interfaces between $Cu^{\delta+}$ and Cu^0 regions are created in the aryl diazonium bonded copper system($0<\delta<1$) (Fig. 1c), a motif analogous to the famous Cu_2O/Cu catalyst proposed by Goddard group14. To clear how the functional group affects the oxidation state of Cu atoms and regulate the CO_2 reduction, the adsorption energy of CO_2 on different $Cu^{\delta+}$ (δ=0,0.10, 0.12, 0.15 and 0.18) atoms were investigated based on the same Cu-NN catalyst system (Fig. 1c, Supplementary Fig.6 and Table 2). And we found that the CO_2 adsorption energy gradually increased with the closer distance of $Cu^{\delta+}$ atoms to Cu-NN atom. The nearest $Cu^{0.18+}$ atom showed the largest CO_2 adsorption energy of -0.468 eV among all $Cu^{\delta+}$ (δ=0,0.10, 0.12, 0.15 and 0.18) atoms while the farthest Cu0 atom had the lowest one. It means that the CO_2 activation and further reduction reaction (CO dimerization) are much easier to conduct on the nearest $Cu^{0.18+}$ atom instead of the farthest Cu^0 atom in Cu-NN catalyst. The lower energy barrier of CO dimerization on Cu-NN catalyst than pristine Cu (Fig. 1d, Supplementary Figs.7 to 11 and Table 3) also proves that the CO dimerization prefers to proceed on the interface of $Cu^{\delta+}/Cu^0$ than Cu^0/Cu^0 in Cu-NN catalyst (Fig. 1e), which is consistent with the classic Cu_2O/Cu catalyst proposed by Goddard et al14 that the interface of Cu^+/Cu^0 promotes the C_{2+} production by decreasing the reaction energy. In general, the grafted electro-withdrawing ability of aryl

diazonium salts on copper improves the oxidation state of part copper atoms and create the new interface region of $Cu^{\delta+}/Cu^0$ and thereby promote C_{2+} production. Moreover, the highest adsorption energy of CO on Cu-NN among all functional groups also proves that CO dimerization on Cu-NN is enhanced by the stronger binding energy of CO compared to pure Cu (Supplementary Fig.12 and Table 4).

Since ethylene and ethanol are generally considered to share the same initial reaction pathway, starting from *COCOH but branching off from the $*CH_2COH$ intermediate[41]. To get insight into the ethylene vs. ethanol selectivity, we explored the role of the oxidation state of $Cu^{\delta+}$ (δ=0, 0.149, 0.206, 0.219, 0.260, 0.493, 0.630 and 0.787 for pristine Cu, $N(C_2H_5)_2$, OCH_3, N, NN, NNN, Br and NO_2, respectively) on the free energy of the successive intermediates along with the ethylene ($*O+C_2H_4(g)$) and ethanol ($*C_2H_4O$) pathways (Supplementary Figs.13 to16). Our results reveal a lowest free energy on Cu-NN ($Cu^{0.26+}$) for $*O+C_2H_4(g)$ (ethylene pathway) than for $*C_2H_4O$ (ethanol pathway). These findings indicate that NN grafted Cu with the oxidation state of δ= 0.26 favors the formation of the $*O+C_2H_4(g)$ intermediate by breaking the C-O bond instead of the direct hydrogenation of the C-H bond to form $*CH_2CH_2OH$[41] (Fig.1f, Supplementary Figs.13 to16 and Table.5). NN functionalized Cu displayed the lowest free energy of -1.625 eV towards ethylene among all catalysts, suggesting a largest selectivity towards the formation of ethylene (Fig.1f). The retained overall trends of a smaller free energy of producing ethylene ($O*+C_2H_4(g)$) than ethanol ($*OCHCH_3$) under a series of different external electric fields also reflect that NN functionalized copper has the higher selectivity towards ethylene than ethanol production[18] (Supplementary Fig. 17 and Table 6). Meanwhile, the free energy of hydrogen evolution reaction (HER) on both bare Cu and Cu-NN were also evaluated, and we found that the free energy of HER on Cu-NN was higher than bare Cu (Supplementary Fig. 18 and Table.7). It means that grafting NN on Cu can not only promotes CO dimerization but also suppress the HER. Using these results as guidelines, we anticipated that the functionalization of copper with substituted phenyl groups induces the formation of $Cu^{\delta+}/Cu^0$ interface on Cu electrodes, which not only benefits for the formation of multi-carbon products compared to Cu^0 but also leads to high selectivity towards ethylene over ethanol.

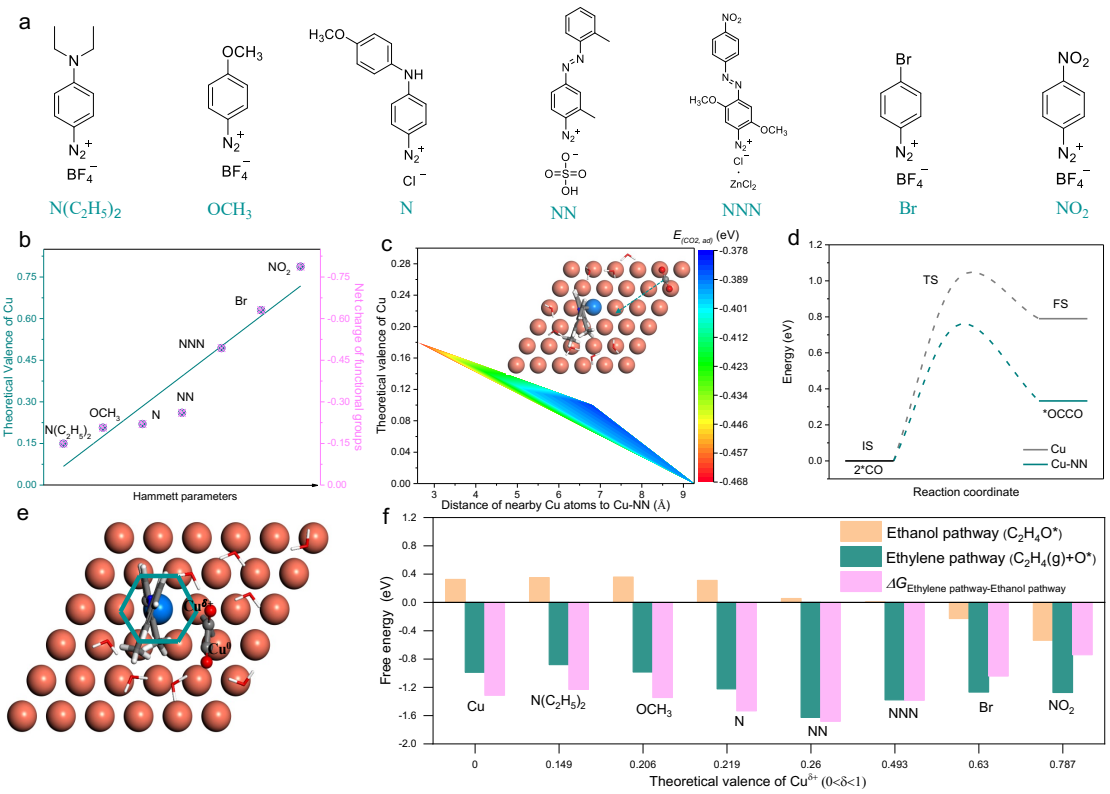

Fig. 1 Density functional theory calculations. (a) Molecular structures of different diazonium salts. **(b)** The relationship between the theoretical valence of the Cu sites and the electro-withdrawing ability of different substitutes on phenyl. **(c)** The relationship among the distance of the nearby Cu atoms to the Cu-NN atom, the theoretical valence of nearby Cu atoms and the related CO_2 adsorption energy on nearby Cu atoms. Inset: the model of CO_2 molecular adsorbed on Cu^0 and nearby $Cu^{\delta+}$ ($0<\delta<1$) atoms. (d) Energy profiles for initial states (ISs), transition states (TSs), and final states (FSs) of CO dimerization on Cu and Cu-NN. (e) The schematic of CO dimerization on nearby $Cu^{\delta+}$ and Cu^0 atoms in NN functionalized copper slab (The blue ball is NN functionalized Cu atom). (f) Gibbs free energy difference associated with the ethylene and ethanol pathways on Cu-X (X refers to NO_2, Br, NNN, NN, N, OCH_3 and $N(C_2H_5)_2$ functional groups), respectively.

4.4.2 Catalyst synthesis and characterization

In light of our numerical simulations, we sought to fabricate a series of copper catalysts via electrodeposition on a gas diffusion layer (GDL). The Cu catalysts were subsequently modified with aryl diazonium salts and labeled hereafter Cu-X where X represents the grafted aryl groups (Fig. 1a). The reactivity of aryl diazonium salts on copper follows two mechanisms: a direct attachment of the phenyl groups or the formation of new azo groups[24,42-45] (Supplementary Figs. 1 and 2). Based on our XPS analyses, we confirmed that the grafting mechanism involves the formation of azo bonds as evidenced by the presence of the signal at 400 eV. Signals from the N=N bonds were detected on all functionalized copper catalysts, including Cu-Br and Cu-OCH_3, with an estimated 3:2 molar ratio of Br/OCH_3 to azo. (Supplementary Fig. 19 and Supplementary Table 8). The morphology and crystal structure of functionalized Cu catalyst do not substantially change after the modification with diazonium salts, suggesting functionalization does not induce amorphization of the Cu surface (Figs. 2a, b and Supplementary Figs. 20 to 22). In particular, high-resolution electron microcopy analyses showed the presence of a continuously

functionalized layer at the surface of the catalysts with a thickness of about 5-8 nm (Figs. 2a, b and Supplementary Fig. 23a). In addition, based on our EELS analyses (Figs. 2b and Supplementary Fig. 23b), we confirmed the presence of C and N in the functionalized layer, which highlights the successful grafting of diazonium molecules at the surface of the Cu catalyst. To further improve the gas and ion transport to the active sites in the MEA cell, a perfluorinated sulfonic acid (PFSA) ionomer was spray-coated on the catalyst (Supplementary Fig. 24). The use of ionomers has been recently introduced to promote gas, water, and ion transport due to their hydrophobic and hydrophilic functionalities and ion transport domains, respectively[7,46-48]. The presence of the PFSA ionomer was further confirmed by its characteristic Raman signatures at 733,1005 and 1130 cm^{-1}, which are associated with the $-CF_2$, C-C, and $-SO_3$ vibrations modes, respectively[7] (Supplementary Fig. 25)[7]. Energy-dispersive X-ray spectroscopy (EDX) elemental mapping further supports the uniform distribution of ionomer on the surface of Cu-NN catalyst (Supplementary Fig. 26).

To elucidate the relationship between the molecular doping properties of the aryl groups and the behavior of the functionalized catalysts properties, we systematically evaluated the CO_2RR properties in a zero-gap MEA cell using a 0.5 M $KHCO_3$ anolyte and 10 sccm of CO_2 as feed for the cathode. Compared to pristine (i.e. non-functionalized) Cu, all the Cu-X electrodes exhibited improved Faradaic efficiency for ethylene (Fig. 2c and Supplementary Fig. 27 and Supplementary Table 9). We found a volcano relationship between the FE of C_2H_4 (FE_{C2H4}) and the applied potential and the Cu-NN catalyst exhibits the highest FE_{C2H4} at 83% for a full cell potential of -3.55 V. To explore the influence of NN thickness on CO_2RR performance, we prepared and examined different Cu-NN samples with different thickness by controlling the concentration of aryl diazonium salt. When we plotted the experimental C_2H_4 and CO Faradaic efficiency versus the thickness of NN, we obtained a volcano plot that peak with an outstanding C_2H_4 Faradaic efficiency of 83± 2% at a thickness of 5~8 nm (Supplementary Fig. 28). Differently, the FE of CO showed a trend of first increasing at a thinner thickness of NN and then decreasing at 5 nm thickness. It indicates that both too thin and too thick NN film were not conductive to *OC-CO* coupling in the CO_2RR process.

To investigate the correlation between the FE_{C2H4} and the oxidation state of different diazonium salts functionalized copper, we plotted the experimental FE_{C2H4} against the valence of the Cu sites predicted by our DFT calculations. We found a volcano trend that peaks at 83% at an average Cu valence of + 0.26, corresponding to the Cu-NN electrodes (Fig. 2d). We also observed a strong correlation between the ratio of FE_{C2H4} to FE_{C2H5OH} as a function of the calculated theoretical valence, confirming the influence of the valence on the selectivity of ethylene over ethanol (Supplementary Fig. 29). A FE_{C2H4}-to-FE_{C2H5OH} ratio as high as 38 is obtained on Cu-NN and agrees with our DFT predictions that $Cu^{\delta+}$ triggers the formation of ethylene rather than ethanol (Supplementary Figs. 29a and b). The performance of Cu-NN and pristine Cu were further increased in the presence of PFSA ionomer, and the Faradaic efficiency for ethylene reached 89±3% and 48±4% at a specific current density of C_2H_4 of 536 mA cm^{-2} and 269 mA cm^{-2}, respectively (Supplementary Figs. 30 and 31). To gauge the stability of our functionalization strategy, we operated the MEA cell at a full cell voltage of -3.55 V

for 120 h using Cu-NN as CO_2RR catalyst. We obtained a stable current at approximately 1 A with an average FE for C_2H_4 of 79% corresponding to a retention of 95% in a neutral medium (Fig. 2e). Furthermore, to examine the stability of functional group (NN) on copper, we also characterized and analyzed the surface of Cu-NN catalyst after 24 hours reaction (hereafter aCu-NN) by using Raman and HRTEM. Compared to before reaction, the specific peaks of aromatic rings (~1600 cm-1) were still kept on aCu-NN catalyst, which means that the functional group (NN) was stable during the reaction (Supplementary Fig. 32). The high-resolution electron microcopy analyses also presented an intactly and continuously functionalized layer at the surface of aCu-NN catalyst with a thickness of about 4-8 nm, which was similar to the unreacted sample, indicating that the excellent stability of aryl diazonium salt (NN) on copper without changing the surface coating morphology during CO_2RR process.

Next, we sought to evaluate the selectivity, the energy efficiency (EE) and the electrical power consumption (EPC) for the production of C_2H_4 in a MEA cell. Compared to other literature benchmarks[6,7,49-52], both Cu-NN and Cu-NN/ionomer catalysts demonstrated improved selectivity towards ethylene and higher energy efficiency at the same specific current density of ~200 mA cm^{-2} (Figs. 2f and g, Supplementary Table 10). Remarkably, the EPC for the formation of ethylene on Cu-NN is 25% lower compared to the best reported catalyst tested in the same device configuration, suggesting a lower threshold to meet industrial requirements (Supplementary Table 10). To confirm the improvement of the intrinsic CO_2RR properties after aryl functionalization, we finally estimated the electrochemically active surface area (ECSA) of pristine Cu, Cu-NN and Cu-NN/ionomer catalysts by using the Pb underpotential deposition method (PbUPD) (Supplementary Fig. 33a and Supplementary Table 11). The ECSA-normalized partial current densities for C_2H_4 measured in the MEA cell are 96 mA cm^{-2} and 212 mA cm^{-2} for Cu-NN and Cu-NN/ionomer, which are ~2 and ~4.5 times higher than in the case of pristine Cu, respectively (Supplementary Fig. 33b). To exclude no preference of aryl diazonium groups grafting on different active sites, we also functionalized both Cu(111) and Cu(100) single crystals with the same geometric area and the same loading amount of aryl diazonium group of NN, and compared their surface coverage by examining their electrochemically active surface areas. As shown in Supplementary Fig. 34 and Table 12, the surface coverage of NN on Cu(111) and Cu(100) single crystals are 20.6% and 21.8%, with the estimated ECSA of 1.20 cm^2, 1.27 cm^2, 0.95 cm^2 and 0.99 cm^2 for Cu(111), Cu(100), Cu(111)-NN and Cu(100)-NN catalysts, respectively, which are close to the surface coverage of 18.5% on electrodeposited Cu-NN. It means that functional groups have no preference when modifying on different active sites.

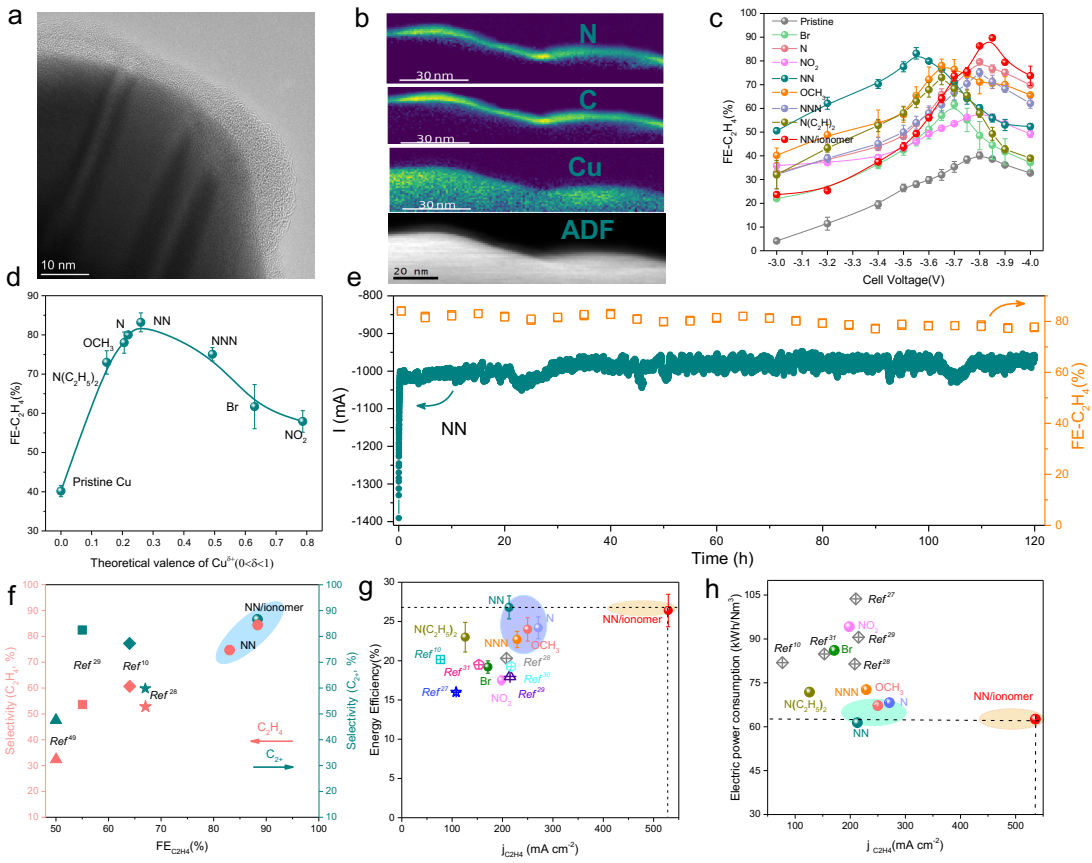

Fig. 2 Structural, compositional and CO_2RR performance for the different Cu-X catalysts measured in MEA flow cells. X refers to NO_2, Br, NNN, NN, N, OCH_3 and $N(C_2H_5)_2$ functional groups. **(a)** HR-TEM image, (**b**) the corresponding N, C and Cu EELS elemental maps and corresponding ADF image taken from a section of Cu surface on the NN-functionalized Cu electrode. (**c**) Comparison of FEs for ethylene on the different Cu electrodes measured at full-cell potentials ranging from -3.0 to −4.0 V and measured in 0.5 M $KHCO_3$. (**d**) The relationship between FE_{C2H4} and the theoretical valences of the Cu sites on the different catalysts. (**e**) CO2RR performance of NN-Cu at a full-cell potential of -3.55 V and with a 10 sccm feed in CO2 over 120 hours. The anolyte consisted in a 0.5 M $KHCO_3$ solution circulating at a flow rate of 30 ml min^{-1}. The blue line represents the current recorded during the extended CO2RR experiment (primary *y* axis). The empty orange symbols represent the FE for C_2H_4 averaged from three independent measurements (secondary *y* axis). Comparison of the selectivity (**f**), energy efficiency (**g**) and electric power consumption (**h**) for C_2H_4 based measured on the different Cu-X cathodes with literature benchmarks for MEA electrolyzers. For each reference, the plotted values are those corresponding to the reported best performance. The error bars in **c** and **d** correspond to the standard deviation of three independent measurements.

4.4.3 Ex-situ and operando investigations

To investigate the impact of the aryl functionalization on the oxidation states of copper, we first performed ex-situ X-ray photoelectron spectroscopy (XPS) on the different Cu-X catalysts. When examining the Cu2p spectra, the absence of satellites confirms that there is no Cu^{2+} (Supplementary Fig. 35). As it is difficult to distinguish the Cu+ from the Cu from the Cu2p spectra, we examined the LMM Auger signals from freshly prepared Cu-X samples to precisely evaluate the oxidation state of copper[53]. According to the deconvolution of the Auger LMM

spectra, we found that the Cu-NO_2 surface has the largest ratio of Cu^+ to Cu and the average oxidation state is estimated to be +0.75, while Cu-$N(C_2H_5)_2$ has the smallest oxidation state at δ=0.13 (Supplementary Table 13). Overall, our Auger analyses qualitatively agree with the results from DFT calculated theoretical valence.

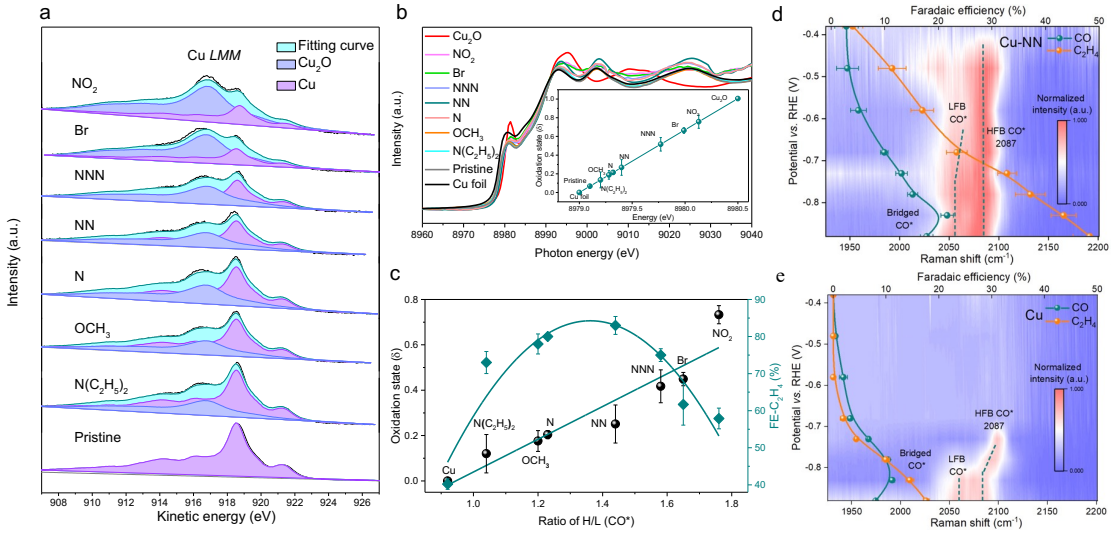

Fig. 3 XAS, Auger and *operando* Raman characterizations. (a) The copper *LMM* Auger spectra of the Cu-X electrodes. The amounts of Cu_2O and Cu contributions were estimated from the integrated area of the corresponding curves. **(b)** Copper K-edge XANES spectra of Cu-X catalysts after being electrochemically reduced. Inset: average oxidation state of copper in Cu-X obtained from copper K-edge XANES. The edge position of each sample is determined from the intercept of the main edge and pre-edge contributions. The error bars represent the standard deviation of three separate measurements for each sample. **(c)** The relationship between the FE for ethylene, the oxidation state of copper in Cu-X and the ratio of H/L CO* obtained from the *operando* Raman spectra of the Cu-X electrodes at -0.88 V versus RHE. H and L refer high frequency and low frequency modes. **(d)** The correlations between the FE_{CO}, the FE_{C2H4} and the *operando* Raman heatmaps of Cu-NN electrode and pristine Cu measured from -0.88 V to -0.38 V *vs.* RHE. Only the CO region is examined here (1900-2200 cm^{-1}). The error bars in **b**, **c**, **d** and **e** correspond to the standard deviation of three independent measurements.

We then carried out X-ray absorption near-edge spectroscopy (XANES) on the Cu-X catalysts to assess the Cu oxidation state. Before testing, a negative potential (-0.7 to -2.0 V versus reversible hydrogen electrode (RHE), 60 mV s^{-1}, 3 cycles) was applied on Cu-X samples to exclude oxygen-containing species. The absorption edges of all Cu-X samples reside between those of pristine copper (Cu0) and Cu2O used as a reference (Cu^+) (Fig. 3b and Supplementary Fig. 36). To obtain a direct comparison of the oxidation state of copper in the different Cu-X catalysts, we plotted the copper oxidation state as a function of energy shift of the Cu K-edge (Fig. 3b inset). From the linear fit of the positions for Cu0 and Cu^+ (Cu_2O), we determined the average oxidation state of the Cu-X catalysts to range between +0.13 to +0.75 as a function of the electron-withdrawing ability of substituted phenyl groups. Cu-NN exhibits an oxidation state of δ=0.27, which remarkably closes to the calculated theoretical valence of copper (δ=0.26) (Supplementary Table 14). To further explore the stability of $Cu^{δ+}$ species on Cu-NN, we performed operando X-ray absorption spectroscopy (XAS) at applied potentials of -0.93 V, -0.88 V, and -

0.83 V vs. RHE (Supplementary Figs. 37 and 38). Close examination of the XAS spectra suggests a minimal perturbation of the oxidation state of Cu during the CO2RR. We determined the average oxidation states of copper in Cu-NN to be +0.25, +0.23, and +0.19 at -0.93 V, -0.88 V, and -0.83 V vs. RHE, respectively close to that obtained from our ex-situ analyzes (Supplementary Tables 15 and 16).

To increase our understanding of the role of different functional groups in promoting the formation of ethylene, we studied the adsorbed CO* on the surface of the Cu-X catalysts using operando Raman spectroscopy (Supplementary Figs. 39 and 40). According to literatures, the LFB-CO* has previously been attributed to adsorbed CO* on top of terrace-like sites and related to OC-CO coupling and ethylene production[54,55], whereas the presence of the HFB-CO* peak at 2087 cm^{-1} is ascribed to adsorbed CO on isolated defect-like sites and more related to gaseous CO production according to previous operando measurements on well-defined systems[56-58]. Therefore, we examined the high-frequency band (HFB-CO*) and the low-frequency band CO* (LFB-CO*) of CO* at ~2087 cm^{-1} and ~2060 cm^{-1}, respectively[54,59,60] (Fig. 3c). These bound CO* configurations were identified and quantified using operando Raman spectroscopy for the different Cu–X catalysts at a fixed potential of -0.88 V vs. RHE (Supplementary Fig. 41 and Supplementary Table 17)[6,54,61,62]. We found that the HFB-CO*-to-LFB-CO* ratio on all Cu–X catalysts are larger compared with bare Cu, and presents a clear linear correlation with the average oxidation state of copper (Fig. 3c). The change of the ratio of HFB-CO*-to-LFB-CO* on Cu–X catalysts derives from the tailored binding energy of CO* by functional groups (Supplementary Fig. 12) that changes the vibrational signals of CO* at low-wave number region, thereby reflecting different adsorbed sites on copper and resulting in different adsorbed H/L-CO* ratios. Our investigations indicate that the average oxidation state of copper should be neither too high nor too low. We found a volcano-shaped relationship between the ethylene selectivity and the HFB-CO*-to-LFB-CO* ratio on the Cu–X surfaces, which highlights the importance of the balance between terrace-like and defect-like sites on Cu for the adsorption of CO* and the promotion of the OC-CO coupling. We note that Cu-NN seats near to the top of the volcano, which further points out to a possible stabilization of HFB-CO* relative to LFB-CO* on mildly oxidized $Cu^{\delta+}$ ($0<\delta<1$).

We compared the operando Raman spectra of Cu-NN and pristine Cu catalysts (Fig. 3d) for different potentials. The Raman heat map of the Cu-NN and pristine Cu revealed a clear enhancement of the signals from adsorbed CO* in the case of Cu-NN, which qualitatively indicates that larger amounts of CO* intermediates are readily available for the further C-C coupling. We also found that Cu-NN displays strong HFB-CO* and LFB-CO* signals for potentials between -0.48 V and -0.7 V vs. RHE up to -0.88 V vs. RHE, while no signals can be detected from pristine Cu (Fig. 3e). This points out to a greater energy barrier to produce CO* intermediates, thus limiting the formation of C_{2+} products. As the final evidence, we plotted the FE for CO and C_2H_4 as functions of the potential to visualize the intertwining between the Raman signatures of adsorbed CO* and the selectivity for C_{2+} products (Figs. 3d and e). To exclude the influence of interactions between CO_2 and "N" atoms from aryl diazonium salts (N, NN, NNN, NO_2 and $N(C_2H_5)_2$), the related aryl diazonium salts functionalized copper was exposed with CO_2 atmosphere. Since diazonium salts $N(C_2H_5)_2$ contains a more nucleophilic nitrogen atom

(tertiary amine) compared to N, NN, NNN, and NO_2 diazonium salts, we decided to investigate the reactivity of diazonium salts $N(C_2H_5)_2$, NN, Cu-$N(C_2H_5)_2$, Cu-NN and pristine Cu by using CO_2-temperature programmed desorption (TPD). Firstly, we tested the thermogravimetric analysis (TGA) and found Cu-$N(C_2H_5)_2$, Cu-NN and pristine Cu kept stable at the range of 50-200 ºC (Supplementary Fig. 42a). Therefore, we tested CO_2-temperature programmed desorption (TPD) with Cu- $N(C_2H_5)_2$, Cu-NN and pristine Cu catalysts at the stable temperature range of 50 to 200 ºC to observe their interactions with CO_2. As shown in Supplementary Fig. 42b, there is no any CO_2 absorption peak on pristine Cu at the temperatures from 50-200 ºC, which means that no interaction happened between CO_2 and pristine Cu at this temperature range. Compared to pristine Cu, both Cu-$N(C_2H_5)_2$ and Cu-NN displayed a small peak at ~68 ºC and ~70 ºC with the similar intensity, indicating the "N" on both NN and $N(C_2H_5)_2$ would interact with CO_2 and enhance the CO_2RR reaction activity by providing additional binding sites for CO_2. The analogical adsorption energy of CO2 on Cu- $N(C_2H_5)_2$ and Cu-NN (Supplementary Fig. 12) also reflect their similar interactions with CO2. However, the FEC2H4 (73%) of Cu-$N(C_2H_5)_2$ catalyst is lower than Cu-NN (FE_{C2H4}=83%) but higher than pristine Cu (FE_{C2H4}=40%), which means that the valence of copper plays the more critical role than the interaction between amine and CO_2 in enhancing CO_2RR.

4.4.4 Direct vs. cascade flow processes for the formation of C_2H_4

The electrical power consumption is one the primary obstacle for the development of the CO_2RR. Although progress has been made in the direct electroreduction of CO_2 to C_2H_4 in MEA cells with appreciable selectivity and high current density, the requested full-cell potential makes the production cost of ethylene uncompetitive compared to industrial-grade ethylene obtained from steam cracking of naphta or natural gas. In addition, the formation of carbonate in the MEA reactor combined to the strongly alkaline conditions leads to poor performance stability and low CO_2 single-pass conversion rate due to the flow of hydroxide ions from anode that reacts with gas CO_2. Technical-economic analyses have suggested that a high current density (>150 mA cm^{-2}), and low operating full-cell potential (< 3 V) are the necessary requirements to compete with the traditional ethylene production process[50]. CO can advantageously replace CO_2 to produce multicarbon species via the CO reduction reaction (CORR). The CORR is compatible with alkaline electrolytes at the anode to prevent the competitive hydrogen evolution reaction without significant carbonate formation that typically plagues the conversion of CO_2[63]. It is also anticipated that the CORR can improve the charge transfer kinetics and the selectivity towards ethylene, while decreasing the energy footprint of the system[10,11,64]. The realization of cascade flow processes has recently been explored to convert CO_2 to CO and then use CO to produce C_{2+} products[65,66].

In light of this, we sought to develop an integrated flow electrochemical system for the energy-efficient conversion of CO_2 to C_2H_4 by coupling two MEA cells using Cu-NN as CORR catalyst. Considering the high market price of iridium (at ~ 6k$ per once, +375% since Nov. 2020), we thought to replace expensive IrOx with NiFe based layered double hydroxide (NiFe LDH) as anode catalyst[67]. We confirmed that NiFe LDH shows a lower overpotential than IrOx toward the OER in 1 M KOH (Supplementary Fig. 43). We then estimated the

CO_2-to-CO performance using electrodeposited Ag and NiFe based layered double hydroxide (NiFe LDH) as cathode and anode, respectively. We achieved a 94% FE for CO at the full-cell potential of -3.55 V and a specific current density for CO of 119 mA cm^{-2} for an inlet flow rate of 10 sccm of CO_2 (Supplementary Fig. 44, and Supplementary Table 18). We evaluated the single-pass conversion efficiency (SPCE) to be ~31% at -3.55 V. To achieve an optimal CO feed of ~4.6 sccm, we set the full-cell voltage of the first MEA cell to -3.8 V corresponding to a FE and specific current density for CO of ~84% and 166 mA cm^{-2}, respectively. The outlet gas from the Ag-based MEA was purified using a CO_2 capture solution containing 30% ethanolamine and then introduced into the second MEA cell for the CO-to-C_2H_4 conversion. We tested the CO-to-C_2H_4 conversion system using pristine Cu, Cu-NN, and Cu-NN/ionomer as cathode, and IrOx as anode catalysts. The FE for C_2H_4 on Cu-NN reached a record-high values for the CORR at ~86.0% and a full-potential of -2.5 V. Cu-NN clearly outperforms Cu and Cu-NN/ionomer with FEC2H4 of ~67.4% and ~72.1%, respectively (Supplementary Fig. 45 and Supplementary Table 19).

The operating cell voltage (ECell) for the CO_2RR is known to be responsible for a significant electrical consumption and the oxidation evolution reaction (OER) at the anode brings a high energy penalty to the process[5]. By operating the cascade MEA cells with NiFe LDH and Cu-NN as anode and cathode catalysts, we achieved an optimal E_{Cell} of -2.3 V for maximizing the production of ethylene with a FE_{C2H4} of ~86% (Fig. 4a and Supplementary Fig. 46 and Supplementary Table 20). We determined a stable full-cell energy efficiency of 39.6% and a 12.3% CO_2-to-C_2H_4 cascade single pass conversion efficiency for the cascade flow process with a specific current density of 154 mA cm^{-2}. For comparison, Cu-NN/ionomer and pristine Cu catalysts exhibit EEs of 30.5% and 27.4% and CO_2-to-C_2H_4 cascade conversion rates of 12.9% and ~6.0% at -2.3 V, respectively (Figs. 4b and c, Supplementary Fig. 47 and Table 21). The formation rates of ethylene on Cu-NN/ionomer increased by 191% compared to pristine Cu electrodes. We estimated an EPC value of only 25.6 kWh Nm-3 for the Cu-NN+NiFe LDH system – lower than for Cu-NN/ionomer and Cu (Fig.4b and Supplementary Table 21). Remarkably, the cascade system maintained a 10.7 % CO_2-to-C_2H_4 conversion rate at an average specific current density of 140 mA cm^{-2} for 100 h (Fig.4d and Supplementary Table 22). We finally compared the performance of the Cu-NN and Cu-NN/ionomer catalysts with previous literature benchmarks[6,7,49,50,52,65,66,68-70] and found that Cu-NN display greater energy efficiency and lower EPC for both the direct and the cascade flow processes (Figs. 5a, b).

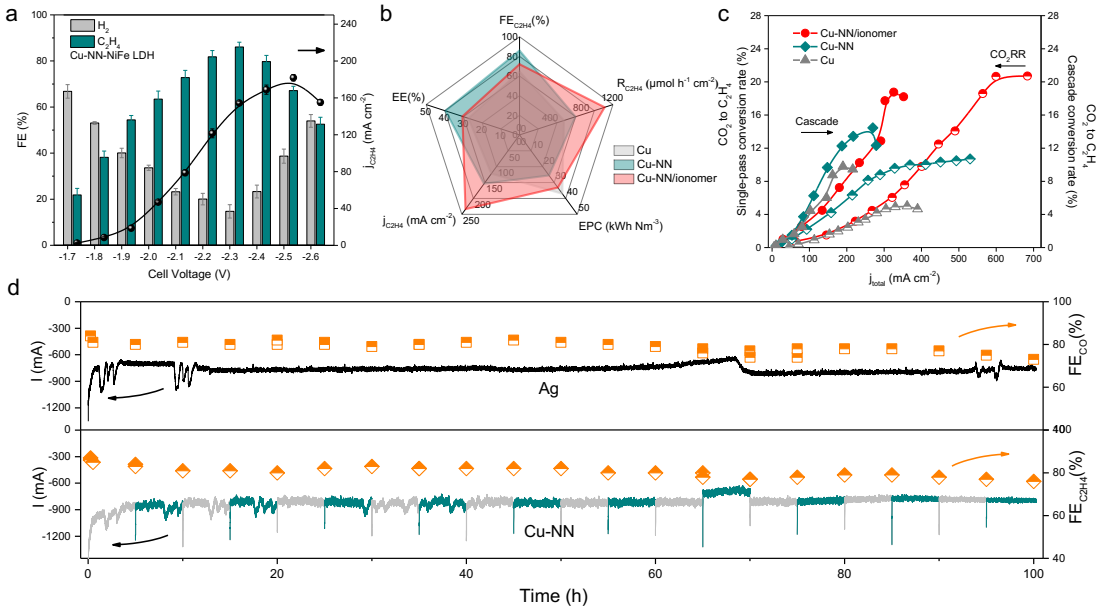

Fig. 4 CO_2-to-C_2H_4 performance in the cascade flow process. (a) The FE for C_2H_4 obtained using CO as feed. (**b**) Comparison of different performance of the Cu-X electrodes: Faradaic efficiency (FE), energy efficiency (EE), specific current density (j), energy power consumption (EPC) and formation rate (R) of C_2H_4. (**c**) Comparison of the CO_2-to-C_2H_4 single-pass conversion measured for a single MEA cell (half-filled sphere) and for the cascade flow process (filled sphere). (**d**) The stability of Ag and Cu-NN catalysts in MEA cells. The error bars in **a** and **c** correspond to the standard deviation of three independent measurements.

To explore the wider application of aryl diazonium salts-tailored catalysts' oxidation state strategy in CO_2RR, we further prepared NN functionalized commercial Cu electrode (cCu-NN) and electrodeposited Ag sample (Ag-NN) (Supplementary Figs. 48 and 49) and examined their performance in MEA electrolyzers. As displayed in Supplementary Fig. 50, the Faradaic efficiency of ethylene on cCu-NN electrode can get to 42%, which is higher than blank cCu electrode (FE_{C2H4}=33%). Furthermore, the Auger LMM and XANES results also prove that the average oxidation state of copper from cCu-NN has been improved after modifying with NN. It means that the strategy of tailoring Cu valence by grafting aryl diazonium salt to improve CO_2RR activity is generalized. Most importantly, the increased oxidation state of Ag and the decreased FE_{CO} from Ag-NN prove that aryl diazonium salt affects the CO_2RR activity by changing the valence of grafted metals instead of directly interacting with CO_2 (Supplementary Fig. 51). From DFT calculations, the almost similar adsorption energy of CO_2 on both Cu and Cu-NN electrodes also indicates that the interaction between functional groups and CO_2 can be neglected, even though there are some nitrogen atoms on it (Supplementary Fig. 6). Furthermore, to exclude the anion's effect on CO_2RR activity, a new aryl diazonium salt with the same anion as NN while the similar cation as N was modified on copper. The new diazonium salt functionalized Cu electrode displayed a ~74% Faradaic efficiency towards C_2H_4 at 3.8 V, which was close to Cu-N instead of Cu-NN catalyst, indicating that the cation's configuration on aryl diazonium salt plays a more important role in affecting the CO_2RR performance than the anion (Supplementary Fig. 52).

To assess the economic viability of electro-reduction of CO_2 to C_2H_4 on Cu, Cu-NN, and Cu-NN/ionomer, we carried out techno-economic analyses by comparing the direct conversion route (CO_2-to-C_2H_4 in a single reactor) with the two steps cascade systems (CO_2-to-CO, and CO-to-C_2H_4 in cascade system). We considered a single MEA cell to convert CO_2 to C_2H_4 using a neutral 0.5 M $KHCO_3$ anolyte, while 0.1 M $KHCO_3$ and 1 M KOH were used as anolytes in the first and the second MEA cells for the CO_2-to-CO, and CO-to-C_2H_4 reactions (See Note S1 in the Supplementary Information for details). We determined the OPEX of the direct and the cascade flow processes for the production of 1 ton of C_2H_4 with/without the use of ionomer. In our calculations, we assumed a catalyst lifetime of one year (8,760 hours) and a total electrode surface of 100 m^2. Figs. 5c and d show the cost distribution for the different parameters, without considering the CO_2 loss due to carbonate formation and membrane crossover as well as the downstream separation costs. We note that the installation costs and the balance of plant are part of the capitalization expenditure (CAPEX) and are not included in our calculations (See Note S2 in the Supplementary Information file). Among the four different MEA configurations, we found that direct conversion of CO_2 to ethylene using Cu-NN and ionomer is the closest to profitability. Importantly the cost of ethylene production decreases from 12,600 \$ ton^{-1} to 4,500 \$ ton^{-1} using pristine Cu and Cu-NN/ionomer electrodes, respectively, which corresponds to a 64% reduction. The analysis of the cost breakdown highlights that, in absence of ionomer, the main expense items for the direct production of the C_2H_4 from CO_2 are the anode catalyst and the membranes for a total of 57.4% of the production cost. The use of ionomer lowers the cost (per ton of C_2H_4) of most parameters due to the improvement of the yield rate of the process and the EPC accounts for most of the expenses (32.6%) (Fig. 5c and d). Conversely, in the cascade configuration, the cost of the anion-exchange membrane (AEM) represents the main expense for Cu-NN and Cu-NN/ionomer conditions at 47.1% and 39.4%, respectively (Fig. 5c and d). These findings point to the opportunity to rapidly improve the profitability of CO_2RR by decreasing the cost to electrolyte membranes (Supplementary Table 23). Overall, aryl functionalized $Cu^{+0.26}$ holds potential to lower the financial gap between the low carbon-footprint CO_2RR technology and the traditional ethylene production based on fossil resources.

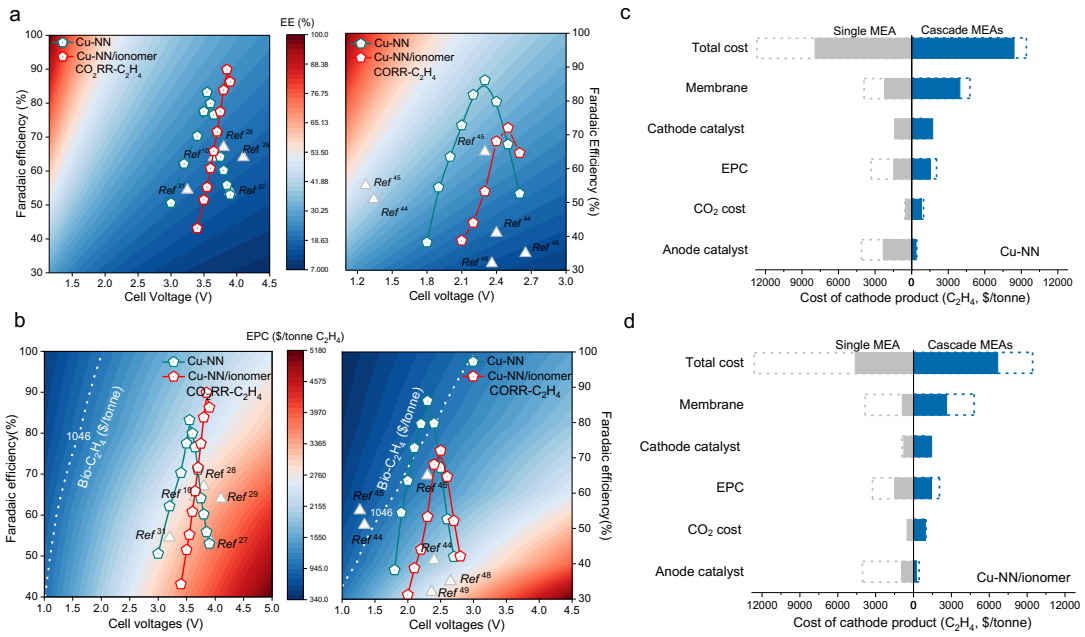

Fig. 5 Techno-economic analyses for the CO_2-to-C_2H_4 conversion based on the direct and the cascade flow processes. The comparison of energy efficiency (EE) (**a**) and the cost of the electrical power consumption (**b**) for the CO_2-to-C_2H_4 and the CO-to-C_2H_4 reactions. Comparison of operational costs for production of C_2H_4 on Cu-NN(**c**) and Cu-NN/ionomer(**d**) in both single MEA and cascade MEA systems (the dash line refers to pristine Cu).

4.5 Conclusions

This work presents a novel approach to orient the CO_2RR and the CORR towards the production of ethylene with record-high selectivity and formation rate. The origin of the high selectivity for C_{2+} products is attributed to the formation of stable $Cu^{\delta+}$ ($0<\delta<1$) as supported by our *operando* and *ex-situ* physical characterizations using XPS, XAS and Raman spectroscopy. We attributed the near-unity selectivity for C_2H_4 among the C_{2+} products to the lower energy associated with the formation of the $*CH_2CH$ intermediate on $Cu^{0.26+}$. When implemented in a neutral MEA cell, the Cu-NN catalyst achieved a FE for ethylene of 83 ± 2 % with a partial ethylene current density of 212± 3 mA cm^{-2}. The full-cell EE and the conversion efficiency for ethylene can be further increased to 39.6% and 12.3%, respectively, with a low record-low EPC of 25.6 kWh/Nm^3 by replacing CO_2 for CO in a cascade flow process. Our findings provide a route towards practical developments for the CO_2-to-C_2H_4 conversion reaction using valence engineering of the Cu sites.

4.6 References

1 Bushuyev, O. S. et al. What should we make with CO_2 and how can we make it? Joule 2, 825-832 (2018).

2 Ager, J. W. & Lapkin, A. A. Chemical storage of renewable energy. Science 360, 707-708 (2018).

3 Jouny, M., Luc, W. & Jiao, F. General techno-economic analysis of CO_2 electrolysis systems. Industrial & Engineering Chemistry Research 57, 2165-2177 (2018).

4 Verma, S., Kim, B., Jhong, H. R. M., Ma, S. & Kenis, P. J. A gross-margin model for defining

technoeconomic benchmarks in the electroreduction of CO_2. ChemSusChem 9, 1972-1979 (2016).

5 Verma, S., Lu, S. & Kenis, P. J. Co-electrolysis of CO_2 and glycerol as a pathway to carbon chemicals with improved technoeconomics due to low electricity consumption. Nature Energy 4, 466-474 (2019).

6 Li, F. et al. Molecular tuning of CO_2-to-ethylene conversion. Nature 577, 509-513 (2020).

7 García de Arquer, F. P. et al. CO_2 electrolysis to multicarbon products at activities greater than 1 A cm− 2. Science 367, 661-666 (2020).

8 Zhong, M. et al. Accelerated discovery of CO_2 electrocatalysts using active machine learning. Nature 581, 178-183 (2020).

9 Ma, S., Luo, R., Moniri, S., Lan, Y. & Kenis, P. J. Efficient electrochemical flow system with improved anode for the conversion of CO_2 to CO. Journal of The Electrochemical Society 161, F1124 (2014).

10 Verma, S., Lu, X., Ma, S., Masel, R. I. & Kenis, P. J. The effect of electrolyte composition on the electroreduction of CO_2 to CO on Ag based gas diffusion electrodes. Physical Chemistry Chemical Physics 18, 7075-7084 (2016).

11 Dinh, C.-T. et al. CO_2 electroreduction to ethylene via hydroxide-mediated copper catalysis at an abrupt interface. Science 360, 783-787 (2018).

12 Weng, L.-C., Bell, A. T. & Weber, A. Z. Towards membrane-electrode assembly systems for CO_2 reduction: a modeling study. Energy & Environmental Science 12, 1950-1968 (2019).

13 Jouny, M., Hutchings, G. S. & Jiao, F. Carbon monoxide electroreduction as an emerging platform for carbon utilization. Nature Catalysis 2, 1062-1070 (2019).

14 Xiao, H., Goddard, W. A., Cheng, T. & Liu, Y. Cu metal embedded in oxidized matrix catalyst to promote CO2 activation and CO dimerization for electrochemical reduction of CO_2. Proceedings of the National Academy of Sciences 114, 6685-6688 (2017).

15 De Luna, P. et al. Catalyst electro-redeposition controls morphology and oxidation state for selective carbon dioxide reduction. Nature Catalysis 1, 103-110 (2018).

16 Arán-Ais, R. M., Scholten, F., Kunze, S., Rizo, R. & Roldan Cuenya, B. The role of in situ generated morphological motifs and Cu (i) species in C2+ product selectivity during CO2 pulsed electroreduction. Nature Energy 5, 317-325 (2020).

17 Eilert, A., Roberts, F. S., Friebel, D. & Nilsson, A. Formation of copper catalysts for CO_2 reduction with high ethylene/methane product ratio investigated with in situ X-ray absorption spectroscopy. The journal of physical chemistry letters 7, 1466-1470 (2016).

18 Zhou, Y. et al. Dopant-induced electron localization drives CO_2 reduction to C2 hydrocarbons. Nature chemistry 10, 974-980 (2018).

19 Lee, S., Kim, D. & Lee, J. Electrocatalytic production of C3-C4 compounds by conversion of CO2 on a chloride-induced bi-phasic Cu_2O-Cu catalyst. Angewandte Chemie 127, 14914-14918 (2015).

20 Pinson, J. Attachment of organic layers to materials surfaces by reduction of diazonium salts. Aryl

diazonium salts, 1-35 (2012).

21 Berisha, A., Chehimi, M. M., Pinson, J. & Podvorica, F. Electrode surface modification using diazonium salts. Electroanalytical Chemistry 26 (2015).

22 Allongue, P. et al. Covalent modification of carbon surfaces by aryl radicals generated from the electrochemical reduction of diazonium salts. Journal of the american chemical society 119, 201-207 (1997).

23 Belanger, D. & Pinson, J. Electrografting: a powerful method for surface modification. Chemical Society Reviews 40, 3995-4048 (2011).

24 Mooste, M. et al. Surface and electrochemical characterization of aryl films grafted on polycrystalline copper from the diazonium compounds using the rotating disk electrode method. Journal of Electroanalytical Chemistry 817, 89-100 (2018).

25 Kendig, M., Hon, M. & Sinko, J. Inhibition of Oxygen Reduction on Copper in Neutral Sodium Chloride. ECS Transactions 1, 119 (2006).

26 Chira, A., Bucur, B. & Radu, G.-L. Electrodeposited organic layers formed from aryl diazonium salts for inhibition of copper corrosion. Materials 10, 235 (2017).

27 Li, D. et al. Surface functionalization of nanomaterials by aryl diazonium salts for biomedical sciences. Advances in Colloid and Interface Science 294, 102479 (2021).

28 Gillan, L., Teerinen, T., Johansson, L.-S. & Smolander, M. Controlled diazonium electrodeposition towards a biosensor for C-reactive protein. Sensors International 2, 100060 (2021).

29 Hetemi, D., Noël, V. & Pinson, J. Grafting of diazonium salts on surfaces: Application to biosensors. Biosensors 10, 4 (2020).

30 Laufer, R. S. & Dmitrienko, G. I. Diazo group electrophilicity in kinamycins and lomaiviticin A: potential insights into the molecular mechanism of antibacterial and antitumor activity. Journal of the American Chemical Society 124, 1854-1855 (2002).

31 Mahouche-Chergui, S., Gam-Derouich, S., Mangeney, C. & Chehimi, M. M. Aryl diazonium salts: a new class of coupling agents for bonding polymers, biomacromolecules and nanoparticles to surfaces. Chemical Society Reviews 40, 4143-4166 (2011).

32 Wei, G. et al. Covalent modification of reduced graphene oxide by means of diazonium chemistry and use as a drug-delivery system. Chemistry–A European Journal 18, 14708-14716 (2012).

33 Shewchuk, D. M. & McDermott, M. T. Comparison of diazonium salt derived and thiol derived nitrobenzene layers on gold. Langmuir 25, 4556-4563 (2009).

34 Kim, C. et al. Insight into electrochemical CO_2 reduction on surface-molecule-mediated Ag nanoparticles. ACS Catalysis 7, 779-785 (2017).

35 Fang, Y. & Flake, J. C. Electrochemical reduction of CO_2 at functionalized Au electrodes. Journal of the American chemical society 139, 3399-3405 (2017).

36 Wang, J. et al. Fastening Br–ions at copper–molecule interface enables highly efficient electroreduction

of CO_2 to ethanol. ACS Energy Letters 6, 437-444 (2021).

37 Knochel, P. et al. Highly functionalized organomagnesium reagents prepared through halogen–metal exchange. Angewandte Chemie International Edition 42, 4302-4320 (2003).

38 Baquero, E. A., Tricard, S., Flores, J. C., de Jesús, E. & Chaudret, B. Highly stable water-soluble platinum nanoparticles stabilized by hydrophilic n-heterocyclic carbenes. Angewandte Chemie 126, 13436-13440 (2014).

39 Hammett, L. P. The effect of structure upon the reactions of organic compounds. Benzene derivatives. Journal of the American Chemical Society 59, 96-103 (1937).

40 Hansch, C., Leo, A. & Taft, R. A survey of Hammett substituent constants and resonance and field parameters. Chemical reviews 91, 165-195 (1991).

41 Li, Y. C. et al. Binding site diversity promotes CO_2 electroreduction to ethanol. Journal of the American Chemical Society 141, 8584-8591 (2019).

42 Hurley, B. L. & McCreery, R. L. Covalent bonding of organic molecules to Cu and Al alloy 2024 T3 surfaces via diazonium ion reduction. Journal of The Electrochemical Society 151, B252 (2004).

43 Doppelt, P., Hallais, G., Pinson, J., Podvorica, F. & Verneyre, S. Surface modification of conducting substrates. Existence of azo bonds in the structure of organic layers obtained from diazonium salts. Chemistry of Materials 19, 4570-4575 (2007).

44 Menanteau, T., Dias, M. n., Levillain, E., Downard, A. J. & Breton, T. Electrografting via diazonium chemistry: the key role of the aryl substituent in the layer growth mechanism. The Journal of Physical Chemistry C 120, 4423-4429 (2016).

45 Cai, J. et al. Chemical grafting of the superhydrophobic surface on copper with hierarchical microstructure and its formation mechanism. Applied Surface Science 436, 950-956 (2018).

46 Kusoglu, A. & Weber, A. Z. New insights into perfluorinated sulfonic-acid ionomers. Chemical reviews 117, 987-1104 (2017).

47 Allen, F. I. et al. Morphology of hydrated as-cast Nafion revealed through cryo electron tomography. ACS Macro Letters 4, 1-5 (2015).

48 Kreuer, K. D. & Portale, G. A critical revision of the nano-morphology of proton conducting ionomers and polyelectrolytes for fuel cell applications. Advanced Functional Materials 23, 5390-5397 (2013).

49 Ozden, A. et al. High-rate and efficient ethylene electrosynthesis using a catalyst/promoter/transport layer. ACS Energy Letters 5, 2811-2818 (2020).

50 Li, J. et al. Silica-copper catalyst interfaces enable carbon-carbon coupling towards ethylene electrosynthesis. Nature communications 12, 1-10 (2021).

51 Wang, Y. et al. Catalyst synthesis under CO_2 electroreduction favours faceting and promotes renewable fuels electrosynthesis. Nature Catalysis 3, 98-106 (2020).

52 Lee, W. H. et al. Highly selective and stackable electrode design for gaseous CO2 electroreduction to ethylene in a zero-gap configuration. Nano Energy 84, 105859 (2021).

53 Zhang, W. et al. Atypical oxygen-bearing copper boosts ethylene selectivity toward electrocatalytic CO_2 reduction. Journal of the American Chemical Society 142, 11417-11427 (2020).

54 Gunathunge, C. M. et al. Spectroscopic observation of reversible surface reconstruction of copper electrodes under CO_2 reduction. The Journal of Physical Chemistry C 121, 12337-12344 (2017).

55 Gunathunge, C. M., Ovalle, V. J., Li, Y., Janik, M. J. & Waegele, M. M. Existence of an electrochemically inert CO population on Cu electrodes in alkaline pH. ACS Catalysis 8, 7507-7516 (2018).

56 Lum, Y. & Ager, J. W. Evidence for product-specific active sites on oxide-derived Cu catalysts for electrochemical CO_2 reduction. Nature Catalysis 2, 86-93 (2019).

57 Hollins, P. The influence of surface defects on the infrared spectra of adsorbed species. Surface Science Reports 16, 51-94 (1992).

58 Kuhl, K. P., Cave, E. R., Abram, D. N. & Jaramillo, T. F. New insights into the electrochemical reduction of carbon dioxide on metallic copper surfaces. Energy & Environmental Science 5, 7050-7059 (2012).

59 Gunathunge, C. M., Li, J., Li, X., Hong, J. J. & Waegele, M. M. Revealing the Predominant Surface Facets of Rough Cu Electrodes under Electrochemical Conditions. ACS Catalysis 10, 6908-6923 (2020).

60 Gunathunge, C. M., Ovalle, V. J. & Waegele, M. M. Probing promoting effects of alkali cations on the reduction of CO at the aqueous electrolyte/copper interface. Physical Chemistry Chemical Physics 19, 30166-30172 (2017).

61 Heyes, J., Dunwell, M. & Xu, B. CO_2 reduction on Cu at low overpotentials with surface-enhanced in situ spectroscopy. The Journal of Physical Chemistry C 120, 17334-17341 (2016).

62 Akemann, W. & Otto, A. Vibrational modes of CO adsorbed on disordered copper films. Journal of Raman spectroscopy 22, 797-803 (1991).

63 Verma, S. et al. Insights into the low overpotential electroreduction of CO_2 to CO on a supported gold catalyst in an alkaline flow electrolyzer. ACS Energy Letters 3, 193-198 (2017).

64 Xiao, H., Cheng, T., Goddard III, W. A. & Sundararaman, R. Mechanistic explanation of the pH dependence and onset potentials for hydrocarbon products from electrochemical reduction of CO on Cu (111). Journal of the American Chemical Society 138, 483-486 (2016).

65 Yadegari, H. et al. Glycerol Oxidation Pairs with Carbon Monoxide Reduction for Low-Voltage Generation of C2 and C3 Product Streams. ACS Energy Letters 6, 3538-3544 (2021).

66 Ozden, A. et al. Cascade CO2 electroreduction enables efficient carbonate-free production of ethylene. Joule 5, 706-719 (2021).

67 Voiry, D. et al. High-quality graphene via microwave reduction of solution-exfoliated graphene oxide. Science 353, 1413-1416 (2016).

68 Ripatti, D. S., Veltman, T. R. & Kanan, M. W. Carbon monoxide gas diffusion electrolysis that produces concentrated C_2 products with high single-pass conversion. Joule 3, 240-256 (2019).

69 Rabinowitz, J. A. & Kanan, M. W. The future of low-temperature carbon dioxide electrolysis depends on

solving one basic problem. Nature Communications 11, 1-3 (2020).

70 Gabardo, C. M. et al. Continuous carbon dioxide electroreduction to concentrated multi-carbon products using a membrane electrode assembly. Joule 3, 2777-2791 (2019).

71 Perdew, J. P., Burke, K. & Ernzerhof, M. Generalized gradient approximation made simple. Physical review letters 77, 3865 (1996).

72 Blöchl, P. E. Projector augmented-wave method. Physical review B 50, 17953 (1994).

73 Henkelman, G., Arnaldsson, A. & Jónsson, H. A fast and robust algorithm for Bader decomposition of charge density. Computational Materials Science 36, 354-360 (2006).

74 Henkelman, G., Uberuaga, B. P. & Jónsson, H. A climbing image nudged elastic band method for finding saddle points and minimum energy paths. The Journal of chemical physics 113, 9901-9904 (2000).

75 Montoya, J. H., Shi, C., Chan, K. & Nørskov, J. K. Theoretical insights into a CO dimerization mechanism in CO_2 electroreduction. The journal of physical chemistry letters 6, 2032-2037 (2015).

76 Goodpaster, J. D., Bell, A. T. & Head-Gordon, M. Identification of possible pathways for C–C bond formation during electrochemical reduction of CO_2: new theoretical insights from an improved electrochemical model. The journal of physical chemistry letters 7, 1471-1477 (2016).

77 Neugebauer, J. & Scheffler, M. Adsorbate-substrate and adsorbate-adsorbate interactions of Na and K adlayers on Al (111). Physical Review B 46, 16067 (1992).

78 Montoya, J. H., Peterson, A. A. & Nørskov, J. K. Insights into C- C Coupling in CO_2 Electroreduction on Copper Electrodes. ChemCatChem 5, 737-742 (2013).

79 Cheng, T., Xiao, H. & Goddard III, W. A. Free-energy barriers and reaction mechanisms for the electrochemical reduction of CO on the Cu (100) surface, including multiple layers of explicit solvent at pH 0. The journal of physical chemistry letters 6, 4767-4773 (2015).

4.7 Notes

4.7.1 Note S1. Techno-economic assessment (TEA) of ethylene performance in CO2RR systems based on membrane-electrode-assembly (MEA) electrolyzers.

To assess the energy and cost associated with CO_2 to ethylene on our catalysts (Cu, Cu-NN and Cu-NN/ionomer), we performed energy and techno-economic assessments (TEA) for two CO_2RR systems based on MEA models. We have compared the energy and cost distributions of producing ethylene for single MEA system (CO_2-to-C_2H_4, Schematic.1) and the cascade MEA systems (CO_2-to-CO and CO-to-C_2H_4, Schematic.1).

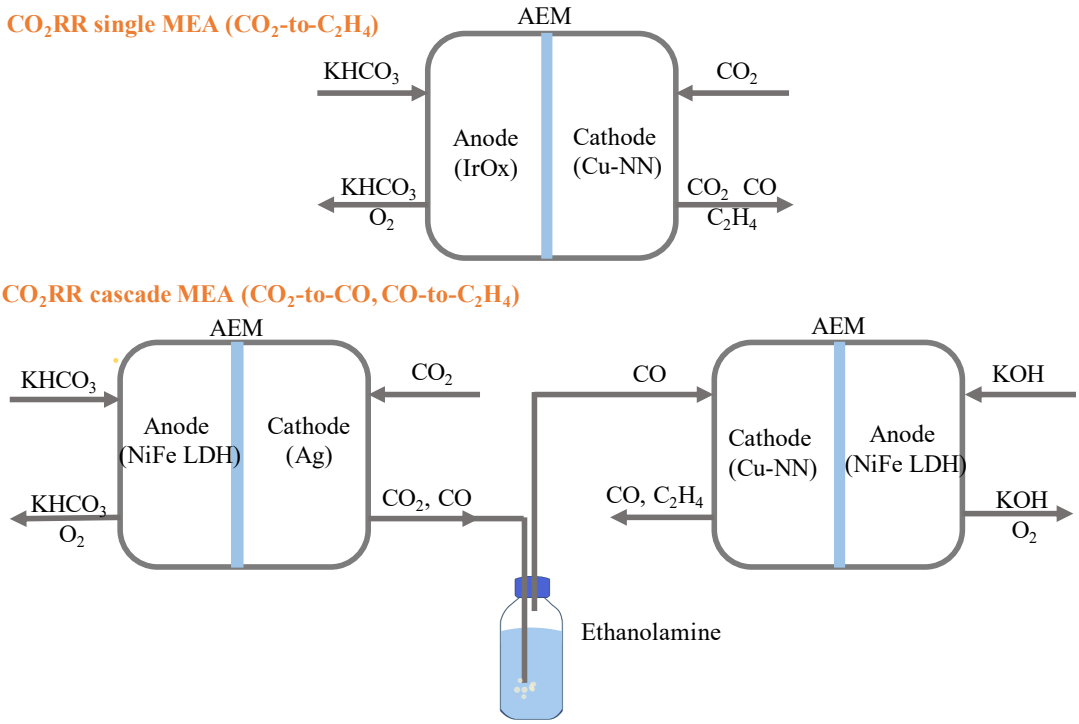

Schematic 1. Models of single CO_2RR MEA system (a) and the cascade CO_2RR MEA system (b).

4.7.2 Note S2. Details of techno-economic assessment (TEA).

In our models, we calculate the cost of producing C_2H_4 per year based on the different C_2H_4 formation rates from our different catalysts (Cu, Cu-NN and Cu-NN/ionomer) without considering the CO2 loss (carbonate formation and cross over the membrane), products separation costs and installation costs, as well as the balance of plant.

For the cathode, we integrate our catalysts (Cu, Cu-NN and Cu-NN/ionomer) into MEA with the physical area of electrode of 100 m^2. In the cascade condition, we use Ag as the cathode for the first electrolyzer. For the membrane, we use anion-exchange membrane (Sustainion® X37-50) (Dioxide Materials) for all electrolyzers and the lifetime is regarded as 1 year. For the anode, the loading amount of 2 mg cm^{-2} IrOx on Ti mesh is used as the anode (physical area of 100 m^2) for single Cu-based MEA. In the cascade Cu-based MEA and Ag-based MEA systems, the NiFe based layered double hydroxide (NiFe LDH) supported on a Ti mesh as the anode. The lifetime for all anodes is also regarded as 1 year.

For the electrolyte, we use 0.5 M $KHCO_3$, 0.1 M $KHCO_3$ and 1 M KOH as the anolyte for single Cu-based MEA, Ag-based MEA and cascade Cu-based MEA systems, respectively. The amount of electrolyte required in our TEA model was calculated using the ratio of 100 L electrolyte per m^2 of electrolyzer. This ratio is based on approximate ratios used in lab-scale experiments and it provides a starting point to estimate electrolyte costs. Once a total volume of electrolyte is calculated, it is assumed to be circulated through the electrolyzer constantly for one year before being completely replaced. Therefore, the total cost of purchasing electrolyte with a 100 L/m^2 ratio is reduced to a daily cost to find the cost per tonne of product. This calculation provides an estimate of the cost of electrolyte.

In the cascade system, to adsorb the unreacted CO_2 from the gas outlet side of Ag-based MEA, 30 wt% ethanolamine solution is applied to this cascade system. According to real testing condition in 4 cm^2 MEA electrolyzer, we calculate the required ethanolamine in 100 m^2 MEA electrolyzer and the amount for 30 wt% ethanolamine is around 10000 L for one year MEA operation. And we think the unreacted CO_2 is completely adsorbed by 30 wt% ethanolamine. It is assumed that the only by-product produced on the cathode side is hydrogen and that the anode performs OER, producing only oxygen. Once the total amount of electrolyzer materials, input chemicals, and electricity are purchased, there are some external systems that are modelled.

Cathode input CO_2 cost

For single MEA system, we first calculate the different conversion rates of CO_2 to C_2H_4 on different catalysts (Cu, Cu-NN and Cu-NN/ionomer) based on their C_2H_4 formation rates. Then we can multiply the market price of CO_2 (30$/ton) to get the total cost of cathode input CO_2. And here we calculate the data of Cu-NN as an example.

The calculation is given by:

$$CO_2\ required\left(\frac{tonne\ CO_2}{tonne\ C_2H_4}\right) = C_2H_4\left(tonne\ \frac{C_2H_4}{day}\right) \times \frac{molecular\ weight_{CO2}}{molecular\ weight_{C2H4}} \times molar\ ratio\ \left(\frac{CO_2}{C_2H_4}\right) \times \frac{1}{conversion\ rate(CO_2\ to\ C_2H_4)} \quad (1)$$

Plugging in numbers gives us:

$$CO_2\ required\ \left(\frac{tonne\ CO_2}{tonne\ C_2H_4}\right) = 0.443\ \left(tonne\ \frac{C_2H_4}{day}\right) \times \frac{44\frac{g}{mol}}{28\frac{g}{mol}} \times \frac{2}{1} \times \frac{1}{8.35\%}$$

$$= 16.67\ \frac{tonne\ CO_2}{tonne\ C_2H_4} \quad (2)$$

$$Cost\ of\ cathode\ input\ CO_2\ \left(\frac{\$}{tonne\ C_2H_4}\right) = 30\frac{\$}{tonne\ CO_2} \times\ 16.67\ \frac{tonne\ CO_2}{tonne\ C_2H_4}$$

$$= 500.1\frac{\$}{tonne\ C_2H_4} \quad (3)$$

Electrolyzer cost

In single MEA system, to find the cost of the electrolyzer, the total power needed was multiplied by the cost per kW provided above.

According to the formation rate of C_2H_4 on Cu-NN (0.443 tonne/day), we can easily know C_2H_4 production (mol/s).

$$C_2H_4 \text{ production}\left(\frac{mol}{s}\right) = \frac{C_2H_4 \text{ production}\left(\frac{g}{day}\right)}{molecular\ weight_{C2H4} \times 86400\left(\frac{s}{day}\right)} = \frac{0.443 \times 10^6\ (\frac{g}{day})}{28\left(\frac{g}{mol}\right) \times 86400(\frac{s}{day})}$$

$$= 0.183\ \frac{mol}{s} \qquad (4)$$

Next, we can find the total current needed to produce this much C_2H_4, taking into account the loss of electrons as the FE is 83% on Cu-NN catalyst.

$$Total\ current\ (A) = \frac{C_2H_4 \text{ production}\left(\frac{mol}{s}\right) \times\ electrons\ transferred\ \times Faraday's\ constant}{FE_{C2H4}}$$

$$= 0.183\frac{mol}{s} \times 12 \times 96485\frac{sA}{mol} \div 83\% = 255278\ A \qquad (5)$$

Now, multiplying by the cell voltage (3.55 V) to give the power consumed:

$$Power\ consumed(W) = total\ current\ (A) \times Cell\ voltage\ (V) \quad = 255278\ A\ \times 3.55\ V = 906238\ W$$

$$= 906.238\ kW \quad (6)$$

Multiplying the price of electrolyzer and scaling by the current density gives:

$$total\ electrolyzer\ cost(\$)$$

$$= power\ consumed\ (kW) \times electrolyzer\ cost\ \left(\frac{\$}{kW}\right) \times \frac{specific\ current\ density_{C2H4}}{input\ total\ current\ density}$$

$$= 906.238\ kW \times 300\ \left(\frac{\$}{kW}\right) \times \frac{212}{256} = 225143\$ \qquad (7)$$

Finally, the cost for producing per tonne C_2H_4 can be calculated as below,

$$Total\ electrolyzer\ cost\left(\frac{\$}{tonne\ C_2H_4}\right) = \frac{total\ electrolyzer\ cost(\$)}{total\ produced\ C_2H_4\ (tonne)} = \frac{225143\$}{162\ tonne}$$

$$= 1389.77\left(\frac{\$}{tonne\ C_2H_4}\right) \qquad (8)$$

For cascade MEA system,

The total electrolyzer cost should include the cost for the first Ag-based MEA (CO_2 to CO) and the second Cu-NN-based MEA (CO to C_2H_4).

For the first MEA (CO_2 to CO), a production rate of 0.75 mol/s for CO can be achieved on Ag cathode according to the FE_{CO} and CO formation rate. Next, we can find the total current needed to produce this much CO, taking into account the loss of electrons as the FE is 84% on Ag catalyst.

$$Total\ current\ (A) = \frac{\text{CO production}\left(\frac{mol}{s}\right) \times\ electrons\ transferred\ \times Faraday's\ constant}{FE_{CO}}$$

$$= 0.75\frac{mol}{s} \times 2 \times 96485\frac{sA}{mol} \div 84\% = 172294\ A \qquad (9)$$

Multiplying by the cell voltage (3.8 V) to give the power consumed:

$$Power\ consumed(W) = total\ current\ (A) \times Cell\ voltage\ (V) \quad = 172294\ A\ \times 3.8\ V = 654.7\ W$$

$$= 654.7\ kW$$

Then, the cost for producing per tonne C_2H_4 (Cu-NN) can be calculated as below,

$$Total\ electrolyzer\ cost_{Ag}\left(\frac{\$}{tonne\ C_2H_4}\right) = \frac{total\ electrolyzer\ cost_{Ag}(\$)}{total\ produced\ C_2H_4\ (tonne)}$$

$$= \frac{654.7kW \times 300\ \left(\frac{\$}{kW}\right) \times \frac{149}{173}}{181.4\ tonne\ C_2H_4} = 932.6\ \left(\frac{\$}{tonne\ C_2H_4}\right) \qquad (10)$$

Next, we can calculate the C_2H_4 production in the second MEA electrolyzer with Cu-NN, bare Cu and Cu-NN/ionomer as the cathodes and the values are 0.199 mol/s, 0.17 and 0.31 mol/s, respectively (the details can be found in the method part of manuscript).

Here, we take Cu-NN as an example.

Now, multiplying by the cell voltage (2.3 V) to give the power consumed:

$$Power\ consumed(W) = total\ current\ (A) \times Cell\ voltage\ (V) \quad = 178609\ A\ \times 2.3\ V = 410800\ W$$

$$= 410.8\ kW \qquad (11)$$

Multiplying the price of electrolyzer and scaling by the current density gives:

$$Total\ electrolyzer\ cost_{Cu-NN}(\$)$$

$$= power\ consumed\ (kW) \times electrolyzer\ cost\ \left(\frac{\$}{kW}\right) \times \frac{specific\ current\ density_{C2H4}}{input\ total\ current\ density}$$

$$= 410.8\ kW \times 300\ \left(\frac{\$}{kW}\right) \times \frac{154}{179} = 106028\$ \qquad (12)$$

Finally, the cost for producing per tonne C_2H_4 can be calculated as below,

$$Total\ electrolyzer\ cost_{Cu-NN}\left(\frac{\$}{tonne\ C_2H_4}\right) = \frac{total\ electrolyzer\ cost(\$)}{total\ produced\ C_2H_4\ (tonne)} = \frac{106028\$}{181.4\ tonne}$$

$$= 584.5\left(\frac{\$}{tonne\ C_2H_4}\right) \qquad (13)$$

$$Total\ electrolyzer\ cost\left(\frac{\$}{tonne\ C_2H_4}\right)$$
$$= \ total\ electrolyzer\ cost_{Ag}\left(\frac{\$}{tonne\ C_2H_4}\right) + total\ electrolyzer\ cost_{Cu-NN}\left(\frac{\$}{tonne\ C_2H_4}\right)$$
$$= 932.6\left(\frac{\$}{tonne\ C_2H_4}\right) + 584.5\ \left(\frac{\$}{tonne\ C_2H_4}\right)$$
$$= 1517.1\ \left(\frac{\$}{tonne\ C_2H_4}\right) \qquad (14)$$

Electricity power consumption (EPC)

In single MEA system, to find the cost of electricity, we can calculate the total energy input according to electricity power consumption formular (Eq. 10 in the manuscript). Using this, we multiply by 24 hours to find the energy required to produce 1 tonne of C_2H_4 (as our production rate is 0.443 tonne C_2H_4 per day) and multiply by the electricity cost. Here, we use an electricity price of 0.03\$ kWh^{-1}, taken from recent onshore wind power auctions. The cost of electricity can be calculated as:

$$Cost\ of\ electricity\left(\frac{\$}{tonne\ C_2H_4}\right) = \frac{Power\ consumption(kw) \times 24\ h \times electricity\ price\left(\frac{\$}{kW\ h^{-1}}\right)}{C_2H_4\ Production\ \left(\frac{tonne\ C_2H_4}{day}\right)}$$
$$= \frac{906.238\ kW \times 24\ h \times 0.03\frac{\$}{kW\ h}}{0.443\ \left(\frac{tonne\ C_2H_4}{day}\right)} = 1472.89\$\ (\frac{1}{tonne\ C_2H_4}) \qquad (15)$$

For cascade MEA system, the total EPC cost should be calculated by adding the cost for the first Ag-based MEA (CO_2 to CO) and the second Cu-NN-based MEA (CO to C_2H_4).

For the first Ag-based MEA (CO_2 to CO), we first calculate the energy input according to the method introduced above, and the input energy is 654.7 kW. The formation rate of C_2H_4 from the second Cu-NN-based MEA is 0.497 tonne per day. Here, we also take Cu-NN as an example. The same calculation methods on bare Cu and Cu-NN/ionomer.

$$Cost\ of\ electricity_{Ag}\left(\frac{\$}{tonne\ C_2H_4}\right) = \frac{Power\ consumption(kw) \times 24\ h \times electricity\ price\left(\frac{\$}{kW\ h}\right)}{C_2H_4\ Production\ \left(\frac{tonne\ C_2H_4}{day}\right)}$$
$$= \frac{654.7\ kW \times 24\ h \times 0.03\frac{\$}{kW\ h}}{0.497\ \left(\frac{tonne\ C_2H_4}{day}\right)}$$
$$= 948.45\$\ \left(\frac{1}{tonne\ C_2H_4}\right) \qquad (16)$$

For the second Cu-NN-based MEA (CO to C_2H_4), the input energy is 412.115 kW. Then we use the same method to get the EPC cost and the value is 597 \$/tonne C_2H_4.

Finally, we plus the cost from the first and the second MEA and divide the amount of C_2H_4.

$$Cost\ of\ electricity\left(\frac{\$}{tonne\ C_2H_4}\right) = cost\ of\ electricity_{Ag}\left(\frac{\$}{tonne\ C_2H_4}\right) + cost\ of\ electricity_{Cu-NN}\left(\frac{\$}{tonne\ C_2H_4}\right) = 948.45\left(\frac{\$}{tonne\ C_2H_4}\right) + 597\left(\frac{\$}{tonne\ C_2H_4}\right) = 1545.55\left(\frac{\$}{tonne\ C_2H_4}\right) \quad (17)$$

Cathode catalyst cost

Since we assume the physical area and lifetime of cathode and anode is 100 m^2 and 1 year, then we can calculate the loading amount of copper and functional groups on the gas diffusion layer. According to price of gas diffusion layer (862 \$/m^2, 22BB, Ion power company), we can calculate the total price of the carbon support is 86200 \$.

The total loading amount of electrodeposited copper can be calculated according to the below formula:

$$m_{Cu} = \frac{molecular\ weight_{Cu}\left(\frac{g}{mol}\right) \times electrodepositing\ current\ \left(\frac{A}{m^2}\right) \times electrodepostion\ time\ (s) \times electrode\ area\ (m^2)}{transfered\ electrons \times e^-(C) \times Avogadro\ constant\ N_A(mol^{-1})} = \frac{64\left(\frac{g}{mol}\right) \times 150\frac{A}{m^2} \times 300\ s \times 100 m^2}{2 \times 1.6 \times 10^{-19} C\ \times 6.022 \times 10^{23}\ mol^{-1}} = 1494.5\ g \quad (18)$$

We use $CuBr_2$ as the source of copper, and the needed mass of $CuBr_2$ is calculated as 3367.338g according to its molecular weight (223.35g/mol) (here, we assume all the copper from $CuBr_2$ have been completely reduced to copper crystal).

Following this method, we can calculate the depositing amount of NN on copper, and it is around 262.7g for 100 m^2 electrode.

So, the price for electrodepositing copper can be calculated according to the unit price of chemicals (200 \$/tonne for $CuBr_2$, 1110 \$/tonne for KOH, 1850 \$/tonne for $C_4H_4Na_2O_6.2H_2O$ and 35.1\$/g for NN), and the total chemical costs is 141307 \$ for preparing 100 m^2 cathode.

By plusing the price of GDL, we can get the total cost for fabricating 100 m^2 cathode and the cost is 141307\$ + 86200\$=227507 \$

As the production rate of C_2H_4 in single MEA system is 0.443 tonne per day, we can calculate the total amount of C_2H_4 produce in one year (161.69 tonne C_2H_4 per year). Then the cathode price of producing per tonne C_2H_4 in single MEA system is:

$$Cathode\ catalyst\ cost\ \left(\frac{\$}{tonne\ C_2H_4}\right) = \frac{GDL\ cost\ (\$) + catalyst\ cost(\$)}{total\ amount\ of\ C_2H_4(tonne)} = \frac{227507\$}{161.69\ tonne C_2H_4} =$$

$$1407.1\ \left(\frac{\$}{tonne\ C_2H_4}\right) \qquad (19)$$

The same calculation methods for the cascade MEA systems.

Membrane cost

As we use 100 m^2 cathode, so the physical area of membrane should be at least 100 m^2. And here, we calculate it based on 100 m^2 membrane size and we consider the membrane lifetime is 1 year. The price of anion-exchange membrane (Sustainion® X37-50, Dioxide Materials) is 3587.66 \$/m^2. So, using the total price of membrane (358766\$) divides the total amount of C_2H_4 (161.69 tonne per year) in single MEA system, we can get the cost of membrane of 2218.9 \$/tonne C_2H_4. The same calculation methods for the cascade MEA systems.

Anode catalyst cost

In single MEA system, we use the physical area of 100 m^2 IrOx-coated on Ti mesh as the anode with the loading amount of IrOx of 2 mg cm^{-2}. Since we obtain IrOx from $IrCl_3.xH_2O$, and then we can calculate the needed amount of $IrCl_3.xH_2O$ by assuming the conversion rate and the utilization rate of $IrCl_3.xH_2O$ to IrOx are 100%. According to the needed amount of $IrCl_3.xH_2O$ in 4 cm^2 MEA system (10.7 mg), we can deduce the needed amount of $IrCl_3.xH_2O$ for 100 m^2 anode (2663.3 g). By multiplying the price of $IrCl_3.xH_2O$ (147\$/g, 206245, Sigma-Aldrich), we can get the cost of 346190\$ of $IrCl_3.xH_2O$ for 100 m^2 anode.

Next, we calculate the cost of Ti mesh. As the price of Ti mesh is 324.2 \$ per m^2, we can get the total price of Ti mesh of 32420 \$ for 100 m^2.

Then, we can get the cost of anode catalyst for producing per tonne C_2H_4,

$$Anode\ catalyst\ cost\left(\frac{\$}{tonne\ C_2H_4}\right) = \frac{total\ anode\ catalyst\ price\ (\$)}{total\ C_2H_4\ produced\ for\ 1\ year\ (tonne)} = \frac{(346190 + 32420)\$}{161.69\ \ tonne}$$

$$= 2342\ \frac{\$}{tonne} \qquad (20)$$

For cascade MEA systems, we use NiFe-LDH on Ti mesh as the anode for whole system, including the first Ag-based MEA (CO_2 to CO) and the second Cu-NN-based MEA (CO to C_2H_4). Therefore, once we calculate one anode cost, doubling the cost of anode is the total anode cost for cascade system. The total cost of anode to produce per tonne C_2H_4 can be obtained by using the total anode cost divides the produced amount of C_2H_4 from the second Cu-NN-based MEA.

Firstly, we will calculate the needed amount of $Ni(NO_3)_2$ and $Fe(NO_3)_3$, because we prepare NiFe-LDH catalyst from $Ni(NO_3)_2$ and $Fe(NO_3)_3$ by hydrothermal method (the details can be found in the method of manuscript).

Here, the costs of $Ni(NO_3)_2$ and $Fe(NO_3)_3$ are 926 and 617 \$ tonne^{-1}. Next, we can calculate the total needed amount of $Ni(NO_3)_2$ and $Fe(NO_3)_3$ according to the needed mass in 4 cm^2 MEA system(0.0652 g for $Ni(NO_3)_2$ and 0.258 g for $Fe(NO_3)_3$). For 100 m^2 anode, it will need 0.0163 tonne $Ni(NO_3)_2$ and 0.0646 tonne $Fe(NO_3)_3$. Now, we can get the total cost of fabricating NiFe-LDH by multiplying their prices.

Finally, we can calculate the total cost for the whole cascade MEA systems (here, we take Cu-NN as an example).

$$Anode\ catalyst\ cost\left(\frac{\$}{tonne\ C_2H_4}\right) = \frac{total\ anode\ catalyst\ price\ (\$)}{total\ C_2H_4\ produced\ for\ 1\ year\ (tonne)} =$$

$$\frac{First\ Ag-based\ \ MEA + Second\ Cu-NN\ based\ MEA}{total\ C_2H_4\ produced\ for\ 1\ year\ from\ second\ Cu-NN\ based\ MEA(tonne)} =$$

$$\frac{2\times[0.0163tonne\times 926\left(\frac{\$}{tonne}\right)+0.0646tonne\times 617\left(\frac{\$}{tonne}\right)+32420\ \$]}{181.4\ tonne\ C_2H_4} = 358\left(\frac{\$}{tonne\ C_2H_4}\right) \quad (21)$$

Electrolyte (anolyte) cost

Here, we are going to show the calculation for a MEA cell using 0.5 M $KHCO_3$ at a cost of 750 \$ tonne^{-1} and by using a fixed volume factor of 100 L electrolyte m^{-2} of electrolyzer, approximated from common lab-scale experiments. We assume the electrode surface area is 100 m^2 and the lifetime is 1 year. So, the total needed volume of electrolyte is 10000 L.

With this volume, the molecular weight of potassium bicarbonate (100 g mol^{-1}), and the molarity of the anolyte, we can find the mass of potassium bicarbonate required.

The cost is calculated by:

$$Mass\ of\ electrolyte\ salt\ (g)$$
$$= electrolyte\ molarity\left(\frac{mol}{L}\right)\times electrolyte\ volume\ (L)$$
$$\times\ salt\ molecular\ weiught\left(\frac{g}{mol}\right) = 0.5\ \frac{mol}{L}\times\ 10000\ L\times 100\ \frac{g}{mol}$$
$$= 5\times 10^5\ g \quad (22)$$

The total cost of anolyte is found by multiplying by the price of potassium bicarbonate and the price of water (5 \$ tonne^{-1}):

$$Cost\ of\ electrolyte\ (\$) = mass\ of\ salt\ (tonne)\times price\ of\ salt\ \left(\frac{\$}{tonne}\right) + water\ volume\ (L)\times$$
$$water\ price\ \left(\frac{\$}{kg}\right) = 0.5\ tonne\times 750\frac{\$}{tonne} + 10000L\times 0.005\frac{\$}{kg} =$$
$$425\ \$ \quad (23)$$

Here, we do not consider the capital recovery factor of electrolyte. Finally, we go to find the price of producing per tonne of C_2H_4 on Cu-NN electrode,

$$Cost\ of\ electrolyte\ \left(\frac{\$}{tonne}\right) = \frac{cost\ of\ electrolyte\ (\$)}{produced\ C_2H_4\ in\ one\ year\ (tonne)} = \frac{425\$}{161.9\ tonne\ C_2H_4} = 2.63\left(\frac{\$}{tonne}\right) \quad (24)$$

Note that for cascade MEA system, 1 M KOH electrolyte was used with a cost of 1000 \$ tonne^{-1}.

Ethanolamine cost

For cascade MEA system, we use 30 wt% ethanolamine solution to adsorb the unreacted CO_2 from the outlet of Ag-based MEA. Since 40 ml 30 wt% ethanolamine solution is needed to completely absorb the unreacted CO_2 for the 4 cm^2 electrode MEA electrolyzer, around 10000 L 30 wt% ethanolamine solution is required for 100 m^2 electrode MEA electrolyzer. After dividing the concentration (30 wt%), we can get the needed amount pure ethanolamine of 0.3 tonne. As the cost of ethanolamine is 1500 \$/tonne, we can calculate the total cost of 450 \$ for pure ethanolamine. Then we calculate the water mass and the mass is 9.7 tonne. Multiplying the cost of water (5\$/tonne), we can get the total water cost of 48.5 \$. So, the total cost of 498.5 \$ for 10000 L 30 wt% ethanolamine solution. Dividing the C_2H_4 production on Cu-NN electrode, we can get the final cost. Here, we take Cu-NN as an example

$$ethanolamine\ cost_{Cu-NN}\left(\frac{\$}{tonne}\right) = \frac{total\ cost\ (\$)}{C_2H_4\ production\ (tonne)} = \frac{498.5\ \$}{181.4\ tonne} = 2.75\left(\frac{\$}{tonne}\right) \quad (25)$$

4.8 Supplementary Information

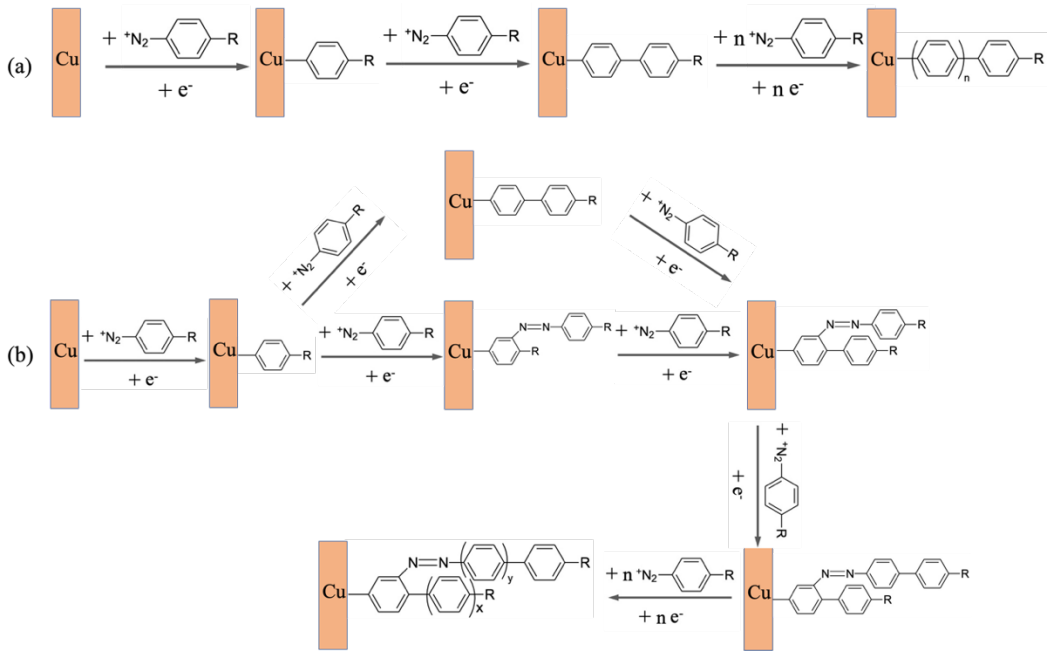

Supplementary Fig.1 The possible reaction mechanisms of diazonium salts on copper under electrochemical reductive current.

These mechanisms have been widely proved by many researches[1-5].

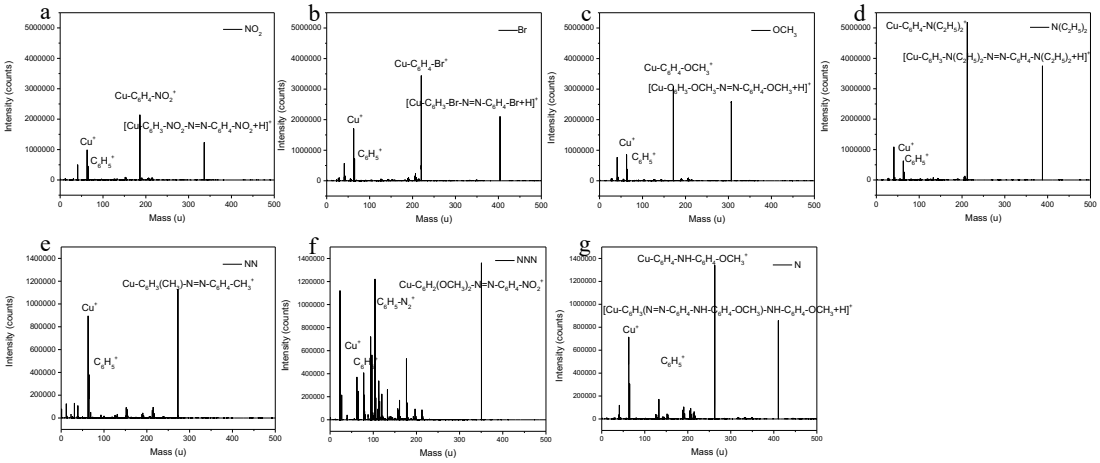

Supplementary Fig.2 Time-of-flight secondary-ion mass spectrometry (TOF-SIMS) Spectra of Cu-X (X= NO_2, Br, NNN, NN, N, OCH_3 and $N(C_2H_5)_2$).

Time-of-flight secondary-ion mass spectrometry (TOFSIMS) data were acquired using a TOF-SIMS V spectrometer (ION-TOF GmbH). The analysis chamber was maintained at less than 5×10^{-7} Pa under operating conditions. The total primary ion flux was below 1012 ions cm^2 to ensure static conditions. A pulsed 25 keV Bi+ primary ion source (Liquid Metal Ion Gun, LMIG) at a current of about 1 pA (high current bunched mode), raster over a scan area of 500 × 500 μm, was used as the analysis beam.

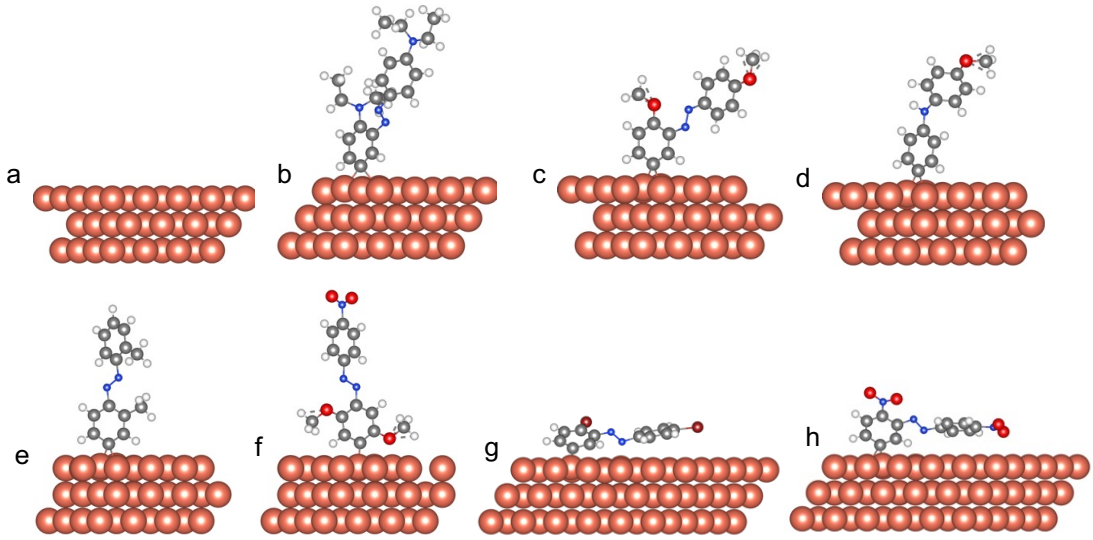

Supplementary Fig.3 The configurations for different functional groups bonded on copper (side view), a. Cu, b. Cu-$N(C_2H_5)_2$, c. Cu-OCH_3, d. Cu-N, e. Cu-NN, f. Cu-NNN, g. Cu-Br, and h. Cu-NO_2.

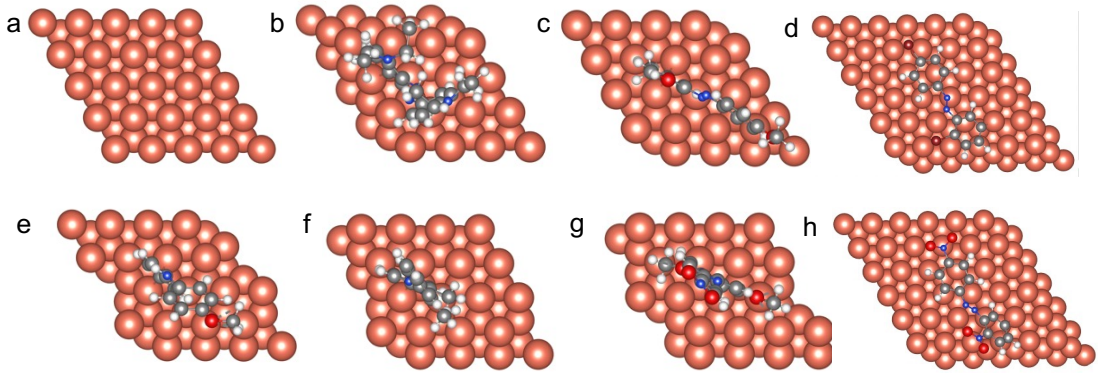

Supplementary Fig.4 The configurations for different functional groups bonded on copper (top view). a. Cu, b. Cu-$N(C_2H_5)_2$, c. Cu-OCH_3, d. Cu-Br, e. Cu-N, f. Cu-NN, g. Cu-NNN, and h. Cu-NO_2.

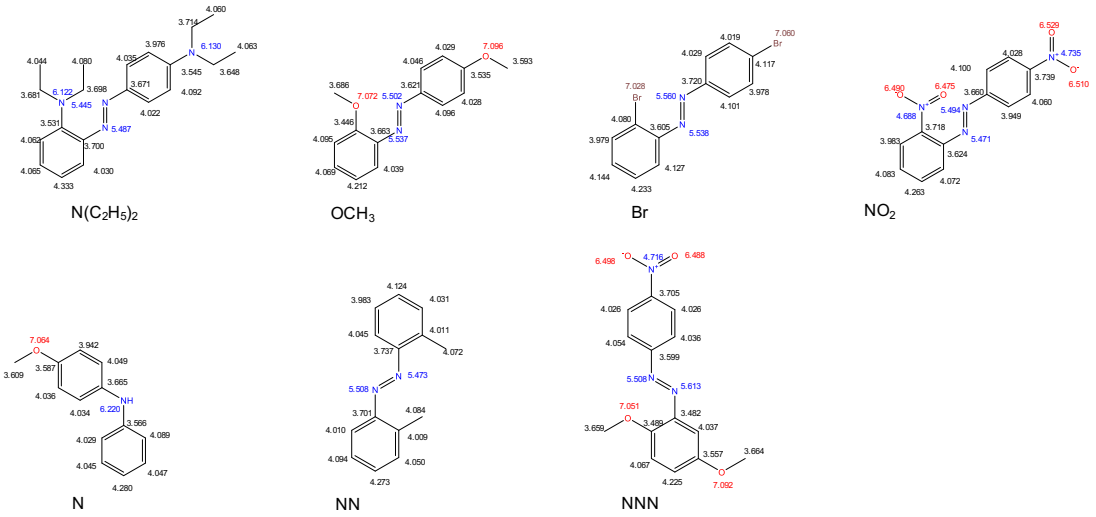

Supplementary Fig.5 Formal Bader charges of different aryl diazonium salts on copper.

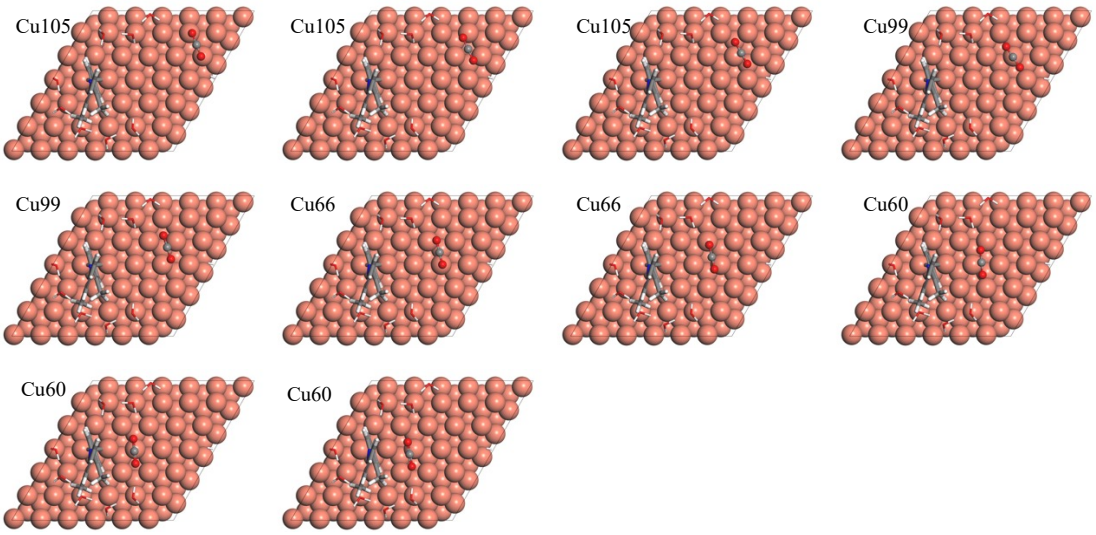

Supplementary Fig.6 The models of CO_2 molecular adsorbed on neighboring $Cu^{\delta+}$ (δ=0, 0.10, 0.12 and 0.18) atoms around NN-bonded Cu atom in NN bonded Cu system.

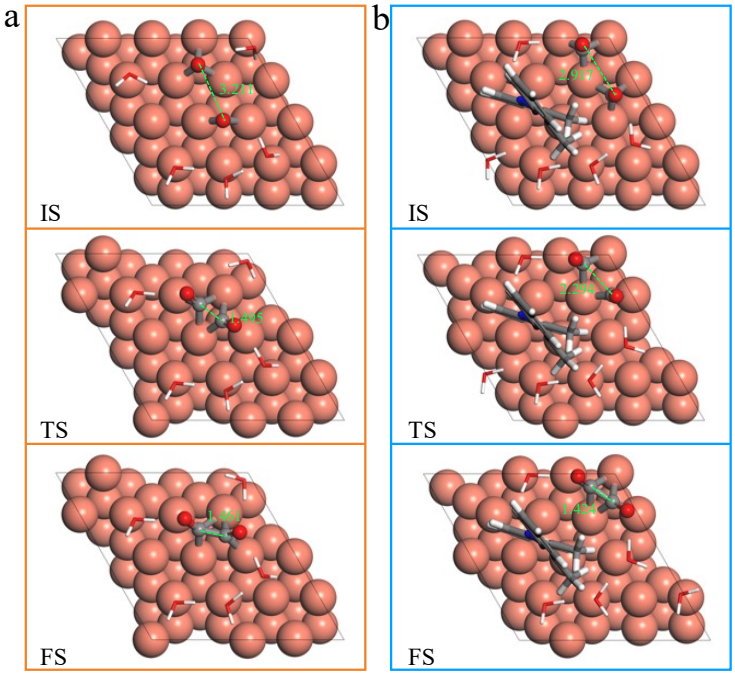

Supplementary Fig. 7 Geometries of CO dimerization process from initial status, transition state to final state. Cu (a) and Cu-NN (b).

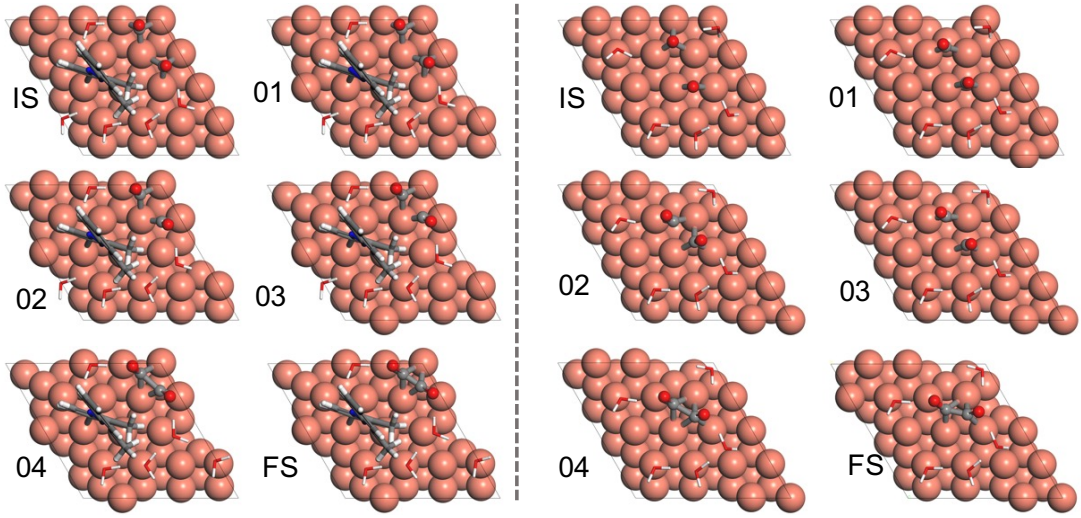

Supplementary Fig. 8 The inserted windows between the initial state (IS) and the final state (FS) to find the transition state (TS) when calculating CO dimerization process on both Cu (right) and Cu-NN (left).

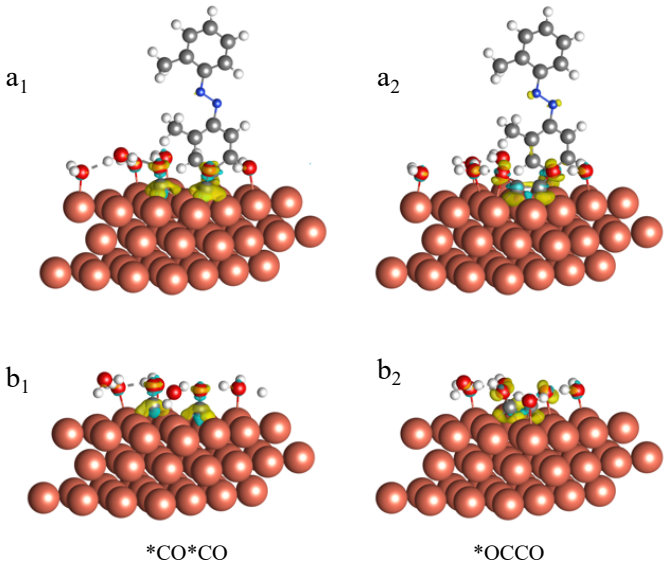

Supplementary Fig. 9 The oblique view of electron density difference plots for Cu-NN and Cu with two adsorbed *CO (a_1 and b_1) and *OCCO (a_2 and b_2), as well as one water layer, respectively. Yellow contours represent charge accumulations, and blue contours denote charge depressions.

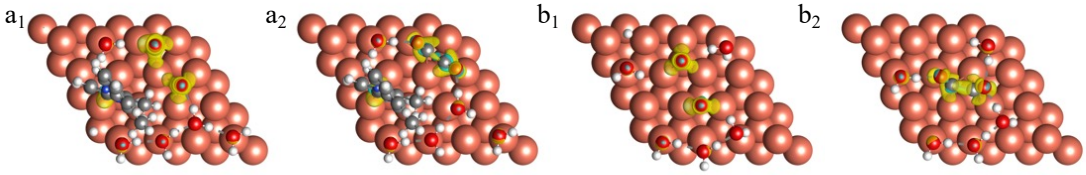

Supplementary Fig. 10 The top view of electron density difference plots for Cu-NN and Cu with two adsorbed *CO (a_1 and b_1) and *OCCO (a_2 and b_2), as well as one water layer, respectively. Yellow contours represent charge accumulations, and blue contours denote charge depressions.

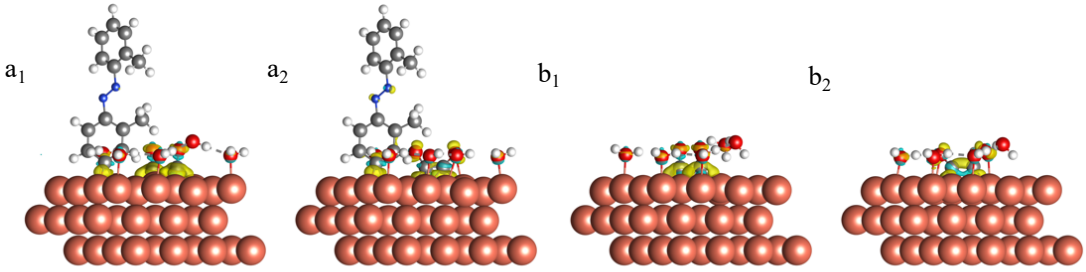

Supplementary Fig. 11 The side view of electron density difference plots for Cu-NN and Cu with two adsorbed *CO (a_1 and b_1) and *OCCO (a_2 and b_2), as well as one water layer, respectively. Yellow contours represent charge accumulations, and blue contours denote charge depressions.

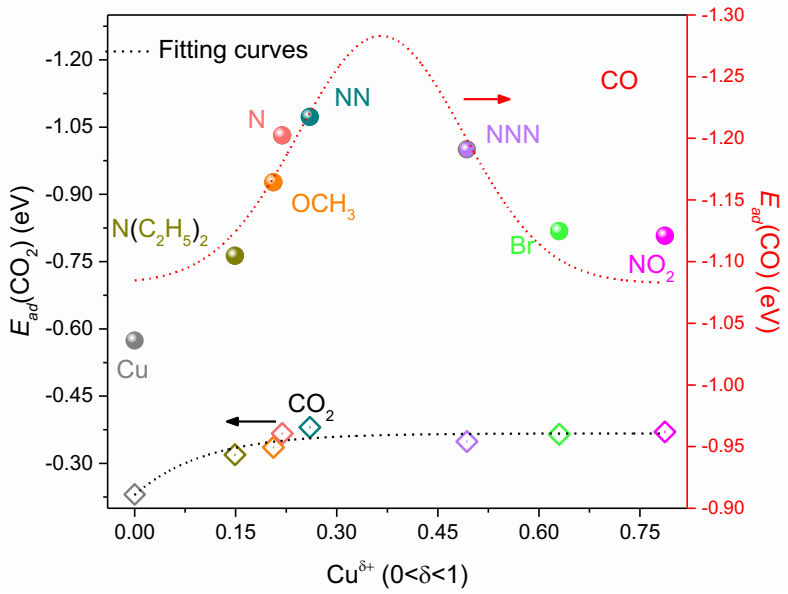

Supplementary Fig.12 The adsorption energy of CO_2 and CO on Cu-X catalysts (X= NO_2, Br, NNN, NN, N, OCH_3 and $N(C_2H_5)_2$.

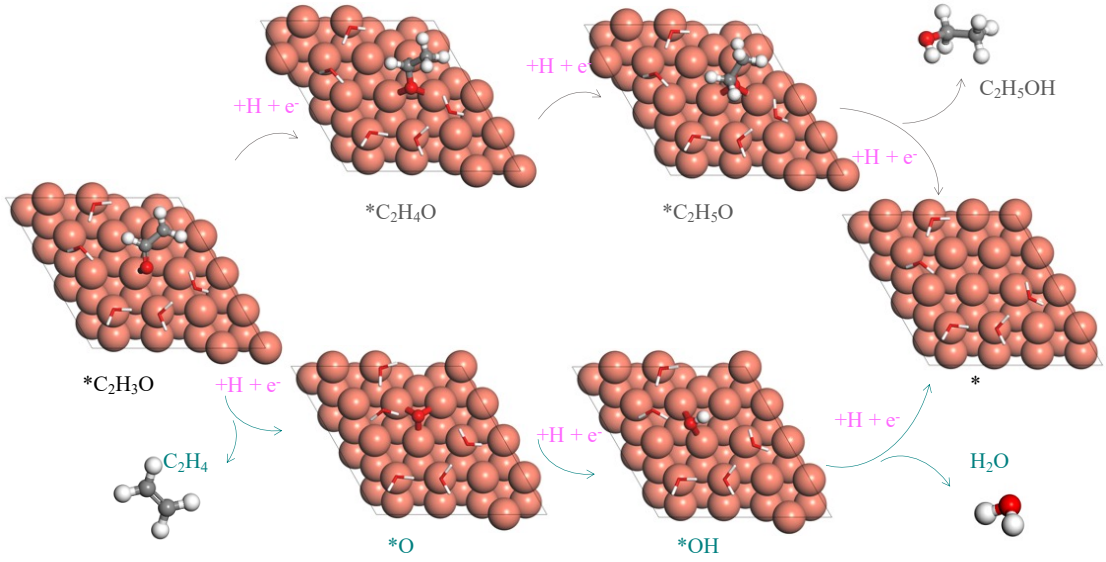

Supplementary Fig.13 Reaction pathways for ethylene *vs* ethanol on Cu surface.

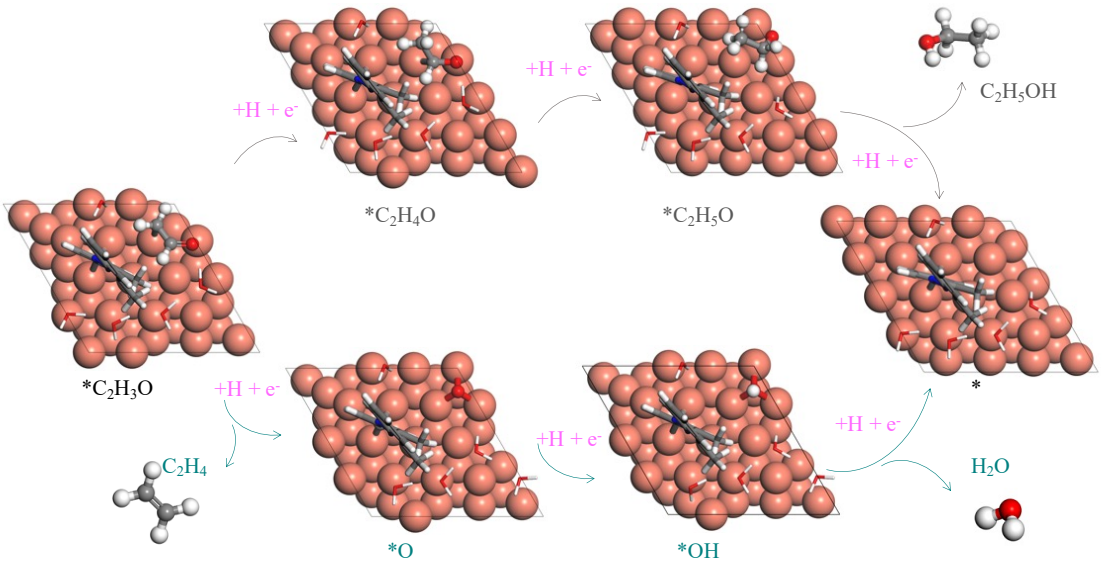

Supplementary Fig.14 Reaction pathways for ethylene *vs* ethanol on Cu-NN surface.

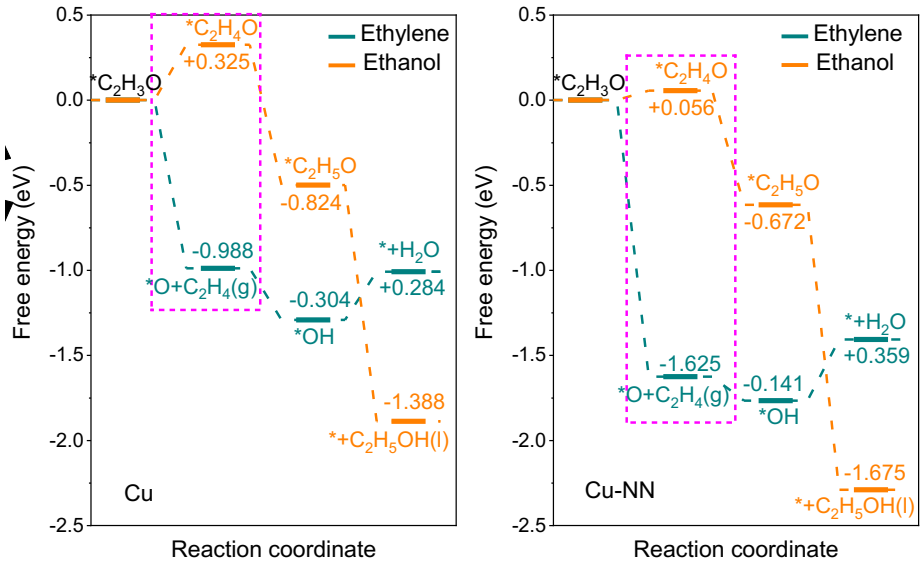

Supplementary Fig.15 Energy profile to form ethylene (blue line) and ethanol (orange line) for pure Cu and Cu-NN.

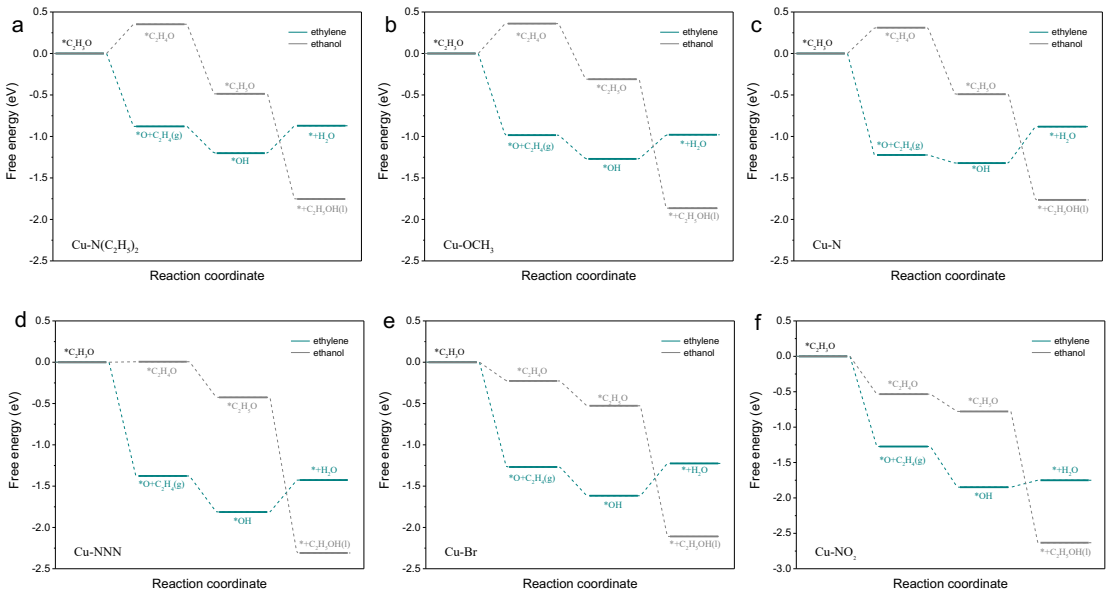

Supplementary Fig.16 Energy profile to form ethylene (blue line) and ethanol (gray line) for a Cu-N(C_2H_5)$_2$, b Cu-OCH_3, c Cu-N, d Cu-NNN, e Cu-Br and f Cu-NO_2.

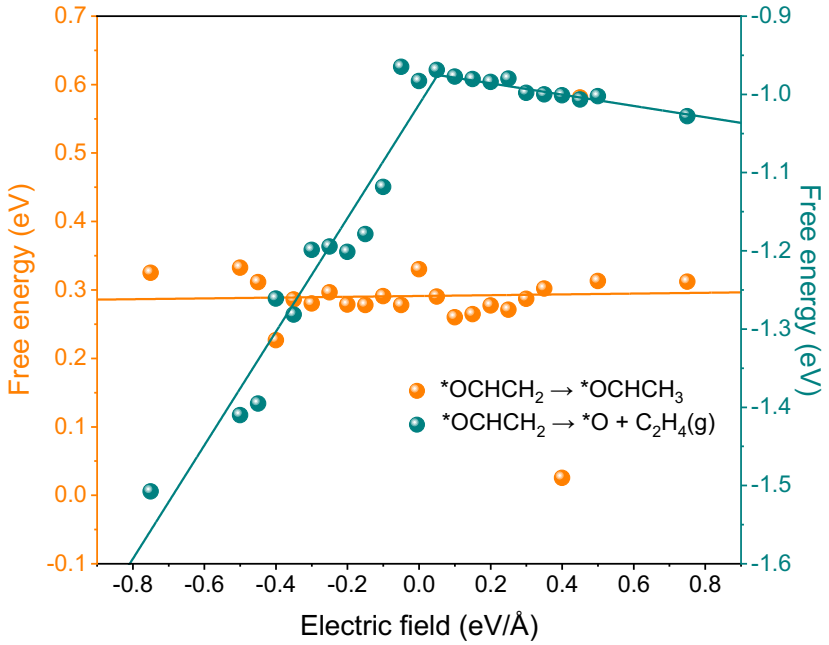

Supplementary Fig. 17 The applied field effects on the free energy of the selectivity-determining step of ethylene and ethanol over Cu-NN surface.

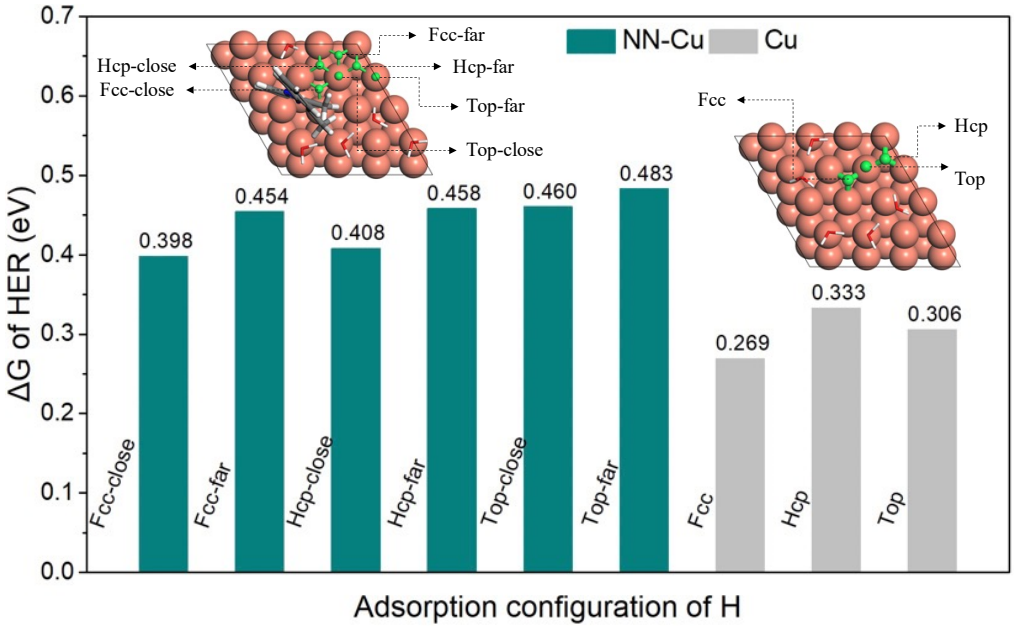

Supplementary Fig.18 The free energy of hydrogen evolution reaction on both bare Cu and Cu-NN catalysts.

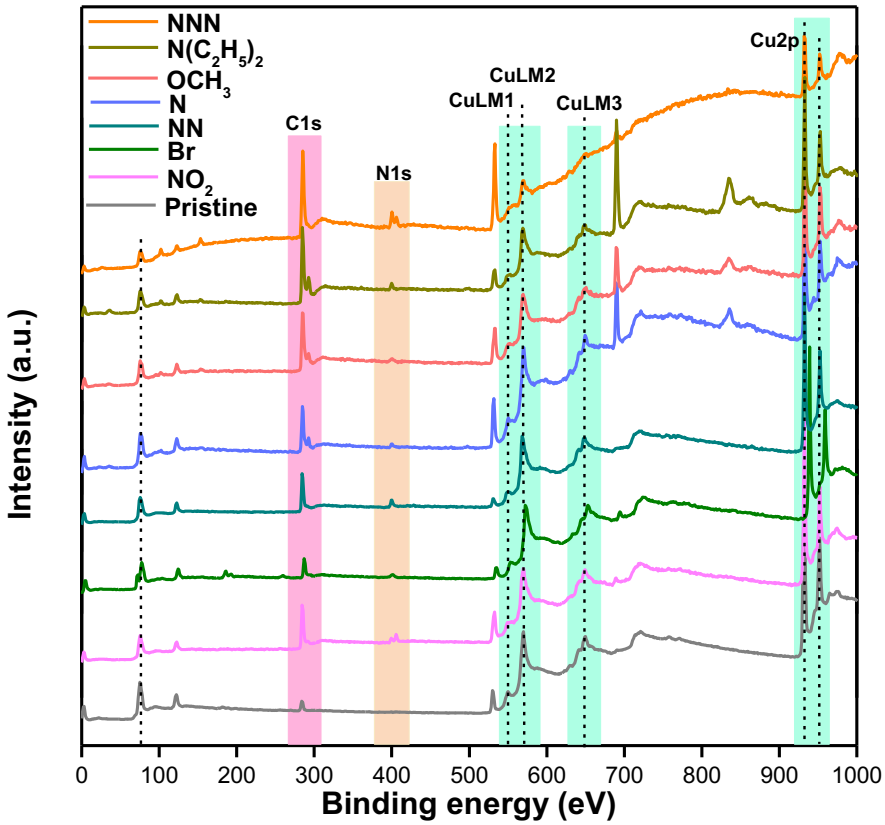

Supplementary Fig. 19 XPS of different diazonium salts grated copper catalysts.

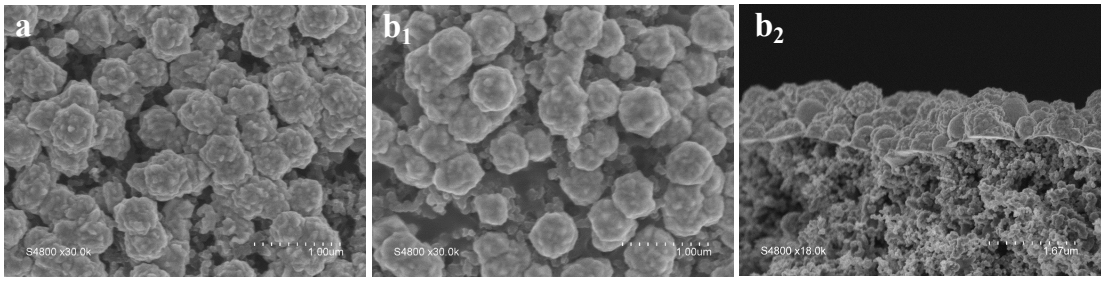

Supplementary Fig.20 Low-magnification scanning electron microscopy (SEM) images for the pristine and NN functionalized Cu catalysts. (a) pristine (Cu), (b_1) Cu-NN and (b_2) the cross-section of Cu-NN.

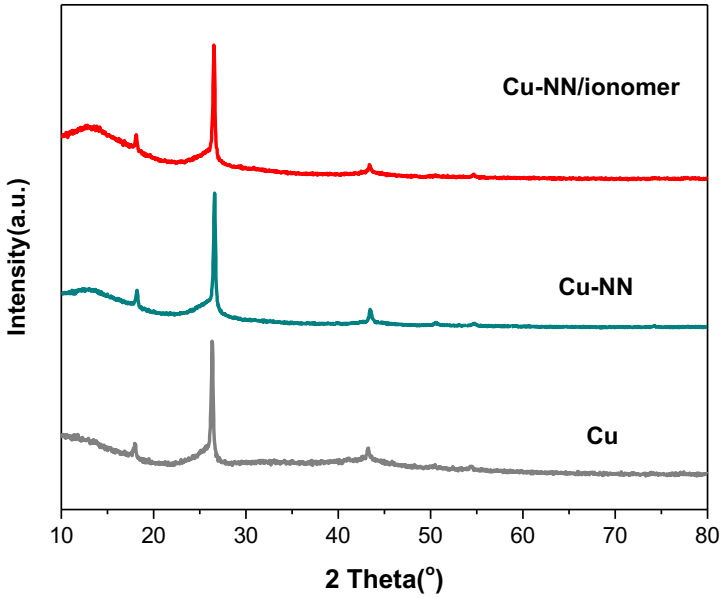

Supplementary Fig.21 XRD of Cu, Cu-NN and Cu-NN/ionomer catalysts.

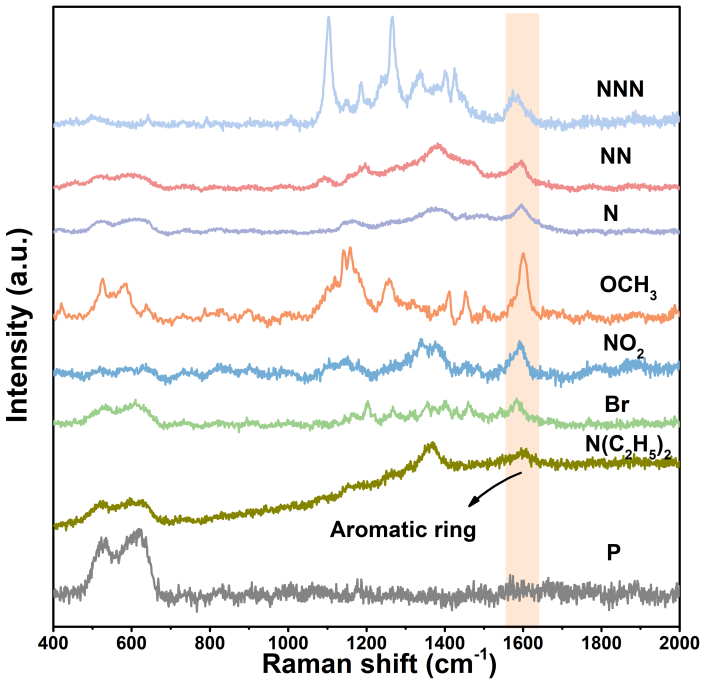

Supplementary Fig.22 Ex-situ Raman spectra of different diazonium salts functionalized catalysts.

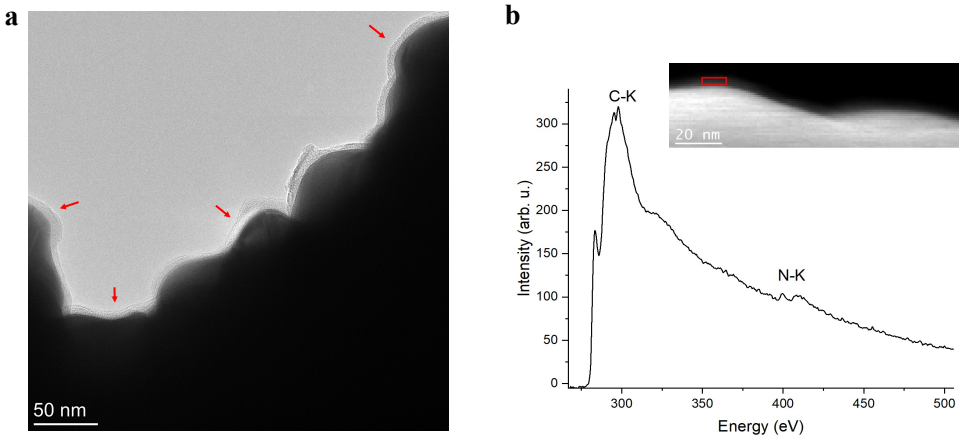

Supplementary Fig. 23 Medium magnification TEM image showing the presence of the functionalized layer at the surface of the Cu-NN catalyst (a). Monochromated EELS spectrum acquired at the surface of the Cu-NN catalysts. The inset shows the corresponding ADF image acquired simultaneously as the EELS dataset. The red rectangle highlights the area used to extract the EELS spectrum (b).

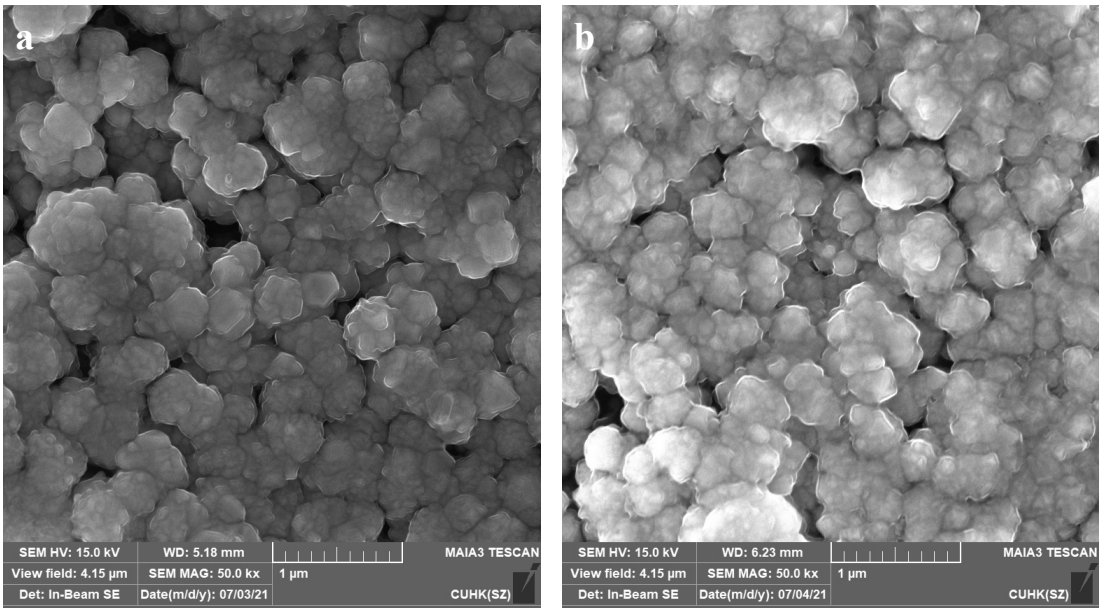

Supplementary Fig. 24 Scanning electron microscopy (SEM) images for the Cu-NN(a) and Cu-NN/ionomer(b) catalysts.

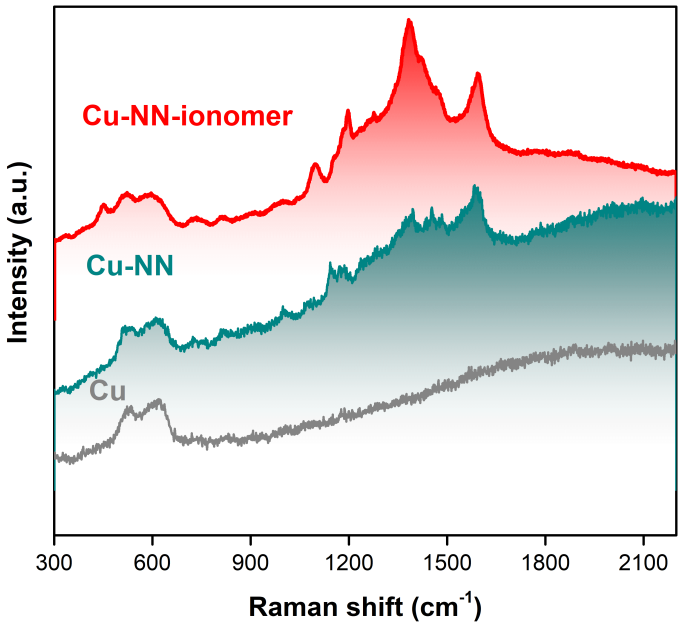

Supplementary Fig. 25 Ex-situ Raman spectra of different catalysts.

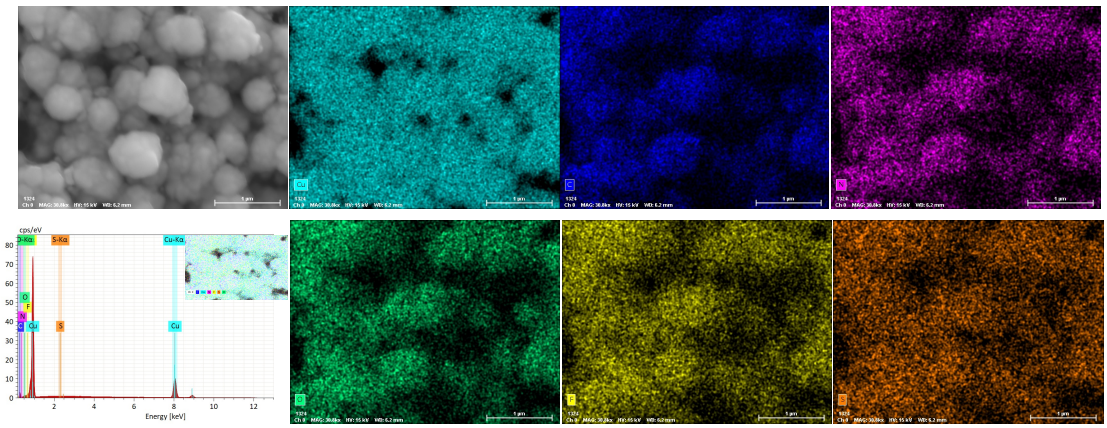

Supplementary Fig.26 Energy-dispersive X-ray spectroscopy (EDX) elemental mapping of ionomer coated Cu-NN catalyst.

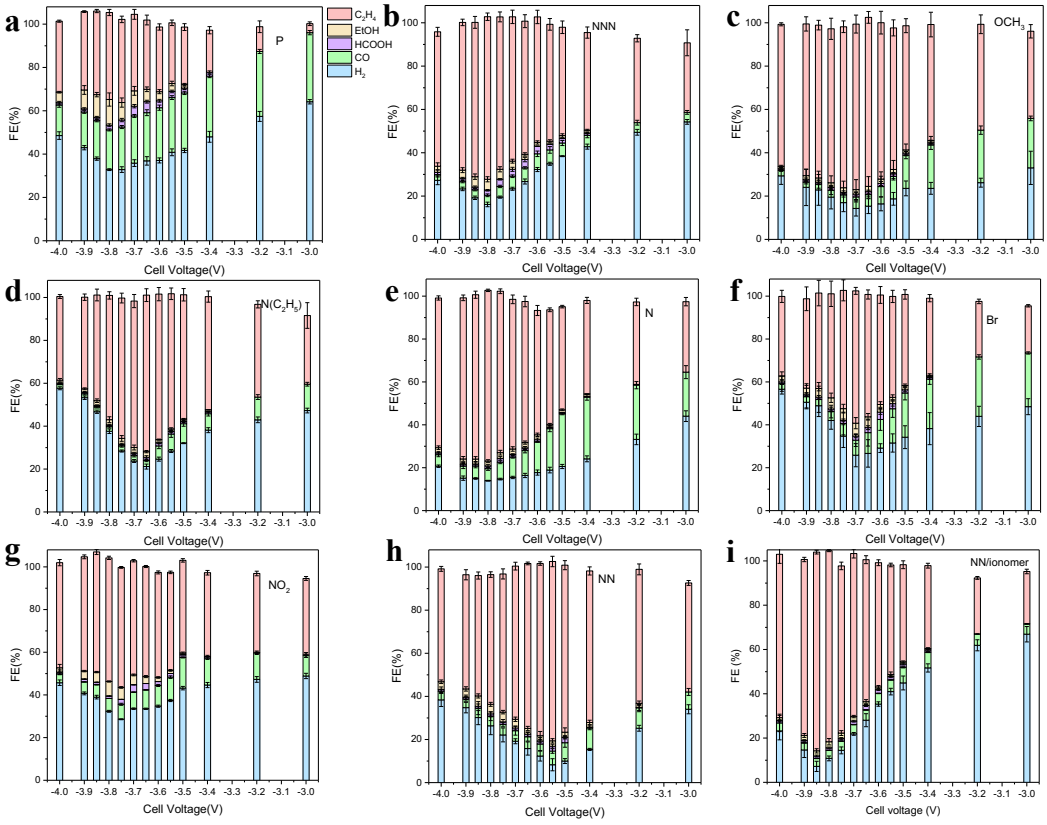

Supplementary Fig.27 Comparisons of the Faradaic efficiencies on the different catalysts measured in the MEA reactors. Bare Cu (a), Cu-NNN (b), Cu-OCH_3 (c), Cu-$N(C_2H_5)_2$ (d), Cu-N (e), Cu-Br (f), Cu-NO_2 (g) and Cu-NN (h), as well as Cu-NN/ionomer (i) electrodes.

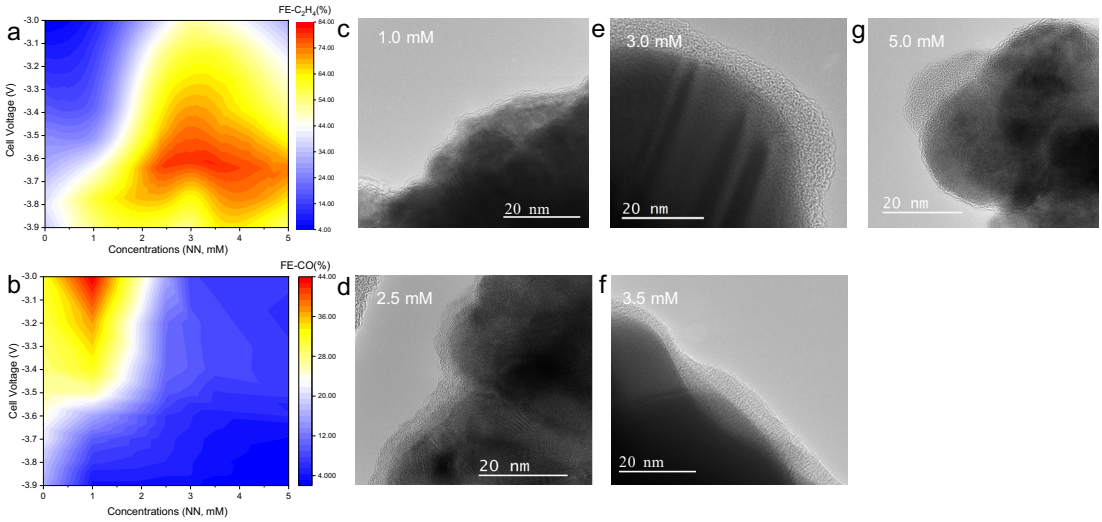

Supplementary Fig. 28 The relationships among the Faradaic efficiency of C_2H_4(a), CO(b) and the concentrations of NN, as well as the related thickness of functional groups (NN). And the High-resolution transmission electron microscope (HR-TEM) micrograph (c to g) of Cu-NN electrodes with different concentrations of NN.

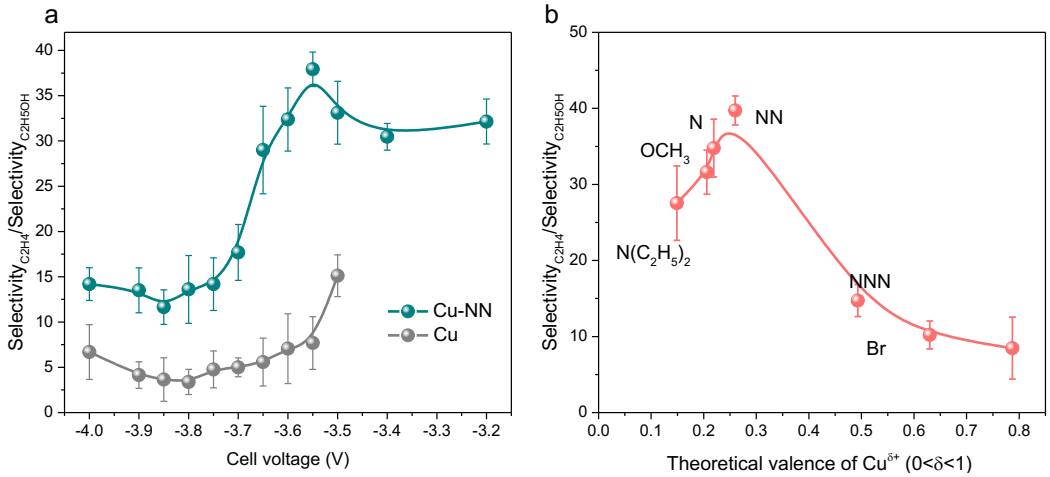

Supplementary Fig.29 (a) The ratio of $Selectivity_{C2H4}/Selectivity_{C2H5OH}$ on Cu-NN and bare Cu catalysts in MEA reactors. (b) The relationship between $Selectivity_{C2H4}/Selectivity_{C2H5OH}$ and theoretical valences of Cu on Cu-X catalysts. (The X in Cu-X catalysts refers to NO_2, Br, NNN, NN, N, OCH_3 and $N(C_2H_5)_2$ functional groups).

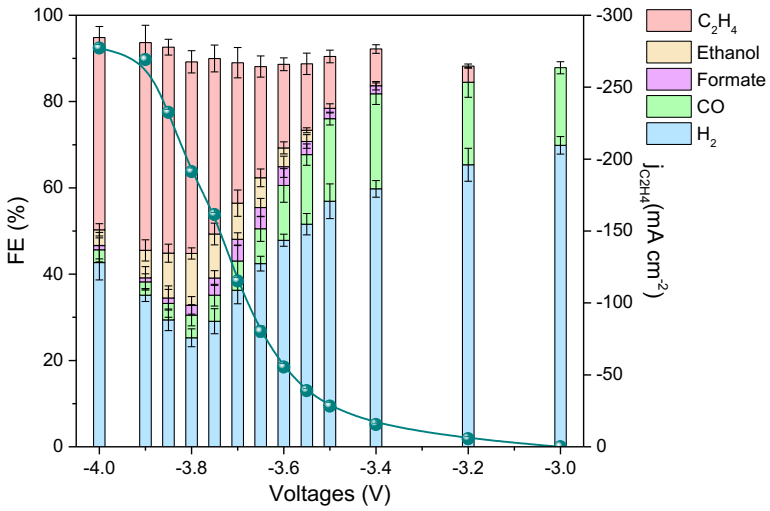

Supplementary Fig. 30 Electrocatalytic CO2RR performance of the MEA reactor using the Cu/ionomer catalyst.

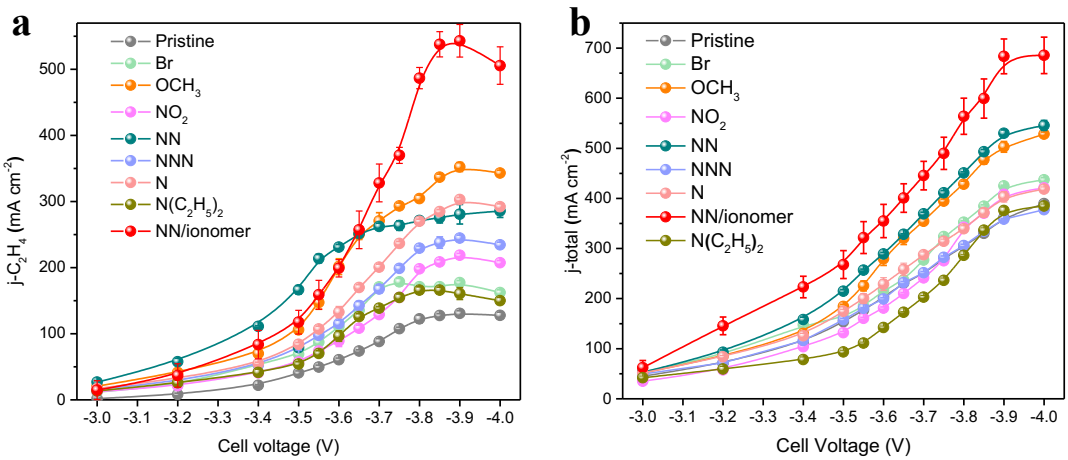

Supplementary Fig. 31 Electrocatalytic CO2RR properties of the MEA reactors using the different Cu-X catalysts (X refers to Br, OCH_3, NO_2, NN, NNN, N, $N(C_2H_5)_2$ and NN/ionomer). (a) C_2H_4 specific current density, (b) total current density.

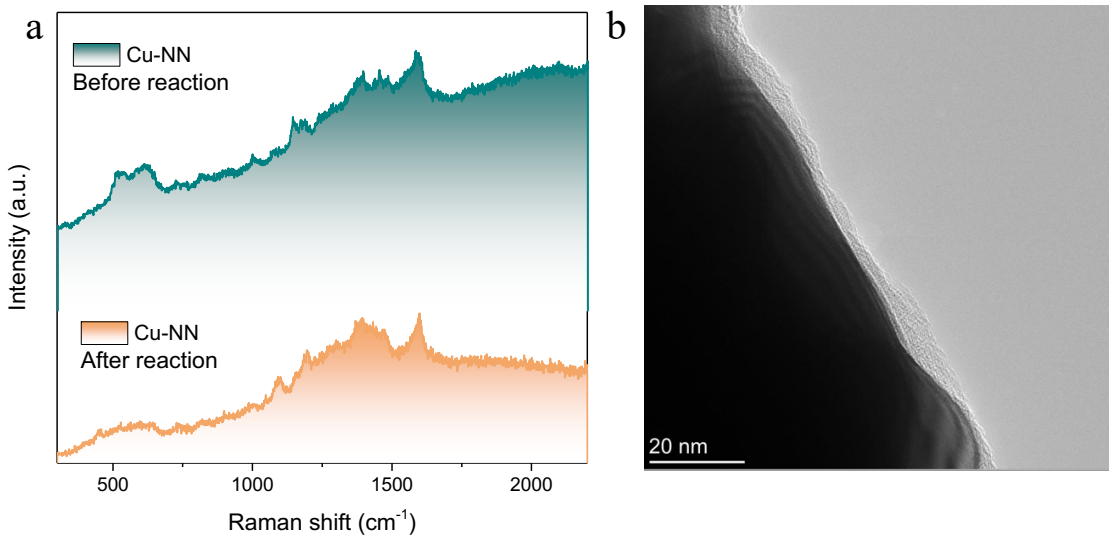

Supplementary Fig. 32 Ex-situ Raman spectra of Cu-NN after reaction (a) and medium magnification TEM image showing the presence of the functionalized layer at the surface of the Cu-NN catalyst (b).

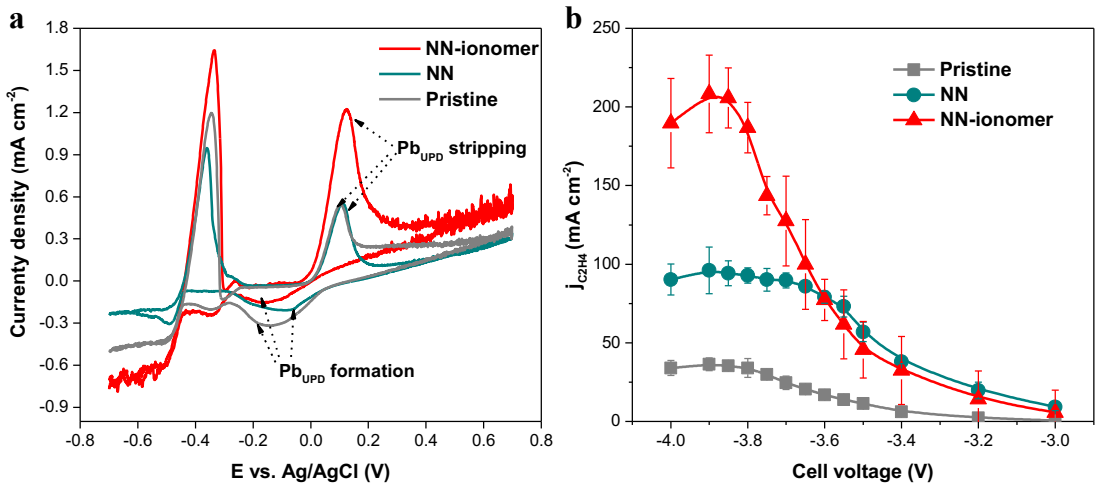

Supplementary Fig.33 CVs for different samples measured in 100 mM HClO4 + 1 mM Pb(ClO4)2 (a), partial ethylene current density normalized to Cu ECSA for Cu and Cu-NN and Cu-NN/ionomer catalysts for CO2RR in MEA reactors (b).

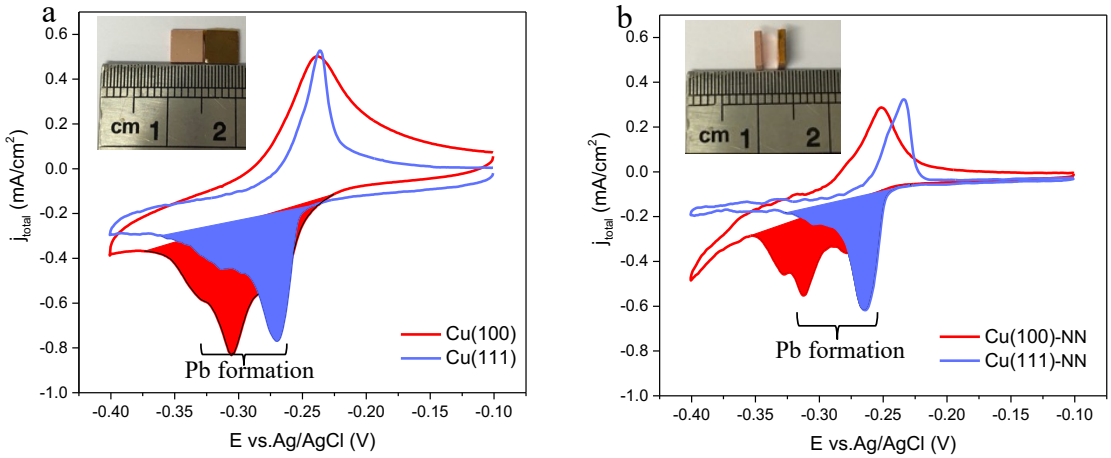

Supplementary Fig. 34 CV curves for different Cu single crystals measured in 100 mM $HClO_4$ + 2 mM $Pb(ClO_4)_2$.

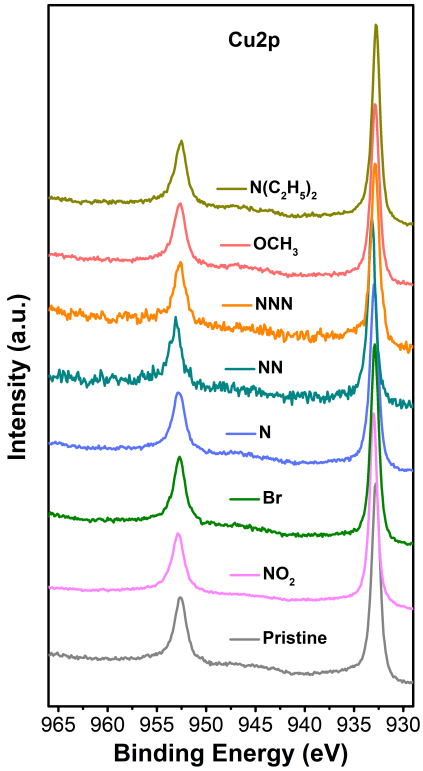

Supplementary Fig. 35 The high-resolution XPS spectra of Cu*2p* in Cu-X catalysts X refers to NO_2, Br, NNN, NN, N, OCH_3 and $N(C_2H_5)_2$ functional groups.

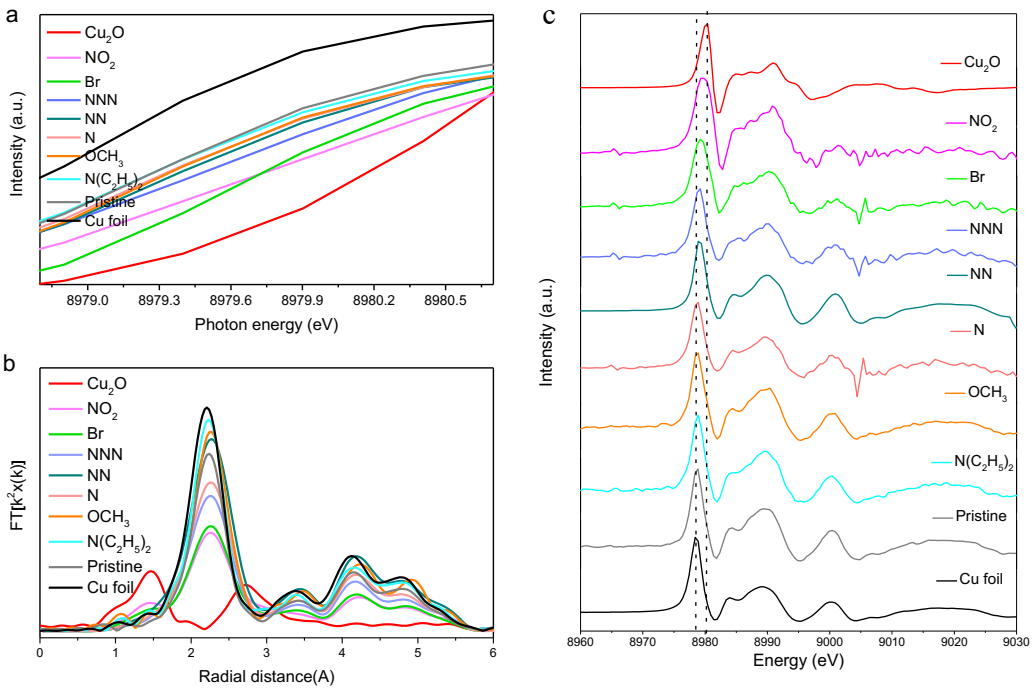

Supplementary Fig.36 Cu K-edge X-ray absorption near edge structure (XANES) spectra(a) and R space (b) of the different Cu-X catalysts. (c) the first derivatives of the Cu K-edge XANES spectra of Cu-X catalysts. X refers to NO_2, Br, NNN, NN, N, OCH_3 and $N(C_2H_5)_2$ functional groups.

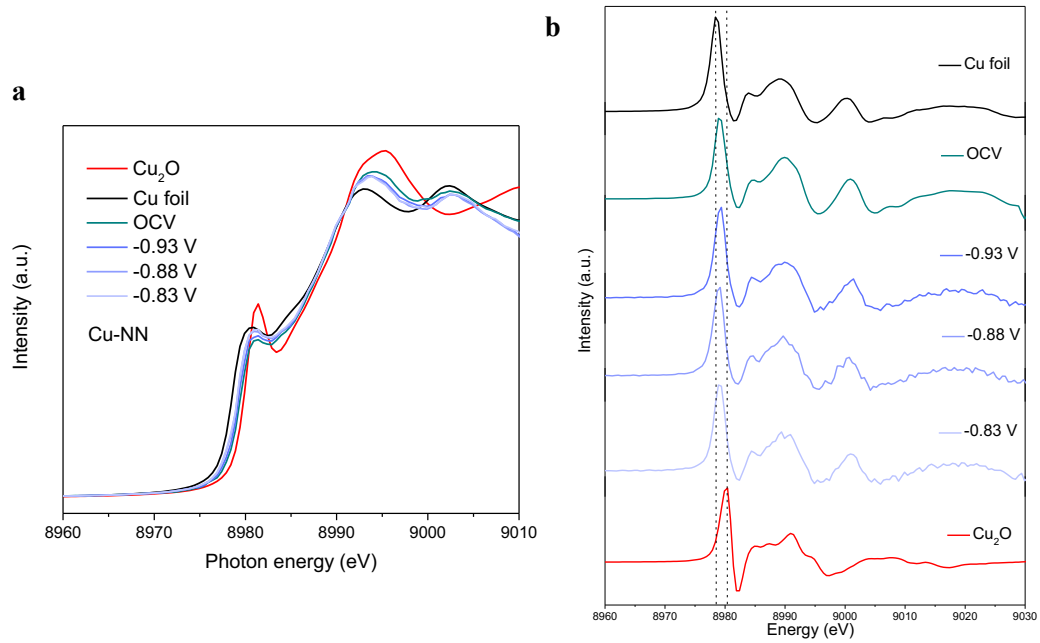

Supplementary Fig.37 In *operando* Cu K-edge XANES spectra of Cu-NN catalyst under different reductive potentials (-0.93 V, -0.88 V and -0.83 V versus RHE) during CO_2RR for 15 minutes(a), and the related first derivatives of the Cu K-edge XANES spectra (b). Bulk Cu foil and Cu_2O are listed as references.

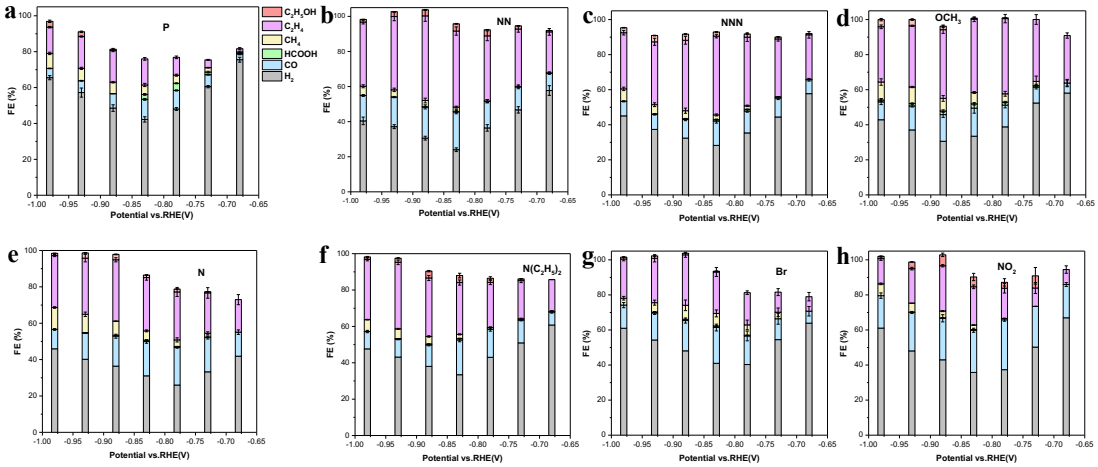

Supplementary Fig.38 Comparisons of the Faradaic efficiencies on the different catalysts measured in the H-cell reactors. The Faradaic efficiency for the different products on bare Cu (a), Cu-NN (b), Cu-NNN (c), Cu-OCH_3(d), Cu-N (e), Cu-$N(C_2H_5)_2$ (f), Cu-Br(g), and Cu-NO_2 (h) electrodes.

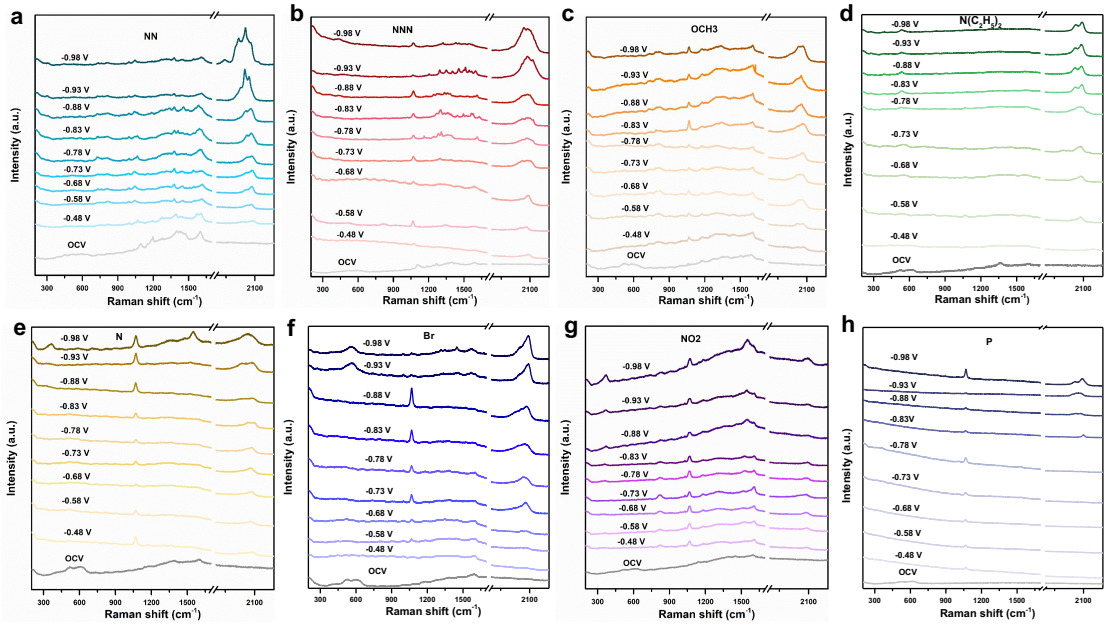

Supplementary Fig.39 *Operando* Raman spectra of (a) NN-, (b) NNN-, (c) OCH_3-, (d) $N(C_2H_5)_2$-, (e) N-, (f) Br-, (g) NO_2-functionalized Cu electrodes compared with (h) pristine Cu. The *operando* Raman measurements were carried out between -0.48 V and -0.98 V vs. RHE in a CO2-saturated KOH solution.

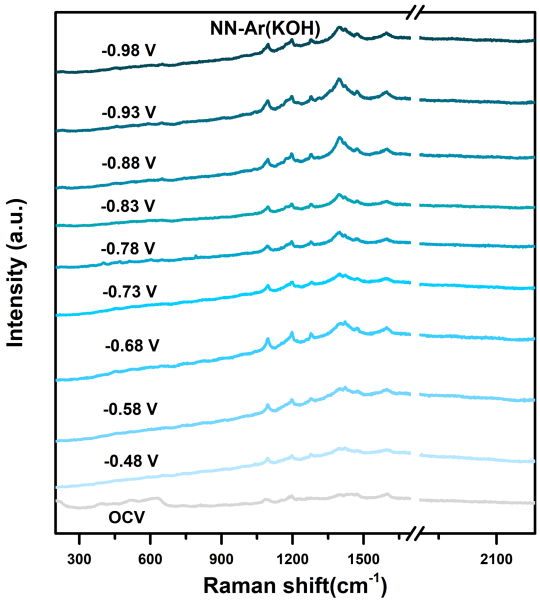

Supplementary Fig.40 *Operando* Raman spectra of Cu-NN sample tested in an Ar saturated KOH electrolyte solution.

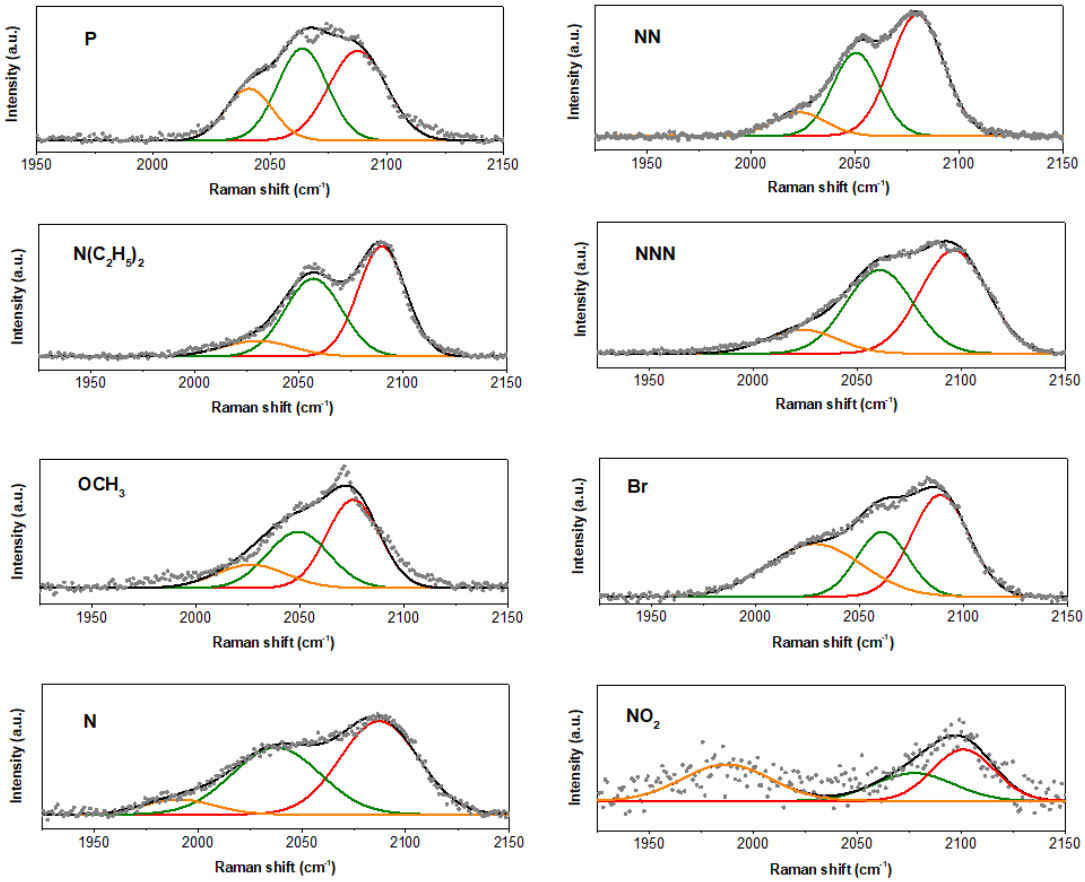

Supplementary Fig.41 *Operando* Raman spectra of the C≡O stretch region of Cu-X electrodes. The asymmetric band is deconvoluted into bands for bridge CO (at ~2030 cm^{-1}), low frequency CO* (LFB-CO*, at ~2060 cm^{-1}) and high frequency CO* (HFB-CO*, at ~2095 cm^{-1}) by Lorentzian fitting. The ratio between the intensities of the HFB-CO* and LFB-CO* was summarized in Supplementary Table 13.

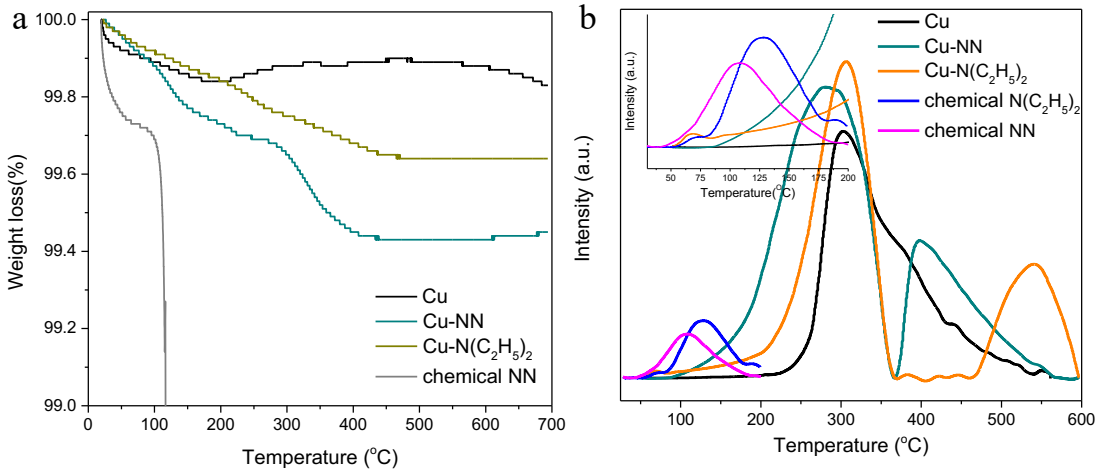

Supplementary Fig. 42 TGA plots of Cu, Cu-NN, Cu-N(C_2H_5)$_2$ and chemical NN in N_2 atmosphere(a), and CO_2-TPD profiles of Cu, Cu-NN, Cu-N(C_2H_5)$_2$, chemical NN and chemical N(C_2H_5)$_2$(b).

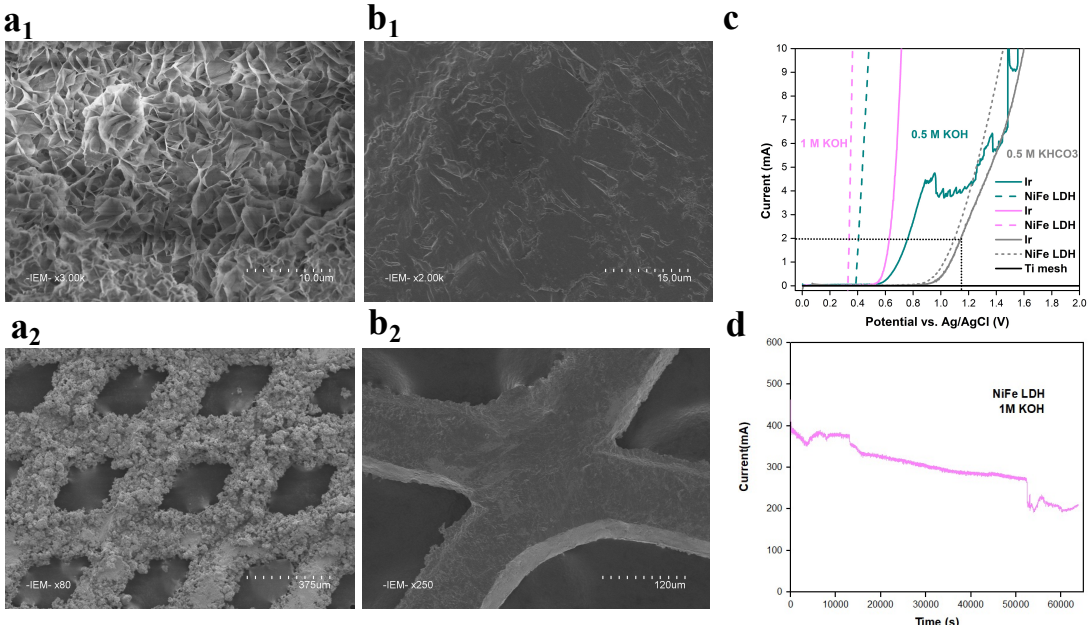

Supplementary Fig. 43 Micromorphology and electrochemical performance of NiFe LDH on Ti mesh. High (a_1) and low(a_2) magnification scanning electron microscopy (SEM) images for NiFe LDH on Ti mesh, and the bare Ti mesh sample (b_1) and (b_2). (c) the different LSV curves of IrOx and NiFe LDH on Ti mesh in different electrolyte, (d) the two-electrode stability test of NiFe LDH electrode in 1 M KOH with the potential of 2.4 V.

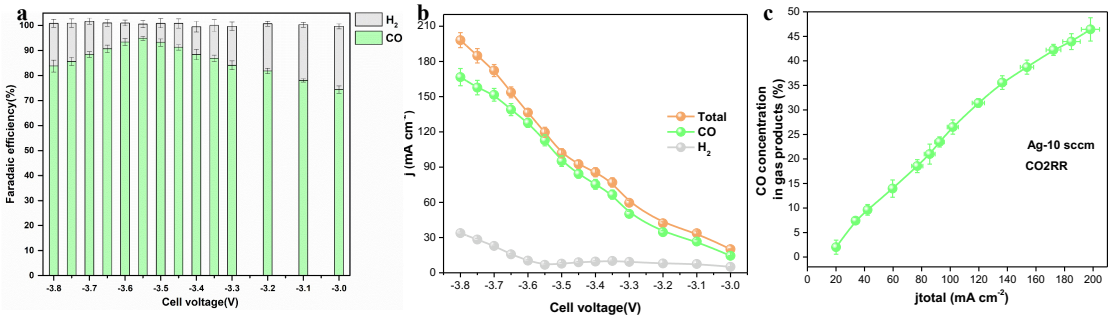

Supplementary Fig.44 CO_2-to-CO conversion on an Ag electrode in a MEA reactor. The FE(a) and specific current density(b) of CO and H_2, and the relationship between CO concentration and total current density(c).

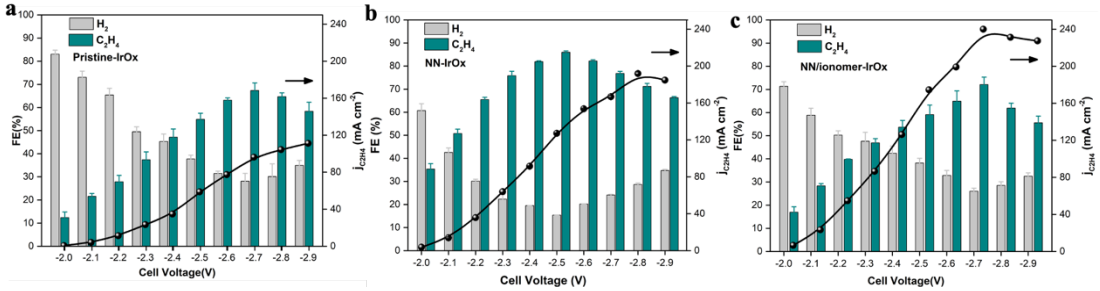

Supplementary Fig. 45 CO-to-C_2H_4 conversion in the cascade MEA system by using IrOx as the anode and bare Cu(a), Cu-NN(b) and Cu-NN/ionomer(c) as the cathodes.

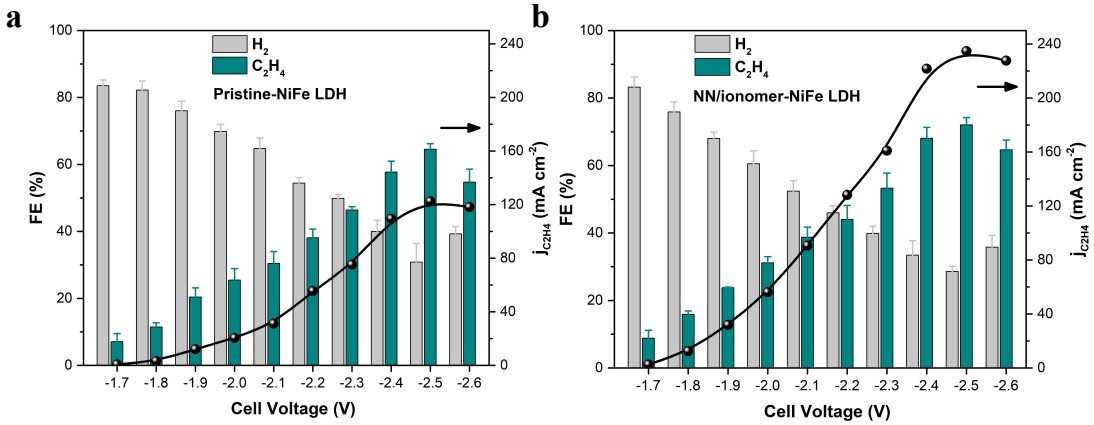

Supplementary Fig. 46 CO-to-C_2H_4 conversion in the cascade MEA system by using NiFe LDH on Ti mesh as the anode and bare Cu(a) and Cu-NN/ionomer(b) as the cathodes.

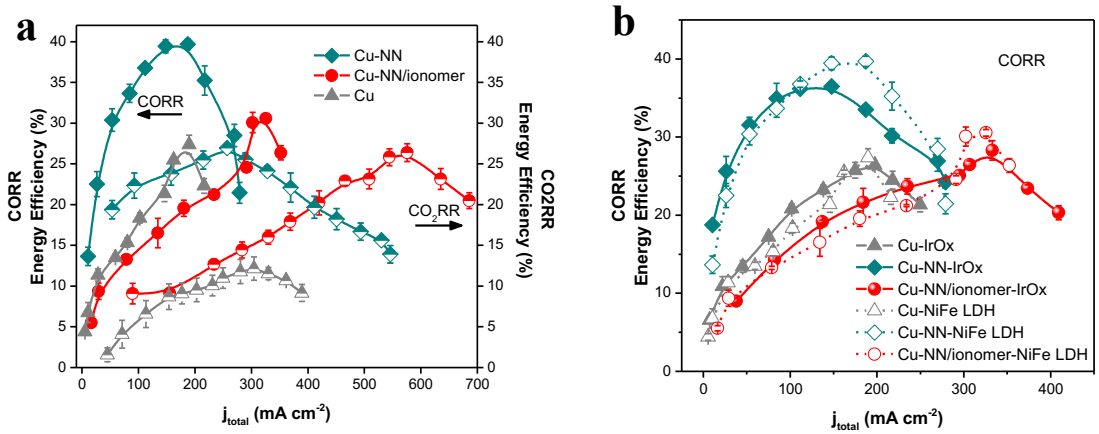

Supplementary Fig. 47 Comparison in energy efficiency on different samples (Cu-X, X refers to NN, NN/ionomer). (a) The relationships between energy efficiency and current density with different samples in both single MEA electrolyzer and cascade MEA system (the half belongs to CO_2RR, and the full belongs to CORR), (b) the difference of energy efficiency on different samples by using IrOx and NiFe LDH as the anode in cascade MEA system condition.

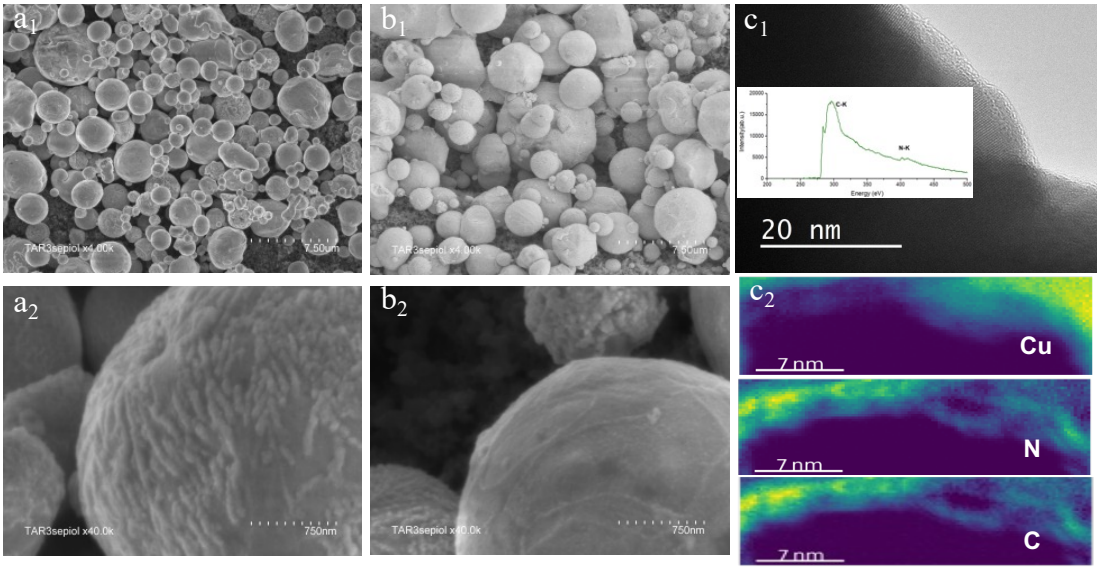

Supplementary Fig. 48 Structural and elemental composition of the functionalized commercial Cu (2~3.5μm) catalysts. Scanning electron microscope (SEM) images of commercial Cu (hereafter, cCu) (a_1 and a_2) and NN modified commercial Cu (**cCu-NN**) (b_1 and b_2) catalysts on gas diffusion electrodes (GDE). High-resolution transmission electron microscope (HR-TEM) micrograph (c_1) of **cCu**-NN electrode. EELS spectrum of the C-K edge with fine structures characteristics of carbon linked to heteroatoms from NN layer on the **cCu** surface (inset). HAADF-STEM image of the cCu surface of NN-functionalized cCu (c_2).

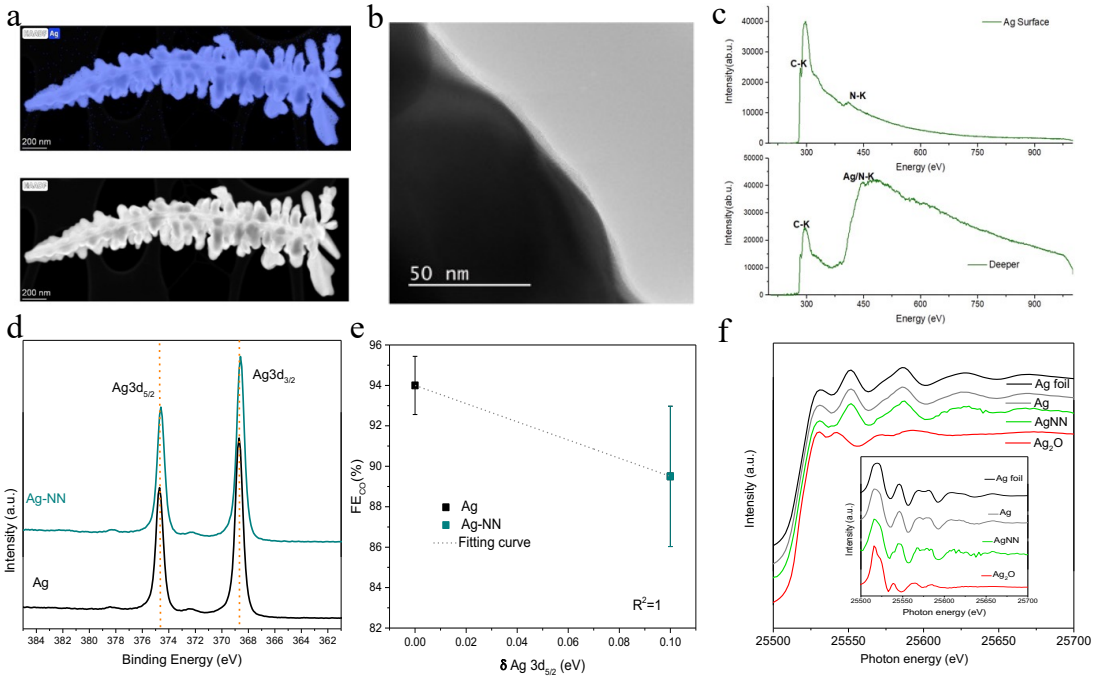

Supplementary Fig. 49 High-angle annular dark-field scanning transmission electron microscopy (HAADF-STEM) image(a) and High-resolution transmission electron microscope (HR-TEM) micrograph (b) of Ag-NN electrode. EELS spectrum of the C-K edge with fine structures characteristics of carbon linked to heteroatoms from NN layer on the Ag surface and deeper (c). X-ray photoelectron spectra for Ag-NN and bare Ag catalysts, showing shifts in the $Ag3d_{5/2}$ peaks(d). Correlation of the XPS shift with the FE_{CO} (e). *Ex-situ* Ag K-edge X-ray absorption near edge structure (XANES) spectra of pristine and functionalized Ag-NN electrodes(f). Inset: the first derives of silver for the corresponding electrodes.

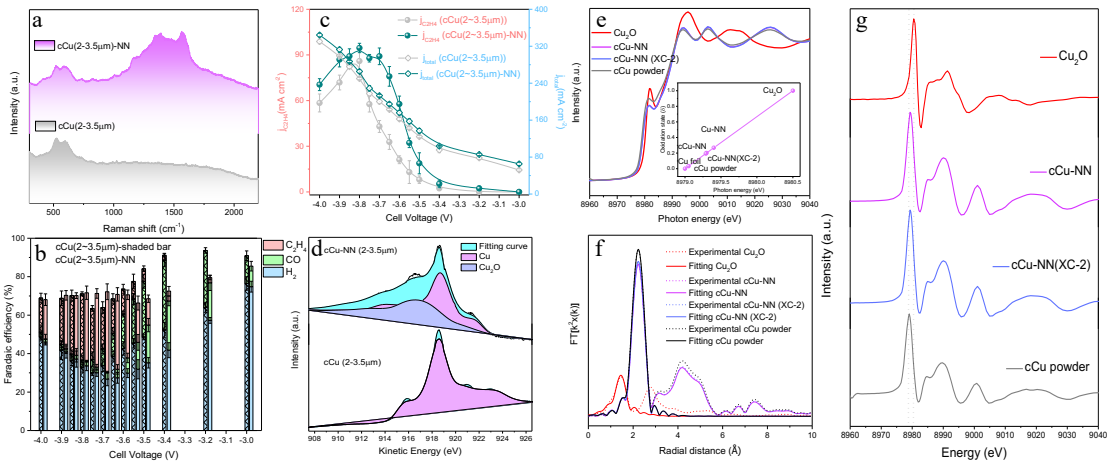

Supplementary Fig. 50 Ex-situ Raman spectra of cCu (2~3.5 μm) and cCu (2~3.5 μm)-NN(a). CO2RR performance of the cCu (2~3.5 μm) and cCu (2~3.5 μm)-NN electrodes in MEA electrolyzer (b). j–V plots of the partial current densities

for the C2H4 product (c). The copper LMM Auger spectra of the cCu (2~3.5 μm) and cCu (2~3.5 μm)-NN electrodes (d). The amounts of Cu2O and Cu contributions were estimated from the integrated area of the corresponding curves. Copper K-edge XANES spectra of cCu and cCu-NN catalysts after being electrochemically reduced (e). Inset: average oxidation state of copper in cCu-NN obtained from copper K-edge XANES. The edge position of each sample is determined from the intercept of the main edge and pre-edge contributions. Copper R space (f) and the first derivatives of the Cu K-edge XANES spectra (g) of cCu and cCu-NN catalysts.

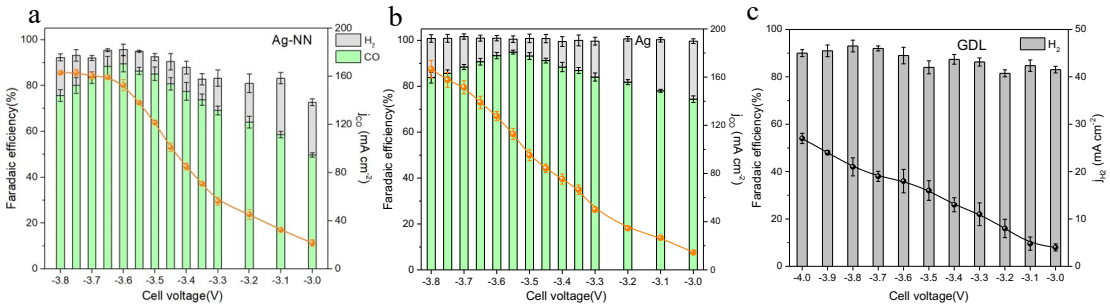

Supplementary Fig. 51 CO_2-to-CO conversion on Ag-NN(a), Ag(b) and GDL-NN electrodes(c) in a MEA reactor.

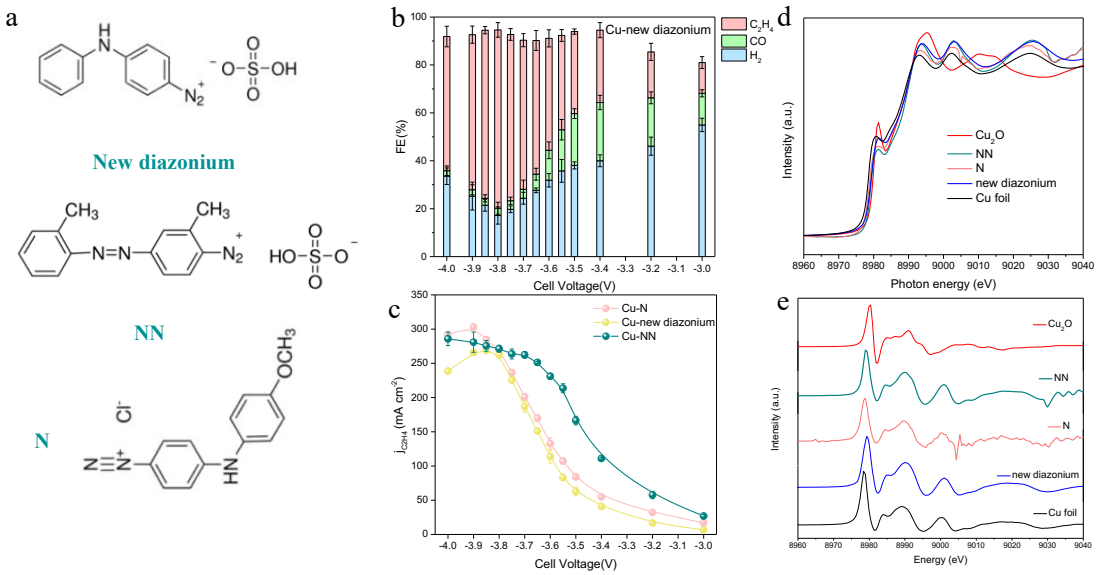

Supplementary Fig. 52 The molecule's structures of new diazonium salt(a), NN(b) and N(c). The Faradaic efficiency (d) and current density(e) from the new diazonium salt modified copper catalyst measured in the MEA reactor.

Supplementary Table 1 Formal theoretical valences of Cu after modifying different electron-withdrawing ability of the substituted phenyl groups.

Samples	$N(C_2H_5)_2$	OCH_3	N	NN	NNN	Br	NO2
Cu theoretical valences	+0.149	+0.206	+0.219	+0.260	+0.493	+0.630	+0.787

Supplementary Table 2 The valence of nearby Cu atoms, the distance of nearby Cu atoms to Cu-NN atom, and the change of CO_2 adsorption energy on different valence Cu atoms in NN functionalized Cu catalyst.

Atoms	valence (δ)	distance (Å)	CO_2 adsorption energy (eV)
	0	9.26073	-0.399
Cu105	0	9.26073	-0.391
	0	9.26073	-0.385
Cu99	0.1	6.80631	-0.38
	0.1	6.80631	-0.388
Cu66	0.12	5.16821	-0.399
	0.12	5.16821	-0.399
	0.18	2.59728	-0.45
Cu60	0.18	2.59728	-0.468
	0.18	2.59728	-0.468

Supplementary Table 3 Activation energies (E_a) and enthalpy changes (ΔH) of CO dimerization on Cu and Cu-NN.

	E_a (eV)	ΔH (eV)
Cu	1.0129	0.7898
Cu-NN	0.7552	0.3329

Supplementary Table 4 The adsorption energies of CO and CO_2 on Cu-X catalysts (X refers to $N(C_2H_5)_2$, OCH_3, N, NN, NNN, Br, and NO_2).

Samples	CO adsorption energy(eV)	CO_2 adsorption energy(eV)
Cu-$N(C_2H_5)_2$	-1.10472	-0.3194
Cu-OCH_3	-1.16435	-0.336
Cu-N	-1.20232	-0.3668
Cu-NN	-1.21724	-0.38057
Cu-NNN	-1.19099	-0.34868
Cu-Br	-1.12475	-0.36483
Cu-NO_2	-1.12089	-0.37045
Cu-$N(C_2H_5)_2$	-1.10472	-0.3194

Supplementary Table 5 Free energies for $*C_2H_3O$ (prebranch), $*C_2H_4O$ (ethanol pathway), and $C_2H_4(g)+O*$ (ethylene pathway) on Cu-X catalysts (X refers to $N(C_2H_5)_2$, OCH_3, N, NN, NNN, Br, and NO_2) by DFT calculations.

	Valence (Cu)	**$C_2H_4(g)+O*$ (ethylene pathway, eV)**	**$*C_2H_4O$ (ethanol pathway, eV)**	$E_{ethylene\ pathway}$-$E_{ethanol\ pathway}$
Cu	0	-0.988	0.325	-1.313
Cu-$N(C_2H_5)_2$	+0.134	-0.879	0.352	-1.231
Cu-OCH_3	+0.188	-0.984	0.36	-1.344
Cu-N	+0.214	-1.223	0.311	-1.534
Cu-NN	+0.268	-1.625	0.056	-1.681
Cu-NNN	+0.516	-1.377	0.006	-1.383
Cu-Br	+0.663	-1.268	-0.227	-1.041
Cu-NO_2	+0.757	-1.274	-0.534	-0.74

Supplementary Table 6 The applied field effects on the free energy of the selectivity-determining step of ethylene and ethanol over Cu-NN surface.

Electrical field (eV/Å)	**Ethylene path way**	**Ethanol path way**
-0.75	-1.50762	0.32507
-0.5	-1.41018	0.33243
-0.45	-1.39522	0.31126
-0.4	-1.26121	0.2266
-0.35	-1.28159	0.28601
-0.3	-1.19885	0.28027
-0.25	-1.19447	0.29642
-0.2	-1.20138	0.27858
-0.15	-1.17853	0.27775
-0.1	-1.11834	0.29096
-0.05	-0.96478	0.27791
0	-0.98297	0.33026
0.05	-0.96875	0.29032
0.10	-0.97745	0.25988
0.15	-0.9804	0.26444
0.2	-0.98421	0.27729
0.25	-0.98002	0.27104
0.30	-0.99817	0.28713

0.35	-1.00016	0.30183
0.40	-1.00129	0.02542
0. 45	-1.00668	0.58109
0.5	-1.00224	0.31297
0.75	-1.02795	0.31199

Supplementary Table 7 The Free energy of HER on bare Cu and Cu-NN catalysts.

Samples	Configurations	Free energy (eV)
Cu	Fcc	0.269
	Hcp	0.333
	Top	0.306
Cu-NN	Fcc-close	0.398
	Fcc-far	0.454
	Hcp-close	0.408
	Hcp-far	0.458
	Top-close	0.460
	Top-far	0.483

Supplementary Table 8 Summary of the atomic ratio of Cu, N, O, Br and C on Cu-X electrodes from XPS results (X refers to Br, OCH_3, NO_2, NN, NNN, N, $N(C_2H_5)_2$ and NN/ionomer).

Electrodes	atomic ratio (at.%)				
	Cu	**C**	**N**	**O**	**Br**
Pristine	100	/	/	/	/
Cu-$N(C_2H_5)_2$	62.4	30.2	7.4	/	/
Cu-OCH_3	71.2	21.5	4.3	3.0	/
Cu-N	51.6	39.0	7.2	2.2	/
Cu-NN	39.3	51.0	9.7	/	/
Cu-NNN	43.4	38.7	11.8	6.1	/
Cu-Br	73.0	19.7	4.1	/	3.2
Cu-NO_2	65.8	19.8	7.8	6.6	/

Supplementary Table 9 Summary of the estimated FEs for Cu-X electrodes measured at different applied potentials in the MEA reactors (X refers to Br, OCH_3, NO_2, NN, NNN, N, $N(C_2H_5)_2$ and NN/ionomer). The standard deviation of the measurements was estimated from three independent samples.

Electrode	**Cell voltages (V)**	**Faradaic efficiency (FE, %)**				
Pristine (Cu)		**H_2**	**CO**	**HCOOH**	**C_2H_4**	**C_2H_5OH**
	-3.0	64.2±1.0	31.9±1.0	0	4.1±0.9	0
	-3.2	57.4±2.3	29.8±0.9	0	11.4±2.7	0
	-3.4	47.9±2.5	27.9±0.7	1.8±0.6	19.4±1.7	0
	-3.5	41.7±0.9	26.6±0.8	2.2±0.6	26.5±1.6	1.8±0.5
	-3.55	40.8±1.6	25.3±0.9	2.8±0.6	28.0±1.3	3.6±1.1
	-3.6	37.1±1.2	24.3±1.2	3.2±0.7	29.8±1.4	4.2±0.9
	-3.65	36.9±1.9	22.2±1.4	5.1±0.6	31.9±2.3	5.7±1.1
	-3.7	35.9±1.5	21.7±0.7	4.5±0.8	35.3±2.3	7.1±2.0
	-3.75	32.8±0.4	19.6±0.7	3.2±0.8	38.4±1.5	8.1±2.1
	-3.8	32.8±0.4	18.4±0.5	2.1±0.7	40.2±1.4	11.9±3.0
	-3.85	37.9±0.8	17.5±0.5	1.4±0.5	38.6±0.8	10.6±1.0
	-3.9	43.9±1.1	16.4±0.6	1.5±0.5	36.2±0.4	8.7±2.0
	-4.0	48.5±1.7	14.1±1.0	1.0±0.6	32.7±0.4	4.9±0.3
Cu-$N(C_2H_5)_2$	-3.0	47.3±1.1	12.3±0.8	0	32.0±5.9	0
	-3.2	42.9±1.3	10.6±1.1	0	43.2±1.6	0
	-3.4	38.1±1.2	8.7±1.1	0.9±0.2	52.7±2.6	0.6±0
	-3.5	32.1±0.2	9.1±1.2	1.0±0.5	57.9±2.9	0.6±0.3
	-3.55	28.4±0.7	7.9±1.5	1.2±0.5	63.0±2.7	0.9±0.5
	-3.6	24.6±0.9	6.2±1.3	1.4±0.4	67.8±3.1	1.4±0.3
	-3.65	21.7±1.2	5.3±0.5	1.5±0.8	72.9±2.9	1.9±0.5
	-3.7	23.7±0.7	4.6±0.6	1.1±0.4	68.3±3.1	2.3±1.1
	-3.75	26.6±0.5	4.1±0.6	0.7±0.5	65.4±2.3	3.2±1.3
	-3.8	37.6±1.0	3.3±0.6	0.7±0.4	57.9±1.7	2.5±1.4

	-3.85	47.9±0.8	2.2±0.5	0.6±0.4	49.3±2.7	2.0±0.8
	-3.9	53.3±0.8	1.8±0.5	0.6±0.4	42.7±1.5	1.6±0.4
	-4.0	57.7±0.6	1.8±0.1	0.5±0.2	39.0±0.8	1.5±0.7
Cu-NNN	-3.0	54.3±1.1	4.4±0.9	0	32.1±6.0	0
	-3.2	49.5±1.3	4.4±1.1	0	38.9±1.7	0
	-3.4	42.8±1.2	5.2±1.1	1.1±0.4	45.1±2.6	1.4±0.4
	-3.5	38.4±0.2	6.1±1.2	2.1±0.2	49.9±2.9	1.3±0.8
	-3.55	34.9±0.7	6.4±1.5	2.6±0.2	53.9±2.7	1.4±0.7
	-3.6	32.3±0.9	7.3±1.3	3.5±0.3	57.9±3.1	1.7±0.8
	-3.65	26.7±1.2	6.3±0.5	3.8±1.0	61.5±2.9	2.4±0.8
	-3.7	23.4±0.7	5.8±0.6	3.2±0.9	66.6±3.1	3.8±0.9
	-3.75	19.5±0.5	4.9±0.6	3.3±0.3	70.4±2.3	4.6±1.2
	-3.8	16.2±1.0	4.2±0.6	2.3±0.4	75.1±1.7	5.1±1.2
	-3.85	19.2±0.8	3.7±0.5	1.2±0.5	71.2±2.7	4.9±1.3
	-3.9	23.3±0.8	3.4±0.5	1.5±0.4	68.2±1.5	3.8±1.1
	-4.0	27.2±2.0	2.5±1.0	1.1±1.0	61.3±2.9	2.7±1.5
Cu-OCH_3	-3.0	33.0±7.7	22.8±1.1	0	40.2±3.1	0
	-3.2	26.2±2.1	24.3±1.9	0	48.9±4.3	0
	-3.4	23.6±2.7	20.1±2.1	0.9±0.3	53.6±5.6	1.0±1.9
	-3.5	23.2±3.4	15.4±1.7	0.9±0.8	57.3±3.2	1.5±2.7
	-3.55	18.7±2.9	10.3±1.6	1.3±0.6	65.4±3.7	2.9±4.2
	-3.6	16.4±3.2	9.0±4.7	1.4±0.8	72.2±5.3	3.1±3.3
	-3.65	15.3±3.4	6.7±1.6	1.5±0.8	78.0±2.7	3.8±4.5
	-3.7	14.3±3.5	5.3±2.3	1.3±0.8	76.4±4.1	5.1±4.6
	-3.75	16.9±4.2	3.6±1.0	1.2±0.7	74.3±2.7	3.8±3.0
	-3.8	19.5±5.4	3.2±1.9	1.4±0.6	71.1±4.9	3.3±3.1
	-3.85	22.8±7.1	2.7±1.9	0.8±0.7	70.6±2.2	2.3±3.1
	-3.9	24.1±8.4	2.4±0.8	1.1±0.8	70.0±3.3	1.9±2.9
	-4.0	29.3±0.9	2.5±0.3	0.8±0.2	65.6±0.6	1.2±0.4
Cu-N	-3.0	47.3±2.5	35.4±3.0	0	15.5±2.0	0

	-3.2	37.2±2.5	34.1±1.7	0.3±0.1	22.5±1.7	0
	-3.4	25.9±1.4	31.8±1.4	0.4±0.1	36.6±1.4	1.1±0.1
	-3.5	22.0±1.0	24.6±0.5	0.5±0.1	43.7±0.6	1.3±0.4
	-3.55	20.8±1.3	19.5±1.4	0.7±0.2	51.7±0.9	1.3±0.6
	-3.6	19.1±1.2	14.2±0.1	1.1±0.7	61.7±2.3	2.3±0.8
	-3.65	17.8±1.0	11.0±1.1	1.2±0.8	68.6±2.5	2.5±0.7
	-3.7	16.3±0.6	9.3±0.4	1.2±0.4	72.7±2.0	2.6±1.0
	-3.75	15.3±0.4	7.1±0.7	1.8±0.8	76.8±1.1	2.7±1.1
	-3.8	14.2±0.2	5.5±0.8	1.2±0.8	79.9±0.5	3.3±0.6
	-3.85	15.5±0.4	5.1±0.9	0.9±0.9	78.1±1.7	3.1±1.1
	-3.9	16.5±1.0	4.7±1.2	0.8±0.8	75.3±1.3	3.1±1.2
	-4.0	20.7±0.5	3.4±0.9	0.5±0.6	72.0±0.9	2.3±0.8
	-3.0	47.3±2.5	35.4±3.0	0	15.5±2.0	0
Cu-NN	-3.0	34.0±2.1	8.0±1.6	0	50.6±1.2	0
	-3.2	25.2±1.4	9.5±1.8	0.2±1.4	62.2±2.5	1.9±1.1
	-3.4	15.4±0.5	10.0±0.4	0.2±1.1	70.3±1.9	2.3±1.0
	-3.5	10.0±1.2	8.5±2.2	2.5±0.8	77.5±2.1	2.3±2.0
	-3.55	8.3±2.8	6.3±1.1	2.3±0.9	83.2±2.4	2.5±1.0
	-3.6	12.3±2.3	5.6±3.0	1.4±0.8	80.0±0.8	2.5±2.0
	-3.65	15.8±3.1	5.4±2.0	1.2±1.0	76.6±0.6	2.6±1.0
	-3.7	19.2±1.2	4.9±2.0	1.3±0.9	71.1±1.8	4.0±1.0
	-3.75	22.1±3.2	4.8±1.1	1.3±1.1	64.1±2.4	4.5±0.8
	-3.8	26.4±4.1	4.4±2.0	1.1±0.9	60.2±1.3	4.4±0.9
	-3.85	30.2±3.3	4.4±3.1	0.9±1.1	55.9±1.6	4.8±1.0
	-3.9	34.8±2.4	4.0±1.2	0.8±1.0	53.0±2.4	3.9±1.1
	-4.0	38.4±3.1	3.9±0.9	0.7±1.3	52.3±1.1	3.6±0.8
Cu-Br	-3.0	48.5±3.7	25.0±0.5	0	21.9±0.5	0
	-3.2	43.9±4.7	27.7±1.0	0	25.9±1.0	0
	-3.4	38.2±7.5	23.1±2.5	0.7±0.9	36.3±1.7	0.7±0.4
	-3.5	34.2±5.3	20.6±3.2	1.5±0.9	42.5±2.2	2.0±0.7

	-3.55	31.5±4.2	15.9±4.0	2.4±1.2	47.0±2.8	2.9±1.2
	-3.6	29.2±2.0	13.4±5.1	3.4±1.1	51.1±3.9	3.5±1.3
	-3.65	26.7±6.4	9.7±6.3	2.3±0.9	57.0±2.1	5.1±1.5
	-3.7	25.8±5.4	7.0±2.9	1.9±0.7	61.7±1.6	6.0±2.6
	-3.75	34.7±5.3	5.9±5.3	1.5±0.6	55.1±4.9	5.5±2.0
	-3.8	42.0±4.1	4.2±2.9	1.2±0.9	48.5±5.9	5.2±2.2
	-3.85	48.9±3.1	2.9±7.9	1.1±0.8	44.5±5.4	4.1±1.1
	-3.9	50.5±3.1	2.6±5.2	0.9±0.7	41.7±5.5	3.1±2.1
	-4.0	56.6±2.1	2.6±3.5	0.8±1.0	37.1±2.8	2.8±1.9
Cu-NO2	-3.0	48.9±1.2	9.8±1.1	0	35.9±0.9	0
	-3.2	47.3±1.3	12.5±0.4	0	37.2±1.1	0
	-3.4	44.6±1.2	12.6±0.6	0.7±0.3	39.3±1.1	0
	-3.5	43.2±0.8	14.4±0.3	1.2±0.2	43.4±0.8	0.8±0.5
	-3.55	37.4±0.5	10.9±0.6	1.7±0.2	45.9±0.6	1.4±0.4
	-3.6	34.7±0.5	9.7±0.5	1.9±0.0	49.2±0.7	1.9±0.4
	-3.65	33.5±0.3	8.9±0.1	2.9±0.4	51.6±0.5	3.2±0.5
	-3.7	33.5±0.4	7.8±0.1	3.5±0.4	53.5±0.6	4.6±0.4
	-3.75	28.6±0.2	7.0±0.5	2.3±0.3	56.3±0.4	5.6±0.4
	-3.8	32.3±0.4	6.0±0.1	1.1±0.2	57.9±0.8	6.8±0.3
	-3.85	38.9±0.9	5.9±0.2	1.1±0.6	56.3±1.2	4.8±0.3
	-3.9	40.7±0.7	5.4±0.1	1.3±0.1	53.6±0.9	3.7±0.3
	-4.0	45.7±1.3	4.2±0.3	0.7±1.1	49.2±1.4	2.0±1.5
Cu-NN/ionomer	-3.0	66.9±3.5	4.6±0.2	0	23.7±1.0	0
	-3.2	61.9±2.5	5.1±0.3	0	25.3±0.6	0
	-3.4	51.7±1.8	7.1±0.2	1.0±0.5	37.4±1.1	0.6±0.4
	-3.5	44.9±3.1	7.1±0.3	1.4±0.5	43.9±1.8	1.0±0.5
	-3.55	40.9±1.5	5.3±0.1	1.5±0.5	49.4±0.8	1.0±1.1
	-3.6	35.4±1.0	4.8±0.1	1.7±0.4	56.1±1.3	1.2±0.6
	-3.65	28.1±2.9	4.7±0.2	2.0±0.5	64.2±1.8	1.7±1.0
	-3.7	21.9±0.6	4.2±0.1	1.5±0.4	73.6±2.0	2.1±0.5

	-3.75	14.4±1.5	4.2±0.1	1.1±0.5	75.5±1.7	2.5±1.1
	-3.8	10.8±1.1	3.6±0.3	1.1±0.4	86.3±0.5	2.8±1.5
	-3.85	7.2±2.3	4.0±0.1	1.1±0.6	89.0±2.9	2.3±1.0
	-3.9	14.6±3.4	3.2±0.4	1.1±0.4	79.5±1.5	2.3±0.9
	-4.0	23.2±4.0	3.6±1.3	0.6±0.9	73.8±2.1	1.7±1.5

Supplementary Table 10. The comparison of energy efficiency (EE) and energy power consumption (EPC) on different diazonium salts functionalized copper catalysts and the literatures benchmarks in single MEA electrolyzer.

Samples	j_{C2H4} (mA cm^{-2})	E_{cell} (V)	FE_{C2H4} (%)	EE_{C2H4} (%)	EPC (kWh/Nm^3)	Notes
Cu-NN/ionomer	536	3.85	89	27.0	62.9	
Cu-NN	212	3.55	83	26.9	61.4	
Cu-NO_2	198	3.80	58	17.5	94.2	
Cu-NNN	229	3.80	75	22.7	72.7	Our work
Cu-N	271	3.80	80	24.2	68.2	
Cu-OCH_3	250	3.65	78	23.6	69.9	
Cu-Br	170	3.70	62	19.1	86.1	
Cu-N(C_2H_5)$_2$	126	3.65	73	23.0	71.8	
Cu-12	76.8	3.6	64	20.2	81.8	Ref [6]
Cu/tetrahydro-phenanthrolinium/ CTPI	208	3.8	67	20.2	81.4	Ref [7]
Cu-CIPH	210	3.9	54	16.0	103.6	Ref [8]
Cu-SiOx	215	4.1	65	18.2	90.5	Ref [9]
Cu-KOH	153	3.25	55	19.4	84.8	Ref [10]
Cu-CO_2-60	217	3.7	62	19.3	85.6	Ref [11]

Supplementary Table 11. Summary of the calculated electrochemically active surface area (ECSA) for Cu and Cu-NN and Cu-NN/ionomer catalysts.

Sample	ECSA (cm^2)	Surface coverage (%)
Cu	14.4	\
Cu-NN	11.7	18.5%

Cu-NN/ionomer	10.2	29.2%

Supplementary Table 12. Summary of the calculated electrochemically active surface area (ECSA) for Cu(111) and Cu(100) single crystals and Cu(111)-NN and Cu(100)-NN single crystals catalysts.

Sample	ECSA (Cu, cm2)	Surface coverage (%)
Cu (111)	1.20	\
Cu (100)	1.27	\
Cu (111)-NN	0.95	20.6%
Cu (100)-NN	0.99	21.8%

Supplementary Table 13. Surface composition. Extracted from the integrated areas of the fits of the Cu-LMM AES data (Figure 3a) with the corresponding reference spectra.

Electrode	Cu (at. %)	Cu_2O (at. %)	Average oxidation state
Cu	100	0	0
Cu-$N(C_2H_5)_2$	86.5	13.5	+0.135
Cu-OCH_3	80.7	19.3	+0.193
Cu-N	77	23.0	+0.23
Cu-NN	73.8	26.2	+0.262
Cu-NNN	49	51.0	+0.51
Cu-Br	34.9	65.1	+0.651
Cu-NO_2	25.3	74.7	+0.747

Supplementary Table 14. Summary of the XANES data. E0 and corresponding oxidation states (δ) of Cu-X catalysts (X refers to NO_2, Br, NNN, NN, N, OCH_3 and $N(C_2H_5)_2$ functional groups).

Electrode	Pristine (Cu)	Cu-$N(C_2H_5)_2$	Cu-OCH_3	Cu-N	Cu-NN	Cu-NNN	Cu-Br	Cu-NO_2
E_0	8979.11	8979.20	8979.28	8979.32	8979.4	8979.77	8979.99	8980.13
δ	+0.067	+0.134	+0.188	+0.214	+0.268	+0.516	+0.663	+0.757

Supplementary Table 15. Summary of the XANES data. E0 and corresponding oxidation states (δ) of Cu-NN under different potentials.

Potentials	OCV	-0.93 (V vs. RHE)	-0.88 (V vs. RHE)	-0.83 (V vs. RHE)
E_0	8979.4	8979.37	8979.34	8979.28
δ	+0.27	+0.25	+0.23	+0.19

Supplementary Table 16. Structure parameters (N^a: coordination numbers; R(Å)^b: bond distance; σ^2(Å^2)^c: Debye-Waller factors; ΔE_0 (eV)^d: the inner potential correction. R factor: goodness of fit.), obtained in fitting of experimental Cu K-edge EXAFS data for ex-situ samples (S_0^2=0.94). Uncertainties of the last digit are given in parentheses.

Sample	Shell	N^a	R(Å)^b	σ^2(Å^2)^c	ΔE_0 (eV)^d	R factor
Cu foil	Cu-Cu	12.0	2.54(2)	0.0091(2)	3.4(1)	0.0003
Cu_2O	Cu-O	2.0(2)	1.84(9)	0.002(1)	2.0(1)	0.008
$N(C_2H_5)_2$	Cu-O	0.2(1)	1.86(3)	0.001(7)	1.6(7)	0.002
	Cu-Cu	6.6(9)	2.54(4)	0.008(7)		
OCH_3	Cu-O	0.3(2)	1.86(2)	0.001(4)	2.0(5)	0.003
	Cu-Cu	6.4(3)	2.54(1)	0.008(3)		
N	Cu-O	0.3(2)	1.86(2)	0.001(4)	2.6(8)	0.003
	Cu-Cu	6.0(1)	2.54(2)	0.008(5)		
NN	Cu-O	0.5(2)	1.86(1)	0.001(3)	3.2(8)	0.003
	Cu-Cu	5.7(9)	2.55(1)	0.008(3)		
NNN	Cu-O	1.2(4)	1.86(1)	0.001(3)	3.3(7)	0.004
	Cu-Cu	5.1(6)	2.54(1)	0.008(4)		
Br	Cu-O	1.5(3)	1.86(2)	0.001(4)	3.2(6)	0.004
	Cu-Cu	5.1(7)	2.53(3)	0.008(1)		
NO_2	Cu-O	1.9(4)	1.86(3)	0.001(3)	3.2(5XANE)	0.004
	Cu-Cu	4.8(7)	2.50(2)	0.008(1)		
Pristine	Cu-Cu	8.8(3)	2.54(2)	0.0085(3)	2.4(3)	0.0004

Supplementary Table 17. The ratio between the intensities of bands for HFB-CO* and LFB-CO* on Cu-X catalysts (X refers to NO_2, Br, NNN, NN, N, OCH_3 and $N(C_2H_5)_2$ functional groups). Two independent sets of samples were measured, and the average values were used for figure plotting and data analysis.

Electrode	Ratio (H/L)		
	Tray 1	Tray 2	average
Cu	0.92	0.89	0.91
Cu-$N(C_2H_5)_2$	1.04	1.02	1.03
Cu-OCH_3	1.20	1.24	1.22
Cu-N	1.23	1.25	1.24
Cu-NN	1.44	1.46	1.45
Cu-NNN	1.58	1.54	1.56
Cu-Br	1.65	1.61	1.63
Cu-NO_2	1.76	1.74	1.75

Supplementary Table18. Summary of the estimated FEs for Ag electrode measured at different applied potentials in the MEA reactor. The standard deviation of the measurements was estimated from three independent samples.

Cell Voltages (V)	Faradaic efficiency (%)	
	CO	H_2
-3.0	74.4±1.4	25.3±1.1
-3.1	78.1±0.6	22.2±1.0
-3.2	81.8±1.1	18.8±1.0
-3.3	84.0±1.8	15.6±1.7
-3.35	86.9±1.3	13.1±2.4
-3.40	88.4±2.0	11.1±2.1
-3.45	91.2±1.0	9.6±1.8
-3.5	93.2±1.5	7.6±1.9
-3.55	94.9±0.8	5.7±1.4
-3.6	93.4±1.4	7.6±1.2
-3.65	90.7±1.4	10.3±1.3
-3.7	88.4±1.1	13.3±1.2
-3.75	85.6±1.6	15.3±1.7
-3.8	83.8±2.4	17.1±1.6

Supplementary Table 19. Summary of the estimated FEs for Cu-X electrodes measured at different applied potentials in the cascade MEA system with IrOx supported on Ti mesh as the anode (X refers to NN and NN/ionomer functional groups). The standard deviation of the measurements was estimated from three independent samples.

Electrodes	voltages (V)	Faradaic efficiency (%)				
		H_2	C_2H_4	C_2H_5OH	CH_3COOH	n-Propanol
Cu	-2.0	83.1±2.9	12.4±1.6	0.5±0.7	0.4±1.0	0.2±0.8
	-2.1	73.0±3.5	21.6±2.6	1.4±0.9	0.5±1.3	0.9±0.5
	-2.2	65.4±3.0	27.9±2.3	1.6±0.5	0.7±0.9	0.9±0.7
	-2.3	49.5±4.9	37.4±3.0	1.7±1.1	0.8±1.0	0.9±0.8
	-2.4	45.3±1.3	47.2±1.5	2.4±1.5	1.2±1.2	1.1±0.5
	-2.5	37.7±2.0	54.9±3.5	2.4±1.3	1.2±1.7	0.9±1.5
	-2.6	31.4±2.9	63.2±5.1	2.8±0.5	1.3±0.9	0.9±1.0
	-2.7	28.1±1.5	67.4±2.9	2.5±2.1	1.0±1.4	0.9±2.1
	-2.8	30.1±4.8	64.7±2.4	2.2±1.9	0.9±0.5	0.9±0.5
	-2.9	34.9±3.6	58.4±1.7	1.2±0.6	0.8±0.5	0.8±1.0
Cu-NN	-2.0	60.7±3.0	35.4±2.3	1.4±1.2	2.0±0.4	1.8±0.7
	-2.1	42.5±1.9	50.7±1.9	1.8±2.5	1.9±0.3	1.9±0.6
	-2.2	30.2±0.8	65.5±1.0	1.4±1.8	1.5±0.6	1.6±0.4
	-2.3	22.4±1.9	75.9±1.9	1.1±1.5	1.1±0.7	1.5±0.9
	-2.4	19.5±0.1	81.9±0.4	1.0±0.8	0.9±0.7	1.6±0.6
	-2.5	15.4±0.4	86.0±0.6	1.1±0.6	0.8±0.3	1.4±0.2
	-2.6	20.2±0.1	82.2±0.6	1.1±1.4	0.9±0.6	1.4±0.4
	-2.7	24.1±0.3	76.8±0.9	1.1±0.9	0.7±1.0	1.4±0.4
	-2.8	28.7±0.6	71.2±1.3	1.0±0.7	0.6±0.5	1.3±0.7
	-2.9	34.7±0.5	66.3±0.5	1.4±0.7	0.6±0.5	1.3±0.5
Cu-NN/ionomer	-2.0	71.0±2.9	16.9±2.5	0.8±2.4	1.5±1.3	1.2±1.1
	-2.1	58.9±1.3	28.3±3.0	0.8±2.0	1.5±1.5	1.0±1.5
	-2.2	50.2±2.0	39.8±1.5	0.6±2.1	1.4±2.5	0.9±2.0
	-2.3	47.6±2.4	46.9±2.5	0.7±1.0	1.3±1.0	0.9±1.5
	-2.4	42.4±2.8	53.6±3.5	0.7±0.5	1.2±0.5	1.0±1.1
	-2.5	38.2±1.9	59.2±5.1	0.8±1.5	1.1±1.0	1.1±0.7
	-2.6	32.8±3.5	64.9±4.0	0.8±1.0	1.2±1.2	1.0±0.5
	-2.7	26.0±2.5	72.1±2.9	0.7±0.7	1.2±1.5	0.8±0.8
	-2.8	28.5±1.4	61.9±1.4	0.6±0.4	1.0±0.7	0.6±0.7
	-2.9	32.5±3.0	55.6±4.9	0.6±1.4	0.9±0.6	0.5±1.0

Supplementary Table 20. Summary of the estimated FEs for Cu-X electrodes measured at different applied potentials in the cascade MEA system with NiFe LDH as the anode (X refers to NN and NN/ionomer functional groups). The standard deviation of the measurements was estimated from three independent samples.

Electrodes	voltages (V)	Faradaic efficiency (%)				
		H_2	C_2H_4	C_2H_5OH	CH_3COOH	n-Propanol
Cu	-1.7	83.5±1.7	7.1±2.4	1.0±0.6	2.2±0.6	1.0±0.2
	-1.8	82.2±2.7	11.5±1.2	1.7±0.8	2.7±0.6	1.4±0.3
	-1.9	76.0±2.9	20.4±2.8	1.8±0.7	2.7±0.1	1.5±0.8
	-2.0	69.8±2.1	25.5±3.4	1.0±0.6	1.5±1.3	1.1±0.8
	-2.1	64.7±3.2	30.4±3.6	0.9±0.8	1.1±0.8	1.0±1.0
	-2.2	54.4±1.7	38.1±2.6	0.9±0.6	1.0±0.3	0.9±1.1
	-2.3	49.9±1.0	46.4±1.0	0.9±0.6	1.1±0.9	0.9±0.6
	-2.4	39.9±3.4	57.7±3.3	0.9±0.9	0.9±1.3	0.9±0.9
	-2.5	30.8±5.6	64.5±1.6	0.8±0.6	0.8±0.6	0.8±0.2
	-2.6	39.3±2.1	54.7±3.9	1.1±0.6	0.8±0.6	0.8±0.7
Cu-NN	-1.7	66.8±2.9	21.9±2.8	1.0±0.7	2.2±0.8	1.0±0.4
	-1.8	53.1±0.6	38.2±2.7	1.7±0.2	2.7±0.5	1.4±0.4
	-1.9	40.1±2.1	54.5±1.9	1.8±0.5	2.7±0.3	1.5±0.6
	-2.0	33.7±1.1	63.5±3.5	1.0±0.6	1.5±0.5	1.1±0.6
	-2.1	23.2±1.4	72.8±3.1	0.9±0.5	1.1±0.6	1.0±0.1
	-2.2	20.1±2.5	81.8±2.7	0.9±1.0	1.0±1.0	0.9±0.6
	-2.3	14.7±2.9	86.1±2.1	0.9±1.5	1.1±0.9	0.9±0.4
	-2.4	23.3±2.8	79.8±2.7	0.9±0.9	0.9±0.6	0.9±1.0
	-2.5	38.7±3.1	67.2±1.9	0.8±0.3	0.8±0.6	0.8±1.0
	-2.6	53.9±2.8	52.6±3.0	1.1±0.8	0.8±0.3	0.8±0.6
Cu-NN/ionomer	-1.7	83.0±3.0	8.8±2.3	2.0±0.9	1.8±0.4	0.6±0.9
	-1.8	75.9±2.9	15.9±1.0	2.3±1.9	2.2±0.6	0.8±0.8
	-1.9	68.0±1.8	23.8±0.2	1.1±1.4	2.5±0.4	1.3±0.8
	-2.0	60.5±3.9	31.2±1.8	0.9±0.6	2.2±0.6	1.3±0.4
	-2.1	52.4±3.1	38.7±3.0	0.9±0.6	1.5±1.0	1.3±0.4
	-2.2	46.0±2.1	44.0±4.1	1.0±0.6	1.4±0.4	1.4±1.0
	-2.3	39.9±2.2	53.3±4.5	0.9±0.8	1.2±1.0	1.0±0.4
	-2.4	33.4±4.3	68.1±3.2	0.8±1.0	1.4±1.3	0.9±0.6
	-2.5	28.6±1.6	72.1±2.1	0.7±1.0	1.2±0.9	0.7±0.6
	-2.6	35.7±3.5	64.6±2.9	0.7±0.5	1.0±1.2	0.6±0.3

Supplementary Table 21. Comparison of the performance metrics of the cascade MEA systems based on bare Cu, Cu-NN and Cu-NN/ionomer cathodes.

Electrodes	j_{C2H4} (mA cm^{-2})	FE_{C2H4} (%)	R_{C2H4} (μmol h^{-1} cm^{-2})	Energy efficiency (EE, %)	Electricity power consumption (EPC, KWh/Nm^3)
Bare Cu	122	64.5	571	27.36	37.08
Cu-NN	154	86	720	39.69	25.56
Cu-NN/ionomer	234	72	1094	30.53	33.20

Supplementary Table 22. Summary of the estimated conversion rate (%) of CO_2 to C_2H_4 in single MEA and cascade MEA systems on Cu-X electrodes measured at different current density (X refers to NN and NN/ionomer functional groups). The standard deviation of the measurements was estimated from three independent samples.

	j_{total} (mA cm^{-2})	CO_2-C_2H_4 (%) (Single MEA)	j_{total} (mA cm^{-2})	CO_2-C_2H_4 (%) (Cascade MEA)
Bare Cu	45.1	0.05248	5.4	0.05914
	70.8	0.4264	10.45	0.26140
	113	0.91512	28.5	0.96744
	153	1.60064	59.375	1.63969
	176	1.97456	80.475	2.49496
	202	2.43704	102.575	4.44169
	230	3.05368	145.8	6.01062
	249	3.40464	162.125	8.75611
	280	4.17872	189.75	9.79168
	304	4.66088	216	9.44685
	330	4.91672		
	361	5.002		
	389	4.65104		
Cu-NN	53.06667	1.02336	10.61333	0.2058
	92.76667	2.20088	26.36	0.679895
	158	4.22464	53.26667	1.4868
	214.66667	6.33805	84.23333	3.730125
	256.8	8.13549	111.68667	6.2601
	289.23333	8.80133	147.78667	9.66575
	328.26667	9.57104	187.04	12.27555
	369.13333	9.98651	217.18667	13.430025
	411.26667	10.03571	269.83333	14.45955
	450.86667	10.332	278.9	12.331725
	493.2	10.48944		
	530.03333	10.69827		
Cu-NN/ionomer	62.05669	0.75112	16.3	0.20700
	145.61473	1.5129	29.325	1.0007
	223.15493	3.18078	78.75	2.55168
	267.90518	4.47556	134.3	4.49133
	321.76597	6.05324	180.25	7.24739
	354.89948	7.57926	233.95	10.25059

	400.87544	9.79162	291.125	12.87568
	445.60173	12.49516	302.25	17.73350
	489.99115	14.08268	325.75	18.76907
	564.02061	18.59022	352.35	18.21300
	599.44034	20.6681		
	683.5718	20.7132		

Supplementary Table 23. Techno-economic assessment. Cost of ethylene produced from CO_2 in different systems with different electrodes.

Single MEA system (CO_2-C_2H_4, neutral case)

Parameters	bare Cu	Cu-NN	Cu-NN/ionomer
Output product	C_2H_4	C_2H_4	C_2H_4
CO_2 cost($/tonne)	30	30	30
Cathode Input CO_2 cost ($/tonne C_2H_4)	515.1	500.1	501.7
Product formation rate (mol/h/cm^2)	$3.8*10^{-4}$	$6.6*10^{-4}$	$16.4*10^{-4}$
Cathode catalyst	Cu	Cu-NN	Cu-NN/ionomer
Cathode catalyst lifetime (year)	1	1	1
Cathode catalyst ($/tonne C_2H_4)	932.87	1407.1	762.8
Membrane (AEM, X-37) ($/tonne C_2H_4)	3854.6	2218.9	893.6
Anode catalyst	IrOx-Ti mesh	IrOx-Ti mesh	IrOx-Ti mesh
Anode Catalyst ($/tonne C_2H_4)	4066.7	2342	942.98
Anolyte Molarity(mol/L)	0.5 M $KHCO_3$	0.5 M $KHCO_3$	0.5 M $KHCO_3$
Anolyte lifetime (year)	1	1	1
Cost of Anolyte ($/tonne C_2H_4)	4.56	2.63	1.06
Electric power consumption (kWh/tonne C_2H_4)	109120	48990	50100
Electric power consumption ($/tonne C_2H_4)	3273.6	1469.7	1503
Cell Voltage(V)	3.8	3.55	3.85
Faradaic efficiency (C_2H_4, %)	40	83	89
Total Current density (mA/cm^2)	304	256	602
Single pass conversion (%)	5.996	10.188	25.205
System lifetime (year)	10	10	10
Ethanolamine ($/tonne C_2H_4)	N/A	N/A	N/A
total cost ($/tonne C_2H_4)	12647.43	7940.33	4620.08

N/A. indicates that the item is not applicable.

Cascade MEA system (CO_2-CO, CO-C_2H_4, base case)

	Cu system		Cu-NN system		Cu-NN/ionomer system	
Parameters	Ag (CO_2-CO)	Cu (CO-C_2H_4)	Ag (CO_2-CO)	Cu (CO-C_2H_4)	Ag (CO_2-CO)	Cu (CO-C_2H_4)
Output product	CO	C_2H_4	CO	C_2H_4	CO	C_2H_4
CO_2 cost ($/tonne)	30	N/A	30	N/A	30	N/A
Cathode Input CO_2 cost ($/tonne C_2H_4)	983.68	N/A	802.13	N/A	938.76	N/A
Product formation rate (mol/h/cm^2)	$26.7*10^{-4}$	$5.7*10^{-4}$	$26.7*10^{-4}$	$7.2*10^{-4}$	$26.7*10^{-4}$	$10.9*10^{-4}$

Cathode catalyst	Cu		Cu-NN		Cu-NN/ionomer	
Cathode catalyst lifetime (year)	1	1	1	1	1	1
Cathode catalyst ($/tonne C_2H_4)	580.5	580	479	1254.2	317.9	1120.5
Membrane (AEM, X-37) ($/tonne C_2H_4)	2396.6	2396.6	1978	1978	1312.5	1312.5
Anode catalyst	NiFe LDH-Ti mesh	NiFe LDH-Ti mesh	NiFe LDH-Ti mesh	NiFe LDH-Ti mesh	NiFe LDH - Ti mesh	NiFe LDH-Ti mesh
Anode Catalyst ($/tonne C_2H_4)	216.9	216.9	179	179	118.8	118.8
Anolyte Molarity(mol/L)	0.1M $KHCO_3$	1M KOH	0.1M $KHCO_3$	1M KOH	0.1M $KHCO_3$	1M KOH
Anolyte lifetime (year)	1	1	1	1	1	1
Cost of Anolyte ($/tonne C_2H_4)	0.57	4.49	0.46	3.71	0.31	2.46
Electric power consumption (kWh/tonne C_2H_4)	38311	29826	31616.2	19901.5	20981	26625.8
Electric power consumption ($/tonne C_2H_4)	1149.3	895	948.45	597	629.43	798.7
Electrolyser cost($/kw)	300	300	300	300	300	300
Electrolyser cost ($/tonne C_2H_4)	1130	659	932.5	584.5	618	657
Cell Voltage(V)	3.8	2.5	3.8	2.3	3.8	2.5
Faradaic efficiency (C_2H_4, %)	84	64	84	86	84	72
Total Current density (mA/cm^2)	173	189	173	179	173	325
Cascade pass conversion (%)	N/A	7.7	N/A	9.8	N/A	14.8
System lifetime (year)	10	10	10	10	10	10
Ethanolamine ($/tonne C_2H_4)	N/A	3.33	N/A	2.75	N/A	1.82
total cost ($/tonne C_2H_4)	9423.87		8401.7		6672.48	

N/A. indicates that the item is not applicable.

4.8.1 References

1. Hurley B L, McCreery R L. Covalent bonding of organic molecules to Cu and Al alloy 2024 T_3 surfaces via diazonium ion reduction[J]. Journal of The Electrochemical Society, 2004, 151(5): B252.
2. Doppelt P, Hallais G, Pinson J, et al. Surface modification of conducting substrates. Existence of azo bonds in the structure of organic layers obtained from diazonium salts[J]. Chemistry of Materials, 2007, 19(18): 4570-4575.
3. Menanteau T, Dias M, Levillain E, et al. Electrografting via diazonium chemistry: the key role of the aryl substituent in the layer growth mechanism[J]. The Journal of Physical Chemistry C, 2016, 120(8): 4423-4429.
4. Cai J, Wang S, Zhang J, et al. Chemical grafting of the superhydrophobic surface on copper with hierarchical microstructure and its formation mechanism[J]. Applied Surface Science, 2018, 436: 950-956.

5. Mooste M, Kibena-Põldsepp E, Marandi M, et al. Surface and electrochemical characterization of aryl films grafted on polycrystalline copper from the diazonium compounds using the rotating disk electrode method[J]. Journal of Electroanalytical Chemistry, 2018, 817: 89-100.
6. Li F, Thevenon A, Rosas-Hernández A, et al. Molecular tuning of CO_2-to-ethylene conversion[J]. Nature, 2020, 577(7791): 509-513.
7. Ozden A, Li F, García de Arquer F P, et al. High-rate and efficient ethylene electrosynthesis using a catalyst/promoter/transport layer[J]. ACS Energy Letters, 2020, 5(9): 2811-2818.
8. García de Arquer F P, Dinh C T, Ozden A, et al. CO_2 electrolysis to multicarbon products at activities greater than 1 A cm^{-2}[J]. Science, 2020, 367(6478): 661-666.
9. Li J, Ozden A, Wan M, et al. Silica-copper catalyst interfaces enable carbon-carbon coupling towards ethylene electrosynthesis[J]. Nature communications, 2021, 12(1): 1-10.
10. Lee W H, Lim C, Lee S Y, et al. Highly selective and stackable electrode design for gaseous CO_2 electroreduction to ethylene in a zero-gap configuration[J]. Nano Energy, 2021, 84: 105859.
11. Wang, Y., Wang, Z., Dinh, CT. et al. Catalyst synthesis under CO_2 electroreduction favours faceting and promotes renewable fuels electrosynthesis. Nat Catal 3, 98–106 (2020).

Chapter 5. Summary and Perspectives

5.1 Summary

Although considerable progress has been made in meeting industrial requirements in terms of Faradaic efficiency (FE) and formation rate, the selectivity towards the formation of a single type of multi-carbon (C_{2+}) product has not been demonstrated to date. Moreover, numerous investigations have reported that partially oxidized copper ($Cu^{\delta+}$, $0<\delta<1$) sites on the surface of copper catalysts can facilitate the conversion of CO_2 to multi-carbons by decreasing the energy barrier associated with the CO dimerization. Nevertheless, the instability of $Cu^{\delta+}$ species, especially the high cathodic potentials to electro-synthesize multi-carbons, made the study of the role of $Cu^{\delta+}$ tedious, and it may eventually lead to a rapid loss of the performance. Therefore, my PhD work have aimed to explore an effective method to control $Cu^{\delta+}$ species on the surface of copper-based electrodes and to investigate the relationship between multi-carbon selectivity and the surface oxidation state of copper modified with electron-withdrawing molecules. By combining density functional theory (DFT) calculations with *operando* Raman and X-ray absorption spectroscopy (XAS), we identified that the grafting of electron-withdrawing functional groups can efficiently dope the surface of Cu leading to the formation of $Cu^{\delta+}(0<\delta<1)$ species. Compared to pristine non-functionalized electrodes, the modified electrodes display a clear improvement of the reaction rates and Faradaic efficiency towards the production of C_{2+} products.

The thesis is organized into five chapters. In the first chapter, we reviewed the fundamentals of CO_2 electrochemical reduction reaction, the methods and parameters of performance evaluation; and the current state of electrochemical CO_2 reduction reaction. The second chapter summarized the reported methods from literatures to suppress the main side reaction (hydrogen evolution reaction, HER) in CO_2 reduction reaction (CO_2RR) and N_2 reduction reaction (NRR). This work was carried out during the first lockdown because of Covid in 2020 and allowed me to get more familiar with the field of CO_2RR. In the third chapter, I presented a strategy to functionalize bimetallic Ag-Cu catalysts with thiadiazole and triazole derivatives. We found that the strong electron withdrawing groups based on aromatic heterocycles can effectively orient the pathway of the CO_2RR reactions towards the synthesis of C_{2+} molecules. This proof of concept was further extended and optimized by the use of aryl diazonium salts (Chapter 4). We identified a library of electron-withdrawing aryl diazonium salts to functionalize Cu catalysts. The functionalized electrodes were fabricated and investigated to elucidate the influence of Cu valence on the high selectivity of ethylene during the CO_2RR. In parallel of these thrusts in the design of Cu catalysts, we successfully integrated our catalysts into flow electrolyzer.

5.2 Perspectives

Despite these successes for converting CO_2 to multi-carbon products, the presented results still require additional efforts to meet high products selectivity, high energy efficiency and competitive current density. I list below some of the important challenges in the field:

(1) In this thesis, high selectivity, high current density and high energy efficiency were obtained by assembling our electrodes and anion exchange membranes (AEM) in a membrane-electrode-assembly (MEA) electrolyzer, which is considered to be an electrolysis system close to the industry applications. However, classic challenges such as both salt precipitation and water flooding at the back side of gas diffusion layer in AEM assembled MEA electrolyzers still exist. This lowers the selectivity of specific products during the long-term stability and hinders the development of MEA electrolyzer towards industry. Therefore, seeking for an effective method to mitigate or solve this problem has become one of the most important tasks. Replacing AEM by bipolar membrane (BPM) has been considered as a promising method, as the BPM works by dissociating water at the sandwiched cation and anion membrane interfaces when anion and cation exchange layer face to anode and cathode respectively, which suppress the crossing of OH^- and react with CO_2 to form carbonate in the CO_2 gas channel. Nevertheless, the BPM assembled MEA usually shows the unsatisfying performance due to the serious HER at the cathode and high internal resistance. Therefore, it will be important to design novel BPM membranes with tailored functional groups and assembling them into a MEA. In this context, we note that more attention has recently been given to the use of BPM membranes for CO_2RR, which therefore involves interdisciplinary research between polymer science, electrochemistry and chemical engineering.

(2) Currently, CO_2 electroreduction to single carbon products (CO and HCOOH) has almost achieved industrial targets in terms of activity and conversion rate with excellent stability. However, the energy efficiency, the single-pass conversion rate and current density of the electrochemical CO_2 reduction to C_{2+} products are still too low to make the technology economically viable and competitive with traditional process based on fossil fuels. This is attributed to losses at kinetic (ohmic loss, internal resistance, charge transfer resistance) and thermodynamic levels (overpotentials).

(3) The formation of multicarbon products still requires large overpotentials due to the high energy required for the dimerization of the *CO/*CHO intermediates. Besides there is currently no catalyst that can optimize the binding of the different reaction intermediates leading to mediocre energy efficiency and poor selectivity.

(4) Encouraged by the recent advances in CO electroreduction, coupling electrochemical CO_2 with the CO reduction reaction can be an effective method to shorten the gap between experiment and industry towards multi-carbons production, while lower cathodic potential. Compared to CO_2RR, the electrochemical CO reduction to C_{2+} products involve less protons coupled electrons transfer process, which makes it easier to get multi-carbons with high selectivity. Moreover, the carbonate-free in CO electroreduction reaction makes it another big advantage. Efforts must therefore be devoted to achieve high selectivity and high energy efficiency towards multi-carbons through cascade reactions.

Recently, many researches paid much attention on the study of copper-based catalysts, since copper is the only one transmit metal can produce multi-carbon products so far in electrochemical CO_2 reduction reaction. Several important contributions have recently led to the identification of other transition metal as alternatives, dopant or as co-catalyst and call for additional investigations. It is necessary to develop advanced catalysts by using novel methodologies combining experiments, ex-situ and operando characterizations and first principal calculations.